LAWRENCE
LIVERMORE
NATIONAL
LABORATORY

UCRL-TR-234800

FY05 HPCRM Annual Report: High-Performance Corrosion-Resistant Iron-Based Amorphous Metal Coatings

J.C. Farmer, J-S. Choi, J.J. Haslam, S.D. Day, N. Yang, T. Headley, G. Lucadamo, J.L. Yio, J. Chames, A. Gardea, M. Clift, G. Blue, W. Peters, J.D.K. Rivard, D.C. Harper, D. Swank, R. Bayles, E.J. Lemieux, R. Brown, T.M. Wolejsza, L.F. Aprigliano, D.J. Branagan, M.C. Marshall, B.E. Meacham, L.F. Aprigliano, D.J. Branagan, M.C. Marshall, B.E. Meacham, E.J. Lavernia, J. Schoenung, L. Ajdelsztajn, J. Dannenberg, O.A. Graeve, J.J. Lewandowski, J.H. Perepezko, K. Hildal, L. Kaufman, J. Boudreau

September 20, 2007

This work was performed under the auspices of the U.S. Department of Energy by University of California, Lawrence Livermore National Laboratory under Contract W-7405-Eng-48.

UCRL-TR-234800

FY05 HPCRM ANNUAL REPORT:

HIGH-PERFORMANCE CORROSION-RESISTANT IRON-BASED AMORPHOUS METAL COATINGS

DOE-DARPA Sponsored HPCRM Team
Prepared by Joseph C. Farmer

AUTHORS & TECHNICAL CONTRIBUTIONS

Joseph C. Farmer, Jor-Shan Choi, Jeffrey J. Haslam & S. Daniel Day
Lawrence Livermore National Laboratory (LLNL)

Nancy Yang, T. Headley, G. Lucadamo, J. L Yio, J. Chames, A. Gardea & M. Clift
Sandia National Laboratory California (SNL CA)

Craig A. Blue, William Peters & John D. K. Rivard, David C. Harper
Oak Ridge National Laboratory (ORNL)

David Swank (TNC Affiliate)
Idaho Natlional Laboratory (INL)

Robert Bayles & Edward J. Lemieux
Naval Research Laboratory (NRL)

Robert Brown & Theresa M. Wolejsza (NRL Affiliate)
Geo-Centers Corporation (GCC)

Louis F. Aprigliano (Naval Surface Warfare Center Retiree)
Strategic Analysis (SA)

Daniel J. Branagan, M. Craig Marshall, Brian E. Meacham & E. Joseph Buffa
The NanoSteel Company (TNC)

M. Brad Beardsley
Caterpillar Incorporated (CAT)

Erique J. Lavernia, Julie Schoenung, Leonardo Ajdelsztajn & Jon Dannenberg
University of California Davis (UCD)

Olivia A. Graeve
University of Nevada Reno (UNR)

John J. Lewandowski
Case Western Reserve University (CWRU)

John H. Perepezko & Kjetil Hildal
University of Wisconsin Madison (UWM)

Larry Kaufman
CALPHAD & Massachusetts Institute of Technology (MIT)

Jay Boudreau
BLE

TABLE OF CONTENTS

FY05 HPCRM ANNUAL REPORT:

HIGH-PERFORMANCE CORROSION-RESISTANT IRON-BASED AMORPHOUS METAL COATINGS

ABSTRACT

New corrosion-resistant, iron-based amorphous metals have been identified from published data or developed through combinatorial synthesis, and tested to determine their relative corrosion resistance. Many of these materials can be applied as coatings with advanced thermal spray technology. Two compositions have corrosion resistance superior to wrought nickel-based Alloy C-22 (UNS # N06022) in some very aggressive environments, including concentrated calcium-chloride brines at elevated temperature.

Two Fe-based amorphous metal formulations have been found that appear to have corrosion resistance comparable to, or better than that of Ni-based Alloy C-22, based on breakdown potential and corrosion rate. Both Cr and Mo provide corrosion resistance, B enables glass formation, and Y lowers critical cooling rate (CCR). SAM1651 has yttrium added, and has a nominal critical cooling rate of only 80 Kelvin per second, while SAM2X7 (similar to SAM2X5) has no yttrium, and a relatively high critical cooling rate of 610 Kelvin per second.

Both amorphous metal formulations have strengths and weaknesses. SAM1651 (yttrium added) has a low critical cooling rate (CCR), which enables it to be rendered as a completely amorphous thermal spray coating. Unfortunately, it is relatively difficult to atomize, with powders being irregular in shape. This causes the powder to be difficult to pneumatically convey during thermal spray deposition. Gas atomized SAM1651 powder has required cryogenic milling to eliminate irregularities that make flow difficult. SAM2X5 (no yttrium) has a high critical cooling rate, which has caused problems associated with devitrification. SAM2X5 can be gas atomized to produce spherical powders of SAM2X5, which enable more facile thermal spray deposition.

The reference material, nickel-based Alloy C-22, is an outstanding corrosion-resistant engineering material. Even so, crevice corrosion has been observed with C-22 in hot sodium chloride environments without buffer or inhibitor. Comparable metallic alloys such as SAM2X5 and SAM1651 may also experience crevice corrosion under sufficiently harsh conditions. Accelerated crevice corrosion tests are now being conducted to intentionally induce crevice corrosion, and to determine those environmental conditions where such localized attack occurs.

Such materials are extremely hard, and provide enhanced resistance to abrasion and gouges (stress risers) from backfill operations, and possibly even tunnel boring. The hardness of Type 316L Stainless Steel is approximately 150 VHN, that of Alloy C-22 is approximately 250 VHN, and that of HVOF SAM2X5 ranges from 1100-1300 VHN.

These new materials provide a viable coating option for repository engineers. SAM2X5 and SAM1651 coatings can be applied with thermal spray processes without any significant loss of corrosion resistance. Both Alloy C-22 and Type 316L stainless lose their resistance to corrosion during thermal spraying. Containers for the transportation, storage and disposal of spent nuclear fuel (SNF) and high-level radioactive waste (HLW) with corrosion resistant coatings are envisioned. For example, an enhanced multi-purpose container (MPC) could be made with suchc coatings, leveraging existing experience in the fabrication of such containers. These coating materials could be used to protect the final closure weld on SNF/HLW disposal containers, eliminate need for stress mitigation. Integral drip shield could be produced by directly spraying it onto the disposal container, thereby eliminating the need for an expensive titanium drip shield. In specific areas where crevice corrosion is anticipated, such as the contact point between the disposal container and pallet, HVOF coatings could be used to buildup thickness, thereby selectively adding corrosion life where it is needed.

Both SAM2X5 & SAM1651 have high boron content which enable them to absorb neutrons and therefore be used for criticality control in baskets. Alloy C-22 and 316L have no neutron absorber, and cannot be used for such functions. Borated stainless steel and Gd-doped Ni-Cr-Mo alloys are being shown to have relatively poor corrosion performance.

NOMENCLATURE

Acronyms

Auger Electron Spectroscopy	AES
Case Western Reserve University	CWRU
Critical Cooling Rate	CCR
Cyclic Polarization:	CP
Corrosion Rate	CR
Defense Advanced Projects Agency	DARPA
Differential Scanning Calorimetry	DSC
Defense Sciences Office	DSO
Differential Thermal Analysis	DTA
Department of Energy	DOE
Energy Dispersive Analysis with X-Rays	EDAX
Electrochemical Impedance Spectroscopy	EIS
Equivalent Weight	EW
Conversion Factor	K
Melt-Spun Ribbon	MSR
High Level Waste	HLW
Hardness Rockwell C	HRC
High-Velocity Oxy-Fuel Process:	HVOF
Idaho National Laboratory	INL
Lawrence Livermore National Laboratory	LLNL
Linear Polarization	LP
Multi-Purpose Container	MPC
McClellan Nuclear Radiation Center	MNRC

Nevada Test Site	NTS
Naval Research Laboratory	NRL
Naval Surface Warfare Center	NSWC
Normal Hydrogen Reference Electrode	NHE
Oak Ridge National Laboratory	ORNL
Office of Civilian Radioactive Waste Management	OCRWM
Office of Science & Technology International	OSTI
Open Circuit Potential	OCP
Potential-Step Test	PST
Quality Assurance	QA
Qualified Supplier List	QSL
Structural Amorphous Metal	SAM
Secondary Ion Mass Spectrometry	SIMS
Scanning Electron Microscope	SEM
Surface Enhanced Raman Spectroscopy	SERS
Standard Hydrogen Reference Electrode	SHE
Spent Nuclear Fuel	SNF
Sandia National Laboratory	SNL
Silver/Silver-Chloride Reference Electrode	SSC
Time-of-Flight SIMS	TOF-SIMS
The NanoSteel Company	TNC
Thermal Gravimetric Analysis	TGA
Transmission Electron Microscopy	TEM
University of California – Berkeley	UCB
University of California – Davis	UCD
University of Nevada – Reno	UNR
University of Wisconsin – Madison	UWM
Vickers Hardness Number	VHN
Wavelength Dispersive Spectroscopy	WDS
Waste Package	WP
Yucca Mountain Project	YMP
X-Ray Diffraction	XRD

Mathematical Symbols

Modulation Frequency	f
Heat Transfer Coefficient	h
Corrosion Current Density	i_{corr}
Thermal Conductivity	k
Dimension	l
Time	t
Direction	x
Direction	y
Direction	z
Electrode Area	A
Tafel Parameter	B

Biot Number	Bi
Critical Potential:	$E_{critical}$
Open Circuit Corrosion Potential:	E_{corr}
Reversal Potential:	E_{rev}
Potential of Anodic Oxidation Peak:	E_{peak}
Repassivation Potential:	E_{rp}
Faraday's Constant	F
Corrosion Current	I_{corr}
Universal Gas Constant	R
Polarization Resistance	R_p
Temperature	T
Glass Transition Temperature	T_g
Recrystallization Temperature	T_x
Melting Point	T_m
Liquidous	T_L
Reduced Glass Transition Temperature	T_{rg}
Complex Impedance	Z
Real Part of the Complex Impedance	Z_{real} *(also Z')*
Imaginary Part of the Complex Impedance	Z_{imag} *(also Z")*
Amplitude of Complex Impedance	$\|Z\|$
Anodic Tafel Slope	β_a
Cathodic Tafel Slope	β_c
Impedance Phase Angle	ϕ
Density	ρ

INTRODUCTION

Corrosion costs the Department of Defense billions of dollars every year, with an immense quantity of material in various structures undergoing corrosion. For example, in addition to fluid and seawater piping, ballast tanks, and propulsions systems, approximately 345 million square feet of structure aboard naval ships and crafts require costly corrosion control measures. The use of advanced corrosion-resistant materials to prevent the continuous degradation of this massive surface area would be extremely beneficial. The Fe-based corrosion-resistant, amorphous-metal coatings under development may prove of importance for applications on ships. The possible advantages of amorphous metals has been recognized for some time [Latanison 1985].

Two Fe-based amorphous metal formulations have been found that appear to have corrosion resistance comparable to, or better than that of Ni-based Alloy C-22, based on breakdown potential and corrosion rate. Both Cr and Mo provide corrosion resistance, B enables glass formation, and Y lowers critical cooling rate (CCR). SAM1651 has yttrium added, and has a nominal critical cooling rate of only 80 Kelvin per second, while SAM2X7 (similar to SAM2X5) has no yttrium, and a relatively high critical cooling rate of 610 Kelvin per second.

Both amorphous metal formulations have strengths and weaknesses. SAM1651 (yttrium added) has a low critical cooling rate (CCR), which enables it to be rendered as a completely amorphous thermal spray coating. Unfortunately, it is relatively difficult to atomize, with powders being irregular in shape. This causes the powder to be difficult to pneumatically convey during thermal spray deposition. Gas atomized SAM1651 powder has required cryogenic milling to eliminate irregularities that make flow difficult. SAM2X5 (no yttrium) has a high critical cooling rate, which has caused problems associated with devitrification. SAM2X5 can be gas atomized to produce spherical powders of SAM2X5, which enable more facile thermal spray deposition.

These new materials provide a viable coating option for repository engineers. SAM2X5 and SAM1651 coatings can be applied with thermal spray processes without any significant loss of corrosion resistance. Both Alloy C-22 and Type 316L stainless lose their resistance to corrosion during thermal spraying. Containers for the transportation, storage and disposal of spent nuclear fuel (SNF) and high-level radioactive waste (HLW) with corrosion resistant coatings are envisioned. For example, an enhanced multi-purpose container (MPC) could be made with suchc coatings, leveraging existing experience in the fabrication of such containers. These coating materials could be used to protect the final closure weld on SNF/HLW disposal containers, eliminate need for stress mitigation. Integral drip shield could be produced by directly spraying it onto the disposal container, thereby eliminating the need for an expensive titanium drip shield. In specific areas where crevice corrosion is anticipated, such as the contact point between the disposal container and pallet, HVOF coatings could be used to buildup thickness, thereby selectively adding corrosion life where it is needed. Such materials are extremely hard, and provide enhanced resistance to abrasion and gouges (stress risers) from backfill operations, and possibly even tunnel boring. The hardness of Type 316L Stainless Steel is approximately 150 VHN, that of Alloy C-22 is approximately 250 VHN, and that of HVOF SAM2X5 ranges from 1100-1300 VHN. Both SAM2X5 & SAM1651 have high boron content which enable them to absorb neutrons and therefore be used for criticality control in baskets, while C-22 and 316L

have no neutron absorber, and cannot be used for such functions. Borated stainless steel and Gd-doped Ni-Cr-Mo alloys are being shown to have relatively poor corrosion performance.

MATERIALS DESIGN AND SYNTHESIS

This project has three primary long-term goals, all directed towards development of advanced amorphous-metal thermal-spray coatings with corrosion resistance superior to: (1) Type 316L stainless steel [UNS # S31603], (2) nickel-based Alloy C-22 [UNS # N06022], and (3) Ti Grade 7 (UNS # R52400). Computational materials science has been used to help guide the design these new materials [Kaufman 2004; Farmer et al. 2004].

Several thermal spray processes have been developed by industry and include: flame spray, wire-arc; plasma spray; water-stabilized plasma spray; high-velocity oxy-fuel; and the detonation gun. Any of these can be used for the deposition of Fe-based amorphous metals, with varying degrees of residual porosity and crystalline structure. The coatings discussed here were made with the high-velocity oxy-fuel (HVOF) process, which involves a combustion flame, and is characterized by gas and particle velocities that are three to four times the speed of sound (mach 3 to 4). This process is ideal for depositing metal and cermet coatings. These coatings have typical bond strengths of about 8,600 pounds per square inch, porosities of less than one percent (<1%), and micro-hardness of 68 HRC.

Full Density Corrosion-Resistant Compositions

The development of an appropriate powder composition for the production of a corrosion-resistant thermal-spray coating requires that the alloy first be tested in a form with no porosity, and with little or no crystalline phases present. Testing of such materials enables determination of the best possible corrosion performance for a given composition. Melt spinning and arc-melting with drop casting have been used as methods to synthesize completely amorphous, Fe-based, corrosion-resistant alloys with near theoretical density, thereby enabling the effects of coating morphology on corrosion resistance to be separated from the effects of elemental composition.

Melt Spinning Process.

Cooling rates as great as one billion Kelvin per second (10^9 K/s) have been achieved with melt spinning. In contrast, the cooling rate in a typical thermal spray process such as HVOF are on the order of ten thousand Kelvin per second (10^4 K/s). The melt-spun ribbons produced with this equipment are several meters long, several millimeters wide, and approximately 150 microns thick.

The melt spinning involves the ejection of a liquid melt onto a rapidly moving copper wheel with a pressure-controlled gas. The liquid melt solidifies onto the wheel, with subsequent separation from the wheel by thermal contraction and centrifugal force, and collection in a chamber. By changing the tangential velocity of the wheel, as well as other processing parameters, the cooling rate can be controlled over a very broad range. The specific processing parameters for the melt-spinning process can be selected to establish cooling rates that are representative of a given

thermal spray process. If a specific cooling rate produces an amorphous, glassy metal during melt spinning, it should also produce a glassy structure during thermal spray. It is therefore possible to use melt spinning to simulate the type of microstructure that can be achievable with thermal spraying, such as the high-velocity oxy-fuel process. Furthermore, an entire series of developmental materials, with different compositions, heat capacities, and thermal conductivity, can be made with the exact same cooling rate, thereby enabling materials scientists and engineers to determine the relative ease of processing.

Several alloy compositions of Fe-based amorphous metals have been produced, characterized, and tested [Farmer et al. 2005]. In principle, all were intended to be compositional modifications of the SAM40 parent material, obeying the following the general formula: $[(SAM40)_{100-x} + Y_x]$ where Y is the added element, and x is the amount of the addition in atomic percent. Additives investigated included nickel, chromium, molybdenum, tungsten, yttrium, titanium and zirconium. The nickel and molybdenum additions are known to greatly influence the electrochemical properties of conventional stainless steel alloys [Asphahani 1980]. The yttrium, titanium, and zirconium additions, while not normally added to steels are known to form very stable oxides and are expected to increase the stability and passivity of the oxide film in a variety of environments. The SAM1651 formulation has the same nominal elemental composition as the P-containing Fe-based amorphous metal formulation discussed in the literature by Pang et al. [2002]. These materials have been selected with particular emphasis on glass forming ability, thermal stability, hardness, and corrosion resistance, all under conditions of interest [Farmer et al. 2004].

The melt-spinning process was used to perform a systematic study of various elemental compositions, each based on the Fe-based SAM40 composition, with 1, 3, 5, and 7 atomic percent additions of specific elements believed to be beneficial to glass formation or corrosion resistance (Table 1). Elemental additions investigated included nickel, molybdenum, yttrium, titanium, zirconium, and chromium. The densities of the amorphous metals prepared with melt spinning were determined, and all were less dense than nickel-based N06022 (Alloy C-22), and therefore offer a weight advantage over such classical corrosion-resistant alloys. The first re-crystallization peak for each of melt-spun ribbons was determined with DTA, and was similar to that of the parent material (SAM40). The formula with the yttrium additions showed re-crystallization peaks at higher temperatures than achieved with other formulae, showing that yttrium additions do indeed promote thermal stability and glass formability. Some formulae exhibited a second re-crystallization process at a higher temperature than the first, with titanium and zirconium based formulations showing these processes at the highest temperatures. All of the "as-cast" amorphous metal formulae produced by the HPCRM Team exhibited hardness far superior to many of the conventional materials of interest, such as Type 316L stainless steel, and nickel-based N06022 (Alloy C-22). Thus, coatings of these materials would also be expected to be less prone to erosion, wear and gouging than conventional engineering alloys. Partially de-vitrified samples of the HPCRM materials exhibited dramatic increases in hardness. Thus, carefully controlled heat treatment of these materials can be used to achieve dramatic improvements in resistance to erosion, wear and penetration.

Arc Melting with Drop Casting

In addition to the melt-spinning process, arc-melted drop-cast ingots were synthesized for corrosion testing. These ingots were cast into cylindrical molds, thus forming long rods with a nominal diameter of 2-3 millimeters. By exploring the findings of Poon et al. [2004], it has been learned that additions of 2-3 atomic percent yttrium or zirconium can enhance the glass-forming ability (GFA), and substantially lower the required critical cooling rate (CCR). Such formulations are relatively easily cast as large-diameter (several millimeter) rods. X-ray diffraction (XRD) patterns for a SAM2X5 melt-spun ribbon, and a SAM1651 drop-cast ingot, were determined at various temperatures [Yang et al. 2004]. The data at 150, 300 and 500°C indicate very little crystalline structure, with the broad peaks suggesting the presence of dispersed crystalline phases in an amorphous matrix. These data also show the onset of devitrification of SAM1651 and SAM40 (parent material) at 800°C and above. From the electron backscatter images, the advantages of rare earth additions are evident. The exact composition of this material, which has also been produced as melt-spun ribbon, is published elsewhere [Farmer et al. 2004].

Optimization of the thermal spray process through careful selection of powder size and process temperature, has now yielded coatings of SAM40 (non-optimized elemental coating) that are virtually pore-free, and for all practical purposes, fully dense. These new coating architectures have also been shown, through detailed examination with XRD and SEM, to be amorphous. An optimized thermal spray process is now being used to render SAM2X5 and SAM1651 amorphous metal formulations as high-performance corrosion-resistant coatings, with nearly full density, no significant porosity, and good bond strength.

ELECTROCHEMICAL CORROSION TESTING

Range of Environments

Actual Yucca Mountain brines are categorized with the trilateral diagram shown in Figure 1. The boundary between the sulfate-chloride ((SO_4^{-2}) and calcium chloride (Ca^{+2}) regions is idealized. Many of the water compositions that fall in the idealized calcium chloride (Ca^{+2}) region may actually evolve to sulfate-chloride (SO_4^{-2}) or bicarbonate (HCO_3^-) type brines due to the presence of fluoride. The matrix of test solutions now being used at LLNL for the evaluation of iron-based amorphous metals is given in Table 3, and represents extremes of composition that could evolve from the evaporative concentration of natural ground waters and dust deliquescence.

Determining Critical Potential with Cyclic Polarization

Spontaneous breakdown of the passive film and localized corrosion require that the open-circuit corrosion potential exceed the critical potential:

$$E_{corr} \geq E_{critical}$$

The resistance to localized corrosion is quantified through measurement of the open-circuit corrosion potential (E_{corr}), the breakdown potential ($E_{critical}$) and the repassivation potential (E_{rp}). The greater the difference between the open-circuit corrosion potential and the repassivation potential (ΔE), the more resistant a material is to modes of localized corrosion such a pitting and crevice corrosion.

Cyclic polarization (CP) is used as a means of measuring the critical potential ($E_{critical}$) of corrosion resistant materials, relative to their open-circuit corrosion potential (E_{corr}). In the published scientific literature, different bases exist for determining the critical potential from electrochemical measurements. Some have defined the critical potential for crevice corrosion of Alloy 22 as the point where the current density increases to 1 to 10 $\mu A/cm^2$ (10^{-6} to 10^{-5} A/cm^2) during the forward (anodic) scan, whereas others define the repassivation potential as the point where the current density drops to 0.1 to 1 $\mu A/cm^2$ (10^{-6} to 10^{-7} A/cm^2), and use the repassivation potential as a conservative estimate of the critical value [Farmer et al. 2000a].

Cyclic polarization measurements have been based on a procedure similar to ASTM G-5, with slight modification [American Society for Testing and Materials]. For example, ASTM G-5 calls for an electrolyte of 1N H_2SO_4, whereas natural seawater, synthetic bicarbonate brines, synthetic sulfate-chloride brines, 4M NaCl solutions, and 5M $CaCl_2$ solutions with various levels of nitrate were used in this study. The compositions of the synthetic brines are given in the literature [Farmer et al. 2000]. Furthermore, ASTM G-5 calls for the use of de-aerated solutions, whereas aerated and de-aerated solutions were used here. After a 24-hour hold period, during which the open circuit corrosion potential is determined, the potential is scanned in the positive (anodic) direction from a level slightly more negative than the corrosion potential (cathodic limit), to a reversal potential (E_{rev}) near that required for oxygen evolution (anodic level). During the positive scan, anodic oxidation peaks may be observed (centered at E_{peak}) that have been correlated with the oxidation of molybdenum at the alloy surface (passive film), as well as current excursions that are usually associated with breakdown of the passive film. During the negative (cathodic) scan, a hysteresis loop will be observed in cases where passivity has been lost. As the scan continues, the current density may eventually decrease to a level equivalent to that experienced during the positive scan, and indicative of reformation of the passive film. The potential at which this occurs is known as the repassivation potential (E_{rp}).

Temperature-controlled borosilicate glass (Pyrex) electrochemical cells like the one shown in Figure 2 were used for cyclic polarization and other similar electrochemical measurements. This cell has three electrodes, a working electrode (test specimen), the reference electrode, and the counter electrode. A standard silver silver-chloride electrode, filled with near-saturation potassium chloride solution, is used as the reference, and communicates with the test solution via a Luggin probe placed in close proximity to the working electrode, thereby minimizing Ohmic losses. Numerical corrections for the reference electrode junction potential have been estimated, and have been found to be insignificant (Farmer et al. 2000). The electrochemical cell is equipped with a water-cooled junction to maintain reference electrode at ambient temperature, thereby maintaining integrity of the potential measurement, and a water-cooled condenser to prevent the loss of volatile species from the electrolyte.

There competing methodologies (Methods A, B and C) for the determination of the threshold potential for localized corrosion from cyclic polarization curves are shown in Figure 3, which is an actual cyclic polarization curve for Alloy C-22 in 5M $CaCl_2$ at 105°C. Method A is the point during the anodic potential scan when the passive oxide film breaks down, thereby allowing anodic dissolution of the underlying metal, with a relatively high anodic current density. The current density corresponding to a complete loss of passivity is assumed to be either 20 or 200 $\mu A/cm^2$. When it can be accurately measured, this is the true "critical potential." Alternatively, the repassivation potential can be determined with either Methods B or C. The repassivation potential is determined during the reverse scan, and is the point following passive film breakdown where the current density decreases to a level known to correspond to the passive current density (the current density that can be sustained by an intact oxide film). The passive current density can either be assumed, shown as Method B, or it can be established from the intersection of the forward and reverse potential scans, shown as Method C. Method C is considered to be the most rigorous approach for determining the repassivation potential, since the intersection point occurs at the actual (not assumed) passive current density.

- Method A – Initial Breakdown of Passive Film
  - Critical Potential ($E_{critical}$) = Breakdown Potential (E_{20} *or* E_{200})
  - Based Threshold Current Density of 20 or 200 $\mu A/cm^2$
- Method B – Repassivation of Surface
  - Critical Potential ($E_{critical}$) = Repassivation Potential (E_{R1} *or* E_{R2})
  - Based Threshold Current Density of 1 or 2 $\mu A/cm^2$
- Method C – Repassivation of Surface
  - Critical Potential ($E_{critical}$) = Repassivation Potential (E_{RP})
  - Intersection of Forward Scan with Hysteresis Loop (Cross-Over Point)

As illustrated by Figure 4, the repassivation potential, determined by Method C in most cases, has been used as a quantitative metric for screening elemental compositions of competing iron-based amorphous metals, thereby determining the specific composition (of those tested) with the best resistance to passive film breakdown in the test solution. A wide variety of alloy compositions, which are shown in Table 1, were explored using cyclic polarization as a screening method. However, as will be evident in the discussion of subsequent potential-step test data, superior and more credible methods exist for the determination of the critical potential. The potential step-methods are used after the initial screening, and provide better results.

Alloy Screening with Cyclic Polarization

As shown in Figure 5, cyclic polarization was used as a means of evaluating the relative passive film stability of a drop-cast ingot of SAM1651, a disk of wrought nickel-based Alloy C-22 (reference material), and a thermal spray (high-velocity oxy-fuel or HVOF) coating of Alloy C-22. The test was conducted in Half Moon Bay seawater at 30°C, and the potential was measured relative to a standard silver / silver chloride reference electrode. The scan rate was 0.l667 volts per second. The current density for the 'as-sprayed' Alloy C-22 HVOF coating is based upon apparent electrode area, and was not corrected for surface roughness. In the case of the SAM1651, no passive film breakdown was observed, which is evident from the lack of

hysteresis, even after scanning the voltage to a level close to oxygen evolution. Passive film breakdown was observed with wrought Alloy C-22, with a repassivation potential by Method C easily identified. Surprisingly, the Alloy C-22 coating loses has very poor corrosion resistance in comparison to both the SAM1651 ingot and the wrought Alloy C-22, which is reflected in a low repassivation potential.

As shown in Figure 6, cyclic polarization was used to compare the performance of a drop-cast ingot of SAM1651 against that of wrought Alloy C-22 in 5M calcium chloride at 105°C, which is an extremely aggressive environment. In the case of the drop-cast ingot of SAM1651, no significant passive film breakdown was observed at 0.9 to 1.0 volts. There was no positive hysteresis loop observed with this iron-based amorphous metal. There was hysteresis, but with the observed current density during the reverse less than that observed during the forward scan (indicative of even lower reactivity). In sharp contrast, there is an obvious breakdown of the nickel-based Alloy C-22 passive film at only 0.2 volts, showing a clear vulnerability in this aggressive environment. The repassivation potential is easily identified from the intersection of the hysteresis loop with the forward scan.

Cyclic polarization of melt spun ribbons was used to compare the relative corrosion resistance of a large number candidate alloy compositions in 5M $CaCl_2$ at 105°C, with the results summarized in Figure 7. The alloy compositions are defined in Table 1. As previously discussed, the quantifiable metric used as a basis of comparison was the difference between the open circuit corrosion potential (E_{corr}) and the repassivation potential (E_{rp}). Several of the candidate alloy compositions had a larger metric value (E_{rp}- E_{corr}) than the reference material, which has been established as nickel-based Alloy C-22, due to its own outstanding corrosion performance. Note that DARPA Milestone 1 corresponds to the metric value for Type 316L stainless steel and DARPA Milestone 2 corresponds to the metric value for nickel-based Alloy C-22. It is therefore concluded that several types of iron-based amorphous metals exist which all have passive film stabilities that are comparable to that of the reference material.

Cyclic polarization of melt spun ribbons was also used to compare the relative corrosion resistance of a large number candidate alloy compositions in near-ambient Half Moon Bay seawater at 30°C, with the results summarized in Figure 8. The alloy compositions are defined in Table 1. DARPA Milestone 1 corresponds to the metric value for Type 316L stainless steel and DARPA Milestone 2 corresponds to the metric value for nickel-based Alloy C-22. It is therefore concluded that several types of iron-based amorphous metals exist which all have passive film stabilities in seawater at 30°C that are comparable to that of the reference material.

Cyclic polarization of melt spun ribbons was further used to compare the relative corrosion resistance of a large number candidate alloy compositions in near-boiling Half Moon Bay seawater at 90°C, with the results summarized in Figure 9. The alloy compositions are defined in Table 1. DARPA Milestone 1 corresponds to the metric value for Type 316L stainless steel and DARPA Milestone 2 corresponds to the metric value for nickel-based Alloy C-22. It is therefore concluded that several types of iron-based amorphous metals exist which all have passive film stabilities in seawater at 90°C that are comparable to that of the reference material.

Determining Corrosion Rate with Linear Polarization

The linear polarization method has been used as a method for determining the corrosion rates of the various amorphous metal coatings, including SAM2X5 and SAM1651. This method is based upon experimental determination of electrokinetic parameters in the classic Tafel equation with a potentiostat. The classic Butler-Volmer expression collapses into the well-known anodic Tafel equation at high anodic potential, where the contribution of the electrochemical reduction (cathodic) reaction to the overall current at the electrode surface becomes insignificant (defined as < 1%). At high cathodic potential, where the contribution of the electrochemical oxidation (anodic metal dissolution) reaction to the net electrode current is insignificant, the Butler-Volmer expression becomes the cathodic Tafel equation.

The procedure used for linear polarization testing consists of the following steps:

- Hold the sample for ten (10) seconds at the open circuit potential (OCP).
- Beginning at a potential 20 mV below the OCP (OCP-20 mV), increase the potential linearly at a constant rate of 0.1667 mV per second, to a potential 20 mV above the OCP (OCP+20 mV).
- Record the current being passed from the counter electrode to the working electrode by the potentiostat, as a function of potential relative to the standard/silver silver-chloride (Ag/AgCl) reference electrode.
- Determine the parameters in the cathodic Tafel line by performing linear regression on the voltage-current data from 10 mV below the OCP (OCP-10 mV) to 10 mV above the OCP (OCP+10 mV). The slope of this line is the polarization resistance (R_p).

The polarization resistance (*Rp*) is defined as:

$$R_P = \left(\frac{\partial E}{\partial I}\right)_{E_{corr}}$$

A parameter (*B*) is defined in terms of the slopes of the anodic and cathodic branches of the Tafel line:

$$B = \frac{\beta_a \beta_c}{2.303(\beta_a - \beta_c)}$$

The corrosion current (I_{corr}) is then defined as;

$$I_{corr} = \frac{R}{R_p}$$

The corrosion rate (*CR*) is then calculated as:

$$CR = K \frac{I_{corr}}{A \times \rho}(EW) \text{ (mmpy)}$$

The parameter K is a conversion factor used to express the corrosion rate (CR) in the units of millimeters per year (mmpy) and has a value of 3.27×10^{-3} (mm·g)/(μA·cm·yr); I_{corr} is the corrosion current in microamps (μA); A is the surface area of the sample in square centimeters (cm^2); and ρ is the density of the sample in grams per cubic centimeter (g/cm^3).

Linear polarization was used to determine the approximate corrosion rates of the thermal spray coatings of two amorphous metals of interest (HVOF SAM1651 and SAM2X5 coatings) and the reference material (wrought nickel-based Alloy C-22) in three relevant environments, Half Moon Bay seawater at two temperature levels, and in hot concentrated calcium chloride (5M $CaCl_2$ at 105°C). This data is summarized in Figure 10. In seawater at both 30 and 90°C, the corrosion rates of HVOF SAM2X5 and SAM1651 coatings exhibited slightly lower corrosion rates than either wrought sample of Alloy C-22. The corrosion rates of all materials increased with temperature, as expected. In calcium chloride at 105°C, the corrosion rates of HVOF SAM2X5 and SAM1651 coatings were comparable to, or slightly lower than that of wrought Alloy C-22. In general, the corrosion rates observed in the hot calcium chloride (105°C) were higher than those observed in the heated seawater (90°C), which was also expected.

Validation with Salt Fog Testing

The corrosion resistance of the amorphous metal coatings was verified during salt fog testing. As previously discussed [Farmer et al. 2004], the salt fog test was used to compare various wrought ant thermal-spray alloys, melt-spun ribbons, arc-melted drop-cast ingots, and thermal-spray coatings for their susceptibility to corrosion by salt sprays, like those that might be encountered aboard naval ships (this test is also known as the 'salt spray' test). The most recent tests have focused on refined, state-of-the-art Fe-based amorphous-metal formulations, in the form of arc-melted drop-cast ingots, melt-spun ribbons, and high-velocity oxy-fuel coatings with no significant porosity and near theoretical density. In contrast, the first tests focused on early thermal-spray coatings, which had residual porosity and crystalline structure, and lower resistance to corrosion.

Both salt fog tests were conducted according to ASTM B117 "Standard Test Method of Salt Spray (Fog) Testing." A General Motors (GM) test cycle, GM9540P, was used in both tests. The performance of the test developmental amorphous metal samples was evaluated by qualitative comparison to baseline or reference samples. Four types of reference samples were included to establish baseline performance. These references include: Type 316L stainless steel, nickel-based Alloy C-22 (N06022), Ti Grade 7, and the 50:50 nickel-chromium binary.

Salt fog testing was conducted on several thermal spray coatings, including HVOF coatings of Alloy C-22, Type 316L stainless steel, SAM40 (also referred to as DAR4)), SAM2X5 (also referred to as LDAR2X5) and SAM1651 (also referred to as CBCTL1651 or LDAR7) by Aprigliano et al. [Aprigliano et al. 2005]. After 13 cycles in the ASTM Standard B-117 Salt Fog Test, the 316L stainless steel and SAM40 amorphous metal HVOF coatings experienced

substantial corrosion, as shown in Figure 11. Very slight rust spots were observed on the C-22 coating. In contrast, the newer SAM2X5 and SAM1651 formulations showed no corrosion at 30 cycles. The salt fog testing of SAM2X5 and SAM1651 were continued to almost 60 cycles with no evidence of corrosion.

Threshold for Passive Film Breakdown with Potential-Step Method

Potentiostatic step tests have been used to determine the potential at which the passive film breaks down on the reference material, Alloy C-22, and on the two amorphous metals of primary interest, SAM2X5 and SAM1651. During prolonged periods of potentiostatic polarization, which are typically 24 hours in duration, the current is monitored as a function of time. In cases where passivity is lost, the current increases, and the test sample is aggressively attacked. In cases where passivity is maintained, the current decays to a relatively constant asymptotic level, consistent with the known passive current density. In these tests, periods of polarization are preceded by one hour at the open circuit corrosion potential.

Thresholds for Passive Film Breakdown in Seawater

See Figure 12. Potential-step testing has been performed on wrought Alloy C-22 (reference material); fully dense and completely amorphous melt spun ribbons of SAM2X5; optimized HVOF coatings produced with -53/+30 micron powders of SAM2X5; and optimized HVOF coatings produced with -30/+15 micron powders of SAM2X5. All were tested in Half Moon Bay seawater heated to 90°C. To eliminate the need for surface roughness corrections in the conversion of measured current and electrode area to current density, the SAM2X5 and SAM1651 coatings were polished to a 600-grit finish prior to testing. The curves represent the asymptotic current density reached after 24 hours at the corresponding potential (each data point represents a 24 hour test). The constant potential was applied after 1 hour at the open circuit corrosion potential (OCP). From previous work presented in the FY04 Annual Report (given in references), it has been found that coatings produced with SAM2X5 powders below a critical size are fully dense and are completely amorphous. The coatings produced with finer powders are therefore expected to have lower porosity and less residual crystalline phases present than those produced with larger particles. These data enable a clear and unambiguous determination of the threshold potentials for passive film breakdown in a non-creviced condition. First, it is clear that the passive film on wrought Alloy C-22 commences breakdown at a potential of approximately 200 mV relative to a standard Ag/AgCl reference electrode (approximately 600 mV above the open circuit corrosion potential), and has the least corrosion resistance of any sample evaluated during this test. Passive film breakdown on the SAM2X5 melt-spun ribbon did not occur until a potential in excess of 1200 mV vs. Ag/AgCl (1400 mV above OCP) was applied. Furthermore, the observed passive current density observed with this sample was extremely low. Both HVOF coatings of SAM2X5 (large and small powder sizes) also exhibited outstanding passive film stability, superior to that of the reference material. The passive film on the coating produced with -30/+15 micron powder remained intact until application of 1000 mV vs. Ag/AgCl (1200 mV above OCP), with a current density well within the passive range of several microamps per square centimeter. Similar observations were made with the coating produced with -53/+30 micron powders. Any differences in morphology did not have significant impact on corrosion resistance

See Figure 13. Transients in current density at a constant applied potential of 1000 mV vs. OCP for wrought Alloy C-22 (reference material), a fully dense and completely amorphous melt spun ribbon (MSR) of SAM2X5, HVOF coatings produced with -53/+30 micron powders of SAM2X5, and HVOF coatings produced with -30/+15 micron powders of SAM2X5, all in Half Moon Bay seawater heated to 90°C, are compared. The constant potential was applied after 1 hour at the open circuit corrosion potential (OCP). The passive film on the melt spun ribbon and HVOF coatings of SAM2X5 is more stable than that on wrought nickel-based Alloy C-22 under these conditions, leading to the conclusion that this iron-based amorphous metal has superior corrosion resistance. These coatings were produced with TNC powder by UCD and Plasmatech.

See Figure 14. Transients in current density at various levels of constant applied potential ranging from 100 to 1400 mV vs. OCP for Alloy C-22 in Half Moon Bay seawater at 90°C. This reference material was polished to a 600-grit finish. The constant potential was applied after 1 hour at the open circuit corrosion potential (OCP). Passive film stability is lost above 700 mV vs. OCP. These coatings were produced with TNC powder by UCD and Plasmatech.

See Figure 15. Transients in current density at various levels of constant applied potential ranging from 100 to 1600 mV vs. OCP for a melt-spun ribbon of SAM2X5 in Half Moon Bay seawater at 90°C are indicative of good passive film stability. The constant potential was applied after 1 hour at the open circuit corrosion potential (OCP). The passive film stability of this SAM2X5 sample is maintained at potentials up to 1500 mV vs. OCP, which is approximately 800 mV higher than the critical potential observed with Alloy-C22. At an applied potential of 1600 mV vs. OCP, passivity is lost after several hours. These coatings were produced with TNC powder by UCD and Plasmatech.

See Figure 16. Transients in current density at various levels of constant applied potential ranging from 100 to 1500 mV vs. OCP for a recently optimized SAM2X5 HVOF coating (-30/+15 micron powder) in Half Moon Bay seawater at 90°C are indicative of good passive film stability. The constant potential was applied after 1 hour at the open circuit corrosion potential (OCP). To eliminate the need for surface roughness corrections in the conversion of measured current and electrode area to current density, the SAM2X5 coating was polished to a 600-grit finish prior to testing. The curves represent the asymptotic current density reached after 24 hours at the corresponding potential (each data point represents a 24 hour test). The specified fixed potential was applied after 1 hour at the open circuit corrosion potential (OCP). The passive film stability of this SAM2X5 sample is maintained at potentials up to 1400 mV vs. OCP, which is approximately 700 mV higher than the critical potential observed with Alloy-C22. At an applied potential of 1500 mV vs. OCP, passivity is lost after several hours. These coatings were produced with TNC powder by UCD and Plasmatech.

See Figure 17. Transients in current density at various levels of constant applied potential ranging from 100 to 1500 mV vs. OCP for a recently optimized SAM2X5 HVOF coating (-53/+30 micron powder) in Half Moon Bay seawater at 90°C are indicative of exceptional passive film stability. To eliminate the need for surface roughness corrections in the conversion of measured current and electrode area to current density, the SAM2X5 coatings were polished to a 600-grit finish prior to testing. The constant potential was applied after 1 hour at the open circuit

corrosion potential (OCP). The passive film stability of this SAM2X5 sample is maintained at potentials up to 1400 mV vs. OCP, which is approximately 700 mV higher than the critical potential observed with Alloy-C22. At an applied potential of 1500 mV vs. OCP, passivity is lost after several hours. These coatings were produced with TNC powder by UCD and Plasmatech.

See Figure 18. Potential-step testing has been performed on HVOF coatings of SAM1651 in deaerated Half Moon Bay seawater heated to 90°C. Tests were also performed on the reference material, Alloy C-22, in both wrought and thermally sprayed condition. To eliminate the need for surface roughness corrections in the conversion of measured current and electrode area to current density, the SAM1651 coating was polished to a 600-grit finish prior to testing. The Alloy C-22 thermal spray coating was tested in the as-sprayed condition, so a roughness factor must be applied to convert the apparent current density into actual current density. The curves represent the asymptotic current density reached after 24 hours at the corresponding potential. In this series of experiments, the passive film on wrought Alloy C-22 also commences breakdown at a potential of approximately 600 mV above the open circuit corrosion potential. Passive film breakdown on the HVOF coating of SM1651 occurred at an applied potential between 500 and 600 mV, where breakdown occurred at approximately 400 mV for the Alloy C-22 HVOF coating. In near-boiling seawater, the passive film stability of SAM1651 is comparable to that of Alloy C-22, but inferior to that of SAM2X5.

See Figure 19. Transients in current density at various levels of constant applied potential ranging from 100 to 800 mV vs. OCP for a HVOF coating of SAM1651 in Half Moon Bay seawater at 90°C are indicative of good passive film stability, comparable to that of wrought Alloy C-22. To eliminate the need for surface roughness corrections in the conversion of measured current and electrode area to current density, the SAM2X5 coatings were polished to a 600-grit finish prior to testing. To eliminate the need for surface roughness corrections in the conversion of measured current and electrode area to current density, the SAM1651 coating was polished to a 600-grit finish prior to testing. Passive film breakdown on the HVOF coating of SM1651 occurred at an applied potential between 500 and 600 mV vs. OCP, with a clear loss of passivity at 700 mV. These coatings were produced by TNC and INL before fabrication of the optimized UCD-Plasmatech coatings previously discussed.

See Figure 20. Transients in current density at various levels of constant applied potential ranging from 100 to 800 mV vs. OCP for a polished HVOF coating of SAM1651 on a Type 316L stainless steel substrate (S/N No. E316L409) in Half Moon Bay seawater at 90°C are indicative of good passive film stability, comparable to that of wrought Alloy C-22. To eliminate the need for surface roughness corrections in the conversion of measured current and electrode area to current density, the SAM2X5 coatings were polished to a 600-grit finish prior to testing. To eliminate the need for surface roughness corrections in the conversion of measured current and electrode area to current density, the SAM1651 coating was polished to a 600-grit finish prior to testing. Passive film breakdown on the HVOF coating of SM1651 occurred at an applied potential between 500 and 600 mV vs. OCP, with a clear loss of passivity at 700 mV. The coating represented by this figure is one of the first known thermal spray coatings with the SAM1651 composition, and was produced by TNC and their subcontractor before fabrication of the optimized UCD/Plasmatech coatings, which are represented by the preceding figures.

See Figure 21. Transients in current density at various levels of constant applied potential ranging from 100 to 500 mV vs. OCP for an unpolished (as sprayed) HVOF coating of nickel-based Alloy C-22 on a Type 316L stainless steel substrate (S/N No. E316L255) in Half Moon Bay seawater at 90°C show a clear and unambiguous loss of passivity at the highest potential level. Since this Alloy C-22 coating was tested in the as-sprayed condition, a roughness factor must be applied to convert the 'apparent' current density into the 'actual' current density. The coating represented by this figure was produced by TNC and their subcontractor before fabrication of the optimized UCD/Plasmatech coatings, which are represented by the preceding figures.

See Figure 22. Transients in current density at various levels of constant applied potential ranging from 100 to 736 mV vs. OCP for an unpolished (as sprayed) HVOF coating of SAM1651 on a Type 316L stainless steel substrate (S/N No. E316L410) in Half Moon Bay seawater at 90°C are indicative of good passive film stability, comparable to that of wrought Alloy C-22. Since this as-sprayed SAM1651 coating was tested in the as-sprayed condition, a roughness factor (which is expected to range from a minimum of ×2 to more than ×10) must be applied to convert the 'apparent' current density into the 'actual' current density. While passivity at 158 mV vs. OCP is clear, polished samples with minimal roughness, or unambiguous knowledge of the roughness factor is required to interpret measured 'apparent' current densities at higher applied potential in terms of passivity, or the loss of passivity. From visual inspection, it was evident that passivity was maintained at higher potentials. The ambiguity associated with early electrochemical test data such as this has lead the investigators to use polished samples with 600-grit finish for clear determinations of critical potentials. The coating represented by this figure is one of the first known thermal spray coatings with the SAM1651 composition, and was produced by TNC and their subcontractor before fabrication of the optimized UCD/Plasmatech coatings, which are represented by the preceding figures.

See Figure 23. Transients in current density at various levels of constant applied potential ranging from 100 to 615 mV vs. OCP for an early unpolished (as sprayed) HVOF coating of SAM2X5 on a Type 316L stainless steel substrate (S/N No. E316L445) in Half Moon Bay seawater at 90°C are indicative of good passive film stability, comparable to that of wrought Alloy C-22. Since this as-sprayed SAM2X5 coating was tested in the as-sprayed condition, a roughness factor (which is expected to range from a minimum of ×2 to more than ×10) must be applied to convert the 'apparent' current density into the 'actual' current density. While passivity at 315 mV vs. OCP is clear, current transients are observed at 415 mV on this as-sprayed surface that may be indicative of the onset of passive film breakdown. Such breakdown is clearly evident at a slightly higher potential of 515 mV vs. OCP. While this data shows very good corrosion resistance, more recent optimization has resulted in far better performance with this formulation. The coating represented by this figure is one of the first known thermal spray coatings with the SAM2X5 composition, and was produced by TNC and their subcontractor before fabrication of the new optimized UCD/Plasmatech coatings, which are represented by the preceding figures. The importance of supplier standardization and qualification is illustrated by the enhanced performance that has evolved as we have continued to work with these materials.

See Figure 24. Transients in current density at various levels of constant applied potential ranging from 100 to 460 mV vs. OCP for an early unpolished (as sprayed) HVOF coating of

SAM40XV on a Type 316L stainless steel substrate (S/N No. E316L325) in Half Moon Bay seawater at 90°C are indicative of good passive film stability, comparable to that of wrought Alloy C-22. SAM40XV was an early version of SAM2X5 that TNC prepared for HPCRM with slightly less molybdenum added, and a corresponding lower critical potential. Since this as-sprayed SAMXV coating was tested in the as-sprayed condition, a roughness factor (which is expected to range from a minimum of ×2 to more than ×10) must be applied to convert the 'apparent' current density into the 'actual' current density. While passivity at 100 to 244 mV vs. OCP is clear, current transients observed at 460 and 560 mV are clearly indicative of passive film breakdown. Such high apparent current densities occur at higher potential in the case of SAM2X5. The coating represented by this figure is one of the first known thermal spray coatings with the SAM40XV composition, and was produced by TNC and their subcontractor before fabrication of the new optimized UCD/Plasmatech coatings, which are represented by the preceding figures. The importance of supplier standardization and qualification is illustrated by the enhanced performance that has evolved as we have continued to work with these materials.

Thresholds for Passive Film Breakdown in Hot Calcium Chloride

See Figure 25. Potential-step testing has been performed on HVOF coatings of SAM1651 on a Type 316L stainless steel substrate (S/N No. E316L475) in extremely aggressive 5M $CaCl_2$ heated to 105°C. Tests were also performed on the reference material, Alloy C-22, in both wrought and thermally sprayed condition (S/N Nos. CC-22 4008 and E316L256, respectively). To eliminate the need for surface roughness corrections in the conversion of measured current and electrode area to current density, the SAM1651 coating was polished to a 600-grit finish prior to testing. The Alloy C-22 thermal spray coating was tested in the as-sprayed condition, so a roughness factor must be applied to convert the apparent current density into actual current density. The curves represent the asymptotic current density reached after 24 hours at the corresponding potential. In this series of experiments, the passive film on wrought Alloy C-22 also commences breakdown at a potential of only 240 mV above the open circuit corrosion potential, with evidence of repassivation at potentials above 400 mV. Even with the repassivation at higher potential, the window of vulnerability between 240 to 400 mV is problematic for the reference material (Alloy C-22). Passive film breakdown on the HVOF coating of SAM1651 occurred at a significantly higher applied potential, between 360 and 400 mV, where breakdown of the passive film on thermally sprayed Alloy C-22 was virtually spontaneous. The new SAM1651 coating provides clear advantages for operation in corrosive hot chloride brines with divalent cations, such as calcium.

See Figure 26. Transients in current density at various levels of constant applied potential ranging from 100 to 450 mV vs. OCP for a polished HVOF coating of SAM1651 on a Type 316L stainless steel substrate (S/N No. E316L475) in 5M $CaCl_2$ at 105°C are indicative of good passive film stability, which is superior to that of wrought Alloy C-22 in this environment this very aggressive environment. To eliminate the need for surface roughness corrections in the conversion of measured current and electrode area to current density, the SAM1651 coating was polished to a 600-grit finish prior to testing. Passive film breakdown on the HVOF coating of SAM1651 occurred at an applied potential between 360 and 400 mV vs. OCP, with a clear loss of passivity at 450 mV. The coating represented by this figure is one of the first known thermal spray coatings with the SAM1651 composition, and was produced by TNC and their

subcontractor before fabrication of the optimized UCD/Plasmatech coatings, which are represented by the preceding figures. The performance of this SAM1651 coating was very impressive.

See Figure 27. Transients in current density at various levels of constant applied potential ranging from 100 to 550 mV vs. OCP for wrought Alloy C-22 (S/N No. CC-22 4008) in 5M $CaCl_2$ at 105°C, and shows complete breakdown of the passive film in two potential regimes, one regime located between 300-400 mV vs. OCP (350 mV), and the second located above 500 mV vs. OCP (550 mV). Like the polished SAM1651 coating, this reference was also polished to a 600-grit finish.

See Figure 28. Transients in current density at various levels of constant applied potential ranging from 100 to 350 mV vs. OCP for an unpolished (as-sprayed) HVOF coating of Alloy C-22 on a Type 316L stainless steel substrate (S/N No. E316L256) in 5M $CaCl_2$ at 105°C appears to be passive at 100-150 mV vs. OCP, but has a clear loss of passivity at potentials above 200 mV vs. OCP (250-350 mV). Since this as-sprayed Alloy C-22 coating was tested in the as-sprayed condition, a roughness factor (which is expected to range from a minimum of ×2 to more than ×10) must be applied to convert the 'apparent' current density into the 'actual' current density. The coating represented by this figure was produced by TNC and their subcontractor before fabrication of the optimized UCD/Plasmatech coatings, which are represented by preceding figures.

Effect of Devitrification on Corrosion Resistance

See Figure 29. To assess the sensitivity of these iron-based amorphous metals to devitrification, which can occur at very elevated temperature, melt-spun ribbon of SAM40 (also referred to as DAR40) were intentionally devitrified by heat treating them at various temperatures for one hour. After heat treatment, the samples were evaluated in low temperature seawater (30°C), to determine the impact of the heat treatment on passive film stability and corrosion resistance. The temperatures used for the heat treatment were: 150, 300, 800 and 1000°C. Untreated (as received) ribbons were also tested, and provide insight into the baseline performance. These samples showed no significant hysteresis and change in repassivation potential at heat treatments of 150-300°C, but showed a dramatic loss of corrosion resistance when heat treatments were performed at 800-1000°C, which are above the known recrystallization temperature of approximately 600-650°C (623°C) given in Table 2 (Perepezko et al. 2004). Both ribbons treated at elevated temperature show large hysterisis loops, which are indicative of passive film breakdown, with a clearly defined repassivation potential near -600 mV vs. Ag/AgCl (about 100 mV above the OCP). The operational limit for these materials, when being used for corrosion resistance, appears to be bounded by the recrystallization temperature.

See Figure 30. Melt spun ribbons of SAM40 (DAR40) were also intentionally devitrified by heat treating at 800°C for one hour and then subjected to cyclic polarization in 5M CaCl2 at 105°C. In comparison to the as-received sample, the sample heat-treated at 800C showed a dramatic loss of corrosion resistance. As discussed in regard to the preceding figure, this heat-treatment temperature was known to be above the recrystallization temperature of approximately 600-

650°C (623°C) given in Table 2 (Perepezko et al. 2004). The heat-treated ribbon showed a large hysterisis loop in the hot concentrated calcium chloride solution, which is indicative of passive film breakdown, with a clearly defined repassivation potential neat the OCP. The post heat-treatment microstructural characterization with electron microscopy and X-ray diffraction by Yang et al. verify the existence of a completely amorphous material below the recrystallization temperature, and the development of crystalline precipitates during heat treatment above this limit. These electron microscopy images may also indicate that the corrosive attack of the precipitated crystalline phases occur to a depth of approximately 10 microns. When being used for corrosion resistance in hot geothermal brines such as calcium chloride, the operational limit also appears to be bounded by the recrystallization temperature.

See Figure 31. Melt spun ribbons of SAM2X5 were also intentionally devitrified by heat treating at 800°C for one hour and then subjected to cyclic polarization in 5M CaCl2 at 105°C. In comparison to the as-received sample, the sample heat-treated at 800C showed a dramatic loss of corrosion resistance. As discussed in regard to the preceding figure, this heat-treatment temperature was known to be above the recrystallization temperature of approximately 600-650°C (623°C) given in Table 2 (Perepezko et al. 2004). The heat-treated ribbon showed a large hysterisis loop in the hot concentrated calcium chloride solution, which is indicative of passive film breakdown, with a clearly defined repassivation potential neat the OCP. The post heat-treatment microstructural characterization with electron microscopy and X-ray diffraction by Yang et al. verify the existence of a completely amorphous material below the recrystallization temperature, and the development of crystalline precipitates during heat treatment above this limit. These electron microscopy images may also indicate that the corrosive attack of the precipitated crystalline phases occur to a depth of approximately 10 microns. When being used for corrosion resistance in hot geothermal brines such as calcium chloride, the operational limit also appears to be bounded by the recrystallization temperature.

LONG-TERM CORROSION TESTING

See Figure 32. Temperature controlled baths for long-term corrosion testing of weight loss and crevice corrosion samples, with simultaneous monitoring of the open-circuit corrosion potential, corrosion rate via linear polarization, and passive film stability with electrochemical impedance spectroscopy (EIS). Water cooled condensers are used to prevent the loss of water and other volatiles from the baths, and a water-cooled reference electrode junction is used to enable the Ag/AgCl reference electrodes to be operated at standard temperature, thereby providing a sound thermodynamic reference. The upper photograph show LLNL technicians attending to the test equipment.

Geometries of Coated Samples

See Figure 33. Weight loss and crevice samples for the long term test are 4-inch × 4-inch × ¼-inch Alloy C-22 substrates with a 40-mil thermal spray coating of amorphous metal (SAM2X5, SAM1651, etc.). The crevice samples have a hole in the center to accommodate a crevice former, and are not shown. The long-term measurements of open-circuit corrosion potential, corrosion rate via linear polarization, and electrochemical impedance spectra are done with a ¾-inch diameter Alloy C-22 rod with a hemispherical end, and with a 40-mil thermal spray coating of

amorphous metal (SAM2X5, SAM1651, etc.). Small disks are used for quick screening tests with cyclic polarization, but are not considered truly representative coatings due to their small size and differences in cooling rate experienced by the disks and larger substrates with greater thermal mass and cooling capacity. The granularity of these disks is not representative can be easily seen. While small circular disk samples are relatively inexpensive and easy to produce, and can be employed in standard corrosion test cells with relative ease, they may not provide the best source of data.

Open Circuit Corrosion Potential During Long-Term Exposure

See Figure 34. The long-term corrosion test for the SAM2X5 has been initiated, and the initial open circuit corrosion potentials for this material has been measured in several fully aerated environments, and will be monitored as a function of time for the next year. These environments include Half Moon Bay seawater, 3.5 m NaCl, 3.5 m NaCl with 0.5 m KNO_3, 6.0 m NaCl and 6.0 m NaCl with 0.9 m KNO_3. For each solution composition, tests are being done at two temperature levels, 30 and 90°C.

Corrosion Rates with Linear Polarization During Long-Term Exposure

See Figure 35. In addition to monitoring the open circuit corrosion potential in these fully aerated solutions, linear polarization is also being used periodically to measure the corrosion current, which is normalized by the apparent area of the electrode, and used to estimate the general corrosion rate. The roughness factor for these unpolished (as sprayed) SAM2X5 HVOF samples must be used to convert the apparent current density to the corrosion rate. In this figure, the first series of bars (blue) represent the estimated corrosion rate with no roughness correction, and the second series of bars (magenta) represent the estimated corrosion rate with the minimum estimated roughness factor of 2. The actual roughness may be significantly higher, and is in the process of being quantified. Even without the roughness factor correction, the measured corrosion rates are very low. It is somewhat surprising that in this case, the presence of nitrate appears to accelerate the general corrosion rate, both at 3.5 and 6.0 NaCl concentrations.

Complex Impedance During Long-Term Exposure

See Figure 36. In addition to obtaining corrosion rates with linear polarization during the long term test, electrochemical impedance spectroscopy is used to periodically measure the complex impedance as a function of frequency. Such measurements are made for each environment. The data is presented in the form of a standard Bode plot, with the impedance amplitude as a function of frequency shown here. Interpretation of these data in terms of a simple linear circuit model is enabling the resistance and capacitance of the thermally sprayed samples, along with the electrolyte resistance to be determined as a function of time, temperature and environment. As the nature of the passive film changes, it will be detected through these impedance measurements. The corresponding phase angle of the complex impedance is given in the following figure.

See Figure 37. The phase angle as a function of frequency is shown here for the complex impedance data being gathered during the long-term test, and corresponds to the impedance amplitude in the previous figure.

See Figure 38. This figure shows the gamma pit at LLNL. Actual spent fuel containers will be subjected to relatively high fluxes of gamma radiation, which will cause radiolytic reactions in the aqueous environment, including the production of hydrogen peroxide and other species. Work has begun on making electrochemical corrosion measurements inside the gamma pit, so that the impact of radiation on the amorphous metal coatings, and on the Alloy C-22 reference material can be assessed.

DIFFERENTIAL THERMAL ANALYSIS

The thermal stability of selected iron-based alloys has been investigated, with focus on alloys SAM2X5 and SAM7. Thermal analysis (DSC, DTA) has been performed on melt-spun ribbons, atomized powder, and wedge cast samples like the one shown in Figure 39 [Figure 1, Perepezko]. Wedge cast experiments and heat transfer analysis of SAM7 and SAM2X5 have been performed. The kinetic competition involving glass formation and crystallization of selected Fe-based amorphous alloys has been analyzed in order to develop transformation kinetics diagrams, which yield information about the necessary cooling rate requirements to vitrify the melt as well as the long-term stability of the amorphous phase. Atomized powder of SAM7 and SAM2X5 has been analyzed with XRD and SEM to establish fraction amorphous as a function of particle diameter. The funding for this work is provided by DARPA/DOE through Lawrence Livermore National Laboratory as part of the ongoing efforts to develop and utilize amorphous corrosion-resistant Fe-based alloys for marine and nuclear waste storage applications. The present work is part of a team-based effort to develop Fe-based amorphous alloys for use in HVOF (High Velocity Oxygen Fuel) thermal spray processing. University of Wisconsin-Madison`s (UWM) contribution to the program can be summarized as:

Differential Scanning Calorimetry & Differential Thermal Analysis

Differential scanning calorimetry (DSC) and differential thermal analysis (DTA) are used to determine glass transition (T_g), crystallization (T_x), onset of melting (T_m) and liquidus (T_L) temperatures. The DSC furnace is limited to temperatures up to about 625 °C, which is sufficient to determine T_g and T_x during continuous heating for several of the Fe-based amorphous alloys. In some cases, however, when T_x ~ 625 °C or higher, it is necessary to heat the samples in the DTA furnace in order to acquire T_x. For all alloys, T_L is determined by DTA. The main difference between these modes of operation is that DSC allows for much better temperature control during isothermal annealing, as well as a very high heat flow resolution. All temperature onsets during continuous heating as well as time onsets during isothermal annealing are defined by the tangential intersection method as illustrated in Figure 40 [Figure 2, Perepezko]. Both the DTA and the DSC furnace are calibrated on a monthly basis using the melting points of pure standards and their corresponding heat of fusion to assure the accuracy of the acquired temperature data. The drift between each calibration is typically less than one degree K, depending on how much the unit has been used.

The samples may be melt-spun ribbons, atomized powder or chill-cast ingots. Each of these is processing routes provides for specific cooling rate regimes, and depending on the glass forming ability (GFA) of the alloy one or more of the processing methods may produce amorphous samples. Thermal analysis of these samples allows determination of important thermal properties such as the glass transition temperature (T_g), crystallization temperature (T_x), and melting interval (T_m-T_L). Results from thermal analysis of amorphous metal samples provides initial assessment of the glass forming ability of these materials through conventional metrics, such as T_{rg} (=T_g/T_L), ΔT_x (=T_x-T_g) and γ (=T_x/(T_g+T_L), and can be used to rank alloys based on the expected suitability for thermal spray processing. However, note that the metrics provided by thermal analysis are only initial assessments, and more detailed studies are required to determine GFA of a particular alloy.

Characteristic Thermal Properties of Fe-Based Amorphous Metals

In addition to having enhanced corrosion resistance, these new Fe-based amorphous metals have substantially improved thermal characteristics, which will improve processing ability, and performance in targeted applications, as shown by the University of Wisconsin at Madison [Perepezko et al. 2004; Farmer et al. 2004]. While there was some sample-to-sample variability, results were generally consistent For example, SAM2X5 has a glass transition temperature of ~579°C, a recrystallization temperature of ~628°C, a melting point of ~1133°C, and a reduced glass transition temperature of ~0.57 (with a value of 0.6 being ideal). SAM2X7, an alloy in the same family as SAM2X5, has a glass transition temperature of ~573°C, a recrystallization temperature of ~630°C, a melting point of ~1137°C, and a reduced glass transition temperature of 0.57. Similarly, SAM1651 has a glass transition temperature of ~584°C, a recrystallization temperature of ~653°C, a melting point of ~1121°C, and a reduced glass transition temperature of ~0.55. The critical cooling rates for SAM2X7 and SAM1651, have been determined to be ~ 610 and ≤ 80 K per second, respectively. Clearly, the yttrium additions in SAM1651 enhance glass-forming ability, as reported by Guo and Poon [2003]. A summary of thermal analyses (DTA or DSC) of the Fe-based amorphous metals of interest to HPCRM are shown in Table 2.

MICROSTRUCTURE DETERMINATIONS

Most samples also undergo microstructure characterization in order to establish reaction pathways. In particular, wedge cast samples are carefully examined with SEM, TEM and XRD to determine what phases compete with glass formation. Melt-spun ribbons are annealed at various times and temperatures to establish crystallization pathways. The isothermal annealing experiments that were mentioned earlier allow for determination of the first phase to precipitate from the undercooled liquid (glass). Based on the results from our microstructure analysis of devitrified amorphous samples, Dr. L. Kaufman, another member of the HCPRM team, calculates the driving free energies for precipitation in the undercooled liquid as a function of temperature. This information is then used in the kinetic model to finalize TTT-diagram predictions.

The University of Wisconsin-Madison cooperates with other team members in order to provide the best possible information to allow optimization of amorphous coating quality. Based on

corrosion testing done by other team member, there has been an increasing focus on alloys SAM2X5 and SAM7 (SAM1651) in FY05, thus, the bulk of the results in this report deals with these two alloys. However, we will also present thermal stability predictions for alloys SAM35 and SAM40 that were finalized early in FY05.

WEDGE CASTING

This experimental technique allows accurate determination the cooling rate required to avoid crystallization of the melt upon continuous cooling. The method will be explained in detail in a later section.

Experimental Apparatus

Alloy ingots are prepared by arc-melting its pure constituent elements in a titanium-gettered argon atmosphere. Some ingots were provided by other members of the team (Bill Peter, Oak Ridge National Laboratory) The nominal alloy compositions [Farmer et al., 2004-2005; Branagan et al., 1999-2005] are listed in Table 1, however, note that not all of these alloys have been wedge cast. The ingots are mechanically polished to remove any surface oxide layer before they are coarsely crushed as a final step in preparation for wedge-casting. The sample is subsequently placed inside a quartz-tube with a 1.5 mm-diameter hole at the bottom. The crucible is coated with a thin layer of Y_2O_3 on the inside to minimize chemical reactions between the liquid alloy and the crucible. Yttria is a very stable oxide that is used in many high-temperature applications to prevent reactions between carrier and sample, so reduction of the yttria coating by the Fe-melt will not take place. The melting is done in an argon atmosphere using induction heating of the sample. When the sample is completely molten, a small overpressure of argon forces the liquid through the hole in the crucible and into the copper-mold (10×10×9 cm) with a V-shaped cavity (8 cm high, 4 cm wide with an adjustable opening angle 4 to 14°). The wedge is designed such that heat transfer in the x-z plane, as shown in Figure 39 [Figure 1, Perepezko], is dominant, i.e. the wedge is approximated to be semi-infinite normal to this plane. The cooling of the liquid is recorded using four type-R thermocouples located at different positions in the wedge as shown in Figure 39 [Figure 1, Perepezko]. The thermocouple junctions are exposed directly to the melt in order to optimize accuracy and response time. The thermocouples are connected to a computer using a PCI-DAS-TC input board (Omega Engineering) especially designed for temperature monitoring. This board is a 16-channel thermocouple/voltage 32-bit input board for the PCI bus. The board accepts seven different types of thermocouple input; J, K, E, T, R, S and B. It`s digital output is scaled for temperature in either degrees C or F. An onboard microprocessor handles all the control and math functions including Cold Junction Compensation, automatic gain and offset calibration, scaling (voltage to temperature translation) and thermocouple linearization. This relieves the computer from performing all these functions. The PCI-DAS-TC board is completely plug-and-play and can utilize various data acquisition software. Although the board can process input data up to 1000 Hz, the practical sampling rate of 5 Hz is determined by the thickness of the thermocouple wire and its response time to sudden temperature changes. According to the manufacturer, response times are about one second for a 0.1 mm-diameter wire, which was also our experience during the casting trials. A commercially available software program (Daisy-Lab, Omega Engineering) processes the temperature data for viewing and storage.

Recently, a highly sophisticated pyrometer technique has been utilized in the wedge casting experiments. The substitution of fiberoptic sensors for the thermocouples shown in Figure 39 [Figure 1, Perepezko] allows for a much faster data acquisition rate as well as drastically reduced transient times. We are currently performing the initial trials with the improved setup, and results will become available during FY06. This addition to the experimental setup will improve the accuracy of the heat transfer analysis.

The wedge casting method is by far the most accurate technique to determine critical cooling rates for glass formation. However, as will be discussed later, this experimental setup and subsequent heat transfer analysis have been designed also for prediction of material properties such as thermal conductivity and specific heat. These properties are not otherwise available, but are valuable for the multi-component alloys investigated in this program.

Heat Transfer Analysis

The time-temperature evolution in the wedge is modeled by solving the two-dimensional heat transfer equation, equation (1). The use of only two dimensions is justified by the relatively long width of the wedge (40 mm) as compared to typical heat transfer distances (0.1-5 mm). A 3D-simulation has been utilized to confirm this, and the simulation package ProCAST (www.esi-group.com) yielded identical results to those for the 2-D model for node positions more than 10 mm from the end walls (parallel to the *xz*-plane in Figure 39 [Figure 1, Perepezko]). Expressed in Cartesian coordinates, the 2-D transient heat transfer equation can be written

$$\frac{\partial}{\partial x}\left(\frac{k\partial T}{\partial x}\right)+\frac{\partial}{\partial z}\left(\frac{k\partial T}{\partial z}\right)-\rho c\frac{\partial T}{\partial t}=0 \qquad \text{[Equation 1, Perepezko]}$$

where T is the temperature, $k(T)$ is the thermal conductivity, $\rho(T)$ is the density, $c(T)$ is the specific heat and t is the time. Heat transfer at the mold-melt interface is characterized by a total heat transfer coefficient h. The heat transfer to the argon atmosphere (from the top of the liquid) is negligible compared to the heat transfer to the mold, both because of the short cooling times involved and the poor heat transfer characteristics of argon gas. Radiation to the atomosphere is also negligible compared to the convective heat loss to the mold. Equation (1) is solved numerically using the academic version of FEHT (www.fchart.com), a finite element analysis software. The thermophysical properties and their temperature dependence for a given sample alloy are in general not available and must be estimated.

The density at room temperature can easily be assessed using Archimedes principle, and it is assumed to be constant with temperature with a value of 7.6 g/cm^3. Choy et.al. [1991] measured the thermal conductivity for several Fe-based metallic glasses. It was found that k generally decreases with increasing number of alloying elements. The lowest thermal conductivity was measured in an $Fe_{32}Ni_{36}Cr_{14}P_{12}B_6$ alloy, where values ranged from 6 W/mK at room temperature to 10 W/mK at 500 K. Due to the multicomponent nature of the alloys under study, a slightly lower value for k was used in these calculations. The heat transfer coefficient is obtained through an iterative process where experimental temperature-time (T-t) data are compared to calculated cooling curves until the calculated T-t curve coincides with the experimental data within +/- 5°C

during the quench from the liquidus to the glass transition temperature. In general, the value of h may be a function of z or the interface temperature or both. A spatial dependence in h is typically caused by solidification shrinkage and loss of heat transfer for mold-melt interfaces relatively high up in the wedge. Closer to the tip, complete vitrification of the melt may occur and no significant reduction of specific volume takes place, thus maintaining a good heat transfer contact throughout the quench. The spatial variation of the heat transfer coefficient along the cooling interface during chill casting has also been observed by other investigators. Allowing for both a spatial and interface temperature dependence in h is an effective way of incorporating factors that will influence the overall heat transfer characteristics during wedge casting, such as temperature variations in k, c and ρ, increase of mold temperature and interface contact loss due to shrinkage. As will be further discussed in the results section, in some cases not only the experimental cooling curves are needed for an appropriate heat transfer analysis, but one should also take into account the actual microstructure as it may reveal important information on the local cooling conditions and allow for a better estimation of the alloy properties.

The heat transfer analysis obtained by solving equation (1) is strictly limited to the amorphous part of the wedge, since we do not account for latent heat. Modeling the entire cooling history of the wedge, including the crystalline parts is a tremendous task that is both unrealistic and unnecessary for our purposes. The fitting process requires that one of the thermocouples has measured the cooling history for a vitrified portion of the wedge, thus allowing a straightforward problem where the heat transfer parameters are adjusted within in acceptable range until the calculated cooling curve matches that of the measured (note that microstructure analysis may come into play as explained earlier). However, if none of the thermocouples registers vitrification through the lack of recoalescence on cooling, the fitting is still possible given that sufficient experimental data are available between the time when the melt was poured and the point of solidification. That may not be the case when thermocouples are used due to their intrinsic delay time, but when using fiberoptic sensors this information is available. As such, a heat transfer coefficient can be obtained for cooling between the initial temperature and the recoalescence temperature. It is then assumed that the assigned h also is valid for all surfaces in the proximity of an amorphous phase.

The use of a lumped heat transfer coefficient is the standard approach for all heat transfer analysis as it simplifies problems that often are very complex since no exact information on the material properties of the sample is available, which is the case for the Fe-based SAM alloys. The mold mass is large (~2 kg) compared to the sample mass (50 grams), so the average temperature increase in the mold is moderate (~20-30 degrees K), depending on the sample properties and pouring temperature. It is possible to calculate the heat flow within the mold as well, but this severely increases calculation time and adds nothing to the final result since the effect of a temperature increase in the mold can be accounted for by adjusting the heat transfer coefficient as a function of time and/or the mold temperature. The heat transfer parameters (h and T_{mold}) are not independent, so that there are several combinations of these that will allow for a correct predicition of the experimental time-temperature curves. A detailed description of the software can be found in appendix (excerpt from the manual).

SAM1651 – Cooling Rates & Microstructure

The alloy was prepared by re-melting of atomized powder received from Caterpillar. The subsequent wedge cast experiment and analysis was carried out as outlined earlier in this report. Temperature profiles acquired during the quench are shown in Figure 47 [Figure 9, Perepezko] along with calculated cooling curves. A good fit was found using a time-dependent heat transfer coefficient *h(t)*. The variation with time can be attributed with a temperature increase of the mold due to heat transfer from the sample. It is also possible that a reduction of *h* occurs with changes in specific volume and possible loss of contact between the mold and the undercooled liquid, which was reported by Linderoth et al. [2001]. Finally, it is recognized that the material properties are temperature-dependent, however, little or no information is available for this particular glass forming alloy. The value of *h* was adjusted to achieve good agreement with the lower cooling curve (z=15 mm) since this was the position closest to the glass-crystalline microstructure transition region in the wedge. As can be seen from Figure 47 [Figure 9, Perepezko], the particular selection of *h* also reproduced the cooling curve obtained for z=10 mm, whereas the cooling curves for z=20 and 25 mm were fairly well reproduced although the partial crystallization of the wedge at these z-values and the corresponding heat release causes the model to underestimate the cooling time. However, the effect is small suggesting a relatively low heat of fusion and/or small amount of crystallized liquid. For example, the average cooling rate after 8 seconds is 103 and 108 K/s for the calculated and the experimental curves, respectively.

The relevant thermal properties of the amorphous metals that are shown in Table 2 were assumed constant with respect to temperature. The actual values of these parameters do not significantly influence the heat transfer modeling as they can be accounted for by adjusting *h*. There is an initial transient in the measured cooling curves caused by thermocouple response times to the sudden temperature increase as the melt is injected into the mold. As such, the initial melt temperature T_i could not be measured directly but was assumed to be slightly above the liquidus temperature as measured by DTA. The thermal properties shown in Table 2 were measured with DTA using a sample cut from a 2-mm thick wedge cross-section. The heat flow trace (Figure 48 [Figure 10, Perepezko]) indicates a clear glass transition signal and multiple exothermic crystallization peaks. X-ray diffraction of a powder sample acquired from the same cross-section of the wedge is shown in Figure 49 [Figure 11, Perepezko] (bottom curve). The broad, characteristic peak does not exclude the existence of a nanocrystalline microstructure, but combined with the results from the thermal analysis it is clear that the lower portions of the wedge are fully amorphous. Indeed, this was also confirmed by TEM analysis.

The critical cooling rate for glass formation is commonly defined as the minimum cooling rate to avoid nucleation of crystalline phases upon continuous cooling from temperatures above T_L to below T_g [Jäckle, 1986]. For a wedge-cast sample, the cooling rate is monotonically decreasing along the z-axis for fixed values of x and y. Thus, by using the normal definition of critical cooling rate, one would expect to observe a sharp transition between an amorphous structure and a crystalline structure at a fixed z-value corresponding to a unique cooling rate, which can be measured with the current experimental setup. However, previous work using the same wedge-cast apparatus has shown that it is more appropriate to define a critical cooling rate range that

both is intuitively correct in terms of the stochastic nature of nucleation as well as consistent with experimental observations that were made in this study. This range is determined by the extent of the transition zone between a fully amorphous structure and a fully crystalline structure along the z-axis at x=0 and y∈[-10,10] where the units are given in millimeters. For the alloy examined in this work, the first crystalline phases were observed at a wedge thickness of about 3.3 mm, corresponding to a cooling rate of about 190 K/s. This cooling rate, as well as any other cooling rate referred to in this work, was calculated at the symmetry line (center position) of a random *xz*-plane sufficiently far away from the mold walls (located at y=0 and y=40 mm) such that a 2D heat flow approximation is valid. The completion of the glass-crystalline transition zone occurred at a wedge thickness of about 4.2 mm, corresponding to a cooling rate of 140 K/s. Between these positions (along the z-axis) one may or may not observe crystalline phases (see Figure 46 [Figure 8, Perepezko]), which is consistent with the probabilistic nature of nucleation. On average, however, the volume fraction of crystalline phases increases with lower cooling rates.

The maximum glass thickness for wedge cast samples of $Fe_{48}Cr_{15}Mo_{14}Y_2C_{15}B_6$ is much lower than that reported by Ponnambalam et al. [2004], however, the difference in geometry (wedge vs. cylinder) accounts for a factor of about 2 in thickness for similar cooling rates. In addition, small differences in composition arising from different processing routes may cause relatively large variations in glass forming ability since good glass forming alloys very often form deep eutectics.

Both SEM (Figure 50 [Figure 12, Perepezko]) and TEM (Figure 51 [Figure 13, Perepezko]) analysis were utilized to determine phase selection in the wedge cast samples. Figure 49 [Figure 11, Perepezko] shows a series of back-scattered electron images (BSEI) taken from the transition region. It is clear from Figure 50a [Figure 12a, Perepezko] that the transition from a fully amorphous structure to a fully crystalline structure occurs over a spatial range (along the indicated z-axis). In fact, the extent of the transition zone could not be captured at a single frame as it extended over ~ 8 mm. Figure 50b [Figure 12b, Perepezko] is a magnified BSEI of the insert in Figure 50a [Figure 12a, Perepezko], where three structurally distinct regions can be observed. Although the upper right portion of figure appears featureless, TEM analysis revealed that these regions actually contain a high number of nanosized particles with an $M_{23}C_6$ type structure (Figure 51 [Figure 13, Perepezko]) embedded in an amorphous matrix. Figure 50c [Figure 12c, Perepezko] is the left insert of Figure 50b [Figure 12b, Perepezko], taken from the center portion of a crystalline "island". There is evidence for both coarsening of the initial phase and segregation into a Mo-rich phase. This particular structure resembles that observed for significantly lower cooling rates ~ 1 to 10 K/s. Figure 50d [Figure 12d, Perepezko] is a magnified BSEI of the right insert of Figure 50b [Figure 12b, Perepezko], where the original $M_{23}C_6$ phase has grown dendriticly, however, a second crystalline phase has not formed as in Figure 50c [Figure 12c, Perepezko]. Since the cooling rate is virtually identical for these two areas, the difference is probably related to nucleation at different times, where early nucleation and growth of one phase would allow time for a second phase to form within the interdendritic liquid, whereas for nucleation and growth at later stages would not allow for subsequent phase formation as the deeply undercooled liquid would undergo vitrification.

Based on TEM analysis of samples selected for a range of z-position, the lower part of the wedge below the transition region the structure is fully amorphous (Figure 51a [Figure 13a, Perepezko]). A detailed study of the two-phase structure encountered in the transition region (Figure 51b-c [Figures 13b-c, Perepezko]) indicates that both of the lamellar phases are of a $M_{23}C_6$ type structure, with a grain boundary mismatch of about 2.3 %. Since these phases appear with different contrast in BSEI, their composition must differ, however, due to the significant amount of both boron and carbon in these precipitates, as well as their small size (~ 200 nm), composition analysis EDS-techniques cannot be utilized with sufficient accuracy. It is also interesting to note that the growth direction appears to be <110>, as opposed to the typical <100>-direction for cubic crystal structures. Further TEM-work will be carried out to investigate these issues in more detail.

In conclusion, the as-cast microstructure of $Fe_{48}Cr_{15}Mo_{14}Y_2C_{15}B_6$ is fully amorphous for cooling rates below ~ 190 K/s. For cooling rates between 140 and 190 K/s, a mixed structure was found where the majority of the crystalline phases had an $M_{23}C_6$ type structure (Fm3m). In this transition zone, isolated regions appear with a eutectic morphology, while the partially amorphous matrix between these eutectic areas includes a significant number of nanosized $M_{23}C_6$ precipitates. Since this cooling rate range is well below those commonly achieved in thermal spray processing, it is concluded that based on cooling rate requirements, this alloy is well suited for thermal spray applications in order to form amorphous coatings.

Heat Transfer Parameters from Transition Zone Analysis

Wedge-casting of different alloys has shown that the transition zone between a fully amorphous and a fully crystalline microstructure can exhibit quite different features for similar alloy composition. Figures 52 and 53 [Figures 14 and 15, Perepezko] show two extreme situations that have been observed for alloy SAM40 and SAM35, respectively. These two alloys have similar, although different, compositions, but the transition zone appearances in each of the wedge cast samples are vastly different. In Figure 52 [Figure 14, Perepezko], the transition for the onset of crystallization occurs over a distance of about 400 μm. Figure 54 [Figure 16, Perepezko] shows some magnified images that illustrates the morphology of the transition zone in this alloy. The approximate transition boundary band (indicated by the dashed curve) forms a distinct V-shape that is consistent with the presence of substantial thermal gradients in the melt during quenching. Figure 53 [Figure 15, Perepezko] depicts the other extreme, where the crystallization onset transition seems to occur randomly over the cross-section of the wedge, and does not appear upon initial inspection to follow a well-defined geometrical pattern. The spherical regions seen in Figure 53 [Figure 15, Perepezko] between position (a) and (b) are completely surrounded by an amorphous phase, indicating that growth was limited following nucleation of the solid. Figure 55 [Figure 17, Perepezko] depicts some of the microstructural details from the transition of SAM35. Finally, it should be noted that during work on other Fe-based metallic glasses, for example alloy SAM2X7, most transitions between the glass and crystalline microstructures could be classified between the two extremes.

The different appearance of the glass-crystalline transition in the two alloys under study is first considered in terms of the relative heat transfer characteristics of the two alloys; in particular a different value for the Biot number ($Bi=hl/k$), where h is the total heat transfer coefficient at the

mold-liquid interface, l is a characteristic heat transfer distance of the order of the half-width of the wedge and k is the thermal conductivity. In Figures 52 and 53 [Figures 14 and 15, Perepezko], l is about 0.25 mm. A well-defined transition as observed in Figure 52 [Figure 14, Perepezko] would be caused by large thermal gradients during cooling, i.e. high Biot numbers (>0.3). In this case, the different levels of undercooling across the wedge at a given vertical distance z from the tip will produce quite different microstructural features. On the other hand, if a gradual transition is observed along a horizontal band of the wedge, it can be deduced that thermal gradients across the wedge are of little significance to the solidified structure. Here, the undercooling and the cooling rate R will still govern nucleation and growth, but since thermal gradients in the x-direction are negligible, a well-defined pattern as seen in Figure 52 [Figure 14, Perepezko] is not observed.

A finite element heat transfer analysis was performed to determine the influence of changes in the Biot number on thermal gradients across a section of the wedge at a given distance z from the tip of the wedge. The thermophysical properties were taken to be that of a typical cast iron [Gundlach and Doane, 1990], but the thermal conductivity and the heat transfer coefficient were changed in order to yield different Biot numbers, but similar cooling rates. The calculated isotherms for one second after the melt has been poured are presented in Figure 56 [Figure 18, Perepezko]. The results indicate that for compositions with high internal resistance to heat flow, thermal gradients $(\nabla T)_x$ will be important and there may be a substantial difference in the local cooling rate across a horizontal plane (xy-plane) in the wedge. This should be reflected in the observed microstructure. On the other hand, for compositions with high thermal conductivity (i.e. low Biot numbers, ~0.01) the thermal gradients are negligible, and the shape of the transition region is expected to be relatively flat.

The thermal conductivity can now be estimated by first identifying the appearance of the glass-crystalline transition region, i.e. flat or V-shaped, which would indicate whether a relatively high or low Biot number is expected. For example, the transition in Figure 52 [Figure 14, Perepezko] is well-defined with a substantial chill zone along the edges where an amorphous phase is retained. Thus, according to Figure 56c [Figure 18c, Perepezko] a relatively high Biot number is expected (~0.5). The values of h and k were chosen accordingly such that the heat transfer analysis reproduced the measured cooling curves and the estimated Biot number. A preliminary estimate for the SAM40 alloy indicates values of h=3700 W/m^{2}K and k= 4 W/mK. A similar procedure can be applied to the SAM35 alloy. However in this case the appearance of the transition does not allow for a clear assignment of the thermal contours. For example, two limiting contour profiles have been marked on the microstructure in Figure 53 [Figure 15, Perepezko]. The profile with an apex near point a in Figure 52 [Figure 14, Perepezko] could develop if the nucleation rate was rather low for temperatures near T_g for SAM35. The low nucleation density could also be associated with the other limiting profile near point (b) in Figure 52 [Figure 14, Perepezko]. The two limiting profiles will yield different Biot numbers and heat flow characteristics. For the profile near point (a), the Biot number is about 0.3 which yields k_{SAM35}/k_{SAM40} ~6/4. On the other hand, the profile near point (b), calculated using a different set of values for h and k, indicates a Biot number of about 0.05 which yields k_{SAM35}/k_{SAM40} ~10/4. Since the alloy compositions for SAM35 and SAM40 are not drastically different, the thermal conductivities are not expected to show a large difference. Thus, from the heat flow comparison, the profile near point (a) is appropriate for analysis. Further, the different appearance of the

transitions in SAM35 and SAM40 also reflect the different phase selection during nucleation. For SAM35 the initial crystallization involves nucleation of a Fe_2B structure while a metastable Fe_3B structure develops initially in SAM40.

In summary, the heat transfer analysis must not only reproduce the experimental cooling curves, but also account for the microstructural features of the cast wedge, which may indicate whether thermal gradients are significant. The presence of large thermal gradients limits the possible values of *h* and *k*; in particular, it requires that *h* values are relatively high and/or *k* values relatively low. The model allows for a coupling of experimental cooling curves and observed microstructure features to provide constraints on the range of possible *h* and *k* values. As such, the model can provide information on the thermal conductivity of an undercooled liquid alloy which otherwise is not easily accessible without extensive experimental efforts.

SAM2X5 – Cooling Rates & Microstructure

The sample was prepared from atomized powder that was sintered in argon gas and re-melted to make an ingot. The ingot was then wedge-cast using the same procedures as for SAM7. The multi-step ingot preparation likely introduces oxygen into the sample, which is believed to be detrimental to glass-forming ability. The wedge cast experiment of SAM2X5 will be repeated using an arc-melted ingot that was received from Bill Peter at Oak Ridge National Laboratory.

The cooling rates acquired during the wedge-cast experiment are shown in Figure 57 [Figure 19, Perepezko]. The initial thermocouple transient obscures the first part of the cooling curve which makes assessment of pouring temperature difficult. Two thermocouples (at z=10 and 15 mm, see Figure 39 [Figure 1, Perepezko]) shorted out, and only the thermocouples higher up in the wedge acquired temperature data. A preliminary heat transfer analysis has been carried out to assess cooling rates in the lower portions of the wedge (z=0-20 mm).

Some micrographs of the as-cast wedge tip are presented in Figures 58 through 59 [Figures 20 through 22, Perepezko]. The blocky phase that appears with a white contrast has elevated levels of Mo compared to the matrix and is most likely a molybdenum-carbide. The size indicates that this particle did not fully dissolve in the melt prior to pouring. The long dark needle probably did not dissolve either by a similar size argument. However, the dark spots (right image) are small precipitates that formed during cooling. The matrix appears to be amorphous based on the lack of observable contrast (limited to the instrument resolution). With increasing cross-section, corresponding to lower cooling rates, the number density of the dark spots shown in figure 20, right image, increases. At cooling rates below ~ 1000 K/s, the microstructure appears to be fully crystalline.

POWDER ANALYSIS

Comprehensive Characterization

The fraction amorphous in atomized powder as function of powder diameter is being investigated using differential thermal analysis (DTA), differential scanning calorimetry (DSC), X-ray diffraction (XRD), and scanning electron microscopy (SEM). Using a kinetic model, we

can determine the amorphous fraction dependency on powder size as well as exploring possible nucleation mechanism. This method will be described in more detail in a later section. In the thermal spray process, it is crucial that the powder that is fed into the process is fully amorphous, as crystalline precipitates may not melt during the HVOF process, both due to sluggish melting kinetics as well as insufficient temperatures. As such, the results from the powder analysis provide a guide for process optimization.

Crystallization of powders can be analyzed with a procedure outlined by Drehman and Turnbull [Drehman and Turnbull, 1981], where the crystallization process can be described as heterogeneous surface nucleation, heterogeneous volume nucleation or homogeneous nucleation. The fraction amorphous phase present in an ensemble of droplets with different diameter can be described as

$$x = \exp\left[-\left(d/d_0\right)^n\right]$$ [Equation 2, Perepezko]

where d_0 is a scaling parameter and n is representative of the mechanism governing the nucleation process. For a surface controlled nucleation, n~2, for heterogeneous volume nucleation n~3 and for homogeneous volume nucleation n~4.6. Various experimental techniques can be utilized to determine the glassy fraction in atomized powders. XRD analysis allows fraction glass to be established based on the intensity of crystalline phases relative to a baseline diffraction pattern, however, this method is somewhat unpractical for the alloys currently investigated due to the complexity of the devitrification process involving metastable phases, i.e. phase selection during atomization depends on cooling rate (powder size) such that different phases may form depending on the droplet diameter. Electron microscope techniques such as SEM can be very useful combined with image analysis of atomized powder. The main problem though is that very small precipitates, particularly those arising from polymorphic reactions (low or no contrast in back-scattered mode), are not easily resolved with standard scanning electron microscopes, so this method is extremely time-consuming and not accurate. A more effective method is thermal analysis, where powders sieved into different size ranges can be continuously heated through the temperature range where crystallization occurs. The crystallization signal will depend on the fraction amorphous present after normalizing the sample mass, and the amorphous fraction can be assessed as function of droplet size can be assessed.

SAM2X5 Powder

Atomized powder was sieved into various powder size ranges and analyzed with X-ray diffraction to determine crystalline phases present in the powder as well as to estimate the cut-off size for fully amorphous powder. This is crucial for optimizing process parameters during thermal spray-forming of amorphous coatings. For example, during the re-heating of the powder, the times at high temperatures are often so short that immersed crystalline particles with complex structures such as carbides and borides often exhibit very sluggish melting behavior. As such, the as-sprayed coating may contain partially unmelted crystalline phases, which may act as initial corrosion attack sites and also influence the long term thermal stability.

In Figure 41 [Figure 3, Perepezko], the XRD intensity peaks are given for several different size fractions of the powder. These powders arrived pre-sieved from Nanosteel. A second batch of powder (also from Nanosteel) were sieved at UWM, and a similar XRD analysis was performed with the results that are given in Figure 42 [Figure 4, Perepezko]. For powder less than 15 microns, no crystalline peaks are observed. That does not necessarily exclude the presence of nano-sized crystalline precipitates, but it is a strong indicator of fully amorphous material. Coupled with results from thermal analysis (to be presented later), we can conclude that powder less than 15 microns is amorphous for this composition and atomization condition. For the size fraction 15-30 microns, small peaks become visible that indicate the presence of an ordered structure, i.e. crystalline phases. However, the volume fraction is still relatively low, as crystal peaks will completely dominate the XRD pattern for any sizeable amount of ordered structure. With increasing powder size (and correspondingly lower cooling rates during atomization) the fraction of amorphous material is reduced. Powder sizes larger than 50 microns appear to be mostly crystalline. There is still some uncertainty regarding the structure of the precipitates, but some of the peaks found for the largest size fraction are consistent with ferrite. TEM work is ongoing to determine the nature of the other phase that forms prior to the ferrite (no ferrite peaks for particle sizes under 50 microns). By searching in the available databases, a possible match is a tetragonal Fe_3B-type phase, however, the match is not very good. Recent TEM-work suggests that Mo_3B_2 forms in melt-spun ribbons, and a peak calculation of this phase will be carried out to investigate whether the unidentified phase observed in the powders is consistent with this structure. Note that bcc-ferrite nucleates on the grain boundary of Mo_3B_2, as observed from TEM-samples.

It is apparent from the XRD analysis that careful selection of initial powder sizes is a prerequisite for successful generation of fully amorphous thermal-spray formed coatings. For this alloy, one should select relatively small powder sizes (< 20 microns) to avoid a significant volume fraction of crystalline phases and complete melting in the thermally sprayed powders. Further analysis is required to judge whether the fully liquid powders yield a completely amorphous coating following deposition and coating.

Figure 43 [Figure 5, Perepezko] shows some BSE images of sieved powder. The amount of amorphous material in the atomized powder decreases with increasing powder size. Powders under 20 microns were mostly amorphous except for a few carbon-rich precipitates. At this point, it is more likely that these particles are resulting from sample preparation (SiC grinding paper) than actually being part of the original droplet. Powders larger than 32 microns are crystalline, while powders between 20 and 32 micrometers exhibit a mixed structure than can be described as an array of needles (weave-like) randomly orientated. The typical size is only a few hundred nanometers. No phase identification through EDS is possible for such small precipitates, but blocky Mo-rich phases was observed (Figure 43 [Figure 5, Perepezko] – top right) that appear very similar to those found in melt-spun ribbons (to be discussed later).

Sieved powder was also heated in the DTA-furnace (Figure 44 [Figure 6, Perepezko]). As expected, the crystalline fraction in the atomized powder increases as the powders size decreases. The cut-off range is rather narrow, which complicates the analysis due to insufficient mesh ranges of the sieves. For powder less than 20 microns, it is assumed that only a negligible fraction is crystalline (<0.01).

For a powder size range between 20 and 25 micrometer, the relative size of the initial crystallization peak as compared to the smaller sized powder indicates a volume fraction glass of about 0.8, and for powder between 25 and 32 microns the volume fraction glass is about 0.1. As such, the analysis outlined earlier is somewhat speculative as more data is needed to accurately describe volume fraction glass as a function of droplet diameter. Smaller powder size ranges needs to be evaluated to complete this analysis. A preliminary plot of volume fraction glass as a function of diameter is given in Figure 45 [Figure 7, Perepezko].

SAM1651 (SAM7) Powder

This alloy with a superior glass-forming alloy compared to SAM2X5, did not exhibit any crystalline peaks upon XRD analysis of various size ranges of atomized powder as can be seen from Figure 46 [Figure 8, Perepezko]. As such, the cut-off size is above 106 microns. Larger powder sizes were not available in sufficient amounts to perform X-ray diffraction. Based on a glass forming criteria only, it appears as if SAM1651 (SAM7) with a wide size-range can be used and still form an amorphous coating upon thermal spray forming.

TIME-TEMPERATURE-TRANSFORMATION (TTT) DIAGRAMS

In order to use amorphous coatings in application such as nuclear waste storage, it is crucial to determine the long-term stability of the amorphous phase, as precipitation of crystalline phases such as bcc-Fe will severely reduce the overall corrosion resistance of the coating. A convenient way to visualize thermal stability is the calculation of Time-Temperature-Transformation (TTT) curves that consists of the loci of time-temperature for the onset of nucleation of crystalline phases occurs. A kinetic model as been developed that combines information from wedge casting experiments and isothermal annealing experiments and incorporates these into a heterogeneous nucleation model. Based on this model, TTT-diagrams have been assessed for alloys SAM35 and SAM40, whereas work is in progress (preliminary results are available) for determining the TTT-curves for SAM1651 (SAM7) and SAM2X5.

Preliminary TTT-diagrams for alloys SAM35 and SAM40 were reported in the 2004 annual report [Perepezko and Hildal, 2004; Farmer et al. 2004-2005]. Some of these results will be included here, as refinements have been made to the kinetics calculation where the microstructure transition zone appearance is accounted for as described earlier. The method for establishing TTT/CCT diagrams is the same for all alloys investigated, where the experimental information is obtained through wedge casting and determination of the critical cooling rate range as well as isothermal, low-temperature annealing of as-spun ribbons to determine onset times for crystallization as a function of time and annealing temperature. The driving free energies for formation of a nucleus in the undercooled liquid are calculated by Dr. Larry Kaufman. In alloy SAM35, the first phase to precipitate is Fe_2B, while in SAM40, it is Fe_3B.

Development of Procedure – SAM40

The TTT/CCT-diagrams for SAM40 were assessed using the previously described method. Melt-spun ribbons were annealed in the DSC at temperatures between T_g and T_x as measured during

continuous heating, and the crystallization onset times were recorded as a function of temperature [Perepezko and Hildal, 2004; Farmer et al. 2004-2005]. The primary precipitating phase was identified by partial devitrification of melt-spun ribbons with subsequent XRD and TEM analysis and found to be isostructural with Fe_3B. This phase is usually considered to be metastable. The theoretical basis for the analysis was discussed in [UWM2004]. The resulting CCT/TTT diagrams for the SAM40 alloy are shown in Figure 61 [Figure 23, Perepezko]. The high temperature bound is set by the metastable Fe_3B phase liquidus. The liquidus value for the binary Fe-B system is used in Figure 61 [Figure 23, Perepezko] so that this bound will shift when the ΔG_v values for the multicomponent system are available. This refinement will mainly alter the high temperature portion of the transformation diagram. Note that the predicted TTT-curve is extremely sensitive to changes in the viscosity parameters, B and T_0.

Results – SAM1651 (SAM7)

The calculation assumes that $M_{23}C_6$ is the first phase to form both (based on wedge cast results) during continuous cooling and isothermal annealing at temperatures below the nose of the TTT-diagram. The driving free energies was provided by Dr. L.Kaufman, a member of the HPCRM team. Isothermal annealing data are shown in Figure 62 [Figure 24, Perepezko]. The apparent onset times are indicated by the arrows, however, for the lower annealing temperature (600°C) there is no clear but a gradual onset. In addition, there are some initial features for each of the curves that are not well understood yet. For example, the time before the baseline flattens out exceeds 30 minutes for all of the annealing temperatures The delayed time for return to baseline exceeds by a signficant amount the times observed in the previous experiments with SAM35, SAM40 and SAM40X3 where typical transients were of the order one minute. A preliminary TTT-diagram is shown in Figure 63 [Figure 25, Perepezko].

Results – SAM2X5

A preliminary TTT-curve has been calculated (Figure 64 [Figure 26, Perepezko]) for the low temperature regime. However, the isothermal annealing experiments did not give consistent onset times as function of temperature (Figure 65 [Figure 27, Perepezko]). The DSC signal was typical of that of a growth process, i.e. no symmetric peak but a decreasing heat flow signal. Thus, onset times could not be established. The ribbons were melt-spun by Nanosteel, and the intial XRD and TEM analysis suggested that these were amorphous, but based upon the isothermal study some nuclei must have been present in the ribbons, despite the high cooling rates. UWM produced their own set of ribbons, verified these to be fully amorphous by TEM and XRD, but even in this case a heat flow signal consistent with growth was observed in the DSC. Typical annealing temperatures were between 580 and 620°C. For the temperatures above ~605°C, onset signals could be observed, but always after significant growth had taken place. The primary phase is assumed to be M_2B for the initial analysis. Recent TEM-investigations indicate that the primary phase may be Mo_3B_2, as such particles have been detected in as-spun ribbons. This phase can act as a nucleant for the bcc-phase (evident from the TEM analysis), which illustrates the importance of controlling melt process parameters to avoid potentially devastating crystalline phases in spray-formed coatings, as these may both trigger nucleation of secondary phases as well as decrease the thermal stability of the material. The X-ray diffraction

examination of both annealed ribbons and atomized powder has not yet been able to provide answers as to the structure of the primary phase in SAM2X5.

The kinetic transformation diagram is calculated based on parameters for a similar alloy (SAM40X3/SAM2X3). The critical cooling rate determined from the wedge cast experiment restricts the position of the nose, but due to the lack of consistent data in the low temperature region further work is necessary to establish long-term stability of amorphous SAM2X5. It is worth noting that adding Mo to the base alloy SAM40 has a profound effect on the crystallization reaction at low temperatures (Figure 66 [Figure 28, Perepezko]), and further work is required to fully understand the devitrification process in SAM2X5 and similar alloys.

MECHANICAL PROPERTIES

Case Western Reserve University is developing mechanical property information on SAM2X5 and SAM1651. Project work begun in mid-2005 has initially focused on measurements of microhardness, microhardness as a function of temperature, and evolution of microhardness with exposure time at elevated temperature for bulk amorphous SAM1651 prepared by ORNL. This information is being developed to provide fundamental information on the microhardness/strength of baseline Fe-based bulk amorphous alloys at temperatures of interest to DOE/DARPA. The information being generated is also relevant to both the ongoing processing and microstructure evolution studies being conducted by other members of the HPCRM team. The summary provided below has been provided to the HPCRM team and has been discussed in various HPCRM scientific and applications telecons, with input received on additional test temperatures and thermal exposures of interest to the HPCRM team.

Drop cast ingots of SAM1651 were prepared by ORNL in the form of 4.7 mm diameter x 25-50 mm long cylindrical rods, as well as 4 mm thick x 12 mm wide x 30-50 mm long rectangular bend bars. X-ray diffraction analyses of both the as-cast cylindrical rods and bend bars revealed diffuse diffraction peaks without any evidence of crystallinity, indicative of an amorphous sample for the sizes analyzed. This is consistent with the experimental determination of the low (i.e. 80K/sec) critical cooling rate for SAM1651 determined by other members of the HPCRM team and summarized elsewhere in this report.

Microhardness Measurements

Microhardness testing was conducted using a NIKON QM-2 hot microhardness testing machine capable of operating in vacuum or inert environment at temperatures up to 800^{o}C. Right circular cylindrical samples, 6 mm in length, were prepared from the drop cast SAM1651 rods. The surface to be indented was metallographically polished to a 0.5 micrometer finish using a variety of grit papers followed by polishing with diamond paste to ensure a flat and parallel surface for subsequent indentation. The NIKON QM-2 utilizes a diamond pyramid indenter that is heated separately from that of the sample, which is also heated by a separate furnace surrounding the sample enclosure. Temperature is measured via a thermocouple attached to the sample holder. The indentation load selected was 500 grams based on the expected high hardness of the Fe-based amorphous alloys, with an indentation time of 15 seconds for each test. Initial microhardness tests (at 500 grams load) of the SAM1651 were conducted at room temperature,

in addition to the following test temperatures: 100°C, 150°C, 200°C, 300°C, 400°C, 450°C, 500°C, 525°C, 550°C, 575°C, and 600°C. Microhardness tests were conducted in triplicate at all test temperatures. In these initial tests, a single sample was tested in the NIKON QM-2. After the room temperature test was conducted, both the sample and the indenter were heated to 100°C. The temperature was then allowed to stabilize by waiting for 5 minutes at 100°C prior to indentation. A series of three (3) microhardness indentations were taken sufficiently far apart to eliminate any possibility of the deformation fields overlapping. The indenter and sample temperature were then increased to 150°C and the sample was allowed to stabilize by holding for 5 minutes at 150°C prior to indentation. Another series of three (3) indentations were taken at 150°C sufficiently removed from each other and the indentations previously performed at 100°C. This procedure was repeated for each subsequent test temperature (e.g. 200°C, 300°C, 400°C, 450°C, 500°C, 525°C, 550°C, 575°C, and 600°C). After the final three (3) indentations were performed at 600°C, the sample and indenter were cooled to room temperature. The indented surface of the sample was then examined at room temperature using both optical and scanning electron microscopy in order to determine the indentation size(s) at each test temperature and the microhardness values were subsequently calculated using standard techniques.

Microhardness Data

Figure 67a [Figure 1a, Lewandowski] summarizes the effects of changes in test temperature on the microhardness of SAM1651, presented in kg/mm^2. Figure 1b plots the same data for the microhardness using GPa. Figure 1c converts the microhardness data shown in Figure 1b to an estimated compressive strength, using the relationship: Compressive strength = VHN/3.

Figures 67a and 67b [Figures 1a and 1b, Lewandowski] illustrate the extreme hardness of SAM1651 at temperatures near room temperature (i.e. 1200 kg/mm^2, 12 GPa), which is converted to the estimated room temperature compressive strength of about 4000 MPa, shown in Figure 1c. No cracks were observed around the microhardness indentations taken at any of the test temperatures shown in Figures 67a through 67c [Figures 1a through 1c, Lewandowski]. These figures also illustrate the tremendous drop in microhardness/strength that is obtained upon approaching the glass transition temperature, T_g, which has been determined by other HPCRM team members as 584 ° C for this material. The room temperature microhardness obtained after the hot hardness studies were completed were somewhat in excess of 1200 kg/mm^2 (i.e. 12 GPa), producing estimated room temperature compressive strengths in excess of 4000 MPa. These increased microhardness values obtained after exposure to temperatures as high as 600°C are likely the result of structure evolution in the SAM1651, as discussed further below.

Figures 68a through 68c [Figures 2 a through 2c, Lewandowski] summarize the microhardness of 316L (supplied by Lawrence Livermore National Lab) tested over a similar temperature range, while Figures 69a through 69c [Figures 3a through 3c, Lewandowski] compare the microhardness of the SAM1651 and 316L over the range of temperatures tested. The tremendous softening exhibited near T_g in SAM1651 provides the potential of unique deformation processing at relatively low loads and stresses, provided that the microhardness/strength remains low with continued exposure at elevated temperature. In order to investigate the effects of continued exposure to temperatures near T_g , a series of microhardness tests were conducted to evaluate the effects of exposure time at different

temperatures on the microhardness evolution at that test temperature. Temperatures selected for evaluation were chosen both below T_g, (e.g. 562°C, 575°C) as well as above T_g (e.g. 600°C, 620°C) in conjuction with ongoing microstructural evolution studies being conducted by other HPCRM team members.

The effects of increased exposure times at different test temperatures on the microhardness/strength were determined using the NIKON QM-2 hot microhardness testing machine described above. Separate right circular cylindrical samples, 6 mm in length, were prepared from the drop cast SAM1651 rods for each exposure temperature (i.e. 562°C, 575°C, 600°C, 620°C) of interest. Duplicate samples were prepared for some test temperatures (e.g. 562°C, 600°C) in order to determine the reproducibility of the data. The surfaces to be indented were metallographically polished to a 0.5 micrometer finish using a variety of grit papers followed by polishing with diamond paste to ensure a flat and parallel surface for subsequent indentation. The indentation load selected was 500 grams with an indentation time of 15 seconds for each test. In a typical test, the sample and indenter were heated directly from room temperature to the temperature of interest (e.g. 562°C, 575°C, 600°C, or 620°C) at a heating rate of approximately 10°C/min. Upon reaching the (constant) temperature of interest, microhardness indentations were performed at that (constant) temperature after various exposure times, including: 0 minutes, 5 minutes, 10 minutes, 30 minutes, and 60 minutes. Additional exposure times (e.g. 120 minutes, 150 minutes, 180 minutes, 290 minutes) at (constant) temperature were evaluated for some samples. Three (3) microhardness tests were conducted at each temperature/exposure time and the microhardness indentations were taken sufficiently far apart to eliminate any possibility of the deformation fields overlapping. After the final three (3) indentations were performed at the longest exposure time for each sample, the sample and indenter were cooled to room temperature. The indented surface of each sample was then examined at room temperature using both optical and scanning electron microscopy in order to determine the indentation size(s) at each test temperature/exposure time. The microhardnesses were subsequently calculated using standard techniques.

Figure 70a [Figure 4a, Lewandowski] summarizes the evolution of microhardness (kg/mm^2) with increased exposure time for SAM1651 held at 620°C. Figure 4b plots the same data for the microhardness using GPa. Figure 4c converts the microhardness data shown in Figure 4b to an estimated compressive strength, using the relationship: Compressive strength = VHN/3.

Figures 70a and 70b [Figures 4a and 4b, Lewandowski] illustrate the low initial microhardness of SAM1651 at 620°C in addition to the rapid increase of microhardness with increasing time at 620°C, followed by a plateau of microhardness for exposure times from 60 minutes to 150 minutes. Figure 70a [Figure 4c, Lewandowski] summarizes the estimated compressive strength of SAM1651 held at 620°C for the various times shown. The low initial estimated strength (e.g. 200 MPa) rapidly increases to nearly 900 MPa within the first 60 minutes exposure at 620°C, indicative of rapid structure evolution in the initially amorphous SAM1651. Subsequent room temperature x-ray analysis of the sample shown in Figures 70a through 70c [Figures 4a through 4c, Lewandowski] revealed the presence of crystalline peaks after the 150 minute exposure to 620°C, consistent with information being developed by other HPCRM team members investigating microstructure evolution in these systems.

Separate samples tested at 600°C in the manner described above revealed a lower initial microhardness/strength and slower evolution of microhardness/strength with increased exposure time at 600°C in comparison to the sample tested at 620°C above, as summarized in Figures 71a through 71c [Figures 5a through 5c, Lewandowski].

Reducing the exposure temperature (e.g. 575°C) to below T_g (i.e. 584°C) produced a lower initial microhardness and significantly slower evolution of microhardness/strength with increasing exposure time compared to the exposure studies conducted at 620°C and 600°C, as summarized in Figures 72a through 72c [Figures 6a through 6c, Lewandowski].

Reducing the exposure temperature (e.g. 562°C) even further below T_g (i.e. 584°C) produced essentially no change in microhardness/strength at 562°C with exposure times up to 60 minutes, indicating the lack of significant structure evolution in SAM1651 over that exposure period.

Figures 74 [Figure 8, Lewandowski] summarizes the microhardness (GPa) evolution data for all of the different temperatures (e.g. 562°C, 575°C, 600°C, 620°C) and exposure times up to 60 minutes. It is clear that both the exposure temperature and time are important in affecting the evolution of microhardness/strength in SAM1651. Temperatures above T_g (e.g. 600°C, 620°C) exhibit more rapid evolution of microhardness/strength with increased exposure times at temperature, while testing below T_g (e.g. 575°C) produces a much slower evolution of microhardness/strength with increased exposure times at temperature. Finally, testing at temperatures further below T_g (e.g. 562°C) revealed essentially no change in microhardness/strength with increased exposure time. The rapid evolution of structure for the 620°C exposures is being documented by other members of the HPCRM team, while it appears that no significant structure evolution has occurred for SAM1651 held at 562°C for 60 minutes. This is consistent with the relative differences in evolution of microhardness with increasing exposure time at the temperatures summarized in Figures 74 [Figure 8, Lewandowski].

ADDITIVES FOR ENHANCED DAMAGE TOLERANCE

Yttrium Oxide Nanoparticles

The HPCRM Team has observed a dispersion of Y_2O_3 nanoparticles in the SAM1651 formulation, which is probably formed by the reaction of yttrium with oxygen. It is believed that this dispersion of nanoparticles may enhance both hardness and fracture toughness of these materials, through interruption of shear banding. The HPCRM Activity known as 'Production of Test Materials' will enable further enhancement of the SAM1651 formulation, with the intentional introduction of Y_2O_3 nanoparticles to control hardness and fracture toughness, and achieve overall enhancement of the material properties.

The tasks in this activity called for the preparation of significant quantities of Y_2O_3 nanoparticles and the introduction of these nanoparticles into HVOF coatings of the SAM1651 formulation. A 100-g batch of powders treated at 1000°C for two hours was delivered to SNL for characterization, and a 2-kg batch of powders was delivered to UCD. These particles will be introduced into coatings being produced by UCD.

Experimental Procedure

The solution/precipitation synthesis process used for the synthesis of the Y_2O_3 powders involves the emulsification of an aqueous phase in an organic solvent. In this type of system, known as a reverse micelle, the high interfacial tension between the water phase and the oil phase is reduced by the addition of a surfactant, as shown in Figure 75 [Figure 1, Graeve]. The surfactant molecules orient themselves according to the polarities of the constituent water and oil phases. Thus, due to the polarity of water, the polar heads of the surfactant molecules orient themselves towards the water droplets.

Because of the capacity to control not only the size, but also the shape of the micelles, the use of these structures for the synthesis of many types of powders offers advantages over other techniques. The micelles can be used as nanometer-scale reactors, with the final powders having approximately the same dimensions as the micelles. Since all of the starting materials are mixed at the molecular level in a water solution (inside the reverse micelle), a high degree of homogeneity is achievable. This project has taken advantage of reverse micellar systems in order to synthesize Y_2O_3 phosphors using the starting materials listed in Table 5 [Table 1, Graeve].

This micellar system is advantageous in that no co-surfactant is required to stabilize the microemulsions. Virtually all of the water is contained within the reverse micelle droplets and essentially all the AOT monomers coat the micelles. The procedure to follow for the synthesis of the powders is shown schematically in Figure 76 [Figure 2, Graeve]. As a first step, a mixture of AOT and iso-octane was stirred for 30 minutes in order for the AOT monomers to dissolve in iso-octane. In a separate beaker, a solution of de-ionized water and rare-earth nitrates was mixed until dissolved. The water-to-surfactant ratio was kept constant at $w_o = 14$. After mixing, the solution turned cloudy, at which point the dry ammonia gas was passed (as the solution was stirring) to form the hydroxide. The solution then displayed properties of a gel-like substance. This gel was dried for 24 hours. After drying, the solution was centrifuged to separate and collect the gel-like white precipitates of yttrium hydroxide. After centrifugation the precipitates were washed with de-ionized water three times and ethanol three times. After washing, the precipitates were placed in a fume hood in ambient air for 24 hours, and then collected for heat treatment. For characterization, the powders were lightly ground by hand using a porcelain mortar and pestle.

The powder morphology and size were characterized by several techniques, as listed in Table 6 [Table 2, Graeve]. XRD was conducted at room temperature with CuKα ($\lambda = 1.5418$ Å) radiation. Line broadening was used to calculate crystallite size by the Williamson-Hall method. Instrumental broadening was determined by using a standard silicon sample. The powders were spread evenly on a 2 mm thick quartz plate with a 20 mm square hole in the center. For DLS, the powders were dispersed with 0.5 g/L of sodium pyrophosphate in de-ionized water. The powders were magnetically stirred and ultrasonicated for one hour in order to achieve a homogeneous dispersion. The measurements were recorded using runs of two minutes.

Results – Powder Synthesis and Morphology

As indicated in the previous section, powders of Y_2O_3 were synthesized and subsequently treated at 500°C, 750°C, and 1000°C for 2 hours. The phases present in the powders treated at 500°C cannot be determined conclusively due to the broad peaks seen in the XRD pattern, shown in Figure 77 [Figure 4, Graeve]. The samples are close to amorphous, but initial crystallization of the Y_2O_3 phase can be seen. The powder diffraction file for the cubic structure of Y_2O_3, is also shown in Figure 77 [Figure 4, Graeve] for comparison with the experimental results. As the temperature is increased from 750°C to 1000°C, the powders exhibit progressive improved crystallinity. From x-ray line broadening, the crystallite size was determined and is also shown in Figure 77 [Figure 4, Graeve].

Figure 78 [Figure 5, Graeve] shows the dynamic light scattering results for the powders treated at the three different temperatures. As can be seen, the particle size decreases as heat treatment temperature increases. This can be attributed to the elimination of organic impurities on the surfaces, which can cause agglomeration. The powders treated at 1000°C have an average particle size around 250 nm, with a distribution between 70 nm and 800 nm.

Since the best particle size was obtained with heat treatment at 1000°C, all subsequent procedures were done using this calcinations temperature. Figure 79 [Figure 6, Graeve] shows the particle size of different batches of the same powder, which proves the consistency of the process. All batches shown in this figure were then mixed and delivered to other members of the Team.

NAVY APPLICATIONS

The Naval Research Laboratory has been the technical lead within the HPCRM Team for coordinating the installation of critical navy parts that are subjected to high corrosions and wear rates with the application of the thermally-sprayed iron-based amorphous-metal SAM2X5 and SAM1651 coatings on acquired navy components. Additional qualification testing is required to support the administrative documents necessary to receive approval from NAVSEA and the Type Commander of the responsible shipyard (in this case Pearl Harbor). Once all T&E has been submitted as a Departure From Specification (DFS), from the determined submarine as a Naval Message, and Temporary Alteration (TEMPALT) to the approving authority and acceptance has been received, NRL will coordinate the ship check, validate fit, form and function and work with the respective shipyard to ensure a dry fit up of the components is satisfactory prior to HPCRM application by Caterpillar. NRL will manage and provide a certified NACE inspector to oversee the HPCRM application process (including substrate preparation) at Caterpillar Incorporated to ensure quality control as required by the navy.

Submarines

The Naval Research Laboratory (R. Brown) has lead the effort for the HPCRM Team to determine whether or not these iron based amorphous metals provide a viable means of protecting parts from corrosion and wear onboard submarines. Initial demonstrations have thus far focused on sail cover plates and brine-pump shafts. Specific activities and tasks are as follows:

- Coordination with Norfolk Naval Shipyard and Puget Sound Naval Shipyard for the identification of submarine pumps and sail cover plates. Conducted inspection of deactivated submarines with Lawrence Livermore National Laboratory (J. Farmer) and determined best candidate components for HPCRM application.
- Established Military Interdepartmental Procurement Request (MIPR) and issued to respective shipyards for the removal of sail cover plates from the 688 class deactivated boats (702 & 693) at Puget Sound Naval Shipyard and two brine pumps (10K GPD & 1.6K GPD) from the Portsmouth in Norfolk Naval shipyard.
- Conducted engineering review with Supervisor of Shipbuilding at Electric Boat, Groton CT to locate all structural and mechanical drawings that correlate to the deactivated boat parts. This includes coordinating efforts with the pump vendor (CARVER) to locate pump drawing details. Also located drawings of active 688 class boats located in Pearl Harbor, San Diego and Norfolk.
- All submarine sail cover plates have been removed from inspected submarines at Puget Sound Naval Shipyard, shipped and received on schedule to Caterpillar (M. B. Beardsley)
- The two Brine pumps have been removed from the ex-Portsmouth and are being shipped to Key West.
- A Plan of Action and Milestones (POA&M) has been developed and sent to NAVSEA's CO7T, Karen Poole and CO5M1, Mark Ingle, with regards to qualification testing and installation in order to expedite the approval process for the DFS.
- Communications and Coordination have begun with Pearl Harbor contacts (Type Commander, Business Agent, Pearl Harbor Naval Shipyard, and Pearl Harbor Naval Submarine Support Center) to determine what level of effort is required to support NRL managed navy component installation. This will include determining ship availability, work force to remove existing components, dry fit of acquired unfinished parts, reinstallation of original parts and then reinstallation of final product.
- Conducted inspection and inventory of non-classified sail cover plates for the 688 class submarine (693 &702 boats) at Caterpillar Inc. Received 12 ~11"x15" plates and 16 ~16 ½-inch x17-inch plates. It is anticipated that minor modifications will be required to these deactivated plates to assure fit, form and function to an active boat.

Parts obtained for deployment onboard submarines include:

- Puget Sound Naval Shipyard – Sail Cover Plates – Figures 80-85 [Figures 1-7, Brown]
  - Sail Cover Plates from 688 Class Submarines
    - Small Size: Approximately 8-inch x 11-inch × 3/8-inch; 18 Parts
    - Medium Size: 16-inch × 17-inch × 3/8-inch; 24 Parts
- Norfolk Naval Shipyard – Brine Pumps Figures 86-88 [Figures 8-10, Brown]
  - 10K Low Pressure Brine Pump (Shafts) from 688 Class Submarines
    - APL 017030722; NSN 3H4320-01-317-3577
    - Manufacturer: Carver Pump Company; Drawing D-NDS-0-98-02
  - 1.6K Low Pressure Brine Pump (Shafts) from 688 Class Submarines
    - APL 017030383; NSN 2SH4320-01-032-9397-A2
    - Manufacturer: Carver Pump Company; Drawing D-NDS-0-98-001
  - 10K & 1.6K Pump Motors
    - APL 173870012; NSN 9G6105-01-175-9774
    - Manufacturer: Hansome Energy Systems, Inc.; Drawing A-203-12
- Norfolk Naval Shipyard – Other Submarine Components
  - Cleats from Class 688 Submarines – Quantity: 3
    - Size: Approximately 1-foot × 2-feet × 1-foot
  - Sail Whistle Door from Class 688 Submarines – Quantity: 1
    - Size: Approximately 12-inch × 8-inch × 3/8-inch
  - Temperature Regulating Valve from Class 688 Submarines – Quantity: 1
    - Size: Approximately 4-inch
  - Steam Trap from Class 688 Submarines – Quantity 1
    - Size: Approximately 4-inch
  - Over Pressure Trip from Class 688 Submarines – Quantity: 1

USS PONCE

The amphibious ship shown in Figure 89 [Figure 1, Bayles] is the USS PONCE, LPD-15, and has been made available for our surface ship test and evaluation effort. PONCE will be at Metro Machine Corporation in Norfolk, Virginia for an extended maintenance availability from November 2005 to August 2006. Robert Bayles and Bucky Glenn briefed the Port Engineer, Bud Hubert, on the HPCRM program and, specifically, the Intake Air Plenum Inserts and the Simulated Intake Plenums that we want to install on PONCE. NRL has a good rapport with the Fleet in Norfolk, having installed a variety of devices and coatings that have proven to be beneficial. Hubert was very supportive of NRL's request to install the HPCRM items on PONCE and he later briefed ship's force on our needs. In order to install our items on the ship we must prepare a Deviation from Specification document to show what we are doing and how any risks are mitigated. While PONCE is in port, these installations and possibly more will be monitored by Bayles and by NRL's on-site personnel. Even while in port the HPCRM will be exposed to the marine and industrial environments. After the availability is complete, PONCE will engage in shakedown cruises and deployments. Upon each of her returns to Norfolk, the HPCRM installations will be examined and documented. A Deviation From Specification document will be prepared and approved for the installation of HPCRM-coated items on the ship.

Intake Plenum Insert

An insert was designed by NRL for installation in the intake air plenum Figures 90 through 92 [Figures 2 through 4, Bayles], to challenge the HPCRM coatings. The insert represents a T-stiffener attached to a bulkhead (wall). The plenum is a large square tube that carries air from a fan room on the ship's main deck to the ventilation system for the lower decks. Due to the continuous flow of moist, salt-laden air, the interior of the plenums experience severe corrosion. The plenum inserts will be installed in a fan room near Frame 120, accessible through a louvered door on a bulkhead. This fan room was selected since it is most likely to be active most of the time during the availability and while in port as well as while at sea. The inserts were sprayed by the A&A Company, South Plainfield NJ using a plasma gun and SAM2X5 powder. The powder size was designated -30 um +15 um One insert was coated using a gun with an extension and right-angle nozzle to simulate spraying difficult to reach surfaces. The plasma gun was used because a right-angle head was not available for A&A's HVOF system. The inserts will be painted with the Ameron 133/333 system typically used in intake plenums. They will be bolted into the plenums, standing off from the bulkhead, oriented so that the T-stiffener is horizontal.

Simulated Intake Plenum

In addition to the inserts, a more elaborate structure has been designed that represents many features of ship construction, including inside corners and edges, holes, pipes, and T-stiffeners. This structure has not been fabricated yet and the final design will depend upon the space available for installation. This item will be located out in the weather, on top of the pilothouse.

Well Deck Tank Hatch Covers

The well deck of this amphibious ship is almost always wet, especially under the wood flooring. Tank hatch cover plates suffer severe corrosion. We will coat several cover plates with HPCRM and install them in the well deck. They will be accessible for inspection by removing a square panel of the flooring Figure 93 [Figure 5, Bayles].

Anchor Chain Covers

The forcastle deck at the front of the ship sees salt air and, occasionally, seawater. Covers for the anchor chain openings in the deck are exposed to this environment and to handling abuse. We will coat one with HPCRM and paint. The second one will be painted but will not have HPCRM coating.

Mooring Line Port Covers

For docking, mooring lines connect the ship to the pier. The aft mooring station has several ports that the mooring lines pass through. When at sea, covers close these ports. The covers are exposed to this environment and to handling abuse.

Howitzer Spades

Marine Corps artillery pieces and other equipment have sliding contact areas of bare steel that require regular maintenance to remove rust. High hardness, in addition to its corrosion resistance, makes HPCRM an ideal candidate for these applications. The Program Manger, Fire Support Systems at MARCORSYSCOM, Quantico has authorized the coating of recoil reaction spades from the M-198 Howitzer. These spades dig into the ground during firing and are always exposed to the weather. Four spades have been sent to Caterpillar for coating with HPCRM Figure 94 [Figure 6, Bayles].

Circulation Pump

A circulation pump for seawater cooling has become available and is being shipped to NRL Key West for disassembly. The shaft of this pump will be prepared and coated with HPCRM by Caterpillar. We may have the impeller coated as well. The pump has been described as a contingency spare onboard a ship, so it may be in very good condition. After the coating is complete, this pump will be run at NRL Key West under conditions typical of the duty cycle of a circulation pump.

Sealer Pull Tests

Thermal spray coatings are usually treated with a sealer to prevent moisture from entering the pores and causing corrosion. In the case of HPCRM, the material itself is corrosion resistant and the intended density is high to prevent the environment from accessing the substrate through continuous pores. Nevertheless, additional protection is afforded by sealing the HPCRM coatings. In many applications the coating must also be painted. In order to ensure that the sealer does not jeopardize paint adhesion, a set of ASTM D-4541 paddy pull tests was performed on two submarine sail cover plates. Each cover plate was sprayed with SAM2X5 by Caterpillar and then dipped halfway into Microseal DS-AC sealer. This is an acetone based sealer (AC) in a double strength (DS). At NRL, one plate was grit blasted to remove excess sealer and the other was left with a noticeable amount of sealer on the surface of the half that was immersed. The cover plates were then painted with Mare Island F-150, a typical primer for the submarine sail. After the paint was cured the pull tests were performed and no substrate/sealer or sealer/paint failures were observed, indicating very good adhesion whether the surface was original HPCRM, sealer blasted to remove excess, or thick sealer. Based on these results it is recommended to seal all HPCRM coatings. Note that the HPCRM coatings, as applied, have an appropriate surface profile (approximately 0.002 inch) for ideal paint adhesion.

Dry film thickness (DFT) measurements using eddy current instruments were erroneous. A destructive measurement (Tooke gauge) of the F-150 primer showed a thickness of 0.005 inch thickness, consistent with the wet film thickness measurements obtained while painting, while two eddy current instruments from different manufacturers indicated 0.018 inch thickness. An ultrasonic-based instrument will be tested shortly. If none of the DFT gauges works, a method for non-destructive DFT measurement will be developed.

JSF

Discussions have been initiated with David S. Cadman, Deputy Director Air Vehicle IPT, F-35 Joint Strike Fighter Program. A briefing on HPCRM will be presented by Bayles and Farmer.

AAAV/EFV

Discussions have been initiated with Sean Griffin, Director, Production and Engineering, DRPM AAA (EFV Program Office). A briefing is planned by HPCRM Team Members.

Wire HVOF

An evaluation has begun to determine the feasibility of using wire, in place of powder, in an HVOF gun to apply HPCRM coatings Figure 95 [Figure 7, Bayles]. The advantages of wire-HVOF include simpler operation (wire is easier to handle than powder), lower cost (making powder in a tight size range is an expensive process with relatively low yield), and more portability (elimination of the powder handling equipment). A disadvantage, which the HPCRM team is working to overcome, is the difficulty of producing suitable HPCRM wire with the necessary toughness and homogeneity. The tip of the wire is ablated by the high velocity combustion products to produce droplets, likely molten. The individual droplets are accelerated to the workpiece by the combustion products. Once the droplets leave the wire there is no opportunity for homgenization, so the wire must be homogeneous to a scale much smaller than the droplet size in order that the resulting splats on the workpiece have the proper composition. To facilitate complete melting and mixing of the constituents of the wire, such as a cored wire containing powdered alloying components, consideration has been given to aspiration of metal from a premelted pool, wire sourced, inside the gun. At this time such an approach is considered too complex, so the focus for producing homogeneous wire is based on wire fabrication processes. ORNL is evaluating the possibility of extruding HPCRM and NRL is in discussions with Nonosteel on this topic since they have produced DAR40 wire.

A&A Company, working with a partner, Plasma Powders Company, is developing a wire HVOF gun, below. This gun has been used to produce a coating for evaluation by the HPCRM team, but further development is needed.

Gehring LP has obtained the rights to a wire HVOF system developed by General Motors for coating engine cylinder bores. It is understood that the Gehring system is much further developed than the Plasma Powders gun. The HPCRM team (Brad Beardsley) is exploring overcoming Gehring's reluctance to sell the gun as a general purpose gun, rather than as a part of an elaborate cylinder coating system, their present business model.

Wire HVOF has great promise as an economical, flexible application method for HPCRM, but it will present challenges, particularly involving wire development.

REPOSITORY APPLICATIONS

Basket Material for Enhanced Criticality Control and Safety

Prevention of nuclear criticality in spent fuel storage and transportation, as well as in geologic repository when the spent fuels are contained in disposal canisters and disposed of, is an important licensing requirement. To prevent nuclear criticality in spent fuel storage, transportation, and/or disposal, neutron-absorbing materials (or neutron poisons, such as borated stainless steel, BORAL™, METAMIC™, Ni-Gd, and others) would have to be applied, usually as structural support baskets holding the spent fuel assemblies inside storage, transportation or disposal containers. When the container internals stay dry and the storage configurations stay intact, the potential for nuclear criticality is very small. However, if water is introduced, e.g., in an accident when a transport cask is dropped into a water body, or in a long-term scenario when the disposal container is breached and water enters the container. The potential for nuclear criticality can't be ruled out, especially in the case of the disposal container where boron in the borated stainless steel basket is preferentially leached out before the other fissionable materials. The applications of a boron-containing HPCRM (SAM1651, SAM2X5, etc.) as a neutron-absorbing coating to the metallic support structure, or as the neutron-absorbing bulk-alloy structural support material, can enhance criticality safety for spent nuclear fuel in storage pool racks; in baskets inside the dry storage containers; inside the transportation cask; and eventually inside the disposal container for repository disposal. The corrosion-resistance of the HPCRM coating, when applied on the surface of the borated stainless steel basket can enhance the basket's corrosion resistance and help prevent the preferential leaching of the boron from the borated stainless steel. The use of these advanced boron-containing, iron-based, corrosion-resistant materials to prevent nuclear criticality in long-term spent fuel storage and disposal would be extremely beneficial. A criticality analysis has been performed and is summarized in Figure 96.

Enhanced Corrosion Resistance of Container

Such materials could also be used to coat the entire outer surface of containers for the transportation and long-term storage of high-level radioactive waste (HLW) spent nuclear fuel (SNF), or to protect welds and heat affected zones, thereby preventing exposure to environments that might cause stress corrosion cracking. In the future, it may be possible to substitute such high-performance iron-based materials for more-expensive nickel-based alloys, thereby enabling cost savings in various industrial applications.

SUMMARY

The current Fe-based amorphous metals include specific elements known to impart corrosion and oxidation resistance, such as Cr, Mo, W. Additions of Y and Zr improve glass formability, while forming protective oxide scales at high temperature. In the future, the addition of titanium may also lead improved passive film stability at higher temperatures, and is being explored.

Ingots and melt-spun ribbons of the Y- and Mo-containing Fe-based amorphous metals have no grain boundaries, and therefore have more corrosion resistance in than nickel-based Alloy C-22. While the passive film on nickel-based C-22 undergoes breakdown in 5M $CaCl_2$ at 105°C at low potential, the passive film on the new Fe-based amorphous metal remains stable at a potential above that required for oxygen evolution.

Electrochemical tests have proven that corrosion performance superior to wrought and thermally sprayed coatings of nickel-based Alloy C-22 can be achieved with the new iron-based amorphous metals. For example, the passive film on wrought Alloy C-22 undergoes breakdown at 100 to 200 mV vs. Ag/AgCl in 5M $CaCl_2$ at 105°C, whereas SAM1651 maintains stable passivity, even as the potential is increased to levels approaching that required for oxygen evolution. These materials are far superior to thermal-spray coatings of Alloy C-22 in seawater. While it has not been possible to render Alloy C-22 as a corrosion resistant, thermal spray coating, such possibilities do exist with the amorphous metal formulations.

These novel materials can be produced as either bulk alloys or coatings. For example, melt spinning and arc melting with drop casting can be used to render these materials as fully dense pore-free bulk alloys. Coatings can be produced with advanced thermal spray processes, or by physical vapor deposition processes such as magnetron sputtering or electron-beam evaporation. The materials can also be rendered as bulk alloys by using HVOF to form large plates on a flat mandrel. Near theoretical density is achieved through precise control of powder size with atomization and classification.

Early HVOF coatings of SAM35, SAM40, SAM40X3 had non-optimal elemental compositions, and were produced with non-optimal thermal spray parameters (powder size, gun pressure, and particle velocity), and exhibited light rusting after 13 cycles in the classic salt fog test. However, additional work with optimized elemental compositions and samples in the form of fully dense pore-free materials, have shown no corrosion after 24 cycles in this aggressive test. The most promising formulations at the present time are believed to be SAM2X5 and SAM1651. Salt-fog testing of HVOF coatings of these materials showed no corrosion after more than 30 cycles (and up to 54 cycles) in the salt fog test. Such performance cannot be achieved with thermally sprayed Type 316L stainless steel, as this material loses most of its desirable corrosion-resistance during the thermal spray process. To a lesser extent, similar difficulties are encountered during the thermal spraying of Alloy C-22.

The reference material, nickel-based Alloy C-22, is an outstanding corrosion-resistant engineering material. Even so, crevice corrosion has been observed with C-22 in hot sodium chloride environments without buffer or inhibitor. Comparable metallic alloys such as SAM2X5

and SAM1651 may also experience crevice corrosion under sufficiently harsh conditions. Accelerated crevice corrosion tests are now being conducted to intentionally induce crevice corrosion, and to determine those environmental conditions where such localized attack occurs.

The minimum cooling rates for glass formation in SAM2X5 and SAM7 have been estimated. Based upon the most recent analyses (FY05), the minimum cooling rate for SAM1651 (SAM7) is approximately 140 to 190 K/s, range given by spatial extent of glass-crystalline transition region. The minimum cooling rate for SAM2X5 is now believed to be approximately 1000 K/s. The partial TTT-diagrams assessed for SAM2X5 and SAM7 have been developed. In the case of SAM1651 (SAM7), the initial crystalline phase that forms is $M_{23}(B,C)_6$. In the case of SAM2X5, the initial crystalline phase is Mo_3B_2 (the analysis is pending). Testing has included the isothermal annealing of as-spun ribbons. In these annealing studies, SAM1651 (SAM7) has exhibited nucleation-controlled transformation. There are some early time features that still need to be clarified. SAM2X5 exhibits growth controlled transformation. This work has lead to several recommendations for future work related to the investigation of thermal stability: (1) avoid possible oxygen contamination in powders by using ingots for melt-spinning and wedge casting; perform more complete analysis of powder and microstructures; further development of TTT-diagrams, including further modeling and conversion to CCT; and enhanced wedge sample analysis with more robust heat flow analysis and microstructure identification.

Ongoing work will continue to develop microhardness data for other relevant exposure temperature/time combinations for SAM1651, as well as determining the effects of different heating rates on the microhardness evolution. The evolution of structure is being documented by other members of the HPCRM team. Similar studies on Alloy C-22, SAM2X5 and/or other Fe-based amorphous alloys of interest to the HPCRM team are planned. Similar studies could be conducted on SAM coatings. The microhardness/structure evolution studies will also be used to select annealing temperatures/times for evaluation of fracture toughness on notched bend bar samples.

Such materials could also be used to coat the entire outer surface of containers for the transportation and long-term storage of spent nuclear fuel, to protect welds and heat affected zones, thereby preventing exposure to environments that might cause stress corrosion cracking, and as a means of criticality control inside containers [Farmer et al. 2000a & 2000b]. In the future, it may be possible to substitute such high-performance iron-based materials for more-expensive nickel-based alloys, thereby enabling cost savings in a wide variety of industrial applications.

ACKNOWLEDGMENTS

Work was sponsored by the Defense Advanced Research Projects Agency (DARPA) Defense Science Office (DSO), and the United States Department of Energy (DOE) Office of Civilian and Radioactive Waste Management (OCRWM). This work was done under the auspices of the U.S. DOE by Lawrence Livermore National Laboratory (LLNL) under Contract No. W-7405-Eng-48.

The HPCRM Team expresses their gratitude to sponsors for financial support, and supportive colleagues for making this work possible. A special thanks to Jeffrey Walker (DOE OSTI), Leo Christodoulou (DARPA DSO), and Joe Payer (Case Western Reserve University) for sharing their considerable knowledge and insight in field of mining and repository operations, engineering and materials science, and for their innovative solutions to many of the technical problems that have been addressed.

Execution of this multi-institutional materials development program would not have been possible without the outstanding administrative support and communication skills of Lesa Christman, and the exceptional resource management expertise of Sharice Tippens. The programmatic support of LLNL's Program Leader for Nuclear Energy, David McCallen has enabled this project to transition to a higher level than would have otherwise been possible.

REFERENCES – ALPHABETICAL LISTING

- ASTM 1989. Designation G 5-87, Annual Book of ASTM Standards, Section 3, Vol. 3.02, pp. 79–85 (1989).
- A. I. Asphahani, Materials Performance, Vol. 19, No. 12, pp. 33–43 (1980).
- A. J. Bard, L. R. Falkner, Kinetics of Electrode Reactions, Chapter 3, pp. 86-118; Techniques Based on Concepts of Impedance, Chapter 9, pp. 316-369: Electrochemical Methods, Fundamentals and Applications, John Wiley & Sons, New York, New York (1980).
- Daniel J. Branagan, Galen R. Smolik, Advanced Neutron Absorber Materials, Filed February 2, 1999, United States Patent 6,125,912, Granted October 3, 2000 [Reference 16, Perepezko].
- Daniel J. Branagan, Joseph V. Burch, Methods of Forming Steel, United States Patent No. 6,258,185, Filed May 25, 1999, Granted July 10, 2001 [Reference 15, Perepezko].
- Daniel J. Branagan, Hard Metallic Materials, Hard Metallic Coatings, Methods of Processing Metallic Materials and Methods of Producing Metallic Coatings, United States Patent Application 20030051781, Filed March 20, 2003 [Reference 28, Perepezko].
- Daniel J. Branagan, Formation of Metallic Thermal Barrier Coatings, United States Patent Application No. 20050013723, Filed February 11, 2004 [Reference 21, Perepezko].
- Daniel J. Branagan, Method for Forming a Hard Metallic Wire, United States Patent Application 20040141868, Filed July 22, 2004 [Reference 25, Perepezko].
- Daniel J. Branagan, Method for Protecting a Surface, United States Patent Application 20040140021, Filed July 22, 2004 [Reference 26, Perepezko].
- Daniel J. Branagan, Hard Metallic Materials, Hard Metallic Materials, United States Patent Application 20040140017, Filed July 27, 2004 [Reference 16, Perepezko].

- Daniel J. Branagan, Methods of Forming Hardened Surfaces, United States Patent No. 6,767,419, Filed November 9, 2000, Granted July 27, 2004 [Reference 61, Perepezko].
- Daniel J. Branagan, Properties of Amorphous/Partially Crystalline Coatings, United States Patent Application No. 20040253381, Filed December 16, 2004 [Reference 22, Perepezko].
- Daniel J. Branagan, Methode of Modifying Iron-Based Glasses to Increase Crystallization Temperature without Changing Melting Temperature, United States Patent Application No. 20040250929, Filed December 16, 2004 [Reference 23, Perepezko].
- Daniel J. Branagan, Highly Active Liquid Melts Used for Form Coatings, United States Patent Application 20040250926, Filed December 16, 2004 [Reference 24, Perepezko].
- D. J. Branagan, M. C. Marshall, Be. E. Meacham, E. J. Buffa, High-Performance Iron-Based HVOF Amorphous Coatings, Submission to Lawrence Livermore National Laboratory for HPCRM Annual Report, NanoSteel Company, Idaho Falls, Idaho, 46 pages, September 17 (2004).
- D. J. Branagan, M. C. Marshall, B. E. Mecham, L. F. Aprigliano, R. Bayles, E. J. Lemieux, T. M. Wolejsza, F. J. Martin, J. C. Farmer, J. J. Haslam, S. D. Day, Wear and Corrosion Resistant Amorphous / Nanostructured Steel Coatings for Replacement of Electrolytic Hard Chromium, UCRL Report, Lawrence Livermore National Laboratory, Livermore, California. 7 pages (2005); Proceedings of the International Thermal Spray Conference and Exposition, American Society of Materials International, Seattle, Washington, May 15-18 (2006).
- D. Chidambaram, C. R. Clayton, M. R. Dorfman, Evaluation of the Electrochemical Behavior of HVOF-Sprayed Alloy Coatings, Surface and Coatings Technology, Vol. 176, pp. 307-317 (2004).
- C. L. Choy, K. W. Tong, H. K. Wong and W. P. Leung, J. Appl. Phys., 70, (9), 4919-4925, 1991 [Reference 1, Perepezko].
- A. J. Drehman and D. Turnbull, Scripta Mat., 15, 543, 1981 [Reference 3, Perepezko].
- J. C. Farmer, G. E. Gdowski, R. D. McCright, H. S. Ahluwalia, Corrosion Models for Performance Assessment of High-Level Radioactive Waste Containers, Nuclear Engineering Design, Vol. 129, pp. 57-88 (1991).
- J. C. Farmer et al., Protective Ceramic Coatings for High-Level Radioactive Waste Containers, UCRL-MI-131293, Presented to Ceramic Peer Review Panel, SRI International, Palo Alto, CA, August 17 (1998a).
- J. C. Farmer, K. R. Wilfinger, Process Level Model for Ceramic Coating, UCRL-ID-131899 Rev. 2, November 14 (1998b).
- J. C. Farmer, R. D. McCright, Crevice Corrosion and Pitting of High-Level Waste Containers: Integration of Deterministic and Probabilistic Models, Paper No. 98160, Symposium 98-T-2A, Annual Meeting of the National Association of Corrosion Engineers (NACE), Corrosion 98, San Diego, CA March 22-27 (1998c).
- J. C. Farmer, R. D. McCright, J. C. Estill, S. R. Gordon, Development of Integrated Mechanistically-Based Degradation-Mode Models for Performance Assessment of High-Level Containers, Proceedings of the Symposium on the Scientific Basis for Nuclear Waste Manatement XXII, D. J. Wronkiewicz, J. H. Lee, Eds., Materials Research Society Symposium Series, Warrendale, PA, Vol. 556, pp. 855-862 (1999).
- J. Farmer, S. Lu, T. Summers, D. McCright, A. Lingenfelter, F. Wang, J. Estill, L. Hackel, H-L. Chen, G. Gordon, V. Pasupathi, P. Andresen, S. Tang, M. Herrera, Modeling and Mitigation of Stress Corrosion Cracking in Closure Welds of High-Level Waste Containers for Yucca Mountain, Proceedings of the Annual Meeting of the American Society of

Mechanical Engineers, Pressure Vessels and Piping, 11 pages, Seattle, Washington, July (2000a).

- J. Farmer, S. Lu, D. McCright, G. Gdowski, F. Wang, T. Summers, P. Bedrossian, J. Horn, T. Lian, J. Estill, A. Lingenfelter, W. Halsey, General and Localized Corrosion of High-Level Waste Container in Yucca Mountain, Proceedings of the Annual Meeting of the American Society of Mechanical Engineers, Pressure Vessels and Piping, 11 pages, Seattle, Washington, July (2000b).
- J. C. Farmer et al., High-Performance Corrosion-Resistant Amorphous Metals, Proc. Global 2003, New Orleans, Louisiana, American Nuclear Society (2003).
- J. C. Farmer, J. J. Haslam, S. D. Day, D. J. Branagan, C. A. Blue, J. D. K. Rivard, L. F. Aprigliano, N. Yang, J. H. Perepezko, M. B. Beardsley, Corrosion Characterization of Iron-Based High-Performance Amorphous-Metal Thermal-Spray Coatings, PVP2005-71664, Proceedings of ASME PVP: Pressure Vessels & Piping Division Conference, Grand Hyatt, Denver, Colorado, July 17-21, 2005, American Society of Mechanical Engineers, Three Park Avenue, New York, New York, 7 pages (2005) [Reference 9, Perepezko].
- J. C. Farmer, J. J. Haslam, S. D. Day, D. J. Branagan, M. C. Marshall, B. E. Mecham, E. J. Buffa, C. A. Bue, J. D. K. Rivard, D. C. Harper, M. B. Beardsley, D. T. Weaver, L. F. Aprigliano, L. Kohler, R. Bayles, E. J. Lemieux, T. M. Wolejsza, N. Yang, G. Lucadamo, J. H. Perepezko, K. Hildal, L. Kaufman, A. H. Heuere, F. Ernst, G. M. Michal, H. Kahn, E. J. Lavernia, High-Performance Corrosion-Resistant Materials: Iron-Based Amorphous-Metal Thermal-Spray Coatings, High-Performance Corrosion-Resistant Materials (HPCRM) Annual Report, UCRL-TR-206717, Lawrence Livermore National Laboratory, Livermore, California, 178 pages, September 28 (2004) [Reference 10, Perepezko].
- J. Farmer, C. Earl, C. Doty, D. Spence, J. Walker, F. Wong, J. Payer, G-Q. Lu, D. E. Clark, D. C. Folz, A. Heuer, O. Graeve, D. Branagan, C. Blue, J. Rivard, J. Perepezko, L. Kaufman, N. Yang, E. Lavernia, J. Haslam, E. Lemieux, L. Aprigliano, B. Beardsley, T. Weaver, B. Edwards, B. Brown, Ar. Halter, B Bayles, J. Lewandowski, DARPA-DOE High Performance Corrosion-Resistant Materials (HCPRM) Principal Investigator's Meeting, Turtle Bay Resort, Oahu, Hawaii, January 10-13, 2005, UCRL-PRES-214672, Lawrence Livermore National Laboratory, Livermore, California, 407 pages [Perepezko, Reference 11].
- D. V. Fix, J. C. Estill, R. B. Rebak, Effect of Small Variation in Composition of Plates and Weld Filler Wires on the General Corrosion Rate of Ni-Cr-Mo Alloys, PVP2005-71173, Proceedings of ASME PVP: Pressure Vessels & Piping Division Conference, Denver, Colorado, July 17-21, 2005, American Society of Mechanical Engineers, 9 pages (2005).
- R. B. Gundlach and D. V. Doane in Metals Handbook, 10th edition: Properties and selection: Irons, Steels and High-Performance Alloys. Eds. J. R. Davis, K. M. Mills and S. R. Lampman, ASM International. 1, 1990 [Reference 7, Perepezko].
- F. Guo, S. J. Poon, G. J. Shiflet, Metallic Glass Ingots Based on Yttrium, Applied Physics Letters, Vol. 83, No. 13, pp. 2575-2577 (2003) [Figure 12, Perepezko].
- J. C. Hamilton, J. C. Farmer, R. J. Anderson, In Situ Raman Spectroscopy of Anodic Films Formed on Copper and Silver in Sodium Hydroxide Solution, J. Electrochem. Soc., Vol. 85, No. 4, pp. 739-745 (1986).
- J. J. Haslam, J. C. Farmer, R. W. Hopper, K. R. Wilfinger, Ceramic Coatings for Corrosion Resistant Nuclear Waste Container Evaluated in Simulated Ground Water at 90C, UCRL-JRNL-206107, Lawrence Livermore National Laboratory, Livermore, California, August 17,

2004 (34 p.); Metallurgical and Materials Transactions A, Volume 36A, May 2005, p. 1085-1095 (2004).

- G. O. Ilvebare, T. Lian, J. C. Farmer, Environmental Considerations in the Studies of Corrosion Resistant Alloys for High-Level Radioactive Waste Containers, Paper No. 02539, NACE Corrosion 2002, Denver, Colorado, April 7-11 (2002).
- J. Jäckle, Rep. Prog. Phys., 49, 171, 1986 [Reference 5, Perepezko].
- K. Kishitake, H. Era, F. Otsubo, Characterization of Plasma Sprayed Fe-10Cr-10Mo-(C,B) Amorphous Coatings, Vol. 5, No. 2, pp. 145-153 (1996).
- W. T. Kim, K. Clay, C. Small, B. Cantor, Heat Treatment of a Melt Spun Fe70Cr18Mo2B10 Alloy, Journal of Non-Crystalline Solids, Vol. 127, pp. 273-286 (1991).
- K. J. King, J. C. Estill, R. B. Rebak, Anodic Behavior of Specimens Prepared from a Full-Diameter Alloy 22 Fabricated Container for Nuclear Waste, PVP2005-71176, Proceedings of ASME PVP: Pressure Vessels & Piping Division Conference, Denver, Colorado, July 17-21, 2005, American Society of Mechanical Engineers, 9 pages (2005).
- R. M. Latanison, Corrosion Resistance of Metastable Alloys Processed by Rapid Solidification, Workshop on Amorphous Metals and Semiconductors, Electric Power Research Institute (EPRI), May 12-18, 1985 [Reference 60, Perepezko].
- L. Kaufman, Calculation of Coating Compositions for Use in Various Corrosive Environments with Pourbaix and Thermal Stability Diagrams, Massachusetts Institute of Technology, Submission to Lawrence Livermore National Laboratory for HPCRM Annual Report, Cambridge, Massachusetts, 38 pages, September 8 (2004).
- S. Linderoth, N. H. Pryds, M. Eldrup, A. S. Pedersen, M. Ohnuma, T.-J. Zhou and L. Gerward, Mat. Res. Soc. Symp. Proc., 644, 2001 [Reference 4, Perepezko].
- Z. P. Lu, C. T. Liu, W. D. Porter, Role of Yttrium in Glass Formation of Fe-Based Bulk Metallic Glasses, Vol. 83, No. 13, Applied Physics Letters, pp. 2581-2583.
- R. William McCallum, Daniel J. Branagan, Carbide/Nitride Refined Rare Earth-Iron-Boron Permanent Magnet and Method of Making, Unites States Patent No. 5,803,992, Filed November 29, 1995, Granted September 8, 1998 [Reference 18, Perepezko].
- R. William McCallum, Timothy W. Ellis, Kevin W. Dennis, Robert J. Hofer, Daniel J. Branagan, Production Method for Making Rare Earth Compounds, United States Patent 5,690,889, Filed February 15, 1996, Granted November 25, 1997 [Reference 19, Perepezko].
- R. William McCallum, Daniel J. Branagan, Carbid/Nitride Grain Refined Rare Earth-Iron-Boron Permanent Magnet and Method of Making, United States Patent 5,486,240, Filed April 25, 1994, Granted January 23, 1996 [Reference 20, Perepezko].
- J. S. Newman, Electrode Kinetics, Chapter 8, pp. 186-211, Electrochemical Systems, 2nd Edition, Prentice Hall International Series in the Physical and Chemical Engineering Sciences, Prentice Hall, Englewood Cliffs, New Jersey (1973).
- S. J. Pang, T. Zhang, K. Asami, A. Inoue, Acta Materialia 50, 489-497 (2002).
- S. Pang, T. Zhang, K. Asami, A. Inoue, Materials Transactions, Effects of Chromium on the Glass Formation and Corrosion Behavior of Bulk Glassy Fe-Cr-Mo-C-B Alloys, Vol. 43, No. 8, pp. 2137-2142 (2002a) [Reference 14, Perepezko].
- S. J. Pang, T. Zhang, K. Asami, A. Inoue, Synthesis of Fe-Cr-Mo-C-B-P Bulk Metallic Glasses with High Corrosion Resistance, Acta Materialia, Vol. 50, pp. 489-497 (2002b) [Figure 13, Perepezko].

- J. H. Perepezko, K. Hildal, Thermal and Kinetic Analysis of Amorphous Fe-Based Alloys for Use in Thermal Spray Processing, Submission to Lawrence Livermore National Laboratory for HPCRM Annual Report, University of Wisconsin, Madison, Wisconsin, 74 pages, September 9 (2004) [Reference 8, Perepezko].
- D. E. Polk, B. C. Giessen, Overview of Principles and Applications, Chapter 1, pp. 2-35, Metallic Glasses, J. J. Gilman, H. J. Leamy, Eds., American Society of Metals, Metals Park, Ohio, 348 p. (1978).
- V. Ponnambalam, S. J. Poon and G. Shiflet, J.Mater.Res., 19 (5), 1320, 2004 [Reference 6, Perepezko].
- N. H. Pryds, M. Eldrup, M. Ohnuma, A. S. Pedersen, J. Hattel and S. Linderoth, Mat. Trans. JIM, 41, (11), 1435, 2000 [Reference 4, Perepezko].
- Charles H. Sellers, Daniel J. Branagan, Timothy A. Hyde, Atomization Methods for Forming Magnet Powders, Filed April 7, 1997, Granted February 8, 2000 [Reference 17, Perepezko].
- H. Shinimiya, A. Nakazawa, Z. Kato, A. A. El Moneium, Y. Niizeki, K. Asami, K. Hashimoto, Corrosion Resistant Bulk Amrophous Ni-Cr-Ta-Mo-Nb-5P Alloys in Concentrated Hydrochloric Acids, Paper 319, Session on Corrosion and Electrochemistry of Advanced Materials in Honor of Koji Hashimoto, 208th Meeting of the Electrochemical Society, Westing Bonaventure Hotel, Los Angeles, California, October 16-21, 2005, Electrochemical Society, Pennington, New Jersey (2005).
- M. Telford, The Case for Bulk Metallic Glass, Materials Today, March 2004, Elsevier Ltd., pp. 36-43 (2004).
- K. R. Wilfinger, J. C. Farmer, R. W. Hopper, T. E. Shell, Corrosion Protection of Metallic Waste Packages Using Thermal Sprayed Ceramic Coatings, Proceedings of the Symposium on the Scientific Basis for Nuclear Waste Manatement XXII, D. J. Wronkiewicz, J. H. Lee, Eds., Materials Research Society Symposium Series, Warrendale, PA, Vol. 556, pp. 927-934 (1999).
- N. Yang, J. Farmer, G. Lucadamo, J. Haslam, Microstructual Factors and Their Implication to Corrosion and Damage Tolerance of Fe-Cr-Mo Based SAM40 and SAM1651, Submission to Lawrence Livermore National Laboratory for HPCRM Annual Report, Sandia National Laboratory, Livermore, California, August 30, 2004, 43 pages.
- A. Yilmaz, P. Pasupathi, R. Rebak, Stifling of Crevice Corrosion in Alloy 22 During Constant Potential Tests, PVP2005-71174, Proceedings of ASME PVP: Pressure Vessels & Piping Division Conference, Denver, Colorado, July 17-21, 2005, American Society of Mechanical Engineers, 10 pages (2005).

TABLES

Table 1 – The melt-spinning process was used to perform a systematic study of various elemental compositions, each based on the Fe-based DAR40 composition, with 1, 3, 5, and 7 atomic percent additions of specific elements believed to be beneficial to glass formation or corrosion resistance. Elemental additions investigated included nickel, molybdenum, yttrium, titanium, zirconium, and chromium.

Original Data	Formula	Fe	Cr	Mn	Mo	W	B	C	Si	Y	Zr	Ti	Ni	P	Other
DAR27	$(Fe_{0.8}Cr_{0.2})_{73}Mo_2W_2B_{16}C_4Si_1Mn_2$	58.4	14.6	2.0	2.0	2.0	16.0	4.0	1.0						
DAR35	$Fe_{54.5}Mn_2Cr_{15}Mo_2W_{1.5}B_{16}C_4Si_5$	54.2	15.0	2.0	2.0	1.5	16.0	4.0	5.0						0.3
DAR40	$Fe_{52.3}Mn_2Cr_{19}Mo_{2.5}W_{1.7}B_{16}C_4Si_{2.5}$	52.3	19.0	2.0	2.5	1.7	16.0	4.0	2.5						
DAR40X3	$Fe_{50.7}Mn_{1.9}Cr_{18.4}Mo_{5.4}W_{1.6}B_{15.5}C_{3.9}Si_{2.4}$	50.7	18.4	1.9	5.4	1.6	15.5	3.9	2.4						0.2
LDAR1	$(DAR40)_{100-x} + Ni_x$														
LDAR1X1	$(DAR40)_{99} + Ni_1$	51.8	18.8	2.0	2.5	1.7	15.8	4.0	2.5				1.0		
LDAR1X3	$(DAR40)_{97} + Ni_3$	50.7	18.4	1.9	2.4	1.6	15.5	3.9	2.4				3.0		
LDAR1X5	$(DAR40)_{95} + Ni_5$	49.7	18.1	1.9	2.4	1.6	15.2	3.8	2.4				5.0		
LDAR1X7	$(DAR40)_{93} + Ni_7$	48.6	17.7	1.9	2.3	1.6	14.9	3.7	2.3				7.0		
LDAR2X1	$(DAR40)_{99} + Mo_1$	51.8	18.8	2.0	3.5	1.7	15.8	4.0	2.5						
LDAR2X3	$(DAR40)_{97} + Mo_3$	50.7	18.4	1.9	5.4	1.6	15.5	3.9	2.4						
LDAR2X5	$(DAR40)_{95} + Mo_5$	49.7	18.1	1.9	7.4	1.6	15.2	3.8	2.4						
LDAR2X7	$(DAR40)_{93} + Mo_7$	48.6	17.7	1.9	9.3	1.6	14.9	3.7	2.3						
LDAR3X1	$(DAR40)_{99} + Y_1$	51.8	18.8	2.0	2.5	1.7	15.8	4.0	2.5	1.0					
LDAR3X3	$(DAR40)_{97} + Y_3$	50.7	18.4	1.9	2.4	1.6	15.5	3.9	2.4	3.0					
LDAR3X5	$(DAR40)_{95} + Y_5$	49.7	18.1	1.9	2.4	1.6	15.2	3.8	2.4	5.0					
LDAR3X7	$(DAR40)_{93} + Y_7$	48.6	17.7	1.9	2.3	1.6	14.9	3.7	2.3	7.0					
LDAR4X1	$(DAR40)_{99} + Ti_1$	51.8	18.8	2.0	2.5	1.7	15.8	4.0	2.5			1.0			
LDAR4X3	$(DAR40)_{97} + Ti_3$	50.7	18.4	1.9	2.4	1.6	15.5	3.9	2.4			3.0			
LDAR4X5	$(DAR40)_{95} + Ti_5$	49.7	18.1	1.9	2.4	1.6	15.2	3.8	2.4			5.0			
LDAR4X7	$(DAR40)_{93} + Ti_7$	48.6	17.7	1.9	2.3	1.6	14.9	3.7	2.3			7.0			
LDAR5X1	$(DAR40)_{99} + Zr_1$	51.8	18.8	2.0	2.5	1.7	15.8	4.0	2.5		1.0				
LDAR5X3	$(DAR40)_{97} + Zr_3$	50.7	18.4	1.9	2.4	1.6	15.5	3.9	2.4		3.0				
LDAR5X5	$(DAR40)_{95} + Zr_5$	49.7	18.1	1.9	2.4	1.6	15.2	3.8	2.4		5.0				
LDAR5X7	$(DAR40)_{93} + Zr_7$	48.6	17.7	1.9	2.3	1.6	14.9	3.7	2.3		7.0				
LDAR6	$Fe_{43}Cr_{16}Mo_{16}B_5C_{10}P_{10}$	43.0	16.0		16.0		5.0	10.0						10.0	
LDAR7	$CBCTL1651 = Fe_{48}Mo_{14}Cr_{15}Y_2C_{15}B_6$	48.0	15.0		14.0		6.0	15.0		2.0					
LDAR8	$(CBCTL161)_{97} + W_3$	46.6	14.6		13.6	3.0	5.8	14.6		1.9					
LDAR9	$(DAR40)_{90} + Mo_7 + Y_3$	47.1	17.1	1.8	9.3	1.5	14.4	3.6	2.3	3.0					
LDAR10	$Fe_{57.3}Cr_{21.4}Mo_{2.6}W_{1.8}B_{16.9}$	57.3	21.4		2.6	1.8	16.9								

Table 2 – Summary of thermal analysis (DTA or DSC) on Fe-based glass forming alloys suitable for spray deposition.

Alloy	T_g (°C)	T_x (°C)	T_m (°C)	T_L (°C)	T_{rg} (°C)
DAR35	545-565	613	1074	1350	0.51
DAR40	568-574	623	1110	1338	0.53
DAR40X3	561-567	630	1130	1260	0.55
LDAR1X1	not clear	612	1121	min. 1270	N.A.
LDAR1X3	560	589	1119	min. 1300	0.53
LDAR1X5	540	572	1115	min. 1300	0.52
LDAR1X7	510	545	1112	min. 1300	0.50
LDAR2X1	575	620	1124	1190-1210	0.57
LDAR2X3	578	626	1131	1190-1210	0.57
LDAR2X5	579	628	1133	1190-1210	0.57
LDAR2X7	573	630	1137	1190-1210	0.57
LDAR3X1	560	614	1108	min. 1320	0.52
LDAR3X3	573	659	1138	min. 1380	0.51
LDAR3X5	590	677	1143	min. 1400	0.52
LDAR3X7	not clear	697	1164	min. 1420	
LDAR4X1	573	621	1135	min. 1300	0.54
LDAR4X3	568	623	1146	min. 1320	0.53
LDAR4X5	580	623	1194	1290	0.55
LDAR4X7	558	616	1198	1255	0.54
LDAR5X1	570	622	1134	min. 1360	0.52
LDAR5X3	575	641	1147	min. 1410	0.50
LDAR5X5	596	659	1193	min. 1420	0.51
LDAR6	580	623 [2)]	995	1238-1250	0.56
LDAR7	584	653 [2)]	1121	1290	0.55
LDAR8	565	637 [2)]	1137	1350-1370	0.52
LDAR9	572	677 [2)]	1146	1223	0.56
LDAR10	535	568 [1)]	1210	1350-1370	0.50
LDAR11	535	572 [1)]	1202	1365-1395	0.49

Table 3 – Current Test Matrix at Lawrence Livermore National Laboratory

Test Matrix at Lawrence Livermore National Laboratory						
Test Solution Type	NaCl	KNO_3	T	$CaCl_2$	$Ca(NO_3)_2$	T
	M or m	M or m	°C	M or m	M or m	°C
Half Moon Bay SW			30, 90			
Half Moon Bay SW			30, 90			
Chloride-Nitrate	1 M	None	30, 90			
Chloride-Nitrate	3.5 m	None	30, 90			
Chloride-Nitrate	3.5 m	0.175 m	30, 90			
Chloride-Nitrate	3.5 m	0.525 m	30, 90			
Chloride-Nitrate	6.0 m	None	30, 90			
Chloride-Nitrate	6.0 m	0.300 m	30, 90			
Chloride-Nitrate	6.0 m	0.900 m	30, 90			
Calcium Chloride				5 M	None	105
Calcium Chloride				12 m	None	130
Calcium Chloride				12 m	6 m	130
Published References: PVP 2005-71173; 71174; 71175; 71176.						

Table 4 – [Table 2, Perepezko] Material Properties Used in Finite Element Heat Transfer (FEHT) Modeling of SAM1651 (SAM7) Wedge Cast Cooling Curve at University of Wisconsin, Madison

Alloy Density ρ (kg/m^3)	Thermal Conductivity k (W/mK)	Heat Capacity C_p (J/kgK)	Heat Transfer Coefficient $H(t)$ (W/m^{2}K)	Mold Temperature T_0 (°C)
7600	40	750	2500-1400	25-60

Table 5. [Table 1, Graeve] Chemicals Used for the Synthesis of the Y_2O_3 Powders

Materials	Purpose	Vendor
Yttrium (III) Nitrate Reacton (99.99%)	Precursor for the Y_2O_3	Alfa Aesar
Sodium [bis (2-ethylhexyl) sulfosuccinate] (AOT)	Surfactant	Sigma Aldrich
Iso-octane	Continuous oil phase	Sigma Aldrich
De-ionized water	Polar phase	
Dry ammonia gas (NH_3)	Formation of $Y(OH)_3$	Fisher Scientific
Ethanol	Washing solvent	Sigma Aldrich

Table 6. [Table 2, Graeve] Characterization Techniques

Technique	Equipment	Purpose
X-Ray Diffraction (XRD)	Philips 3100 Diffractometer	Phase and crystallite size determination
Dynamic Light Scattering (DLS)	Nanotrac 250	Particle size determination

FIGURES

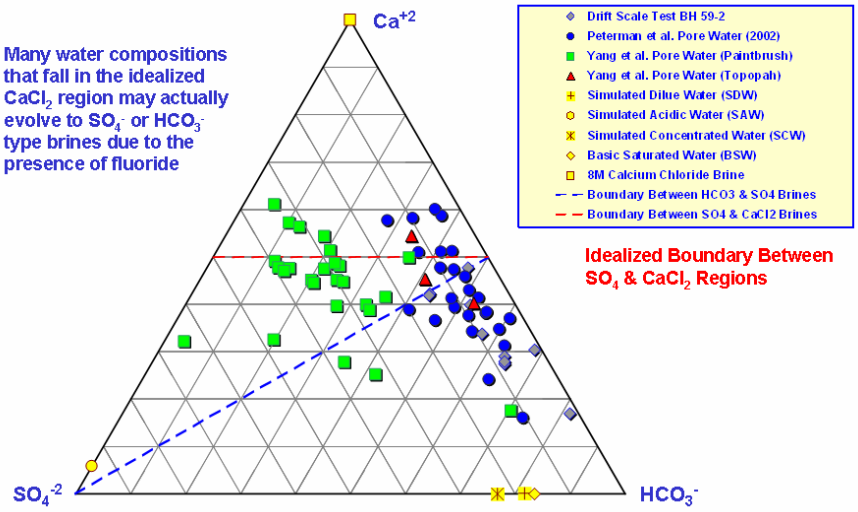

Figure 1. The classification of actual Yucca Mountain brines is shown in this pseudo ternary (trilateral) diagram. The boundary between the sulfate-chloride ((SO_4^{-2}) and calcium chloride (Ca^{+2}) regions is idealized. Many of the water compositions that fall in the idealized calcium chloride (Ca^{+2}) region may actually evolve to sulfate-chloride (SO_4^{-2}) or bicarbonate (HCO_3^-) type brines due to the presence of fluoride.

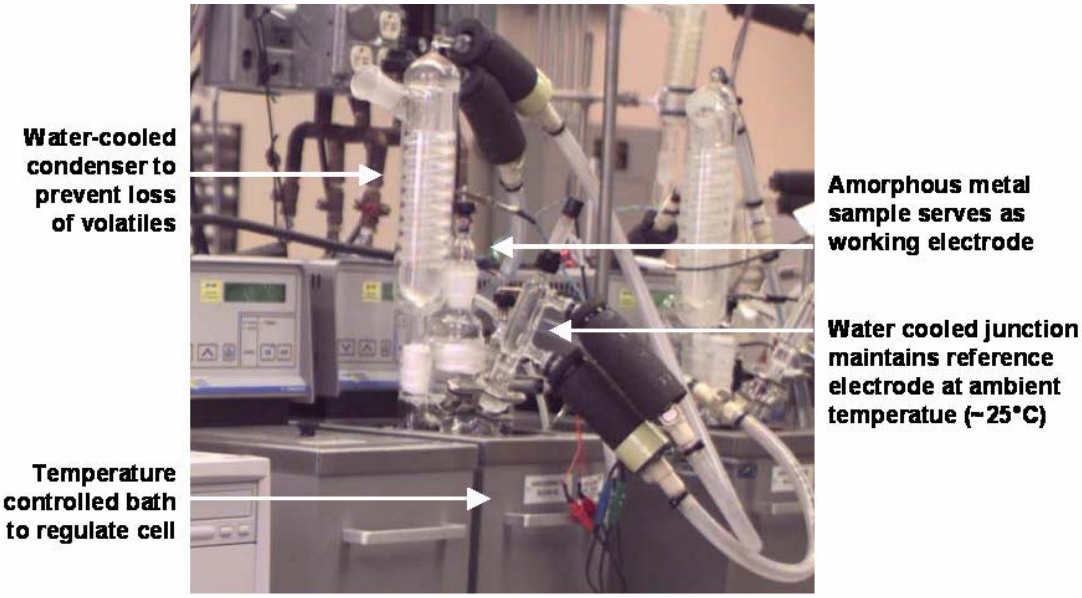

Figure 2. Electrochemical corrosion measurements at LLNL are made in special temperature controlled electrochemical cells which enable testing at elevated temperature for prolonged periods of time (years if necessary). Water cooled condensers are included to prevent the loss of volatiles from the electrochemical cell, while a water cooled junction enables the reference electrode to be maintained at standard temperature during testing, thereby minimizing error.

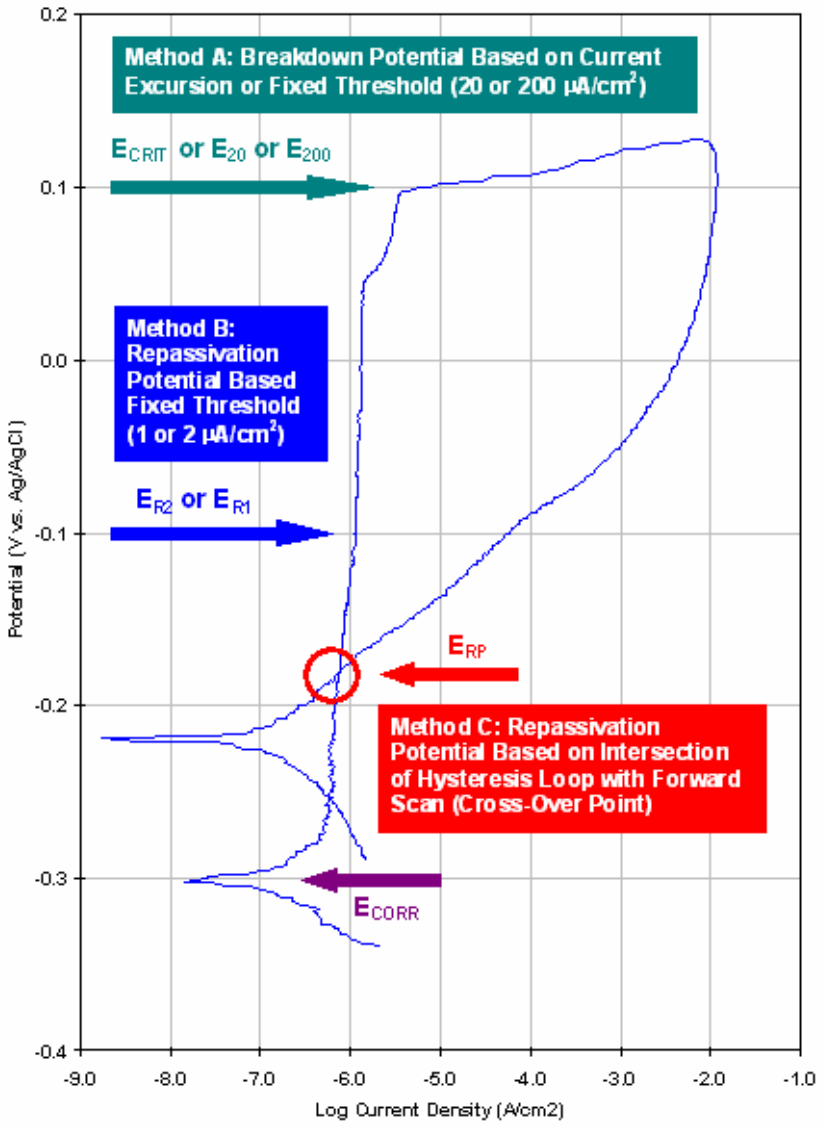

Figure 3. There competing methodologies (Methods A, B and C) are shown for determination of the threshold potential for localized corrosion from cyclic polarization curves, such as the one shown here for nickel-based Alloy C-22 in 5M $CaCl_2$ at 105℃.. Method A is the point during the anodic potential scan when the passive oxide film breaks down, thereby allowing anodic dissolution of the underlying metal, with a relatively high anodic current density. When it can be accurately measured, this is the true "critical potential." Alternatively, the repassivation potential can be determined with either Methods B or C. The repassivation potential is determined during the reverse scan, and is the point following passive film breakdown where the current density decreases to a level known to correspond to the passive current density (the current density that can be sustained by an intact oxide film). The passive current density can either be assumed, shown as Method B, or it can be established from the intersection of the forward and reverse potential scans, shown as Method C. Method C is considered to be the most rigorous approach for determining the repassivation potential, since the intersection point occurs at the actual (not assumed) passive current density.

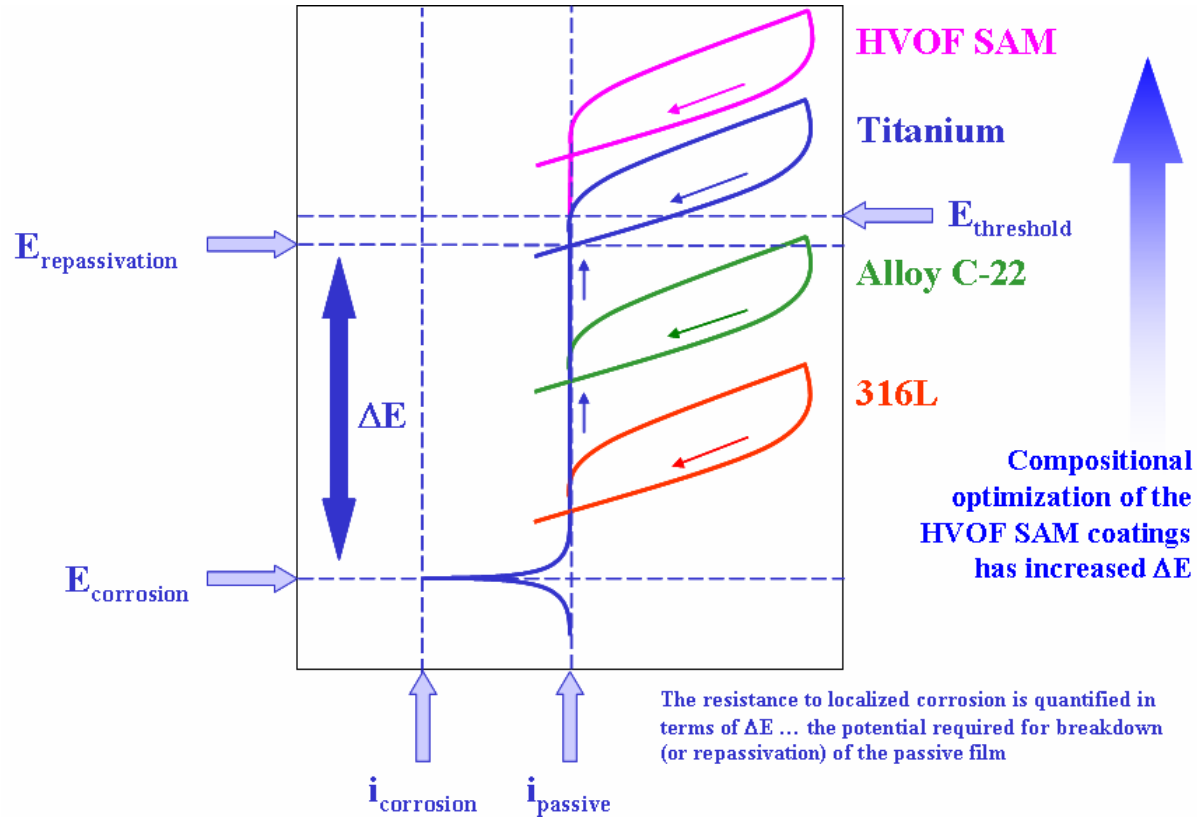

Figure 4. The repassivation potential, determined by Method C in most cases, has been used as a quantitative metric for screening elemental compositions of competing iron-based amorphous metals, thereby determining the specific composition (of those tested) with the best resistance to passive film breakdown in the test solution. A wide variety of alloy compositions, which are shown in Table 1, were explored using cyclic polarization as a screening method. However, as will be evident in the discussion of subsequent potential-step test data, superior and more credible methods exist for the determination of the critical potential. The potential step-methods are used after the initial screening, and provide better results.

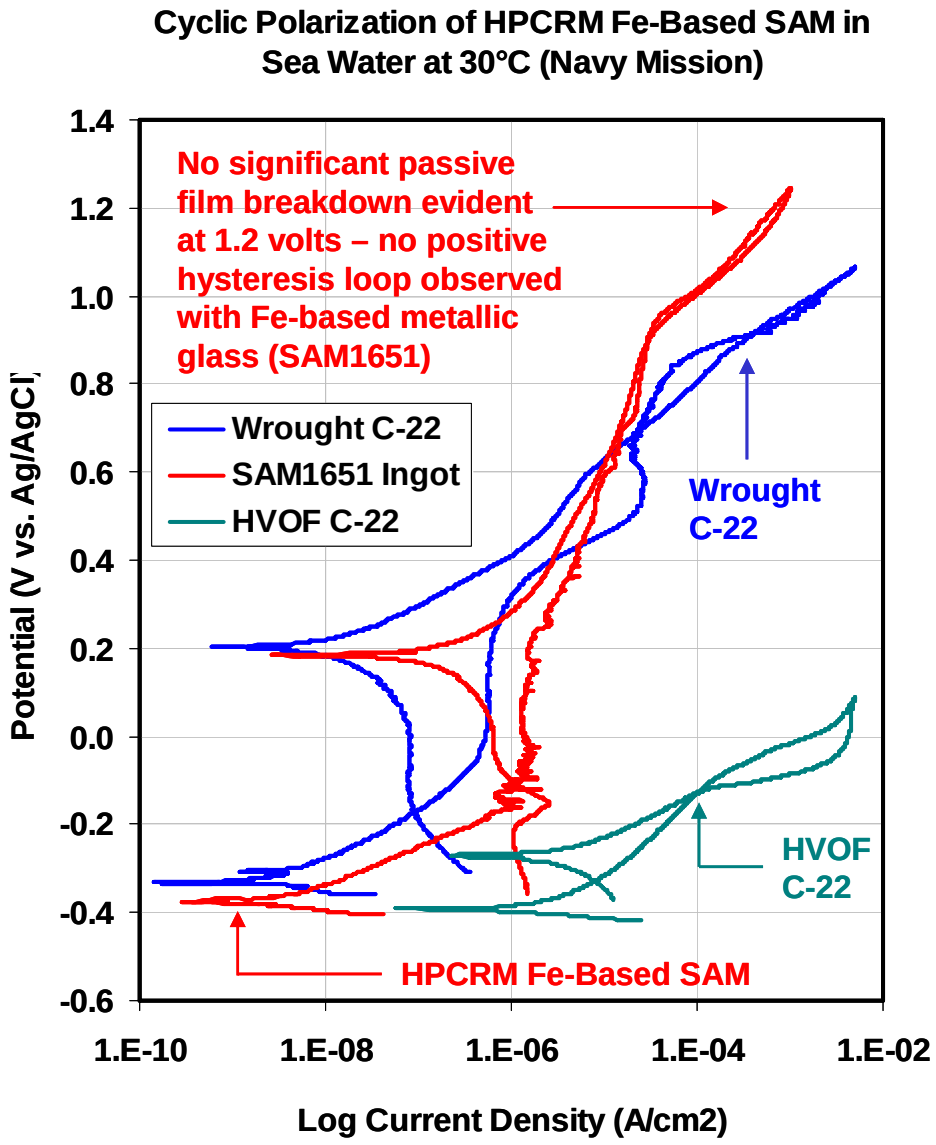

Figure 5. Cyclic polarization was used as a means of evaluating the relative passive film stability of a drop-cast ingot of SAM1651, a disk of wrought nickel-based Alloy C-22 (reference material), and a thermal spray (high-velocity oxy-fuel or HVOF) coating of Alloy C-22. The test was conducted in Half Moon Bay seawater at 30C, and the potential was measured relative to a standard silver / silver chloride reference electrode. The scan rate was 0.l667 volts per second. The current density for the 'as-sprayed' Alloy C-22 HVOF coating is based upon apparent electrode area, and was not corrected for surface roughness. In the case of the SAM1651, no passive film breakdown was observed, which is evident from the lack of hysteresis, even after scanning the voltage to a level close to oxygen evolution. Passive film breakdown was observed with wrought Alloy C-22, with a repassivation potential by Method C easily identified. Surprisingly, the Alloy C-22 coating loses has very poor corrosion resistance in comparison to both the SAM1651 ingot and the wrought Alloy C-22, which is reflected in a low repassivation potential.

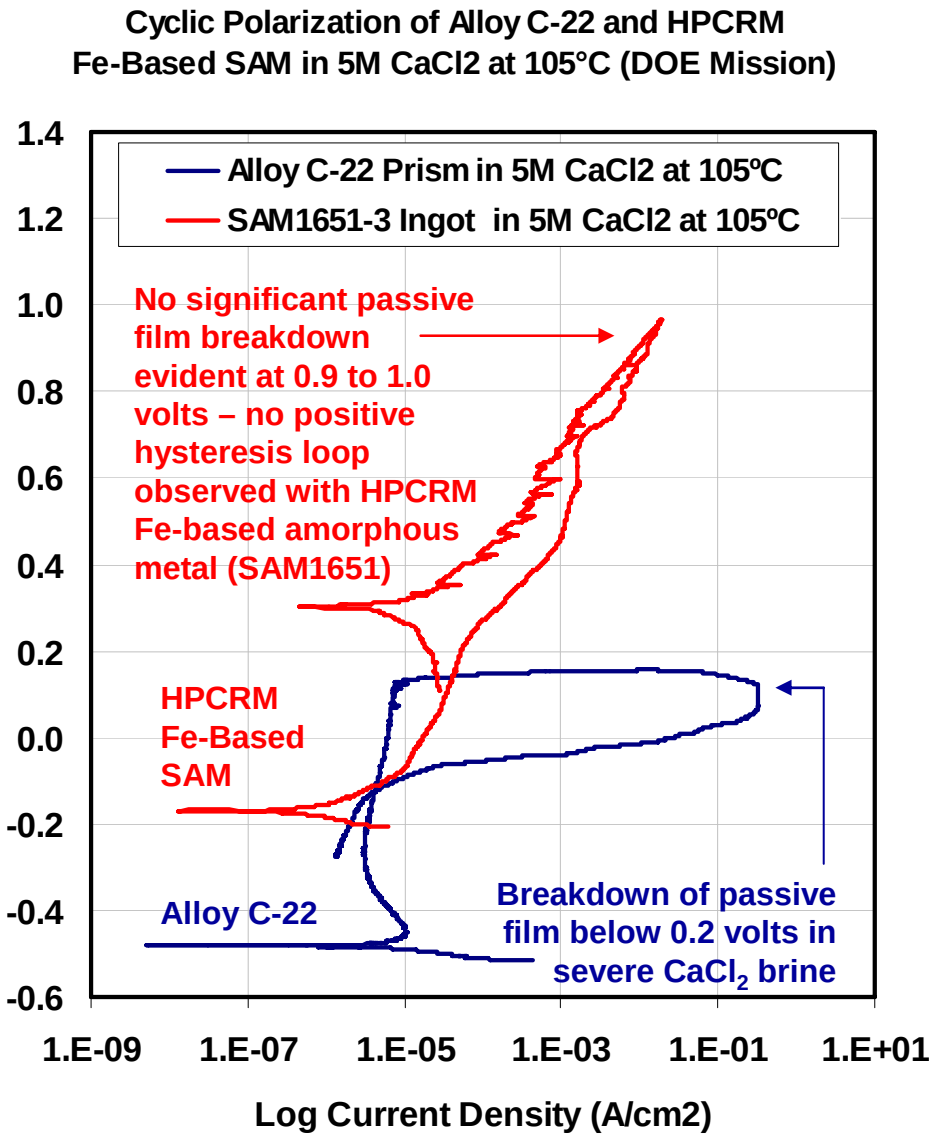

Figure 6. Cyclic polarization was used to compare the performance of a drop-cast ingot of SAM1651 against that of wrought Alloy C-22 in 5M calcium chloride at 105°C, which is an extremely aggressive environment. In the case of the drop-cast ingot of SAM1651, no significant passive film breakdown was observed at 0.9 to 1.0 volts. There was no positive hysteresis loop observed with this iron-based amorphous metal. There was hysteresis, but with the observed current density during the reverse less than that observed during the forward scan (indicative of even lower reactivity). In sharp contrast, there is an obvious breakdown of the nickel-based Alloy C-22 passive film at only 0.2 volts, showing a clear vulnerability in this aggressive environment. The repassivation potential is easily identified from the intersection of the hysteresis loop with the forward scan.

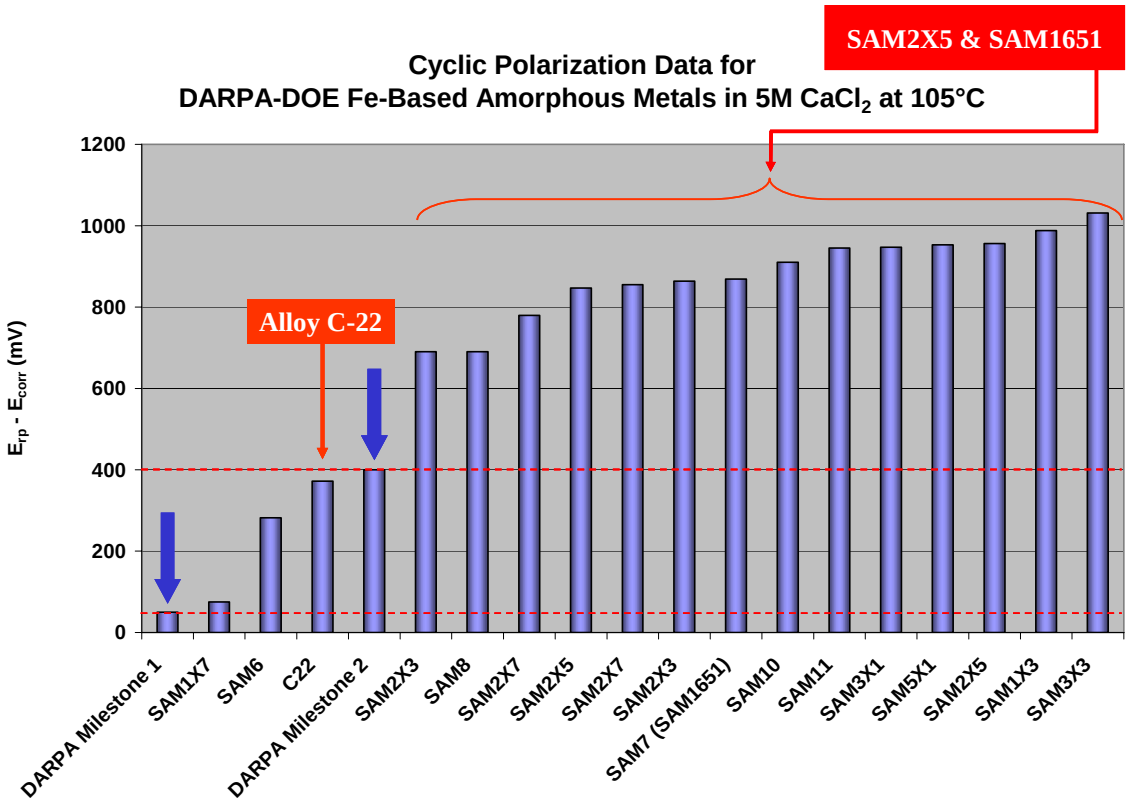

Figure 7. Cyclic polarization of melt spun ribbons was used to compare the relative corrosion resistance of a large number candidate alloy compositions in 5M $CaCl_2$ at 105°C. The alloy compositions are defined in Table 1. As previously discussed, the quantifiable metric used as a basis of comparison was the difference between the open circuit corrosion potential (E_{corr}) and the repassivation potential (E_{rp}). Several of the candidate alloy compositions had a larger metric value (E_{rp}- E_{corr}) than the reference material, which has been established as nickel-based Alloy C-22, due to its own outstanding corrosion performance. Note that DARPA Milestone 1 corresponds to the metric value for Type 316L stainless steel and DARPA Milestone 2 corresponds to the metric value for nickel-based Alloy C-22. It is therefore concluded that several types of iron-based amorphous metals exist which all have passive film stabilities that are comparable to that of the reference material.

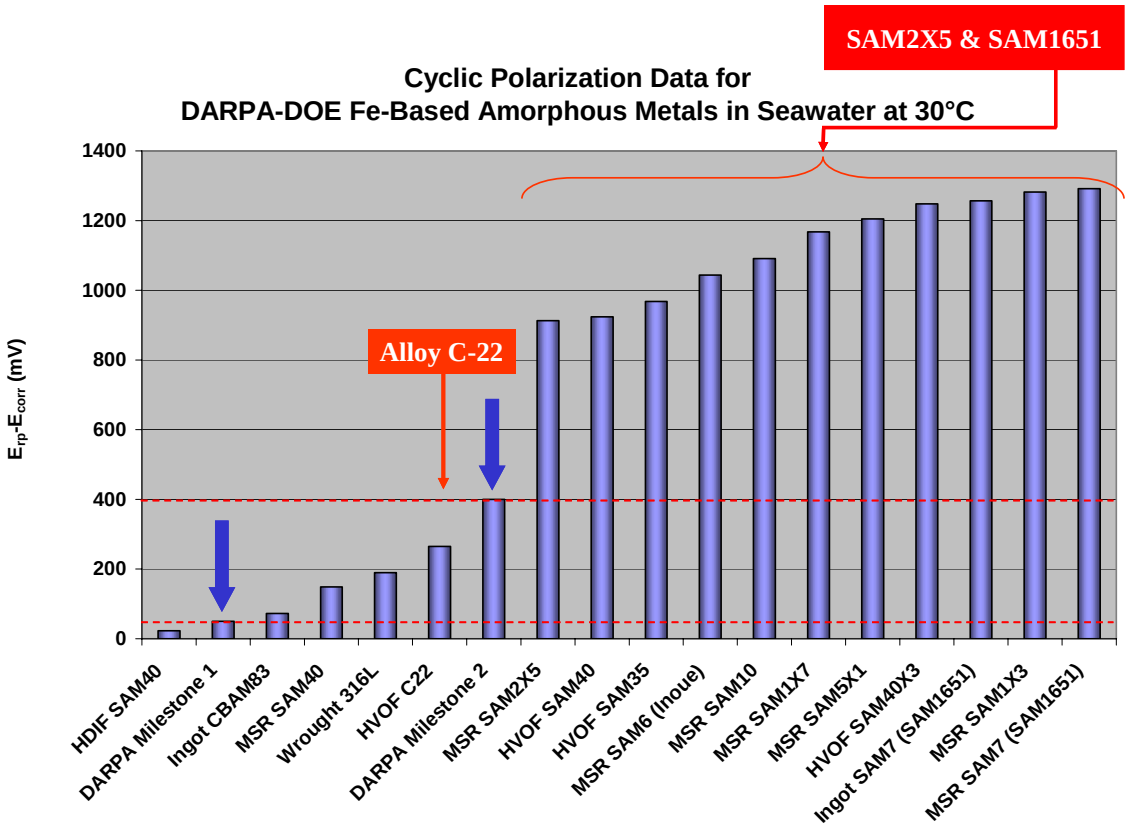

Figure 8. Cyclic polarization of melt spun ribbons was used to compare the relative corrosion resistance of a large number candidate alloy compositions in near-ambient Half Moon Bay seawater at 30°C. The alloy compositions are defined in Table 1. DARPA Milestone 1 corresponds to the metric value for Type 316L stainless steel and DARPA Milestone 2 corresponds to the metric value for nickel-based Alloy C-22. It is therefore concluded that several types of iron-based amorphous metals exist which all have passive film stabilities in seawater at 30°C that are comparable to that of the reference material.

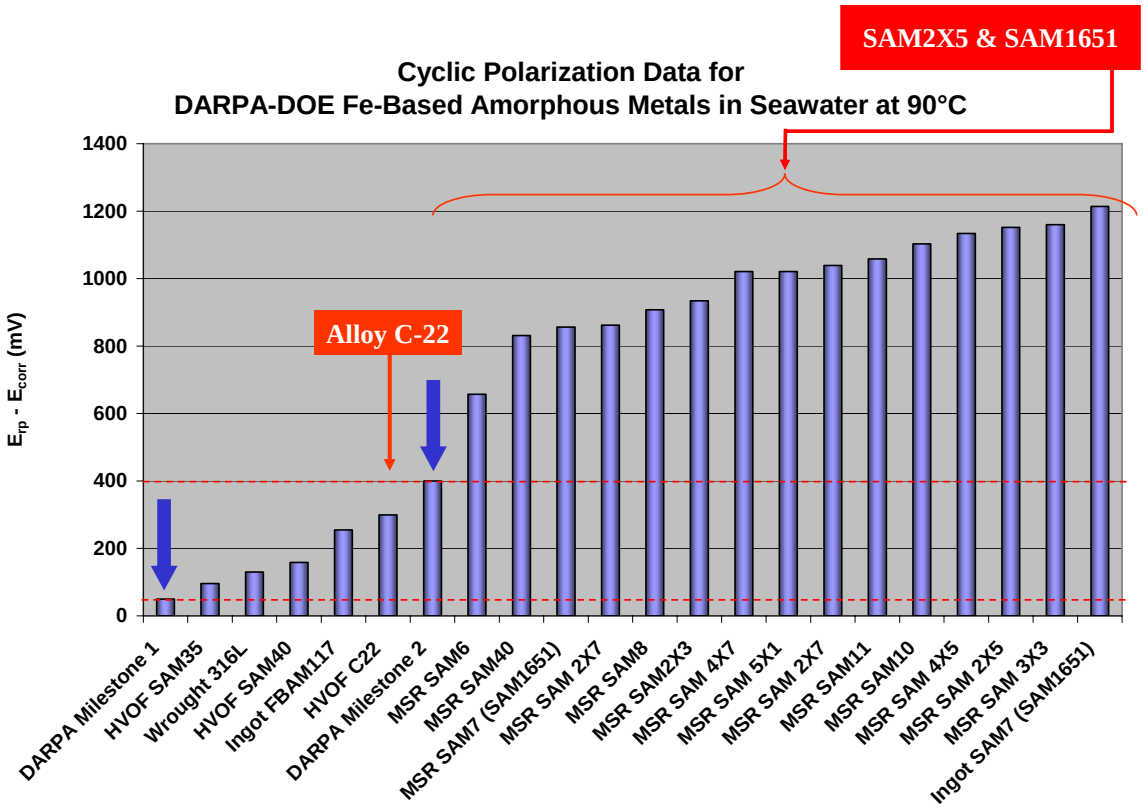

Figure 9. Cyclic polarization of melt spun ribbons was used to compare the relative corrosion resistance of a large number candidate alloy compositions in near-boiling Half Moon Bay seawater at 90°C. The alloy compositions are defined in Table 1. DARPA Milestone 1 corresponds to the metric value for Type 316L stainless steel and DARPA Milestone 2 corresponds to the metric value for nickel-based Alloy C-22. It is therefore concluded that several types of iron-based amorphous metals exist which all have passive film stabilities in seawater at 90°C that are comparable to that of the reference material.

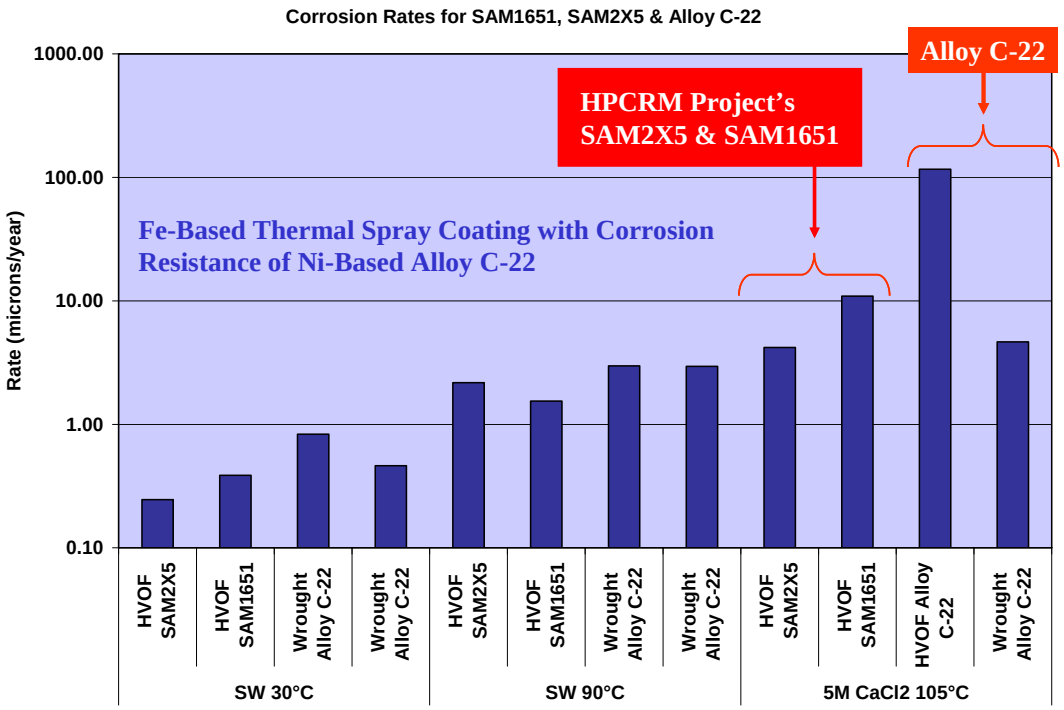

Figure 10. Linear polarization was used to determine the approximate corrosion rates of the thermal spray coatings of two amorphous metals of interest (HVOF SAM1651 and SAM2X5 coatings) and the reference material (wrought nickel-based Alloy C-22) in three relevant environments, Half Moon Bay seawater at two temperature levels, and in hot concentrated calcium chloride (5M $CaCl_2$ at 105°C). In seawater at both 30 and 90°C, the corrosion rates of HVOF SAM2X5 and SAM1651 coatings exhibited slightly lower corrosion rates than either wrought sample of Alloy C-22. The corrosion rates of all materials increased with temperature, as expected. In calcium chloride at 105°C, the corrosion rates of HVOF SAM2X5 and SAM1651 coatings were comparable to, or slightly lower than that of wrought Alloy C-22. In general, the corrosion rates observed in the hot calcium chloride (105°C) were higher than those observed in the heated seawater (90°C), which was also expected.

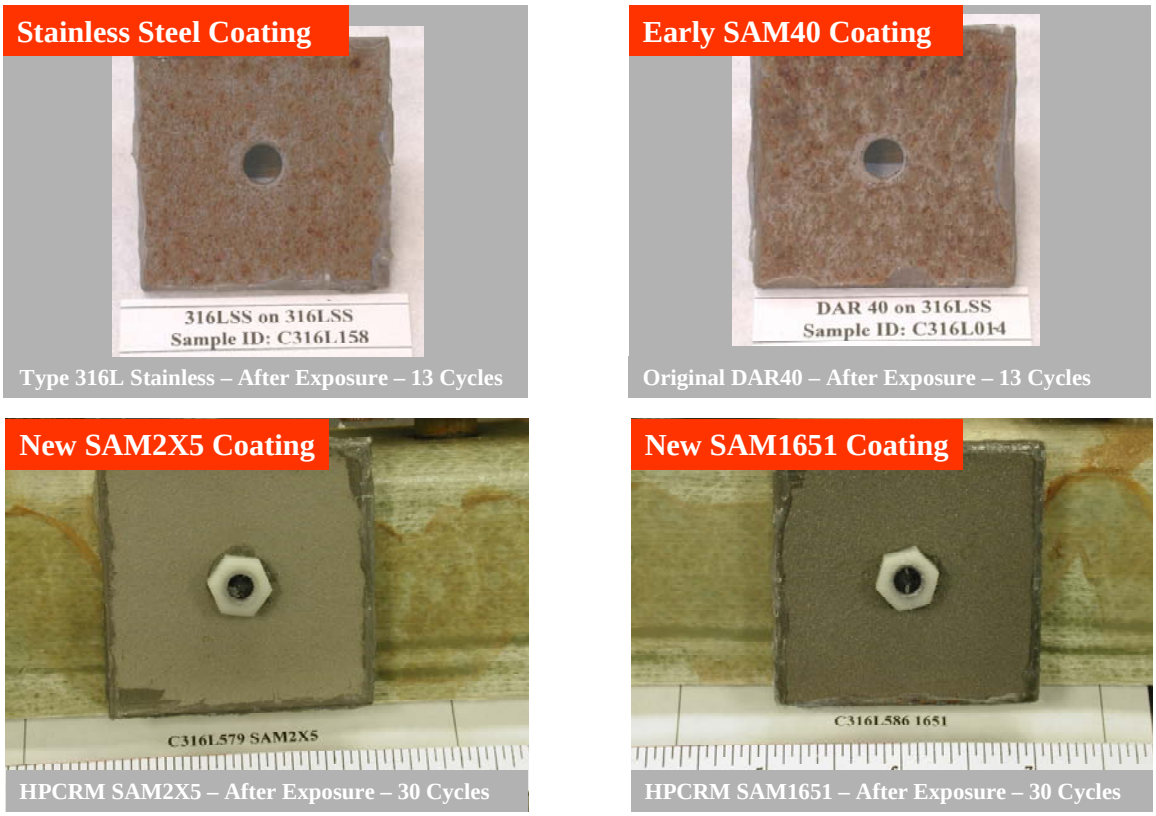

Figure 11. Salt fog testing was conducted on several thermal spray coatings, including HVOF coatings of Alloy C-22, Type 316L stainless steel, SAM40 (also referred to as DAR4)), SAM2X5 (also referred to as LDAR2X5) and SAM1651 (also referred to as CBCTL1651 or LDAR7). After 30 cycles in the ASTM Standard B-117 Salt Fog Test, the HVOF coating of Alloy C-22 showed slight rusting (not shown), while the HVOF coatings of Type 316L stainless steel and SAM40 showed substantial corrosion. In contrast, the newer SAM2X5 and SAM1651 formulations showed no corrosion at 30 cycles. The salt fog testing of SAM2X5 and SAM1651 were continued to almost 60 cycles with no evidence of corrosion.

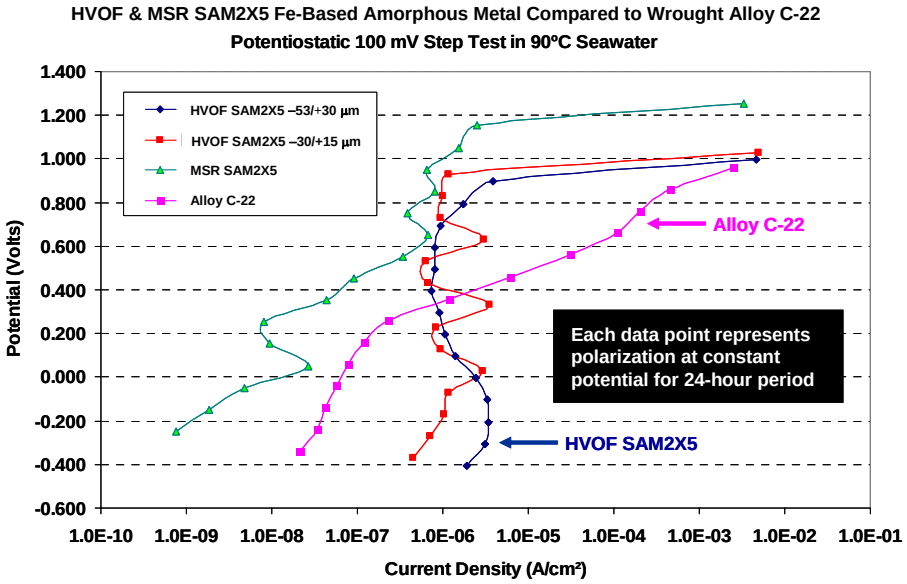

Figure 12. Potential-step testing has been performed on wrought Alloy C-22 (reference material); fully dense and completely amorphous melt spun ribbons of SAM2X5; optimized HVOF coatings produced with -53/+30 micron powders of SAM2X5; and optimized HVOF coatings produced with -30/+15 micron powders of SAM2X5. All were tested in Half Moon Bay seawater heated to 90°C. To eliminate the need for surface roughness corrections in the conversion of measured current and electrode area to current density, the SAM2X5 and SAM1651 coatings were polished to a 600-grit finish prior to testing. The curves represent the asymptotic current density reached after 24 hours at the corresponding potential (each data point represents a 24 hour test). The constant potential was applied after 1 hour at the open circuit corrosion potential (OCP). From previous work presented in the FY04 Annual Report (given in references), it has been found that coatings produced with SAM2X5 powders below a critical size are fully dense and are completely amorphous. The coatings produced with finer powders are therefore expected to have lower porosity and less residual crystalline phases present than those produced with larger particles. These data enable a clear and unambiguous determination of the threshold potentials for passive film breakdown in a non-creviced condition. First, it is clear that the passive film on wrought Alloy C-22 commences breakdown at a potential of approximately 200 mV relative to a standard Ag/AgCl reference electrode (approximately 600 mV above the open circuit corrosion potential), and has the least corrosion resistance of any sample evaluated during this test. Passive film breakdown on the SAM2X5 melt-spun ribbon did not occur until a potential in excess of 1200 mV vs. Ag/AgCl (1400 mV above OCP) was applied. Furthermore, the observed passive current density observed with this sample was extremely low. Both HVOF coatings of SAM2X5 (large and small powder sizes) also exhibited outstanding passive film stability, superior to that of the reference material. The passive film on the coating produced with -30/+15 micron powder remained intact until application of 1000 mV vs. Ag/AgCl (1200 mV above OCP), with a current density well within the passive range of several microamps per square centimeter. Similar observations were made with the coating produced with -53/+30 micron powders. Any differences in morphology did not have significant impact on corrosion resistance.

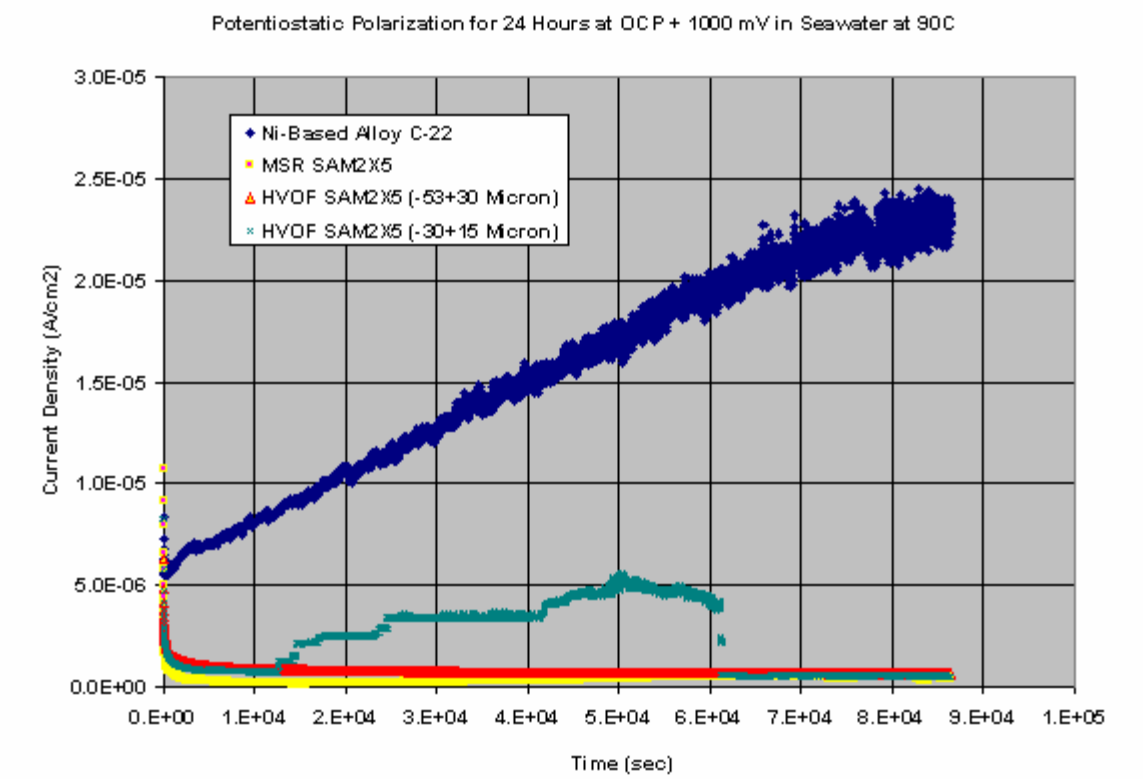

Figure 13. Transients in current density at a constant applied potential of 1000 mV vs. OCP for wrought Alloy C-22 (reference material), a fully dense and completely amorphous melt spun ribbon (MSR) of SAM2X5, HVOF coatings produced with -53/+30 micron powders of SAM2X5, and HVOF coatings produced with -30/+15 micron powders of SAM2X5, all in Half Moon Bay seawater heated to 90 ℃, are compared. The constant potential was applied after 1 hour at the open circuit corrosion potential (OCP). The passive film on the melt spun ribbon and HVOF coatings of SAM2X5 is more stable than that on wrought nickel-based Alloy C-22 under these conditions, leading to the conclusion that this iron-based amorphous metal has superior corrosion resistance. These coatings were produced with TNC powder by UCD and Plasmatech.

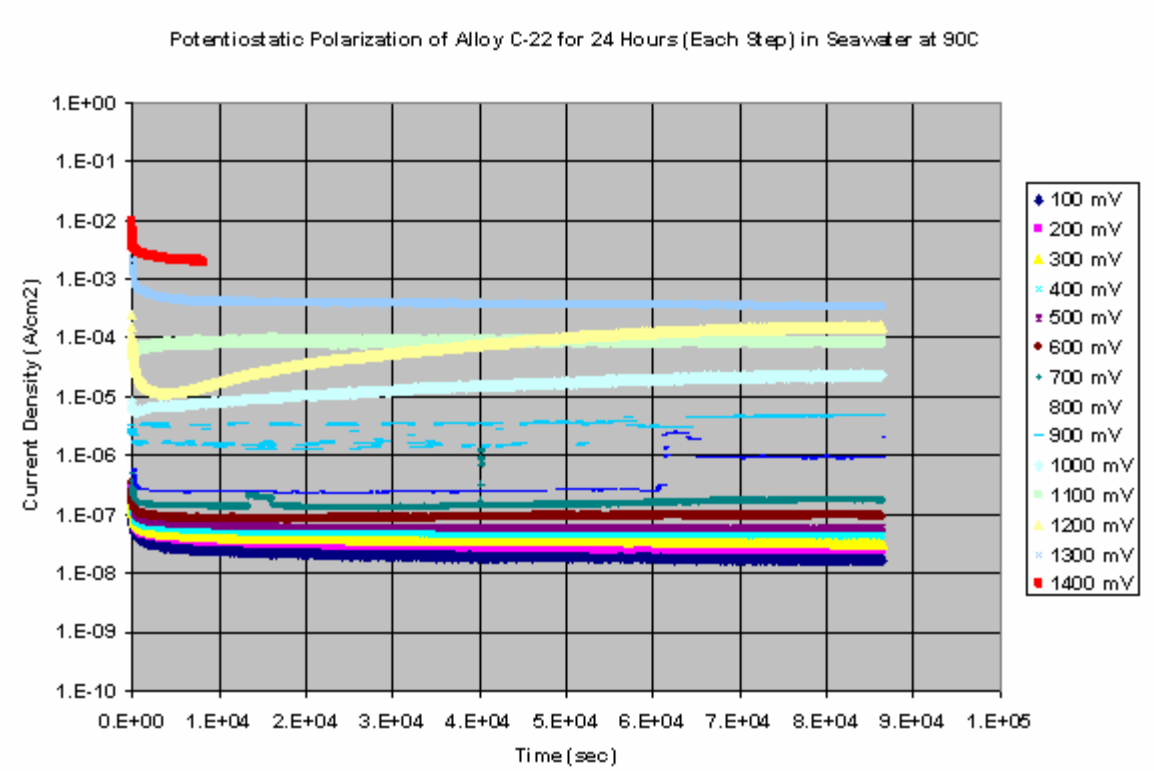

Figure 14. Transients in current density at various levels of constant applied potential ranging from 100 to 1400 mV vs. OCP for Alloy C-22 in Half Moon Bay seawater at 90℃. This reference material was polished to a 600-grit finish. The constant potential was applied after 1 hour at the open circuit corrosion potential (OCP). Passive film stability is lost above 700 mV vs. OCP. These coatings were produced with TNC powder by UCD and Plasmatech.

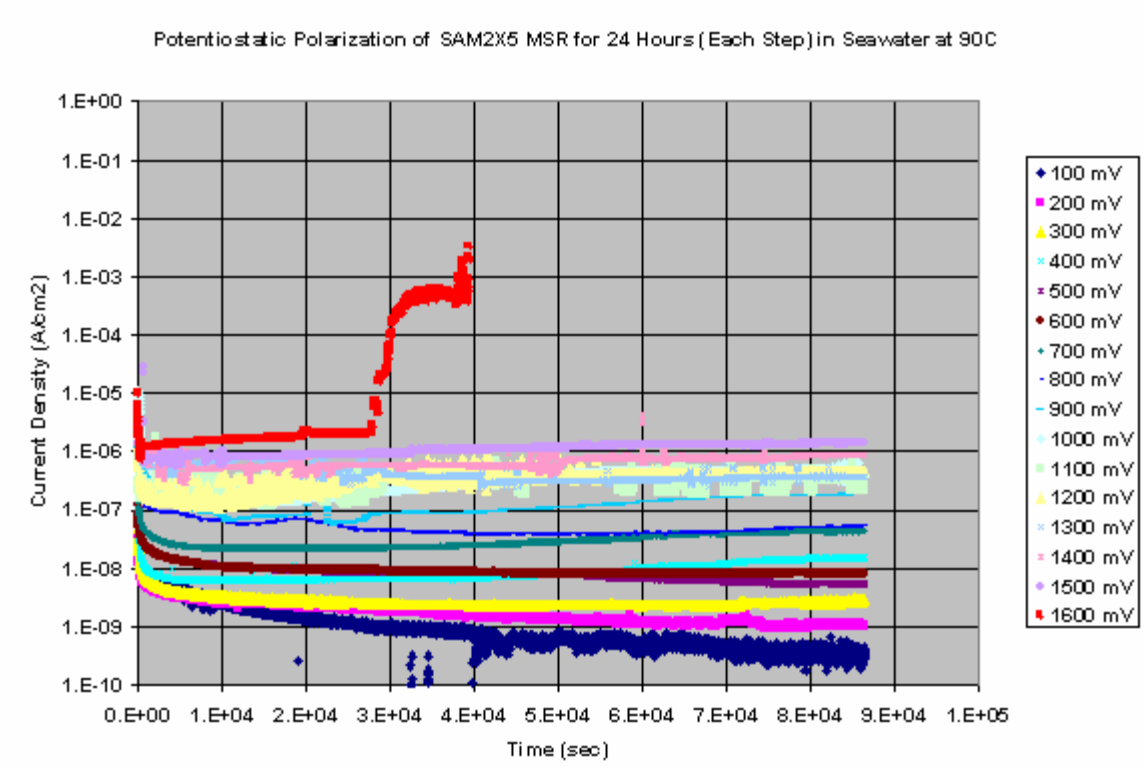

Figure 15. Transients in current density at various levels of constant applied potential ranging from 100 to 1600 mV vs. OCP for a melt-spun ribbon of SAM2X5 in Half Moon Bay seawater at 90℃ are indicative of good passive film stability. The constant potential was applied after 1 hour at the open circuit corrosion potential (OCP). The passive film stability of this SAM2X5 sample is maintained at potentials up to 1500 mV vs. OCP, which is approximately 800 mV higher than the critical potential observed with Alloy-C22. At an applied potential of 1600 mV vs. OCP, passivity is lost after several hours. These coatings were produced with TNC powder by UCD and Plasmatech.

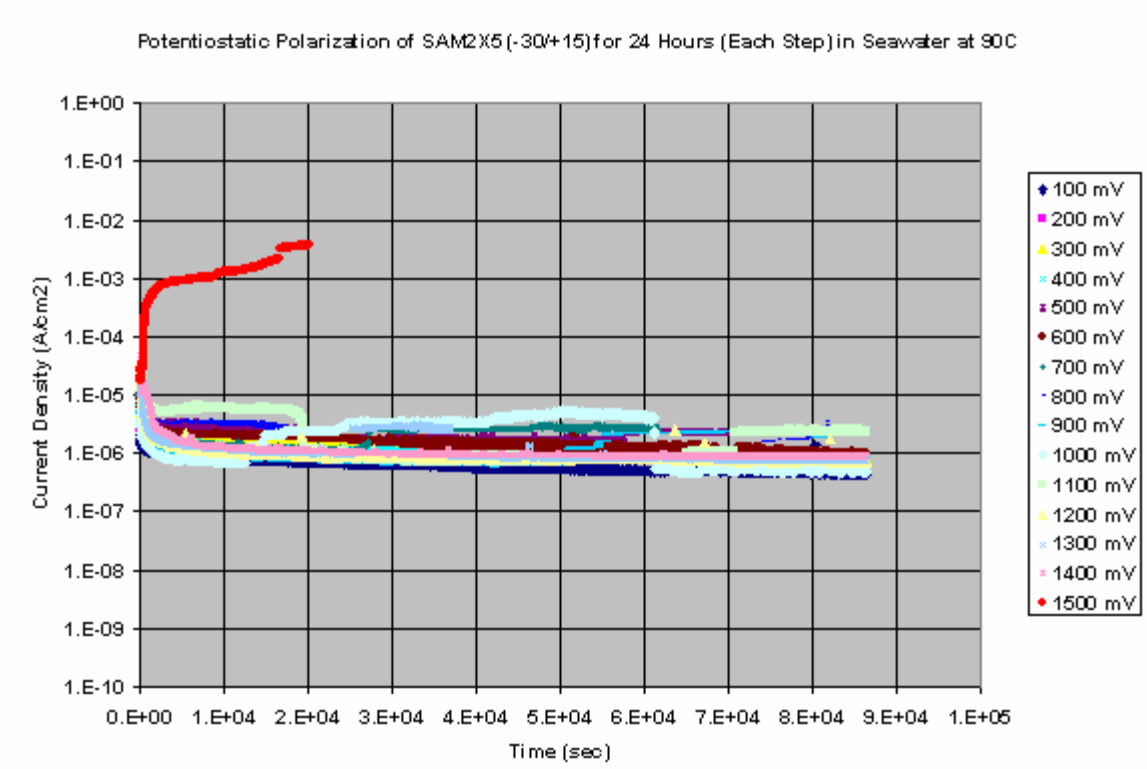

Figure 16. Transients in current density at various levels of constant applied potential ranging from 100 to 1500 mV vs. OCP for a recently optimized SAM2X5 HVOF coating (-30/+15 micron powder) in deaerated Half Moon Bay seawater at 90°C are indicative of good passive film stability. The constant potential was applied after 1 hour at the open circuit corrosion potential (OCP). To eliminate the need for surface roughness corrections in the conversion of measured current and electrode area to current density, the SAM2X5 coating was polished to a 600-grit finish prior to testing. The curves represent the asymptotic current density reached after 24 hours at the corresponding potential (each data point represents a 24 hour test). The specified fixed potential was applied after 1 hour at the open circuit corrosion potential (OCP). The passive film stability of this SAM2X5 sample is maintained at potentials up to 1400 mV vs. OCP, which is approximately 700 mV higher than the critical potential observed with Alloy-C22. At an applied potential of 1500 mV vs. OCP, passivity is lost after several hours. These coatings were produced with TNC powder by UCD and Plasmatech.

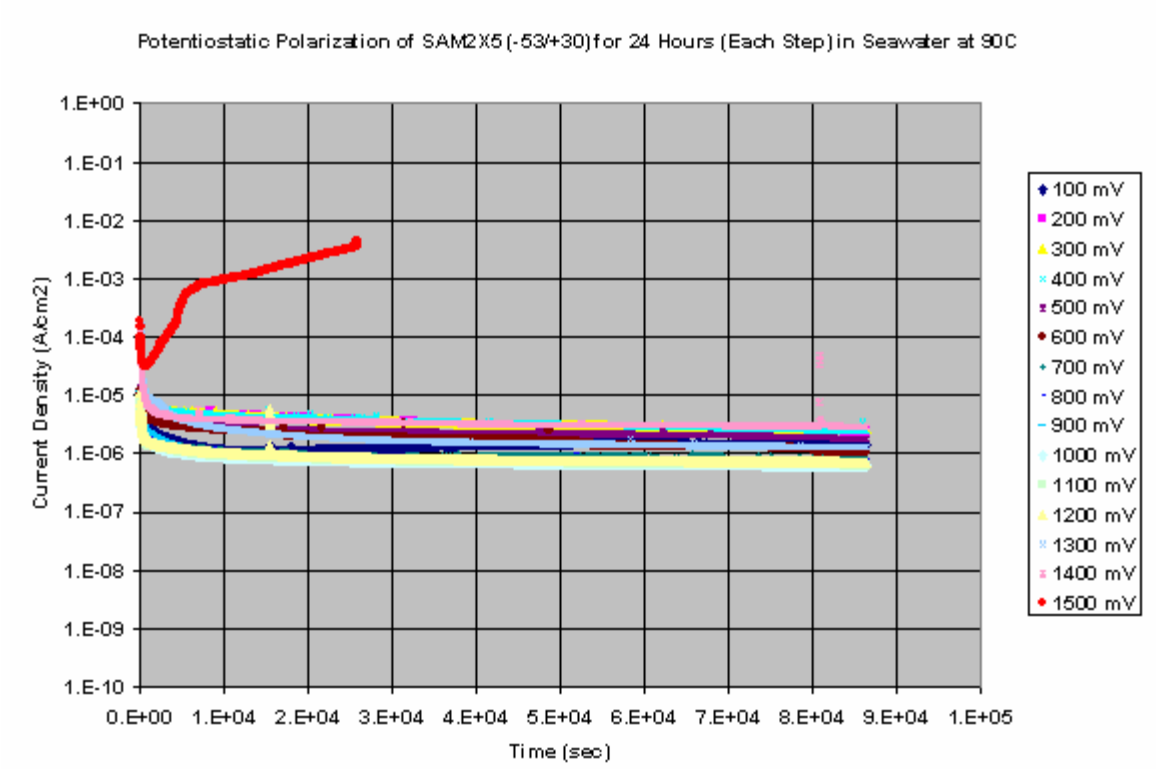

Figure 17. Transients in current density at various levels of constant applied potential ranging from 100 to 1500 mV vs. OCP for a recently optimized SAM2X5 HVOF coating (-53/+30 micron powder) in Half Moon Bay seawater at 90°C are indicative of exceptional passive film stability. To eliminate the need for surface roughness corrections in the conversion of measured current and electrode area to current density, the SAM2X5 coatings were polished to a 600-grit finish prior to testing. The constant potential was applied after 1 hour at the open circuit corrosion potential (OCP). The passive film stability of this SAM2X5 sample is maintained at potentials up to 1400 mV vs. OCP, which is approximately 700 mV higher than the critical potential observed with Alloy-C22. At an applied potential of 1500 mV vs. OCP, passivity is lost after several hours. These coatings were produced with TNC powder by UCD and Plasmatech.

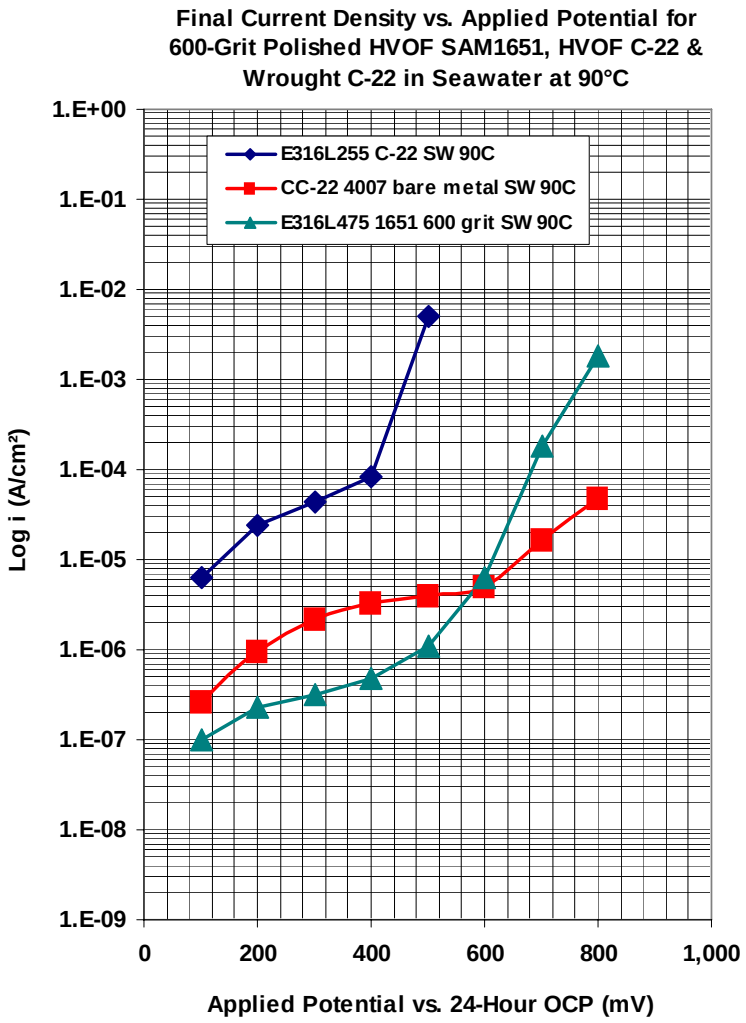

Figure 18. Potential-step testing has been performed on HVOF coatings of SAM1651 in deaerated Half Moon Bay seawater heated to 90°C. Tests were also performed on the reference material, Alloy C-22, in both wrought and thermally sprayed condition. To eliminate the need for surface roughness corrections in the conversion of measured current and electrode area to current density, the SAM1651 coating was polished to a 600-grit finish prior to testing. The Alloy C-22 thermal spray coating was tested in the as-sprayed condition, so a roughness factor must be applied to convert the apparent current density into actual current density. The curves represent the asymptotic current density reached after 24 hours at the corresponding potential. In this series of experiments, the passive film on wrought Alloy C-22 also commences breakdown at a potential of approximately 600 mV above the open circuit corrosion potential. Passive film breakdown on the HVOF coating of SM1651 occurred at an applied potential between 500 and 600 mV, where breakdown occurred at approximately 400 mV for the Alloy C-22 HVOF coating. In near-boiling seawater, the passive film stability of SAM1651 is comparable to that of Alloy C-22, but inferior to that of SAM2X5.

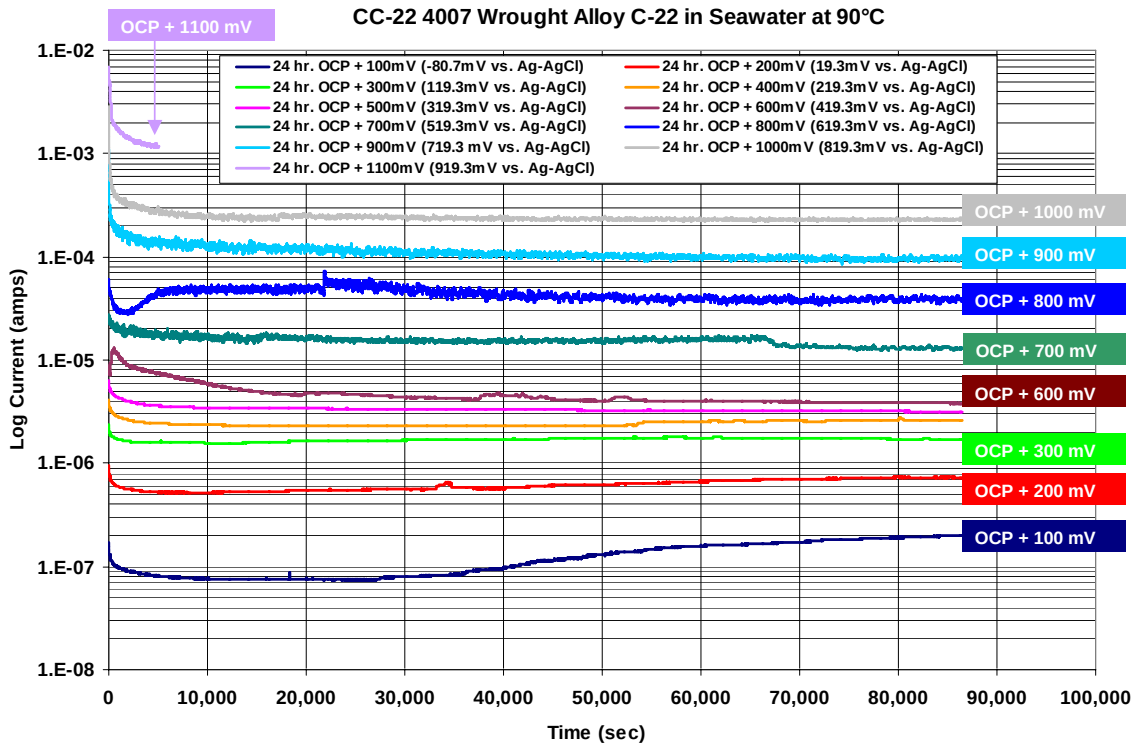

Figure 19. Transients in current density at various levels of constant applied potential ranging from 100 to 800 mV vs. OCP for a HVOF coating of SAM1651 in deaerated Half Moon Bay seawater at 90℃ are indicative of good passive film stability, comparable to that of wrought Alloy C-22. To eliminate the need for surface roughness corrections in the conversion of measured current and electrode area to current density, the SAM2X5 coatings were polished to a 600-grit finish prior to testing. To eliminate the need for surface roughness corrections in the conversion of measured current and electrode area to current density, the SAM1651 coating was polished to a 600-grit finish prior to testing. Passive film breakdown on the HVOF coating of SM1651 occurred at an applied potential between 500 and 600 mV vs. OCP, with a clear loss of passivity at 700 mV. These coatings were produced by TNC and INL before fabrication of the optimized UCD-Plasmatech coatings previously discussed.

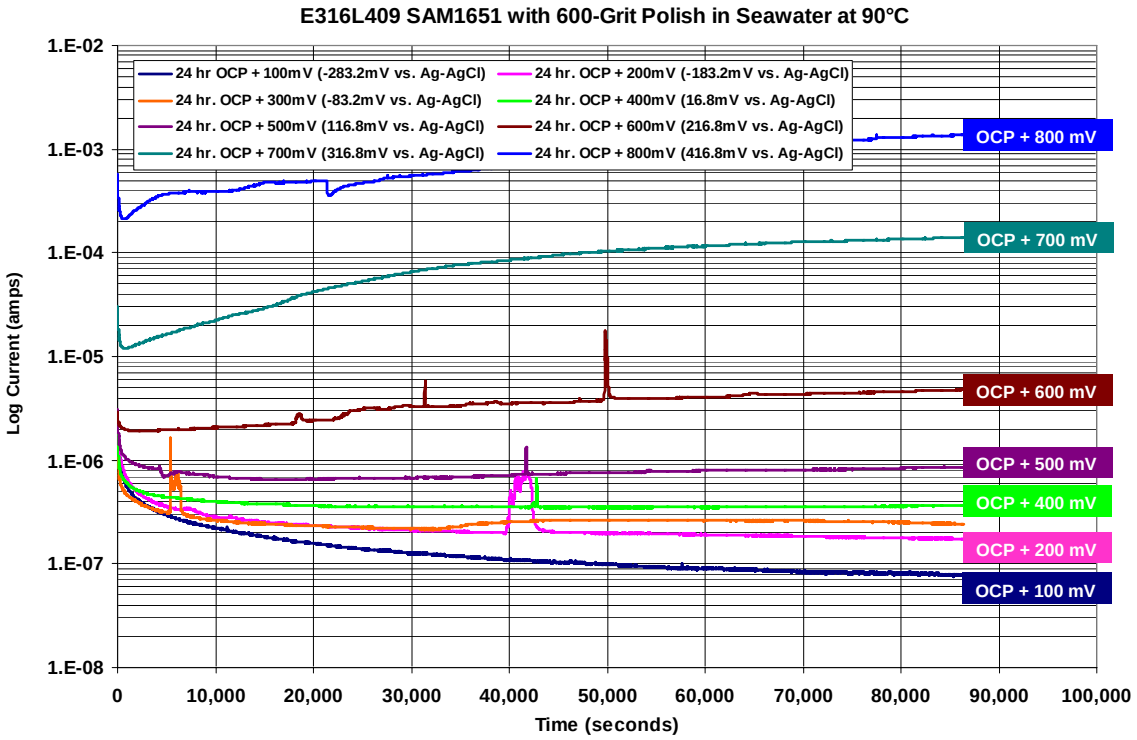

Figure 20. Transients in current density at various levels of constant applied potential ranging from 100 to 800 mV vs. OCP for a polished HVOF coating of SAM1651 on a Type 316L stainless steel substrate (S/N No. E316L409) in Half Moon Bay seawater at 90℃ are indicative of good passive film stability, comparable to that of wrought Alloy C-22. To eliminate the need for surface roughness corrections in the conversion of measured current and electrode area to current density, the SAM2X5 coatings were polished to a 600-grit finish prior to testing. To eliminate the need for surface roughness corrections in the conversion of measured current and electrode area to current density, the SAM1651 coating was polished to a 600-grit finish prior to testing. Passive film breakdown on the HVOF coating of SM1651 occurred at an applied potential between 500 and 600 mV vs. OCP, with a clear loss of passivity at 700 mV. The coating represented by this figure is one of the first known thermal spray coatings with the SAM1651 composition, and was produced by TNC and their subcontractor before fabrication of the optimized UCD/Plasmatech coatings, which are represented by the preceding figures.

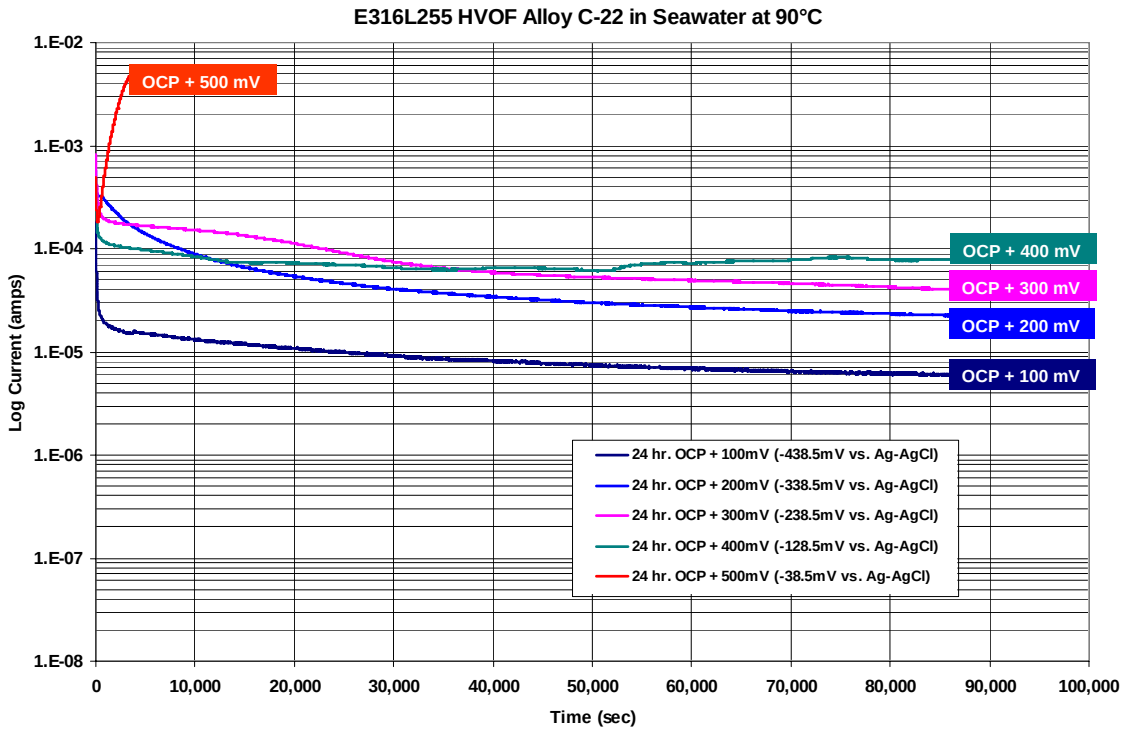

Figure 21. Transients in current density at various levels of constant applied potential ranging from 100 to 500 mV vs. OCP for an unpolished (as sprayed) HVOF coating of nickel-based Alloy C-22 on a Type 316L stainless steel substrate (S/N No. E316L255) in Half Moon Bay seawater at 90°C show a clear and unambiguous loss of passivity at the highest potential level. Since this Alloy C-22 coating was tested in the as-sprayed condition, a roughness factor must be applied to convert the 'apparent' current density into the 'actual' current density. The coating represented by this figure was produced by TNC and their subcontractor before fabrication of the optimized UCD/Plasmatech coatings, which are represented by the preceding figures.

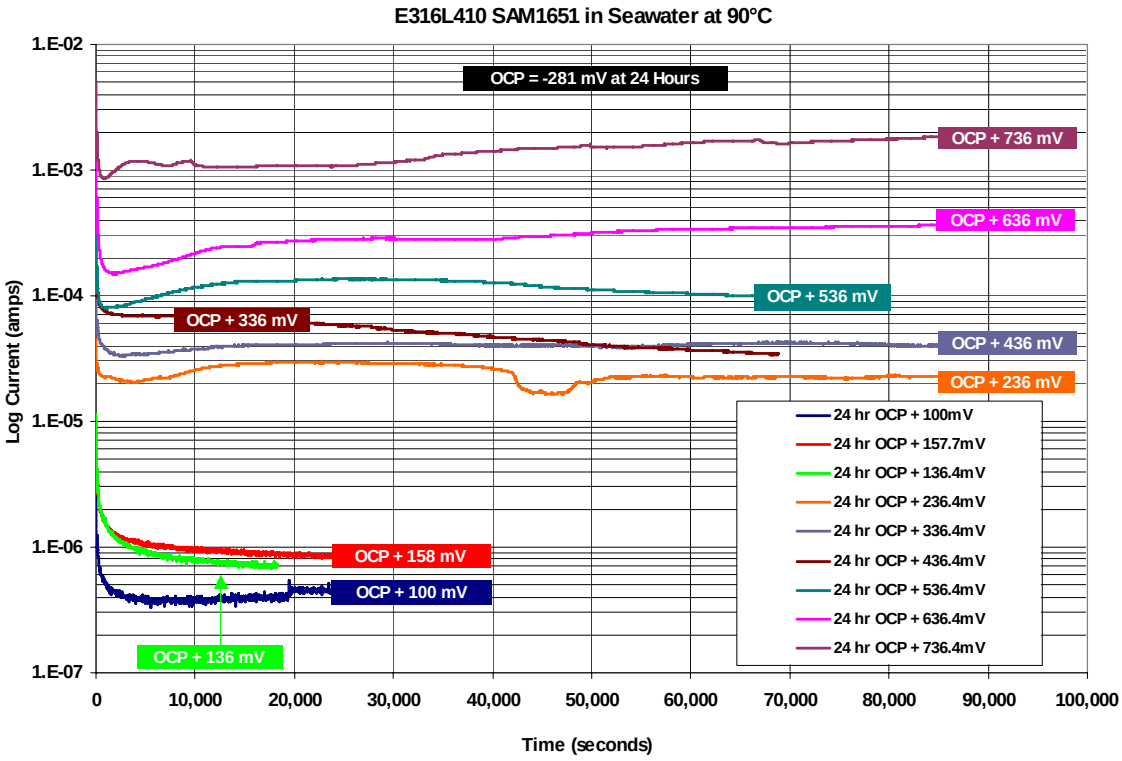

Figure 22. Transients in current density at various levels of constant applied potential ranging from 100 to 736 mV vs. OCP for an unpolished (as sprayed) HVOF coating of SAM1651 on a Type 316L stainless steel substrate (S/N No. E316L410) in Half Moon Bay seawater at 90°C are indicative of good passive film stability, comparable to that of wrought Alloy C-22. Since this as-sprayed SAM1651 coating was tested in the as-sprayed condition, a roughness factor (which is expected to range from a minimum of ×2 to more than ×10) must be applied to convert the 'apparent' current density into the 'actual' current density. While passivity at 158 mV vs. OCP is clear, polished samples with minimal roughness, or unambiguous knowledge of the roughness factor is required to interpret measured 'apparent' current densities at higher applied potential in terms of passivity, or the loss of passivity. From visual inspection, it was evident that passivity was maintained at higher potentials. The ambiguity associated with early electrochemical test data such as this has lead the investigators to use polished samples with 600-grit finish for clear determinations of critical potentials. The coating represented by this figure is one of the first known thermal spray coatings with the SAM1651 composition, and was produced by TNC and their subcontractor before fabrication of the optimized UCD/Plasmatech coatings, which are represented by the preceding figures.

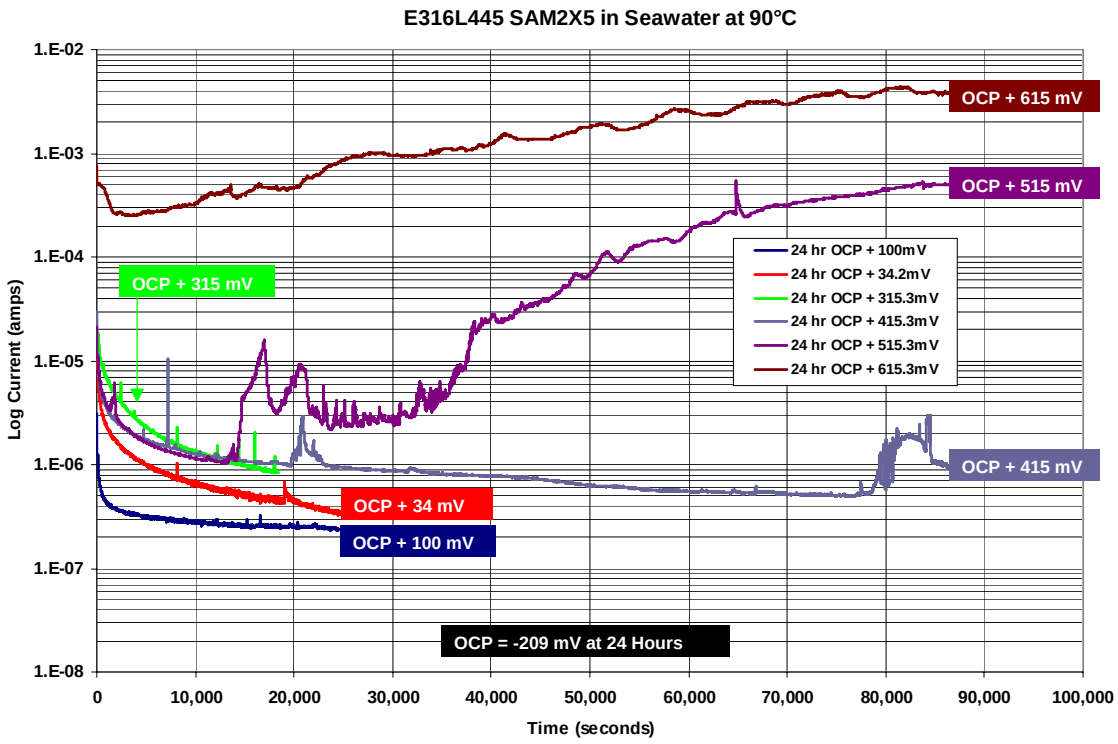

Figure 23. Transients in current density at various levels of constant applied potential ranging from 100 to 615 mV vs. OCP for an early unpolished (as sprayed) HVOF coating of SAM2X5 on a Type 316L stainless steel substrate (S/N No. E316L445) in Half Moon Bay seawater at 90°C are indicative of good passive film stability, comparable to that of wrought Alloy C-22. Since this as-sprayed SAM2X5 coating was tested in the as-sprayed condition, a roughness factor (which is expected to range from a minimum of ×2 to more than ×10) must be applied to convert the 'apparent' current density into the 'actual' current density. While passivity at 315 mV vs. OCP is clear, current transients are observed at 415 mV on this as-sprayed surface that may be indicative of the onset of passive film breakdown. Such breakdown is clearly evident at a slightly higher potential of 515 mV vs. OCP. While this data shows very good corrosion resistance, more recent optimization has resulted in far better performance with this formulation. The coating represented by this figure is one of the first known thermal spray coatings with the SAM2X5 composition, and was produced by TNC and their subcontractor before fabrication of the new optimized UCD/Plasmatech coatings, which are represented by the preceding figures. The importance of supplier standardization and qualification is illustrated by the enhanced performance that has evolved as we have continued to work with these materials.

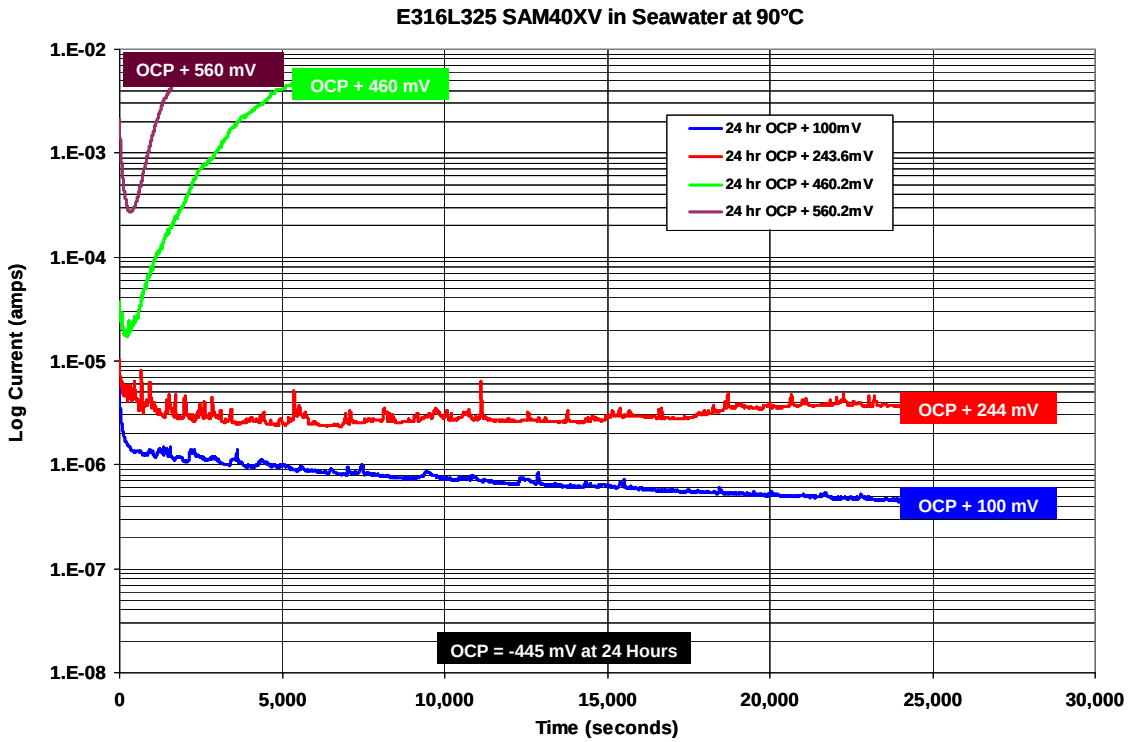

Figure 24. Transients in current density at various levels of constant applied potential ranging from 100 to 460 mV vs. OCP for an early unpolished (as sprayed) HVOF coating of SAM40XV on a Type 316L stainless steel substrate (S/N No. E316L325) in Half Moon Bay seawater at 90°C are indicative of good passive film stability, comparable to that of wrought Alloy C-22. SAM40XV was an early version of SAM2X5 that TNC prepared for HPCRM with slightly less molybdenum added, and a corresponding lower critical potential. Since this as-sprayed SAMXV coating was tested in the as-sprayed condition, a roughness factor (which is expected to range from a minimum of ×2 to more than ×10) must be applied to convert the 'apparent' current density into the 'actual' current density. While passivity at 100 to 244 mV vs. OCP is clear, current transients observed at 460 and 560 mV are clearly indicative of passive film breakdown. Such high apparent current densities occur at higher potential in the case of SAM2X5. The coating represented by this figure is one of the first known thermal spray coatings with the SAM40XV composition, and was produced by TNC and their subcontractor before fabrication of the new optimized UCD/Plasmatech coatings, which are represented by the preceding figures. The importance of supplier standardization and qualification is illustrated by the enhanced performance that has evolved as we have continued to work with these materials.

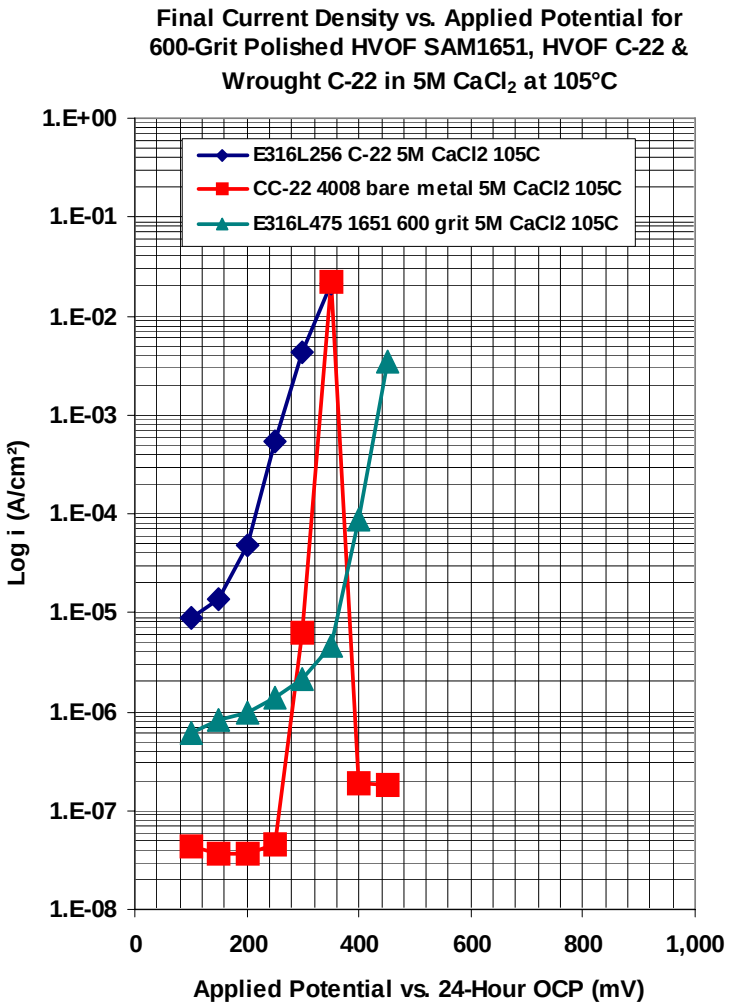

Figure 25. Potential-step testing has been performed on HVOF coatings of SAM1651 on a Type 316L stainless steel substrate (S/N No. E316L475) in extremely aggressive 5M $CaCl_2$ heated to 105°C. Tests were also performed on the reference material, Alloy C-22, in both wrought and thermally sprayed condition (S/N Nos. CC-22 4008 and E316L256, respectively). To eliminate the need for surface roughness corrections in the conversion of measured current and electrode area to current density, the SAM1651 coating was polished to a 600-grit finish prior to testing. The Alloy C-22 thermal spray coating was tested in the as-sprayed condition, so a roughness factor must be applied to convert the apparent current density into actual current density. The curves represent the asymptotic current density reached after 24 hours at the corresponding potential. In this series of experiments, the passive film on wrought Alloy C-22 also commences breakdown at a potential of only 240 mV above the open circuit corrosion potential, with evidence of repassivation at potentials above 400 mV. Even with the repassivation at higher potential, the window of vulnerability between 240 to 400 mV is problematic for the reference material (Alloy C-22). Passive film breakdown on the HVOF coating of SAM1651 occurred at a significantly higher applied potential, between 360 and 400 mV, where breakdown of the passive film on thermally sprayed Alloy C-22 was virtually spontaneous. The new SAM1651 coating provides clear advantages for operation in corrosive hot chloride brines with divalent cations, such as calcium.

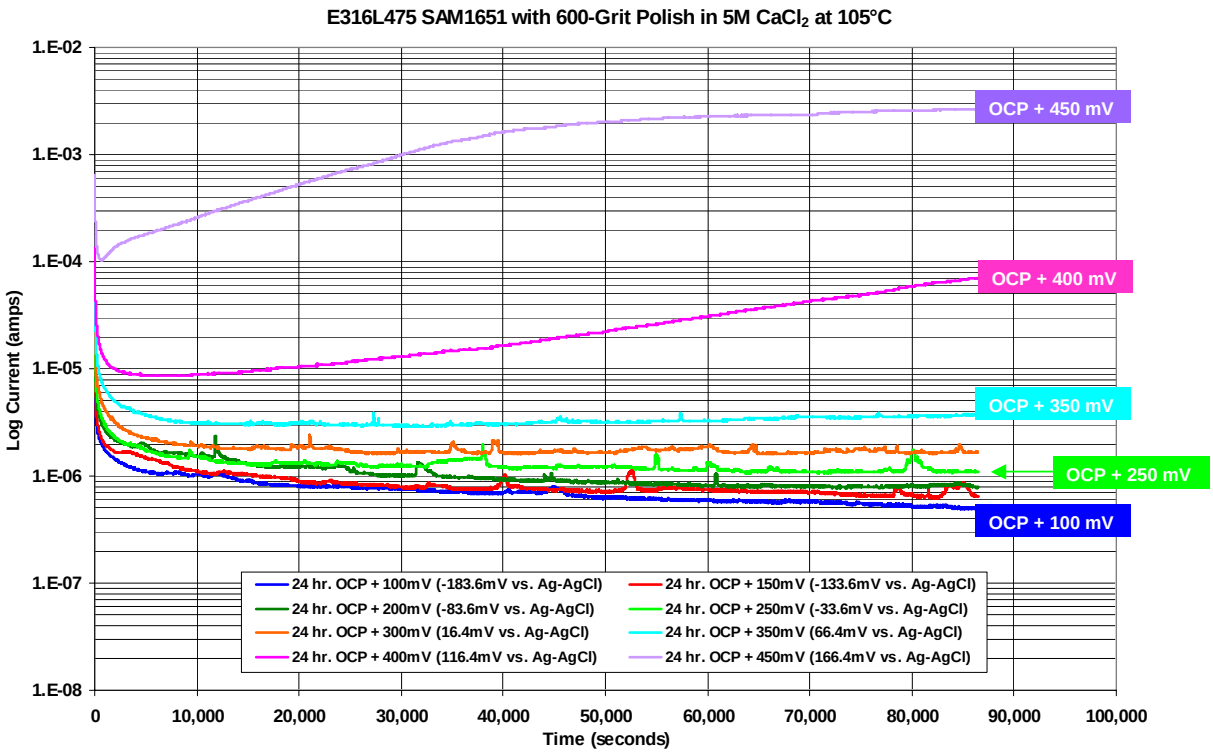

Figure 26. Transients in current density at various levels of constant applied potential ranging from 100 to 450 mV vs. OCP for a polished HVOF coating of SAM1651 on a Type 316L stainless steel substrate (S/N No. E316L475) in 5M $CaCl_2$ at 105°C are indicative of good passive film stability, which is superior to that of wrought Alloy C-22 in this environment this very aggressive environment. To eliminate the need for surface roughness corrections in the conversion of measured current and electrode area to current density, the SAM1651 coating was polished to a 600-grit finish prior to testing. Passive film breakdown on the HVOF coating of SAM1651 occurred at an applied potential between 360 and 400 mV vs. OCP, with a clear loss of passivity at 450 mV. The coating represented by this figure is one of the first known thermal spray coatings with the SAM1651 composition, and was produced by TNC and their subcontractor before fabrication of the optimized UCD/Plasmatech coatings, which are represented by the preceding figures. The performance of this SAM1651 coating was very impressive.

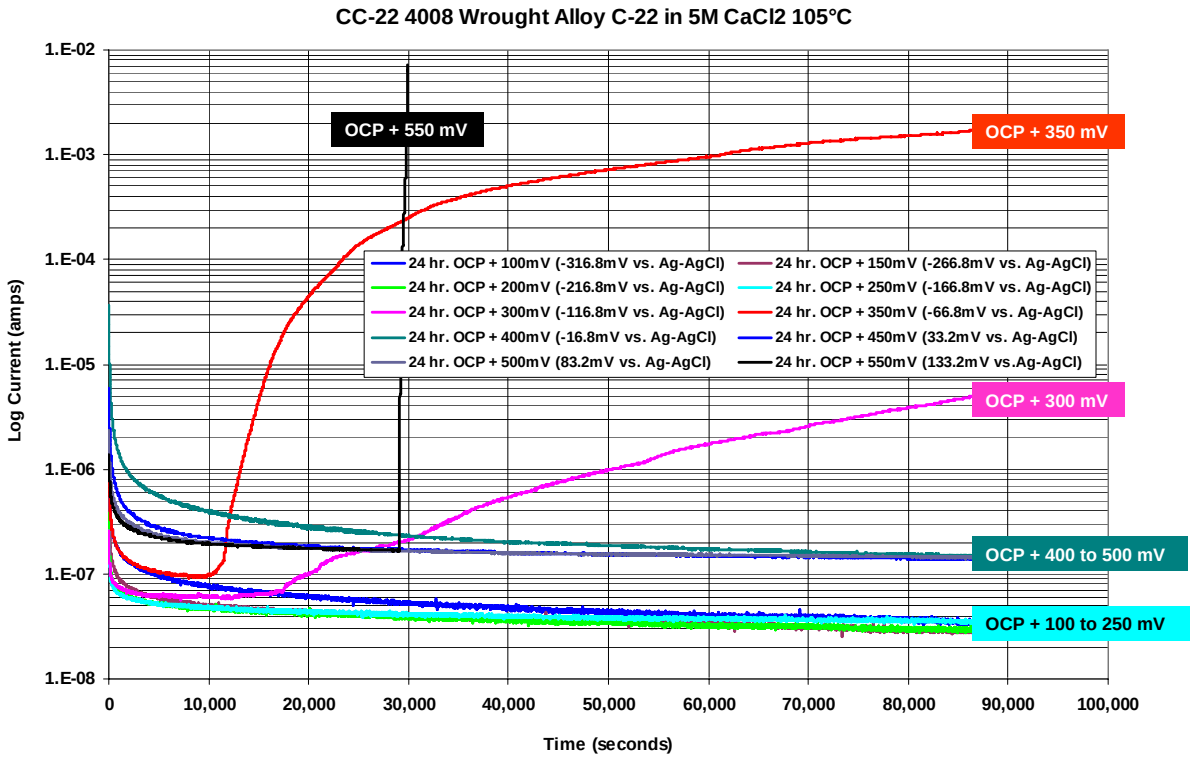

Figure 27. Transients in current density at various levels of constant applied potential ranging from 100 to 550 mV vs. OCP for wrought Alloy C-22 (S/N No. CC-22 4008) in 5M $CaCl_2$ at 105°C, and shows complete breakdown of the passive film in two potential regimes, one regime located between 300-400 mV vs. OCP (350 mV), and the second located above 500 mV vs. OCP (550 mV). Like the polished SAM1651 coating, this reference was also polished to a 600-grit finish.

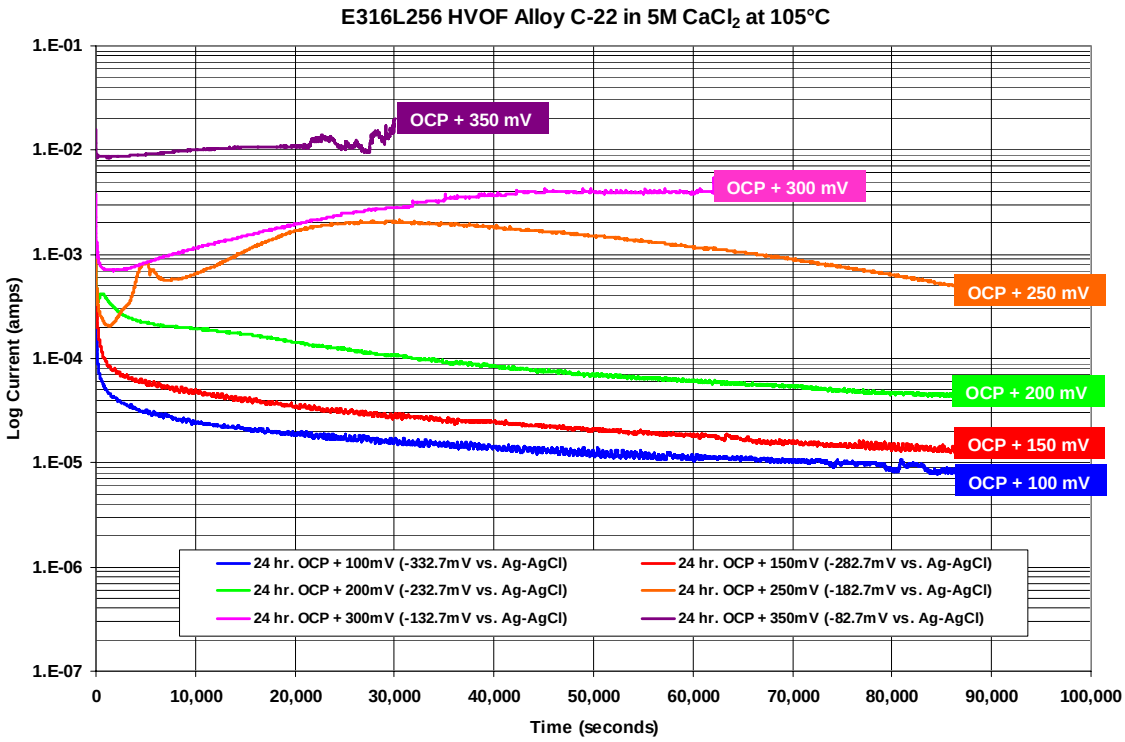

Figure 28. Transients in current density at various levels of constant applied potential ranging from 100 to 350 mV vs. OCP for an unpolished (as-sprayed) HVOF coating of Alloy C-22 on a Type 316L stainless steel substrate (S/N No. E316L256) in 5M $CaCl_2$ at 105°C appears to be passive at 100-150 mV vs. OCP, but has a clear loss of passivity at potentials above 200 mV vs. OCP (250-350 mV). Since this as-sprayed Alloy C-22 coating was tested in the as-sprayed condition, a roughness factor (which is expected to range from a minimum of ×2 to more than ×10) must be applied to convert the 'apparent' current density into the 'actual' current density. The coating represented by this figure was produced by TNC and their subcontractor before fabrication of the optimized UCD/Plasmatech coatings, which are represented by preceding figures.

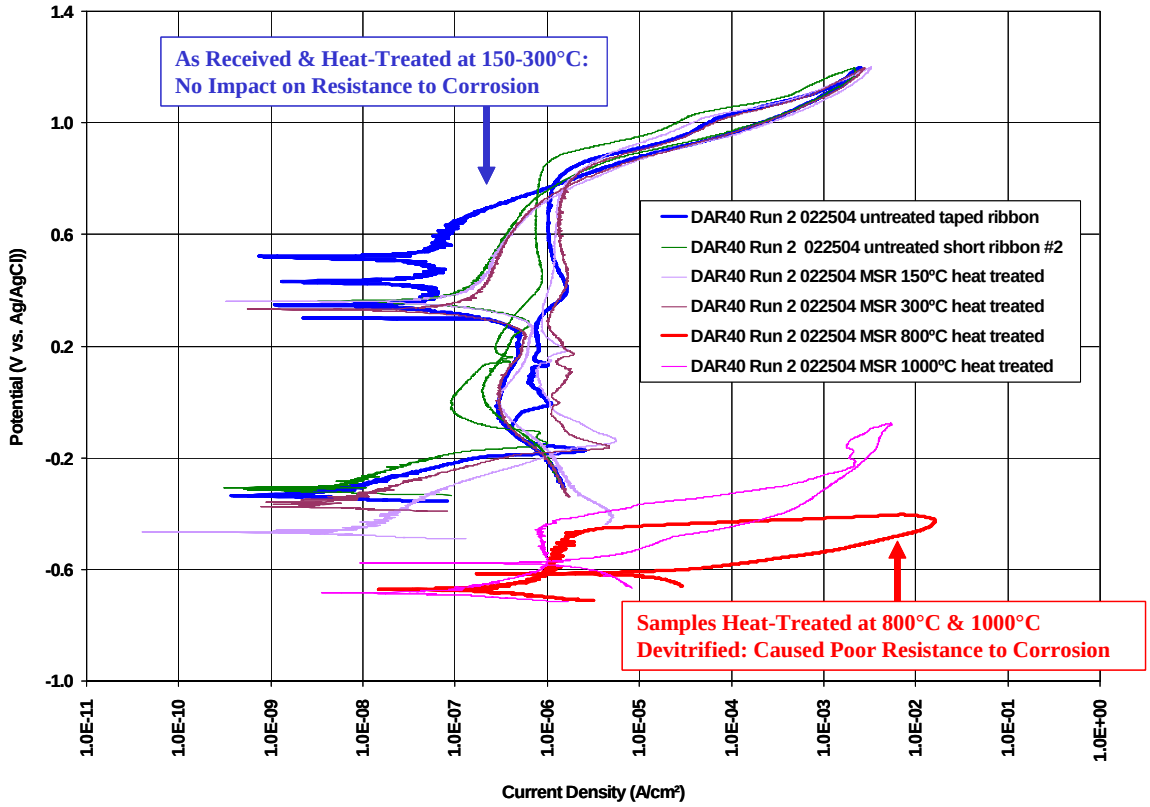

Figure 29. To assess the sensitivity of these iron-based amorphous metals to devitrification, which can occur at very elevated temperature, melt-spun ribbon of SAM40 (also referred to as DAR40) were intentionally devitrified by heat treating them at various temperatures for one hour. After heat treatment, the samples were evaluated in low temperature seawater (30 ℃), to determine the impact of the heat treatment on passive film stability and corrosion resistance. The temperatures used for the heat treatment were: 150, 300, 800 and 1000 ℃. Untreated (as received) ribbons were also tested, and provide insight into the baseline performance. These samples showed no significant hysteresis and change in repassivation potential at heat treatments of 150-300 ℃, but showed a dramatic loss of corrosion resistance when heat treatments were performed at 800-1000 ℃, which are above the known recrystallization temperature of approximately 600-650 ℃ (623 ℃) given in Table 2 (Perepezko et al. 2004). Both ribbons treated at elevated temperature show large hysterisis loops, which are indicative of passive film breakdown, with a clearly defined repassivation potential near -600 mV vs. Ag/AgCl (about 100 mV above the OCP). The operational limit for these materials, when being used for corrosion resistance, appears to be bounded by the recrystallization temperature.

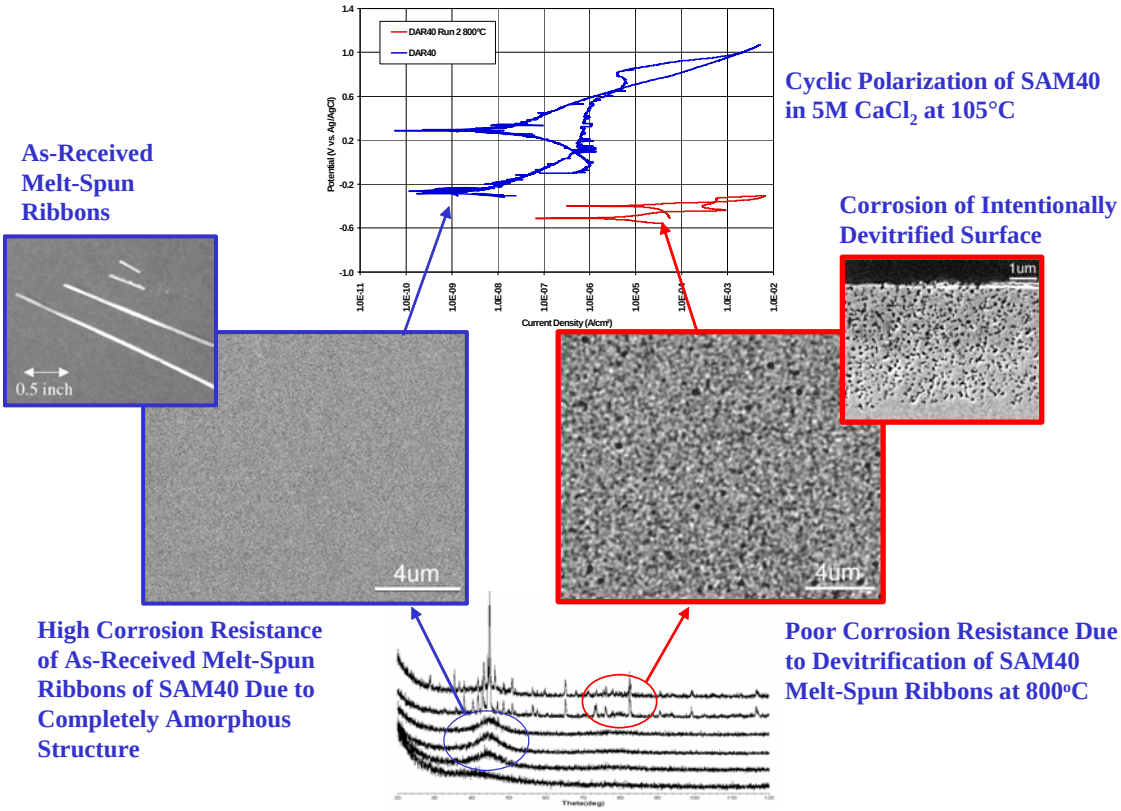

Figure 30. Melt spun ribbons of SAM40 (DAR40) were also intentionally devitrified by heat treating at 800℃ for one hour and then subjected to cyclic polarization in 5M CaCl2 at 105℃. In comparison to the as-received sample, the sample heat-treated at 800C showed a dramatic loss of corrosion resistance. As discussed in regard to the preceding figure, this heat-treatment temperature was known to be above the recrystallization temperature of approximately 600-650℃ (623℃) given in Table 2 (Perepezko et al. 2004). The heat-treated ribbon showed a large hysterisis loop in the hot concentrated calcium chloride solution, which is indicative of passive film breakdown, with a clearly defined repassivation potential neat the OCP. The post heat-treatment microstructural characterization with electron microscopy and X-ray diffraction by Yang et al. verify the existence of a completely amorphous material below the recrystallization temperature, and the development of crystalline precipitates during heat treatment above this limit. These electron microscopy images may also indicate that the corrosive attack of the precipitated crystalline phases occur to a depth of approximately 10 microns. When being used for corrosion resistance in hot geothermal brines such as calcium chloride, the operational limit also appears to be bounded by the recrystallization temperature.

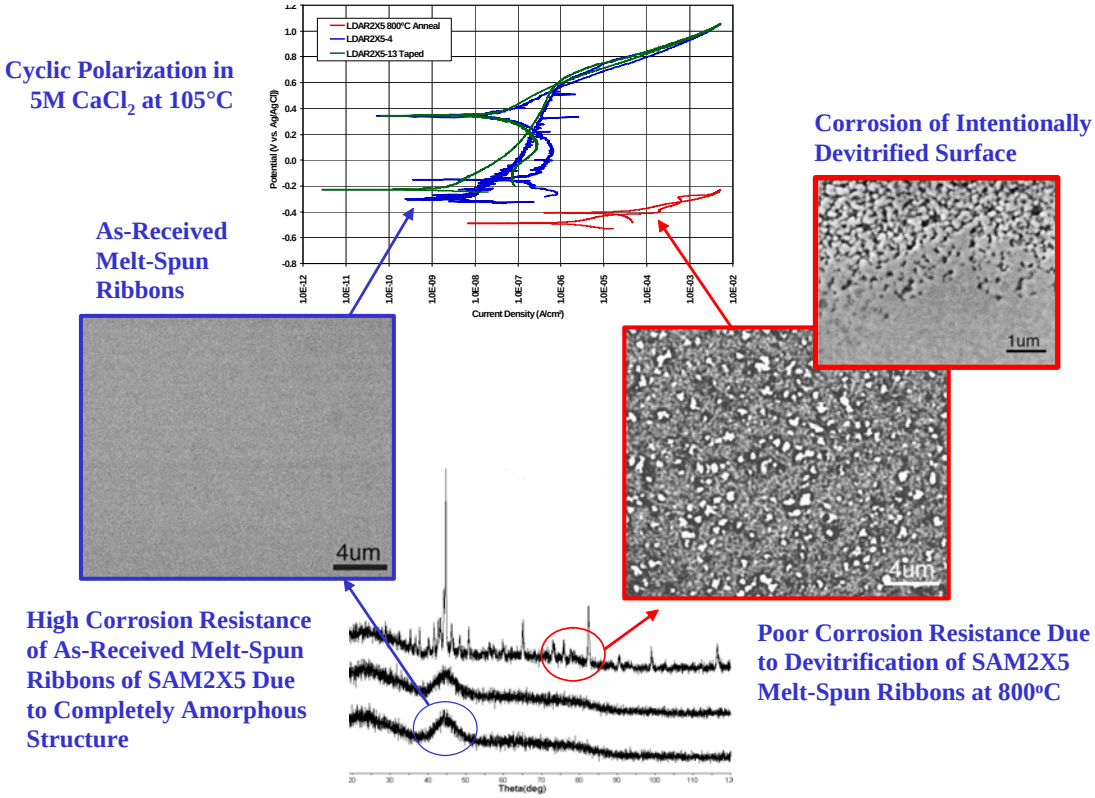

Figure 31. Melt spun ribbons of SAM2X5 were also intentionally devitrified by heat treating at 800℃ for one hour and then subjected to cyclic polarization in 5M CaCl2 at 105℃. In comparison to the as-received sample, the sample heat-treated at 800C showed a dramatic loss of corrosion resistance. As discussed in regard to the preceding figure, this heat-treatment temperature was known to be above the recrystallization temperature of approximately 600-650℃ (623℃) given in Table 2 (Perepezko et al. 2004). The heat-treated ribbon showed a large hysterisis loop in the hot concentrated calcium chloride solution, which is indicative of passive film breakdown, with a clearly defined repassivation potential neat the OCP. The post heat-treatment microstructural characterization with electron microscopy and X-ray diffraction by Yang et al. verify the existence of a completely amorphous material below the recrystallization temperature, and the development of crystalline precipitates during heat treatment above this limit. These electron microscopy images may also indicate that the corrosive attack of the precipitated crystalline phases occur to a depth of approximately 10 microns. When being used for corrosion resistance in hot geothermal brines such as calcium chloride, the operational limit also appears to be bounded by the recrystallization temperature.

Figure 32. Temperature controlled baths for long-term corrosion testing of weight loss and crevice corrosion samples, with simultaneous monitoring of the open-circuit corrosion potential, corrosion rate via linear polarization, and passive film stability with electrochemical impedance spectroscopy (EIS). Water cooled condensers are used to prevent the loss of water and other volatiles from the baths, and a water-cooled reference electrode junction is used to enable the Ag/AgCl reference electrodes to be operated at standard temperature, thereby providing a sound thermodynamic reference. The upper photograph show LLNL technicians attending to the test equipment.

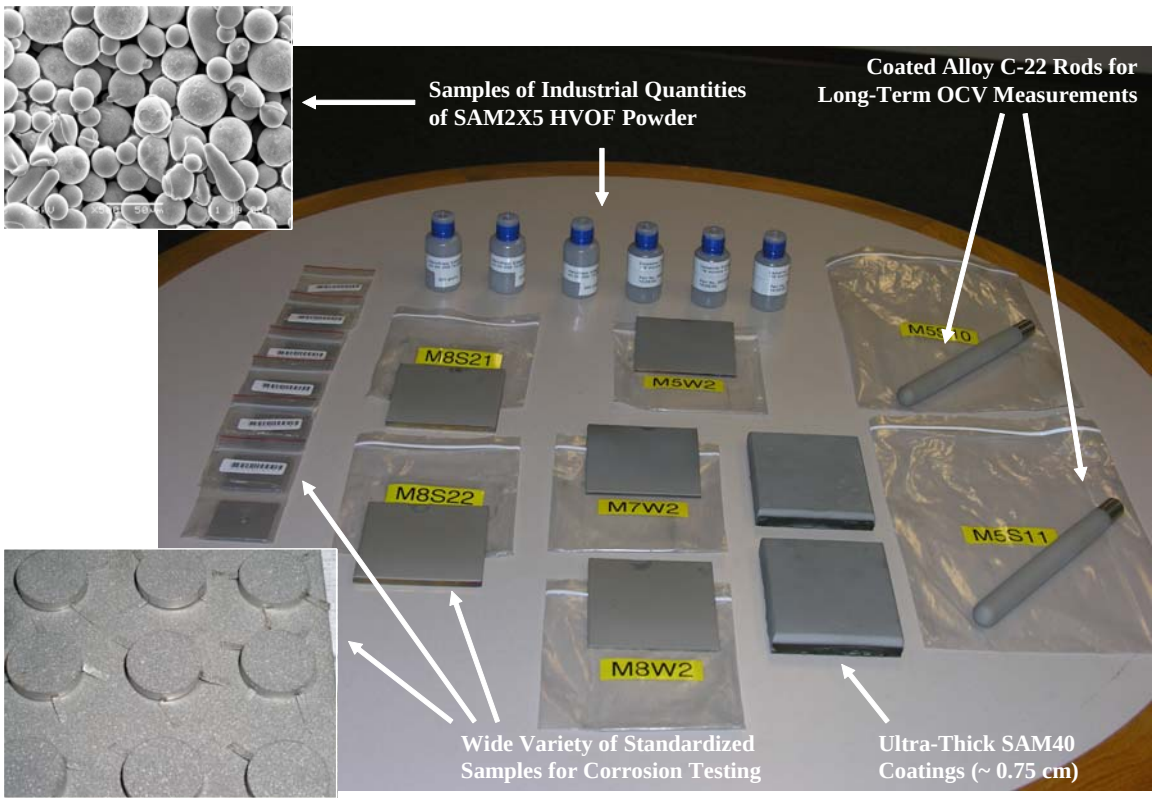

Figure 33. Weight loss and crevice samples for the long term test are 4-inch × 4-inch × ¼-inch Alloy C-22 substrates with a 40-mil thermal spray coating of amorphous metal (SAM2X5, SAM1651, etc.). The crevice samples have a hole in the center to accommodate a crevice former, and are not shown. The long-term measurements of open-circuit corrosion potential, corrosion rate via linear polarization, and electrochemical impedance spectra are done with a ¾-inch diameter Alloy C-22 rod with a hemispherical end, and with a 40-mil thermal spray coating of amorphous metal (SAM2X5, SAM1651, etc.). Small disks are used for quick screening tests with cyclic polarization, but are not considered truly representative coatings due to their small size and differences in cooling rate experienced by the disks and larger substrates with greater thermal mass and cooling capacity. The granularity of these disks is not representative can be easily seen. While small circular disk samples are relatively inexpensive and easy to produce, and can be employed in standard corrosion test cells with relative ease, they may not provide the best source of data.

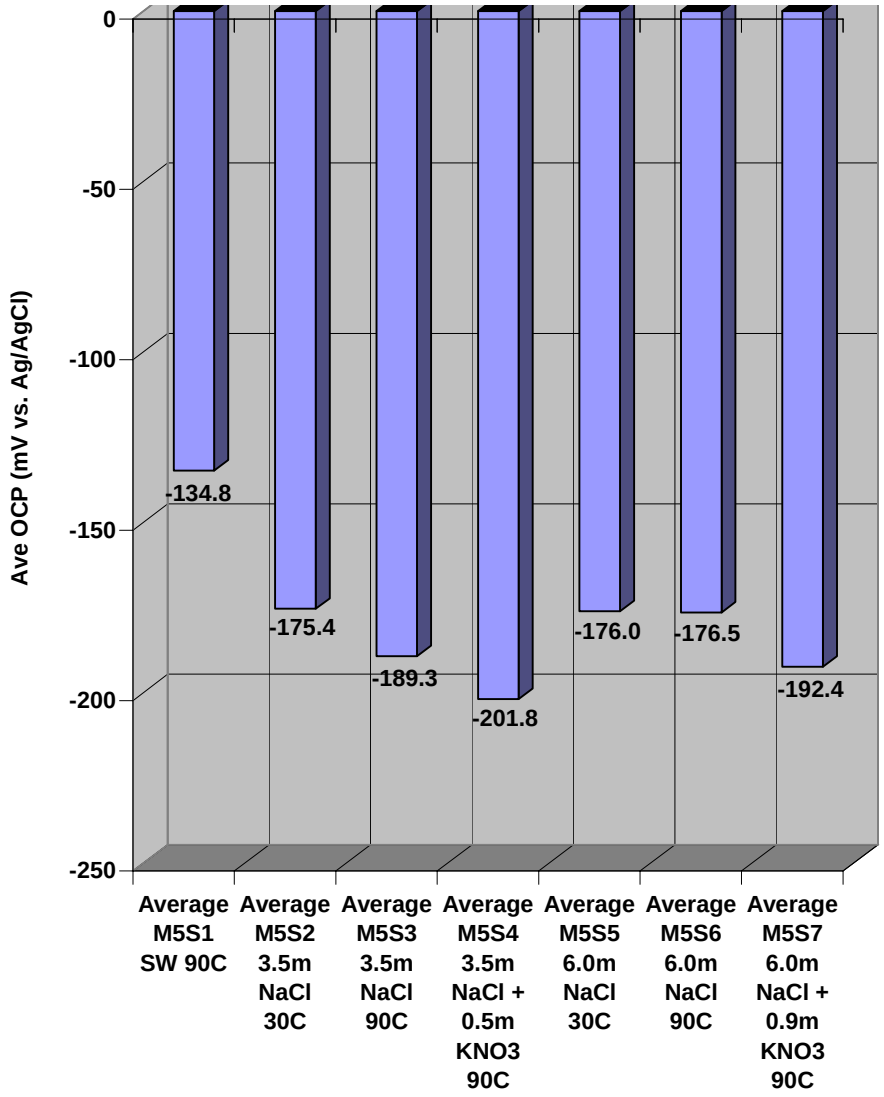

Figure 34. The long-term corrosion test for the SAM2X5 has been initiated, and the initial open circuit corrosion potentials for this material has been measured in several fully aerated environments, and will be monitored as a function of time for the next year. These environments include Half Moon Bay seawater, 3.5 m NaCl, 3.5 m NaCl with 0.5 m KNO_3, 6.0 m NaCl and 6.0 m NaCl with 0.9 m KNO_3. For each solution composition, tests are being done at two temperature levels, 30 and 90 ℃.

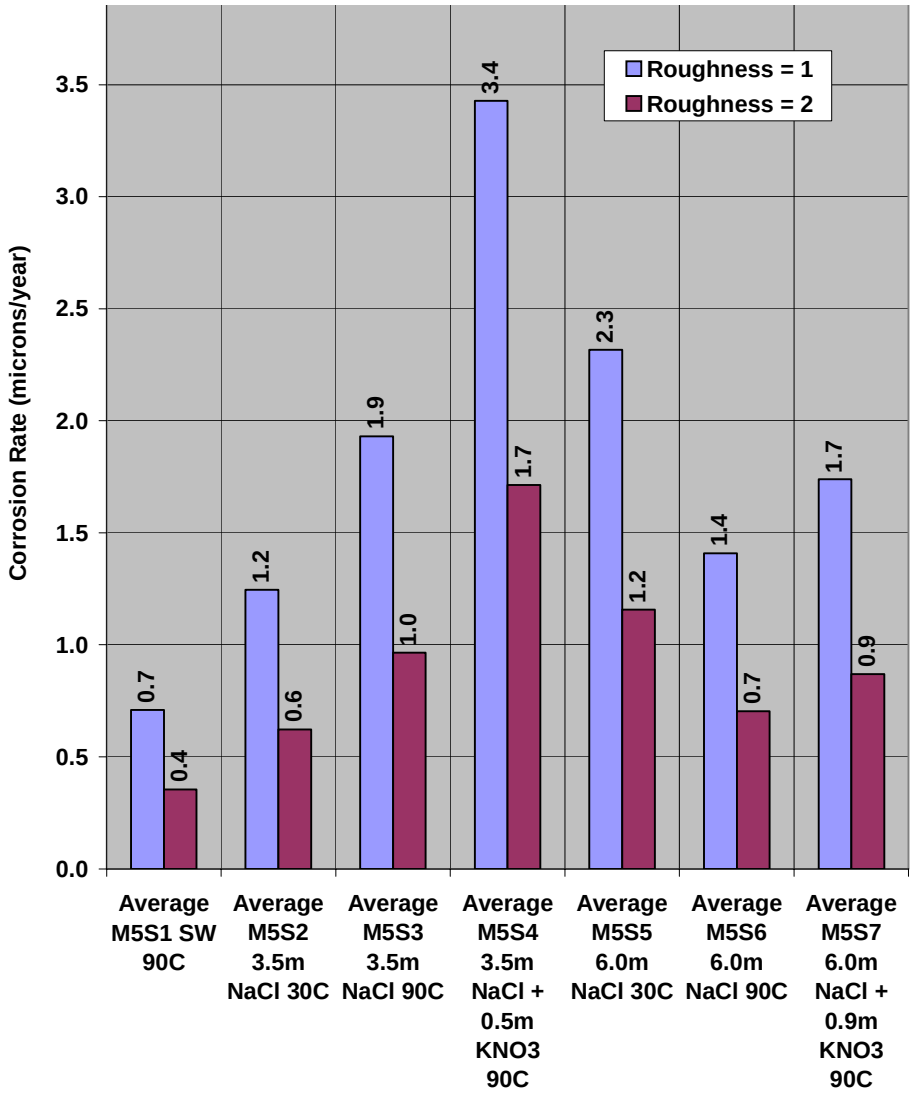

Figure 35. In addition to monitoring the open circuit corrosion potential in these fully aerated solutions, linear polarization is also being used periodically to measure the corrosion current, which is normalized by the apparent area of the electrode, and used to estimate the general corrosion rate. The roughness factor for these unpolished (as sprayed) SAM2X5 HVOF samples must be used to convert the apparent current density to the corrosion rate. In this figure, the first series of bars (blue) represent the estimated corrosion rate with no roughness correction, and the second series of bars (magenta) represent the estimated corrosion rate with the minimum estimated roughness factor of 2. The actual roughness may be significantly higher, and is in the process of being quantified. Even without the roughness factor correction, the measured corrosion rates are very low. It is somewhat surprising that in this case, the presence of nitrate appears to accelerate the general corrosion rate, both at 3.5 and 6.0 NaCl concentrations.

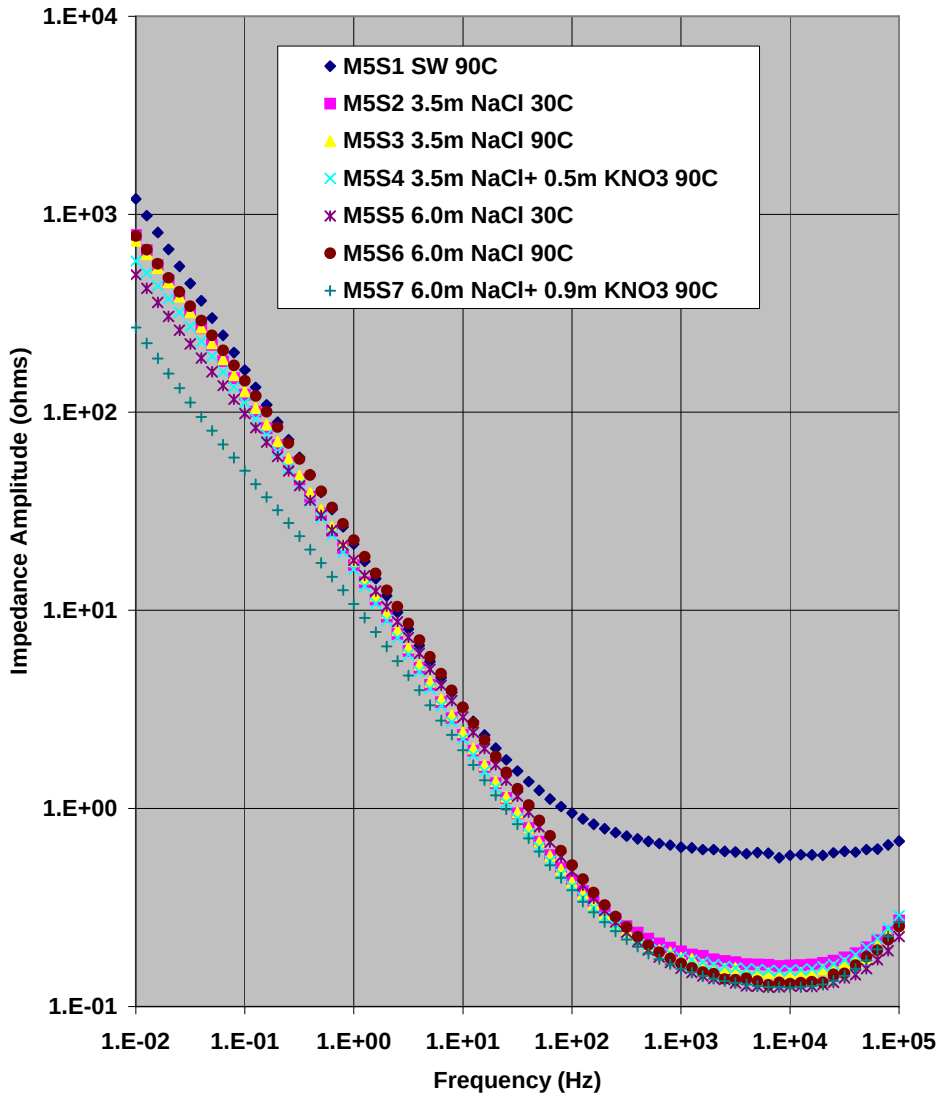

Figure 36. In addition to obtaining corrosion rates with linear polarization during the long term test, electrochemical impedance spectroscopy is used to periodically measure the complex impedance as a function of frequency. Such measurements are made for each environment. The data is presented in the form of a standard Bode plot, with the impedance amplitude as a function of frequency shown here. Interpretation of these data in terms of a simple linear circuit model is enabling the resistance and capacitance of the thermally sprayed samples, along with the electrolyte resistance to be determined as a function of time, temperature and environment. As the nature of the passive film changes, it will be detected through these impedance measurements. The corresponding phase angle of the complex impedance is given in the following figure.

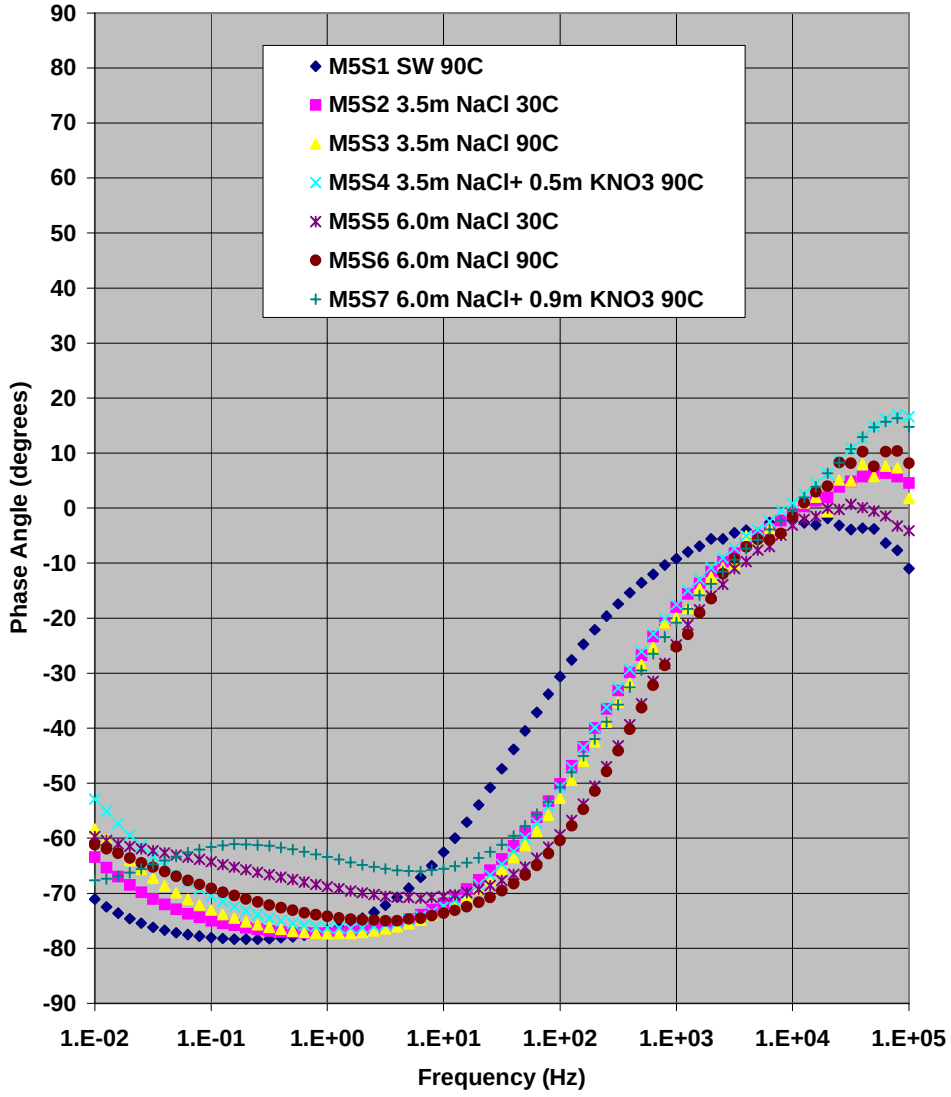

Figure 37. The phase angle as a function of frequency is shown here for the complex impedance data being gathered during the long-term test, and corresponds to the impedance amplitude in the previous figure.

Figure 38. This figure shows the gamma pit at LLNL. Actual spent fuel containers will be subjected to relatively high fluxes of gamma radiation, which will cause radiolytic reactions in the aqueous environment, including the production of hydrogen peroxide and other species. Work has begun on making electrochemical corrosion measurements inside the gamma pit, so that the impact of radiation on the amorphous metal coatings, and on the Alloy C-22 reference material can be assessed.

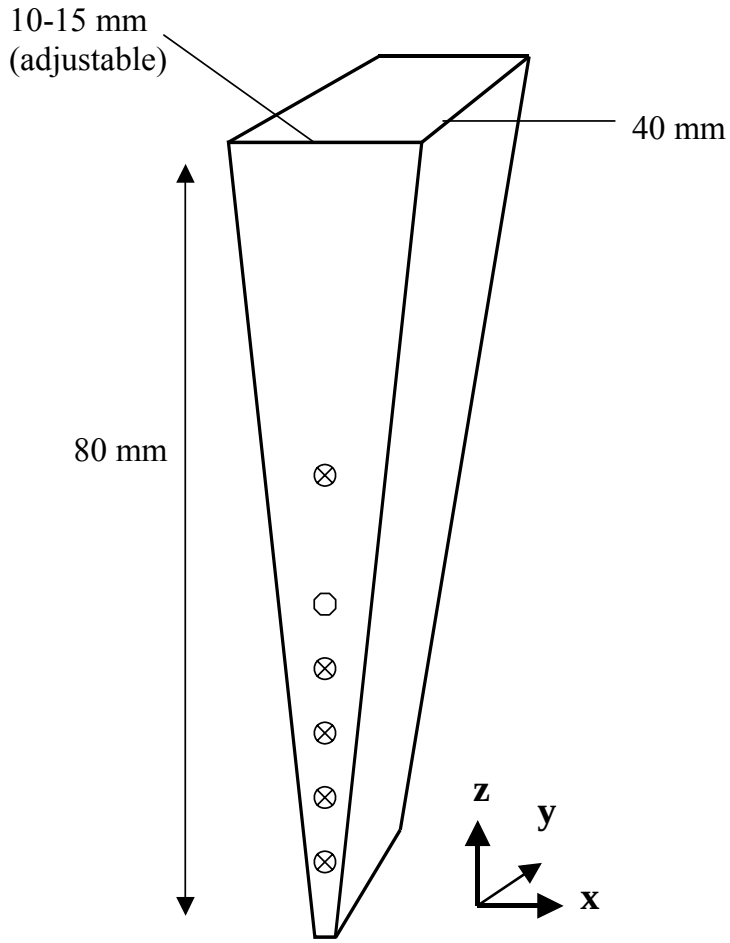

Figure 39. [Figure 1, Perepezko] Schematics of the wedge-shaped cavity in the Cu-mold. Thermocouple positions are indicated with the 'circle and cross' symbols at 10, 15, 20 and 25. mm from the bottom of the mold

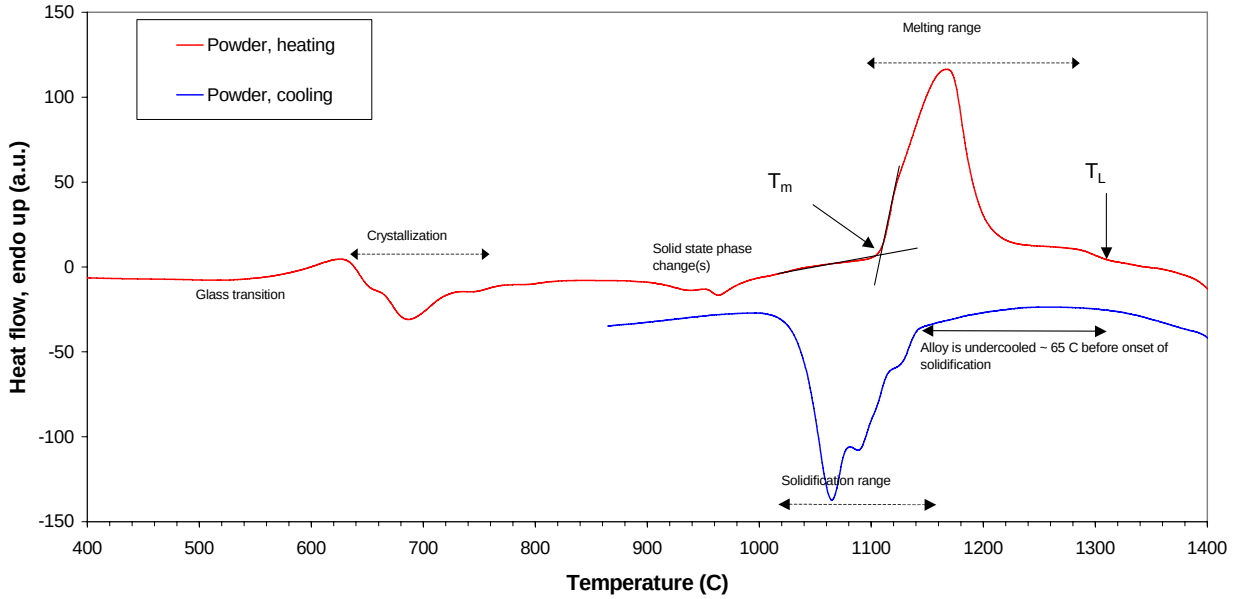

Figure 40. [Figure 2, Perepezko] Heat flow vs. temperature chart obtained during continuous heating of atomized SAM7 powder. The tangent intersection method is illustrated for the onset of melting. The diagram illustrates typical features that are observed during heating of amorphous samples; a glass transition signal (gradual increase of heat flow, endothermic, 550-580 ℃), crystallization (exothermic peaks, 620-760 ℃), phase changes (exothermic peaks, 900-1000 ℃ and a melting range (endothermic, 1120-1280 ℃).

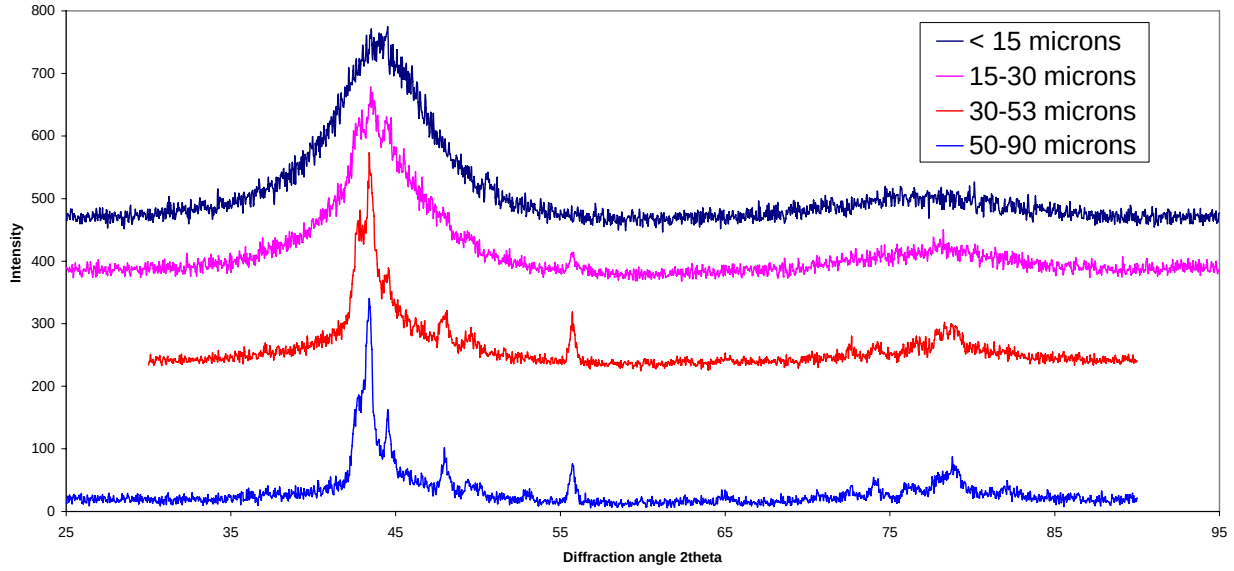

Figure 41. [Figure 3, Perepezko] X-ray diffraction (XRD) analysis of atomized SAM2X5 powder as a function of powder size.

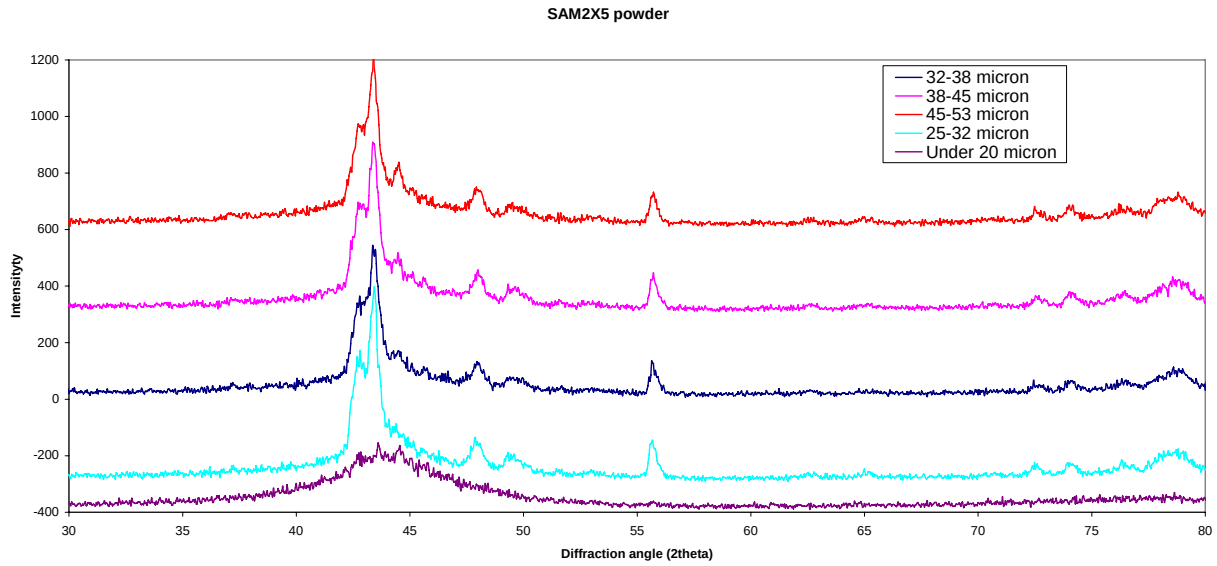

Figure 42. [Figure 4, Perepezko] X-ray diffraction (XRD) of atomized SAM2X5 powder.

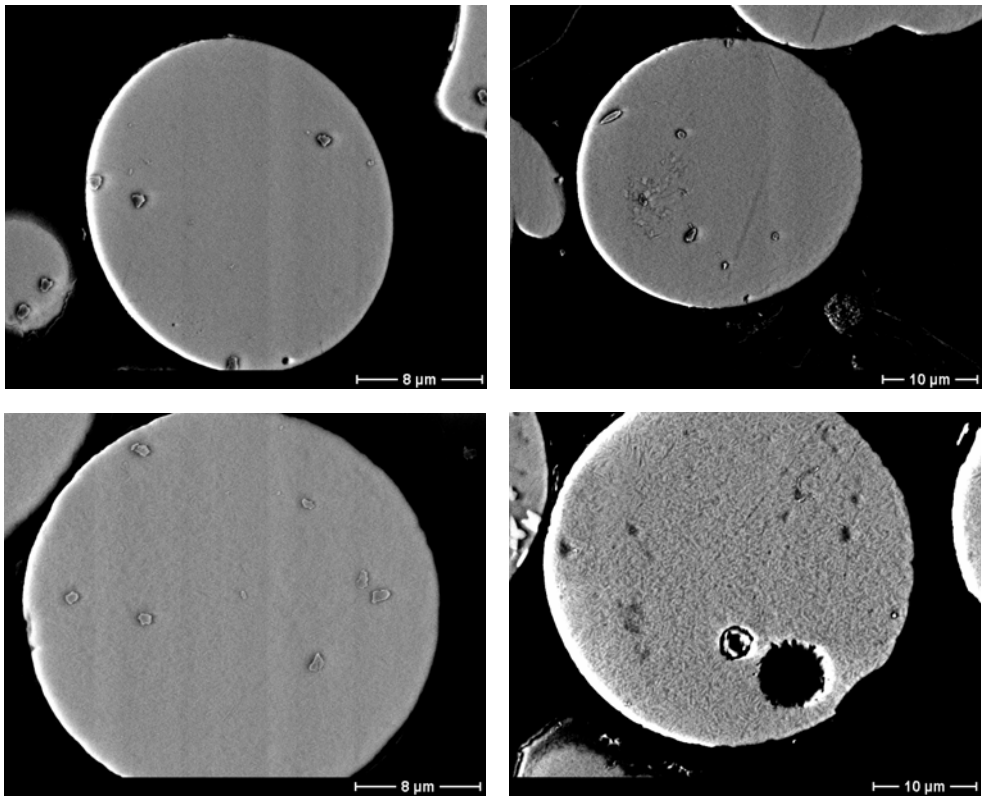

Figure 43 [Figure 5, Perepezko] Back-scattered electron images of SAM2X5 powder, indicating increasing degree of fraction crystalline with increasing powder size. The powder was sieved into size fractions <20 µm (top left), 20-25 µm (top right), 25-32 µm (bottom left), 32-38 µm (bottom right) and 38-45 µm (not shown).

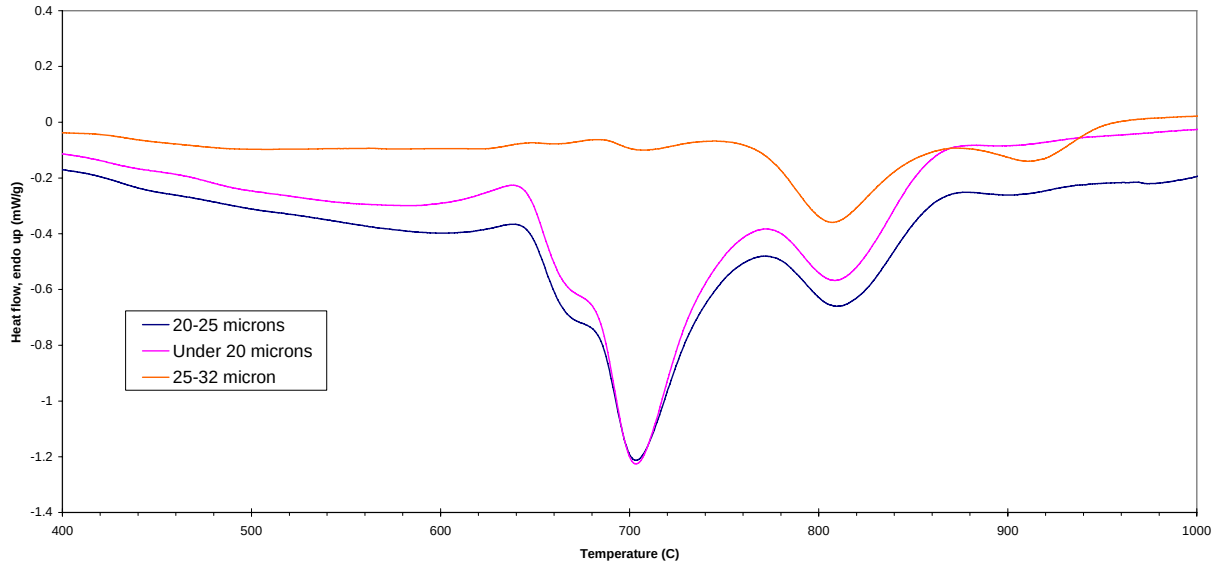

Figure 44. [Figure 6, Perepezko] Differential thermal analysis (DTA) continuous heating of sieved SAM2X5 powder.

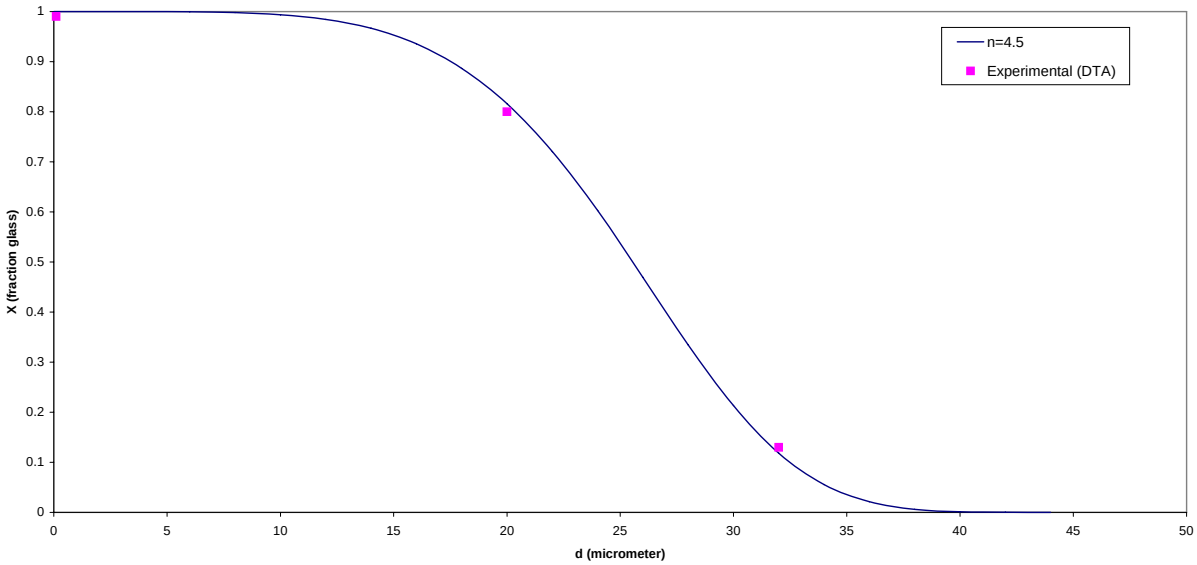

Figure 45. [Figure 7, Perepezko] Preliminary results of powder kinetics analysis for SAM2X5 atomized powder.

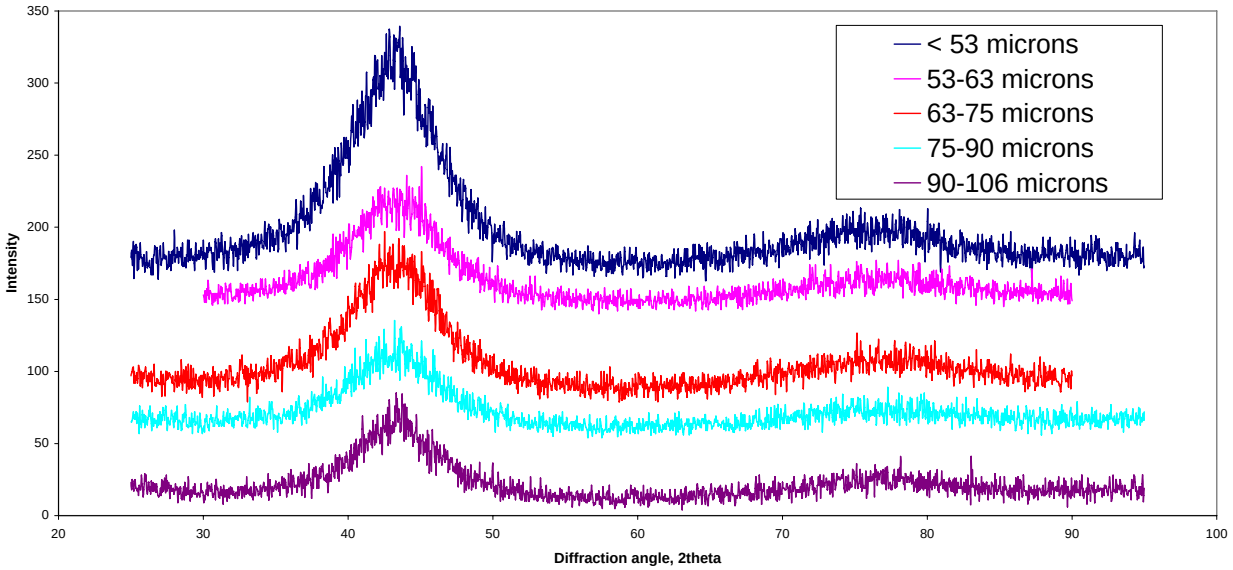

Figure 46. [Figure 8, Perepexko] X-ray diffraction (XRD) analysis of atomized SAM7 powder as a function of powder size.

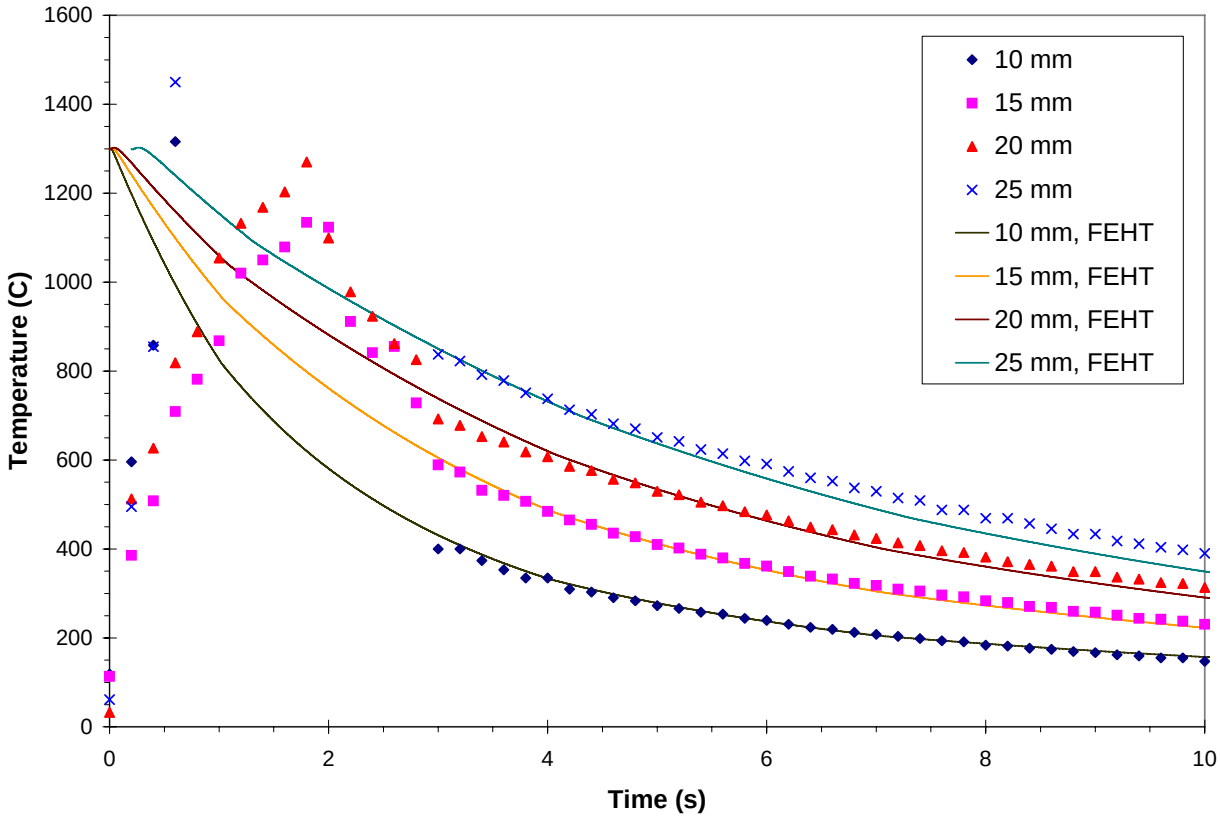

Figure 47. [Figure 9, Perepezko] Measured and fitted cooling curves obtained during wedge casting of $Fe_{48}Cr_{15}Mo_{14}Y_2C_{15}B_6$. The heat transfer coefficient is a function of time only.

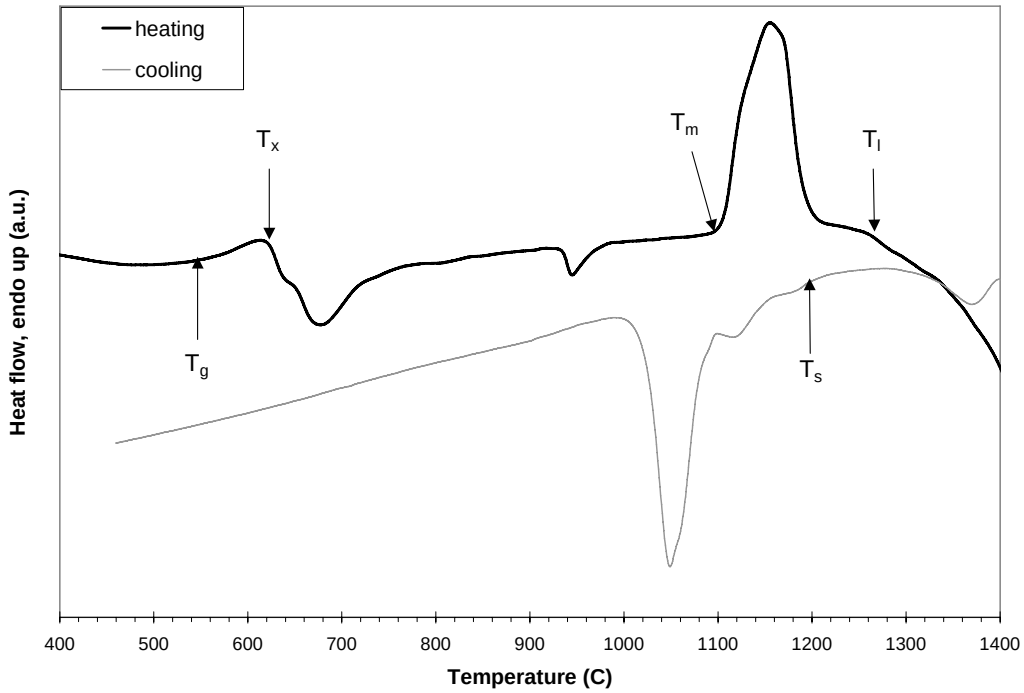

Figure 48. [Figure 10, Perepezko] Differential thermal analysis (DTA) heat flow trace for a wedge cast sample cut from a 2-mm thick wedge cross-section. The onset temperatures for glass transition and crystallization are indicated, as well as the onset of melting and the liquidus temperature.

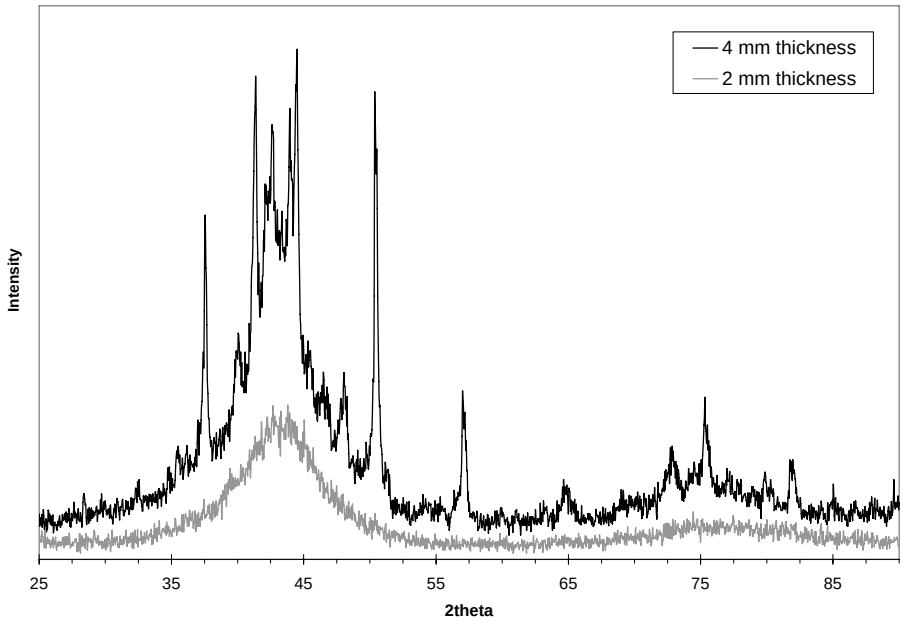

Figure 49. [Figure 11, Perepezko] X-ray diffraction (XRD) intensity pattern of wedge cast samples from two different cross-sections. The majority of the peaks at the upper curve can be indexed according to an $M_{23}C_6$ type crystalline structure, while some still remains unidentified.

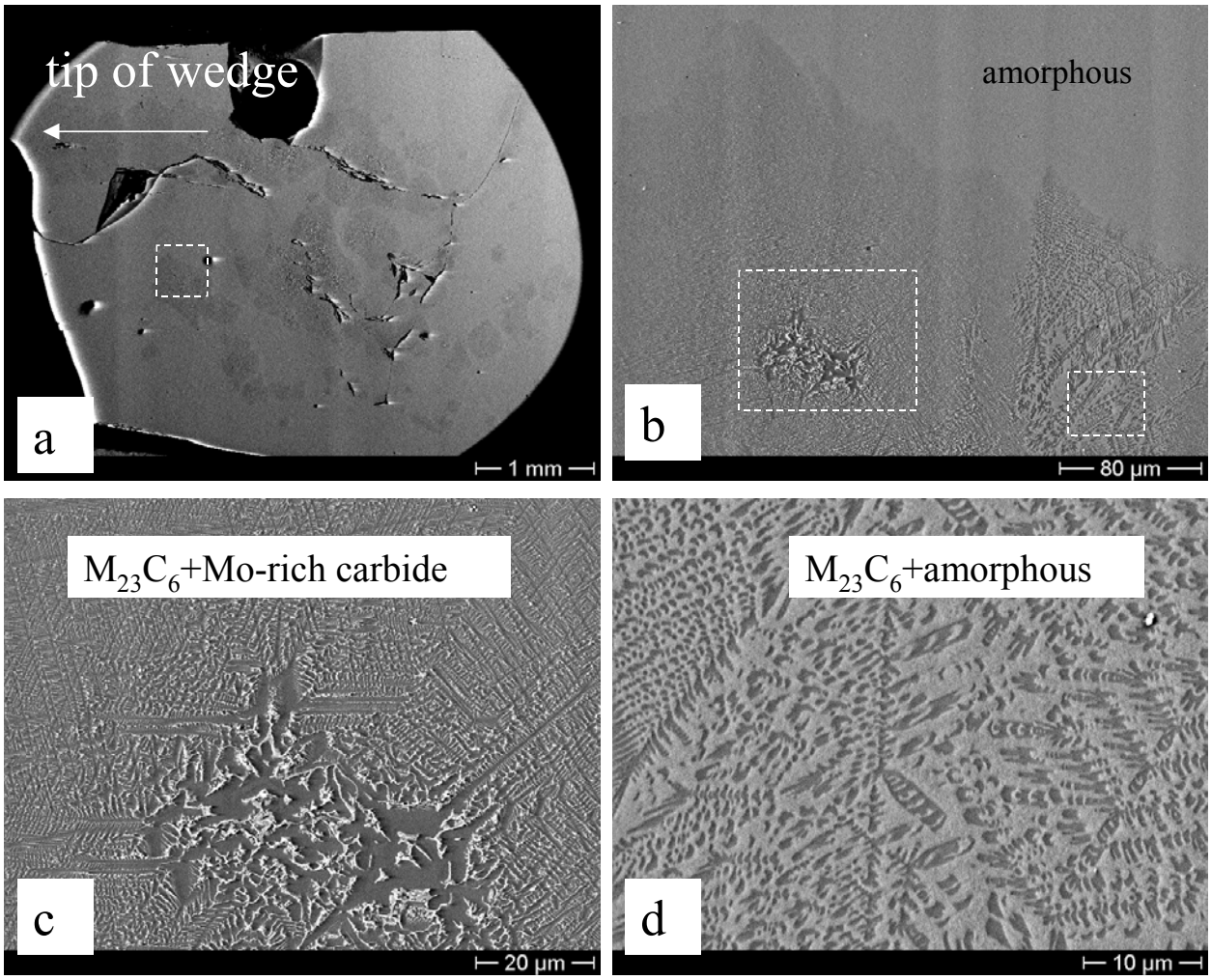

Figure 50. [Figure 12, Perepezko] Back-scattered electron (BSE) images of the wedge cast sample; a) Overview of the lower part of the transition region; b) Crystalline "island" exhibiting different microstructure features, taken from the indicated area in figure 5a. The two indicated areas are shown at larger magnifications in figure c (left box) and d (right box); c) Two-phase structure, $M_{23}(B,C)_6$ (dark) and Mo-rich carbide (bright), taken from the indicated area of figure 5b (left box); d) mixture of amorphous phase (light gray) and $M_{23}(B,C)_6$ (dark dendrites).

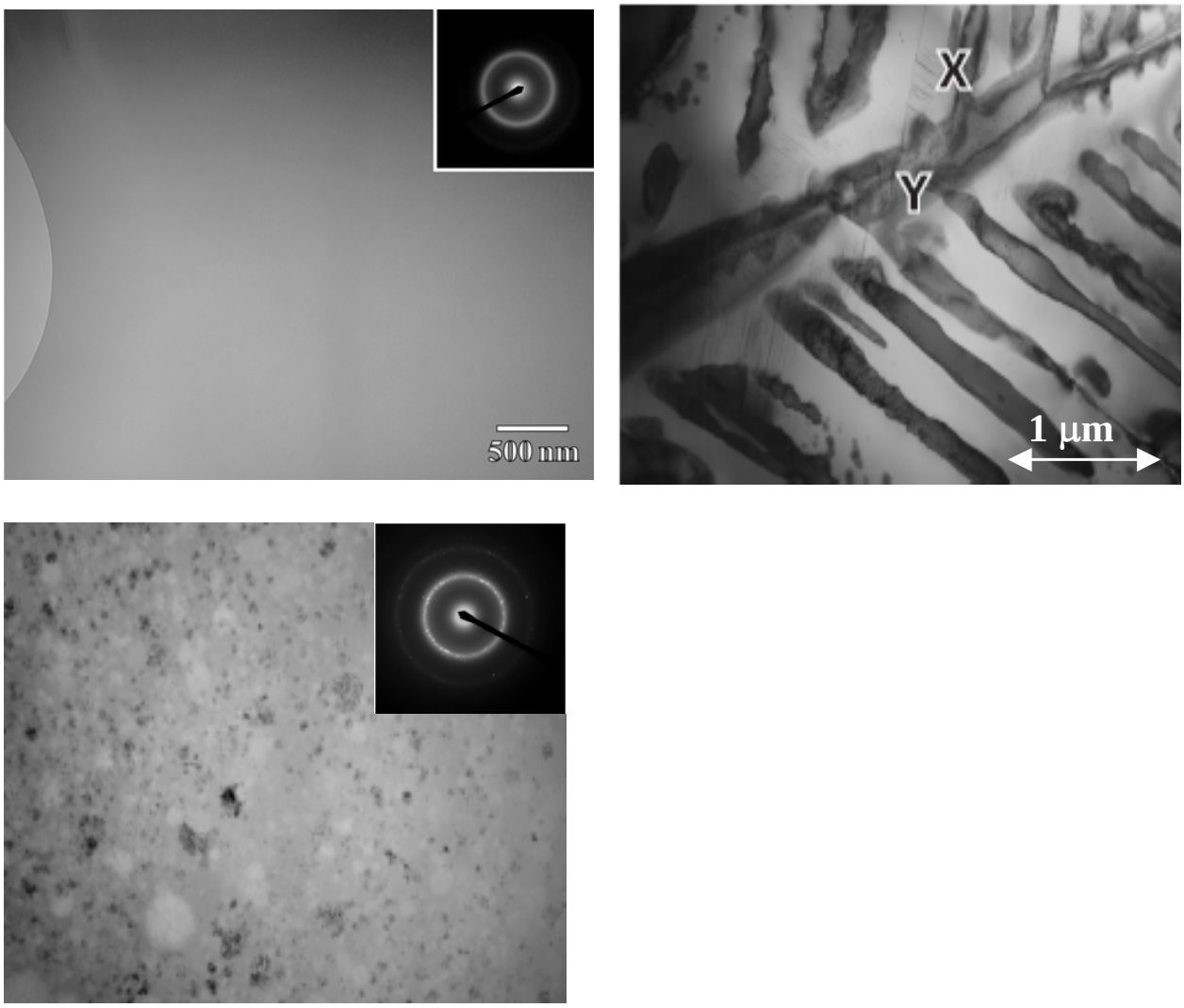

Figure 51. [Figure 13, Perepezko] TEM images of wedge cast sample, a) fully amorphous structure at a wedge thickness of 3 mm, b) Eutectic structure from an isolated region at a wedge thickness of 3.5 mm, c) partially amorphous structure with spherical precipitates at a wedge thickness of 3.5 mm.

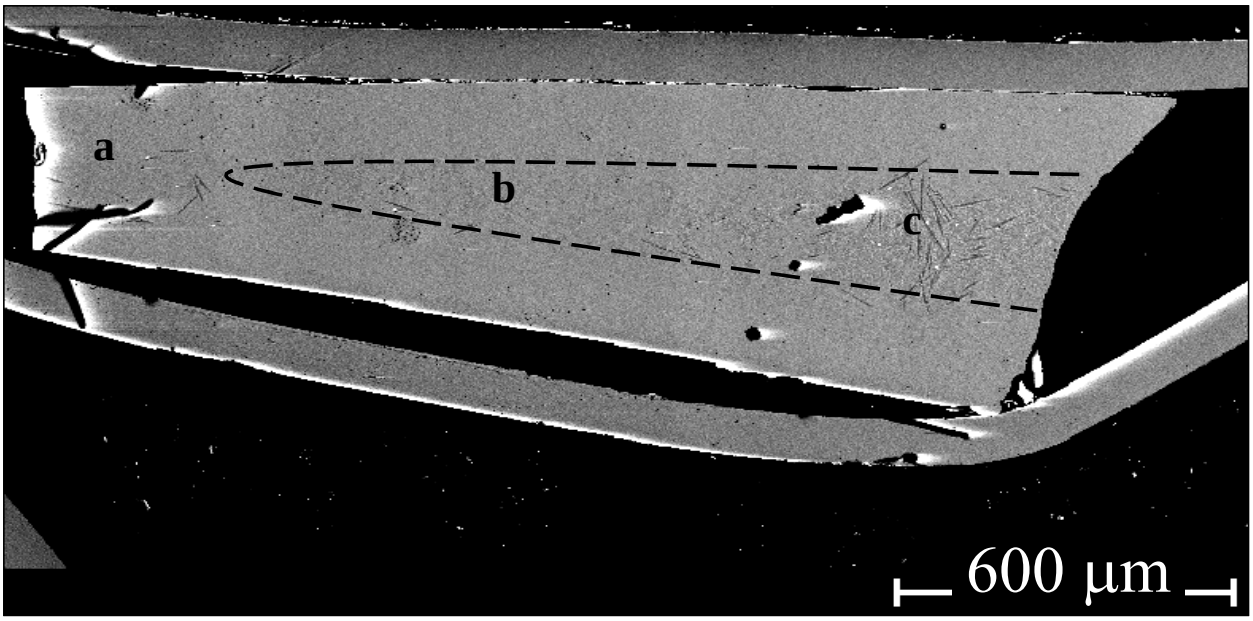

Figure 52. [Figure 14, Perepezko] Backscatter electron (BSE) images of the transition zone appearance in wedge cast SAM40. The dark, stippled line is imposed to indicate the boundary of crystalline phase occurrence.

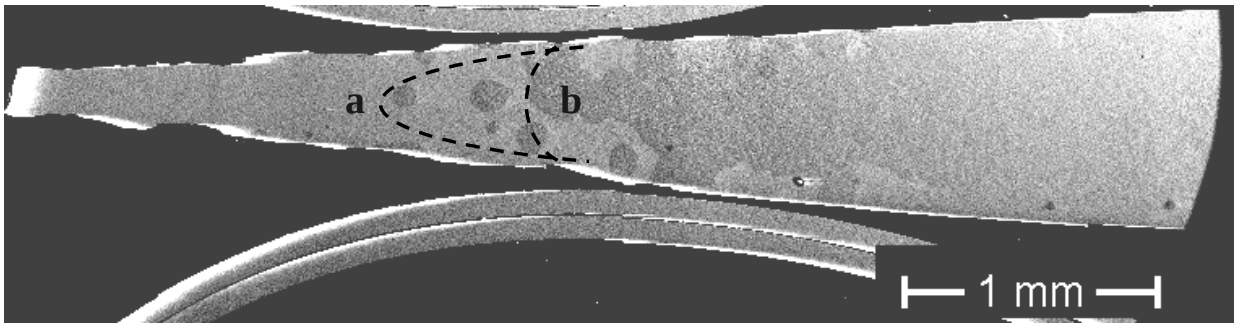

Figure 53. [Figure 15, Perepezko] BSE images of the transition zone appearance in wedge cast SAM35. The two imposed stippled lines indicate the range of possible isothermal contours during cooling based on the appearance of the glass-crystalline transition regions.

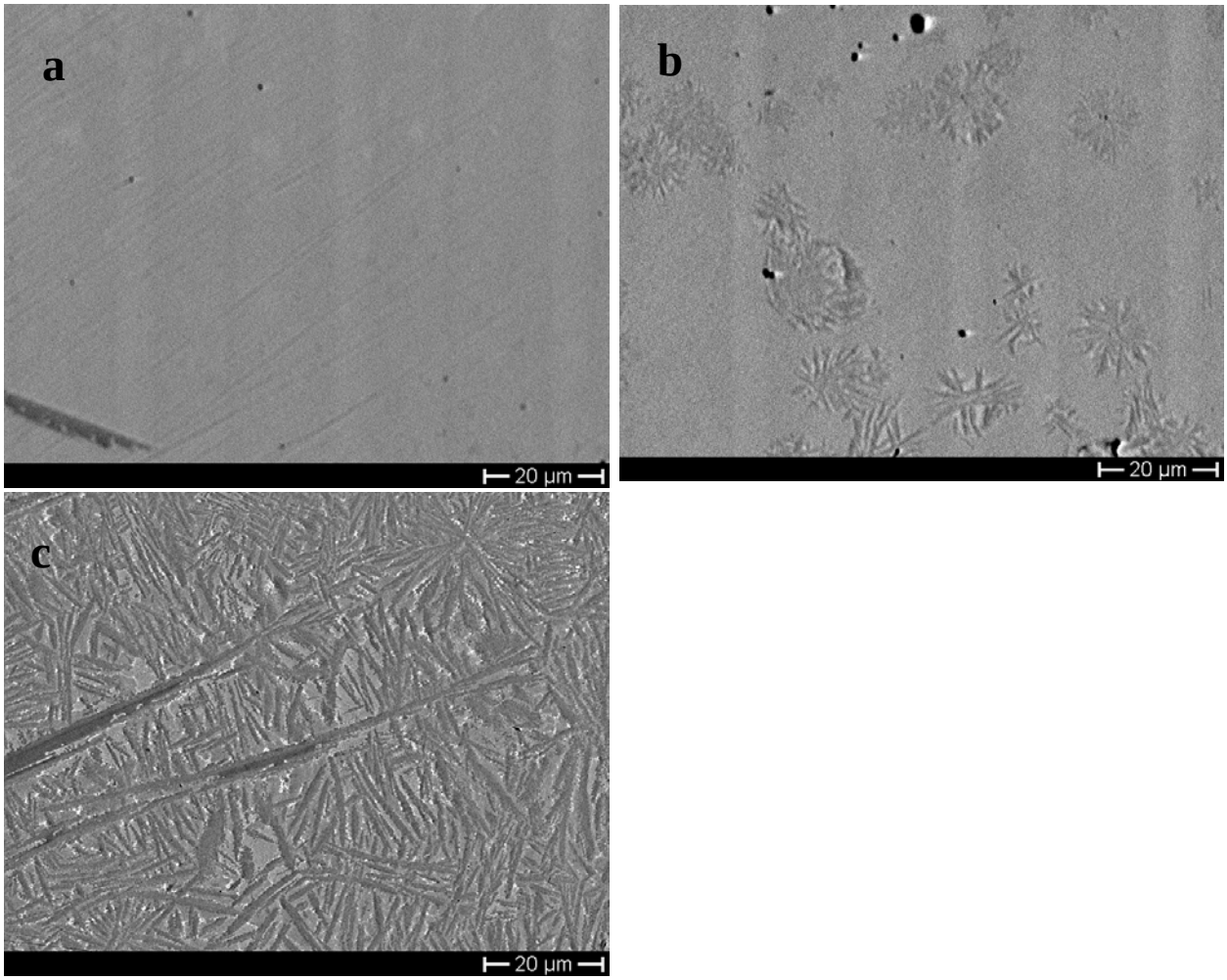

Figure 54. [Figure 16, Perepezko] Backscatter (BSE) images of selected areas as indicated on [Figure 14, Perepezko]: (a) fully amorphous; (b) mixture of glassy phase and dendritic solid phases; and (c) mostly crystalline structure.

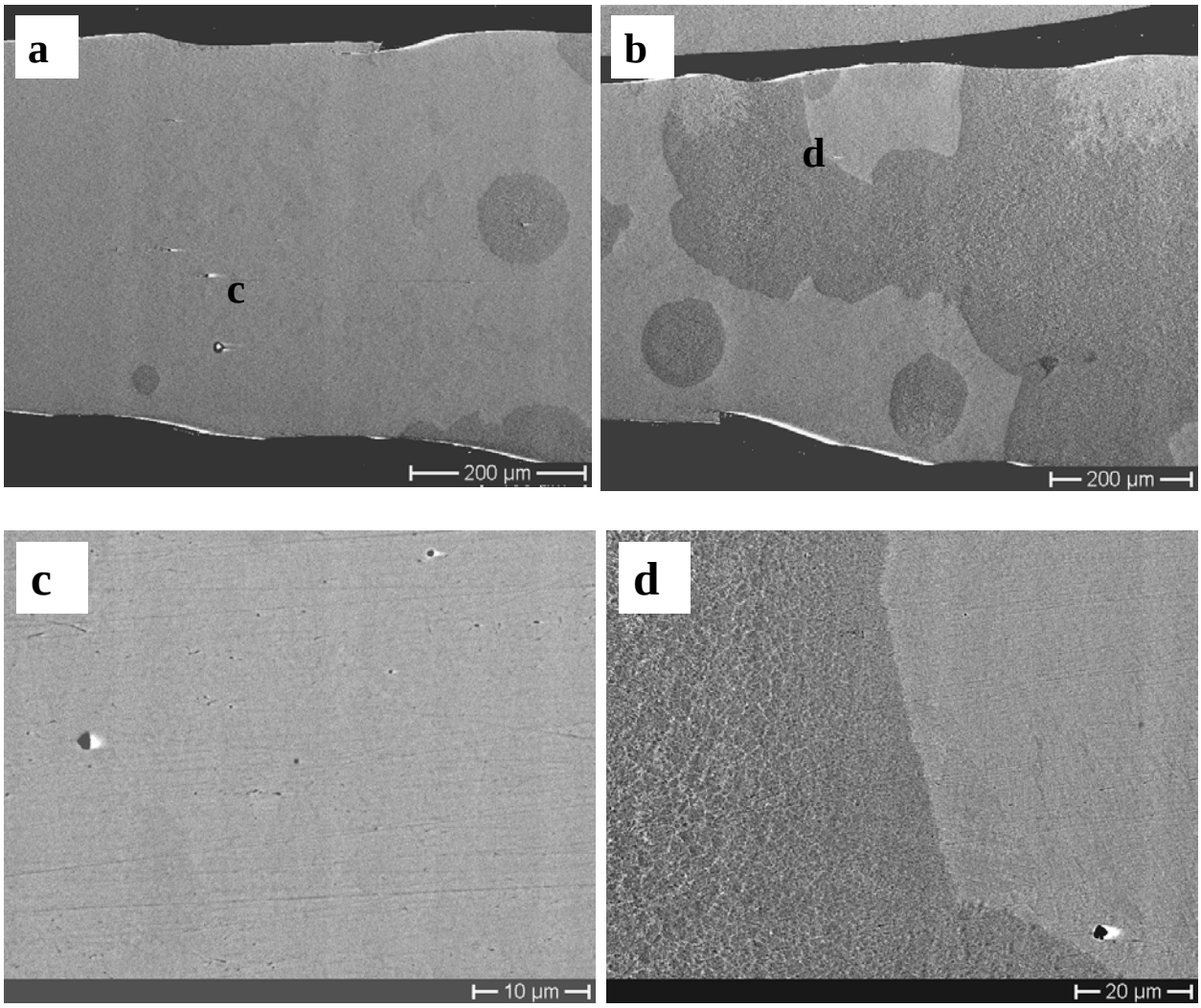

Figure 55. [Figure 17, Perepezko] Backscatter electron (BSE) images of wedge cast SAM35: (a) magnified portion of [Figure 15, Perepezko] corresponding to [Location a]; (b) magnified portion of [Figure 15, Perepezko], corresponding to [Location b]; (c) magnified portion of [Figure 17, Perepezko, Frame a], corresponding to [Location c]; and (d) magnified portion of [Figure 17, Perepezko, Frabme b], corresponding to [Location d].

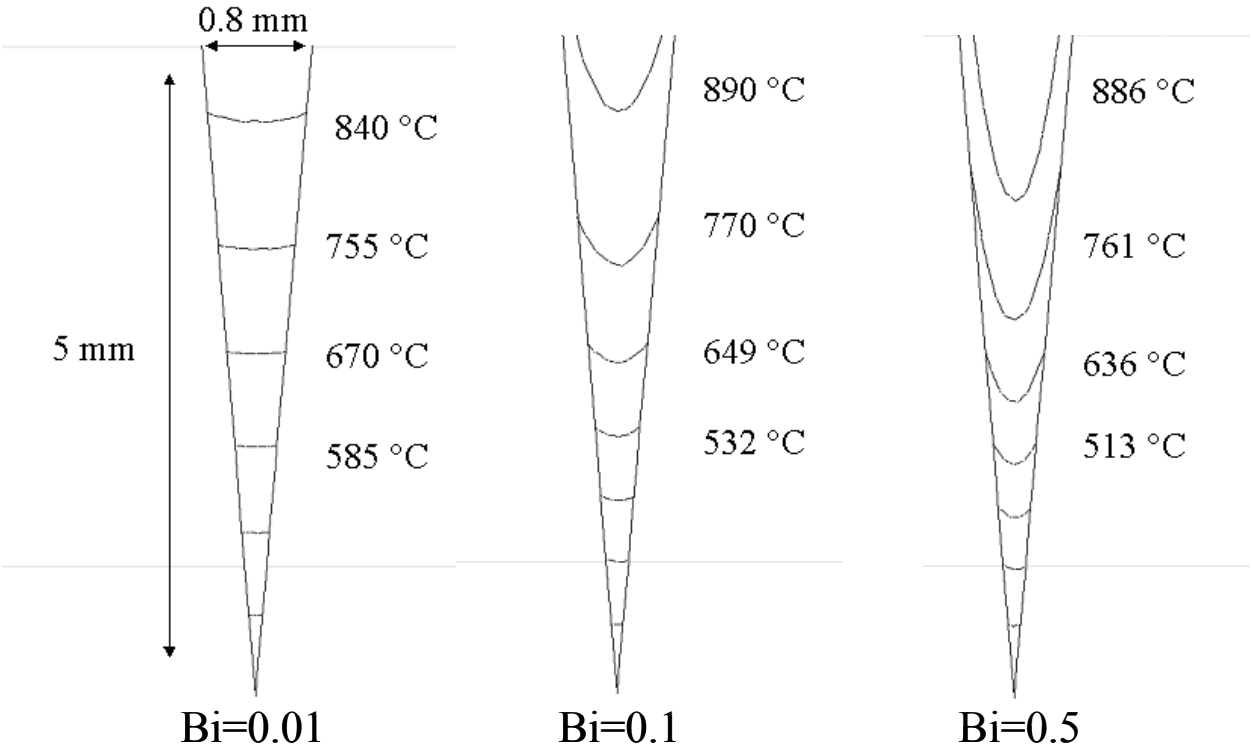

Figure 56. (Figure 18) Isothermal contour plots for different Biot numbers after one second of cooling of a typical Fe-based alloy. The contours shown in figure 18c resemble the shape of the glass-crystal transition zone that was observed in the SAM40 alloy.

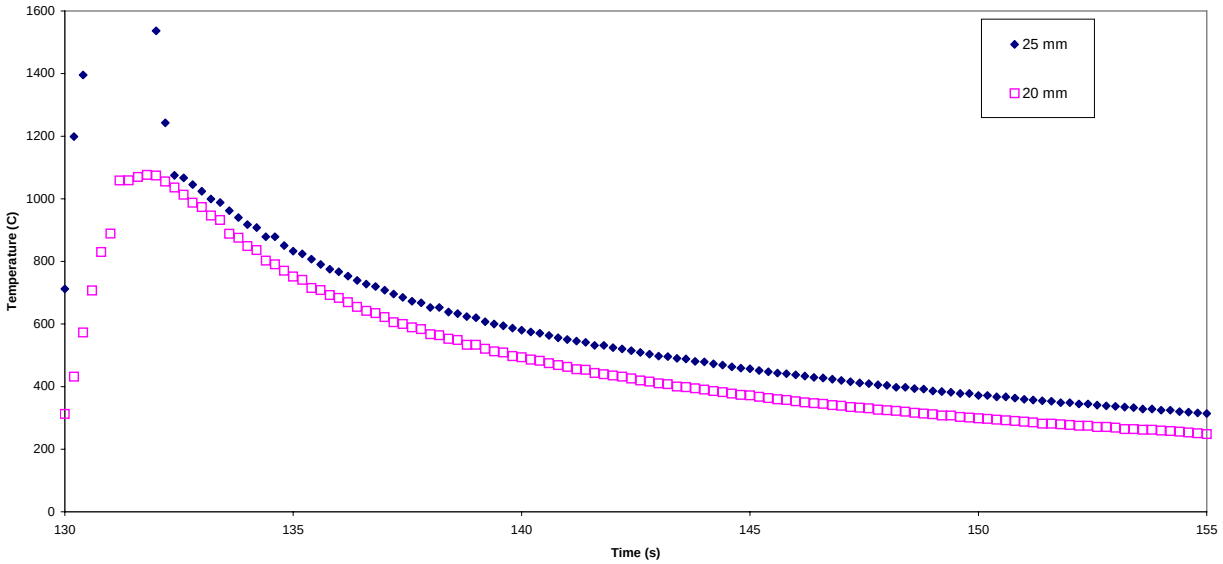

Figure 57. (Figure 19) Cooling rates acquired with type R-thermcouples during wedge cast of SAM2X5.

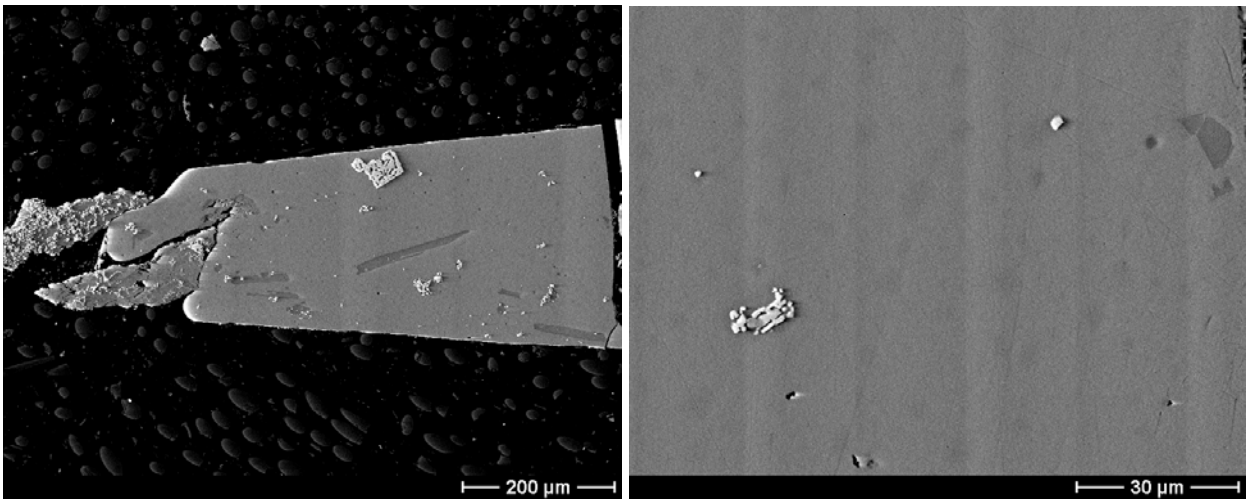

Figure 58. (Figure 20) BSE image of the tip of the wedge cast SAM2X5.

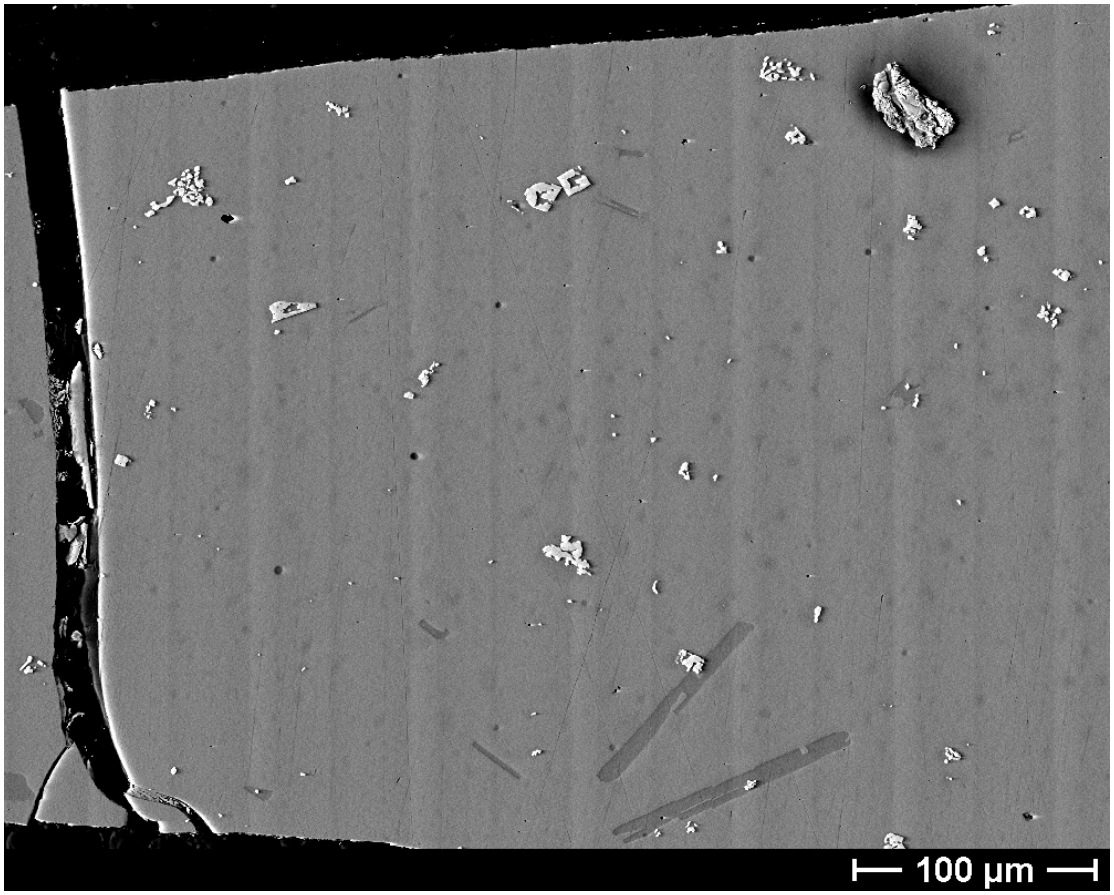

Figure 59. [Figure 21, Perepezko] Backscatter electron (BSE) image of the region adjacent to [Figure 18, Perepezko].

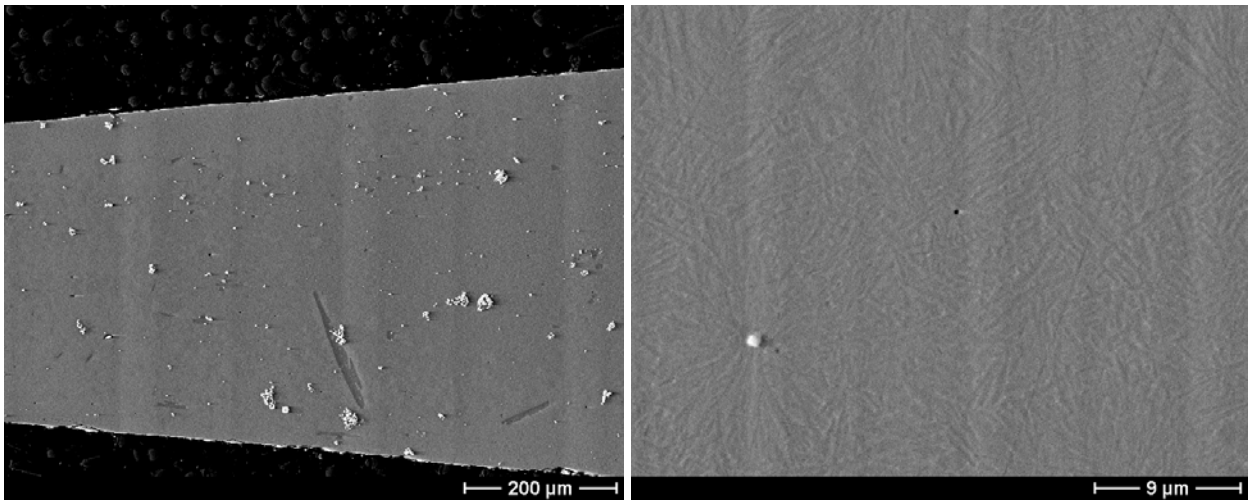

Figure 60. [Figure 22, Perepezko] Backscatter electron (BSE) image indicating the end of the glass-crystalline transition zone of wedge cast SAM2X5. The right image illustrates the fine, needle-like structure similar to that observed in atomized powders [Figure 5, Perepezko].

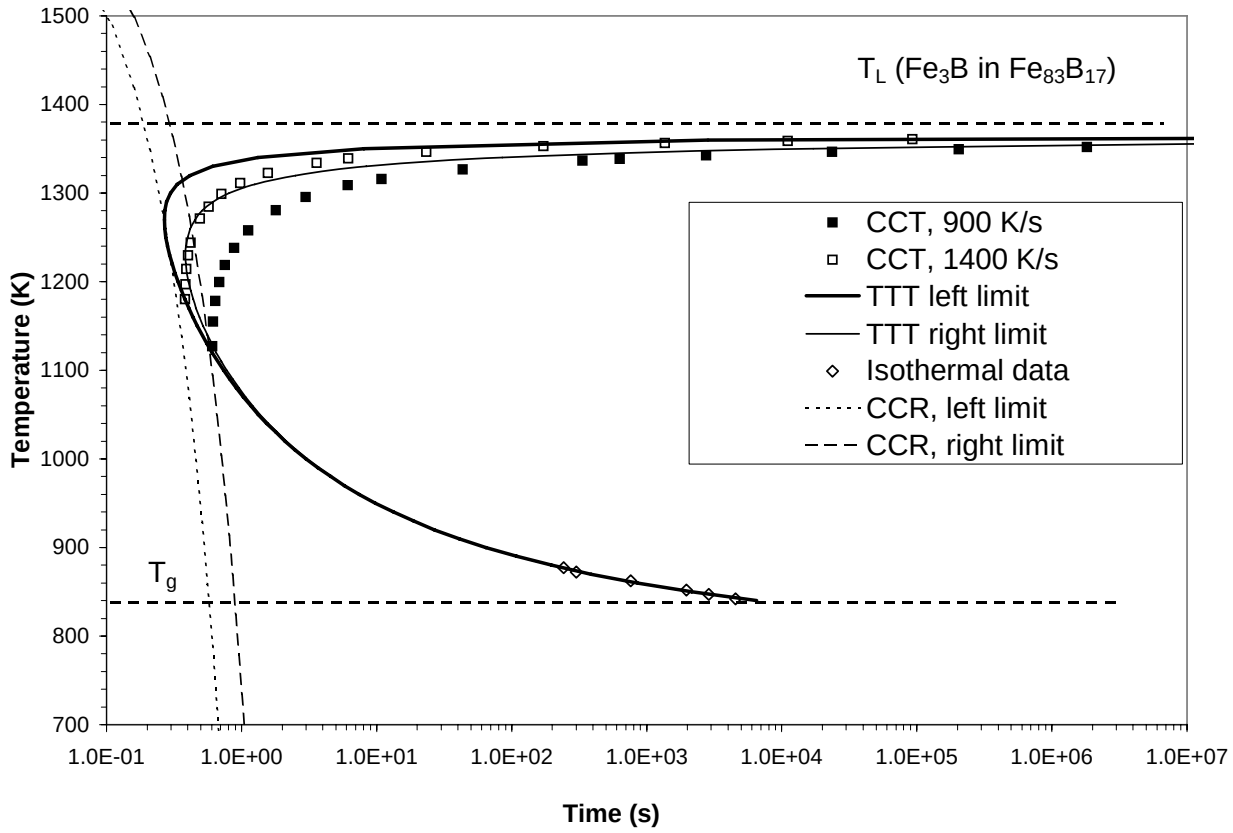

Figure 61. [Figure 23, Perepezko] Isothermal onset times for crystallization, critical cooling rate range and the calculated preliminary time-temperature-transformation (TTT) curve and the derived CCT curve for initial crystallization of the Fe_3B structure type phase in SAM40.

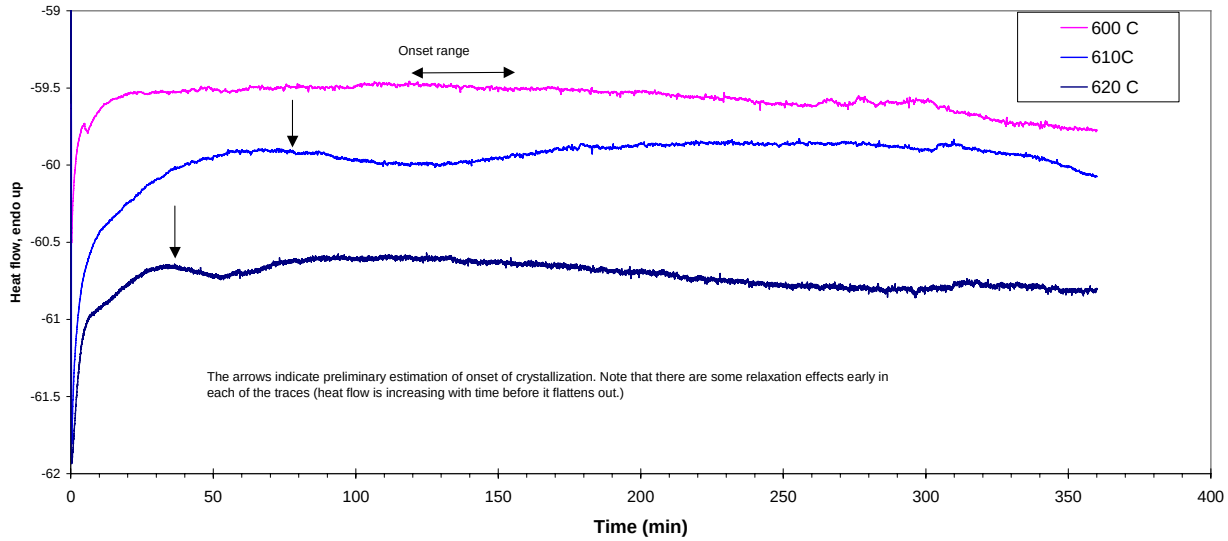

Figure 62. [Figure 24, Perepezko] Isothermal annealing of SAM1651 (SAM7) as-spun ribbons.

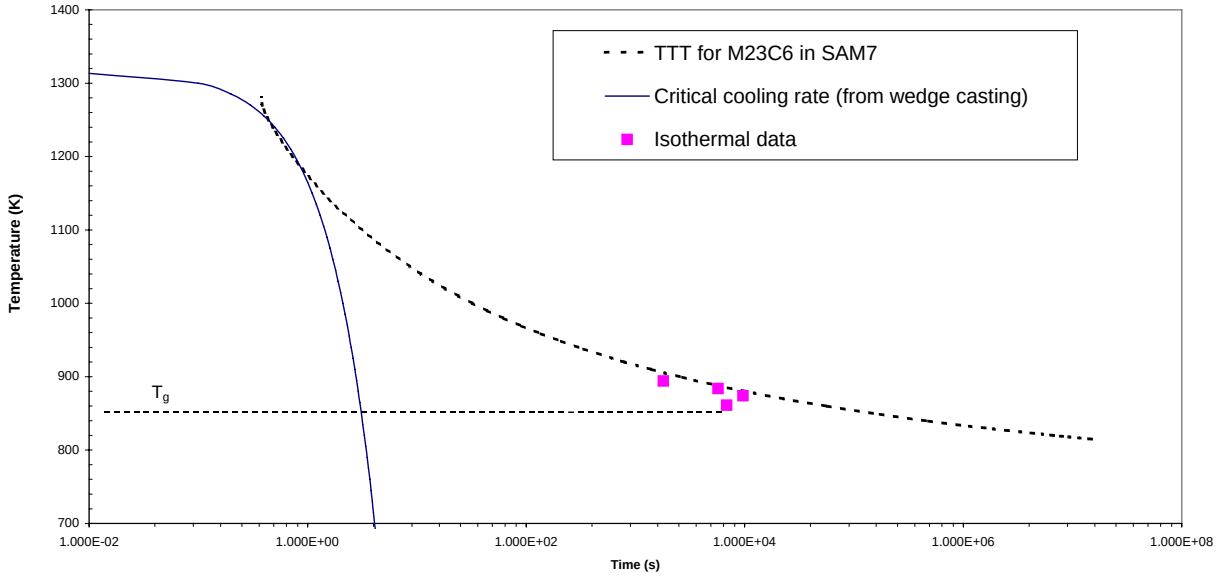

Figure 63. [Figure 25, Perepezko] Preliminary TTT-curve for formation of $M_{23}(B,C)_6$ in amorphous SAM1651 (SAM7).

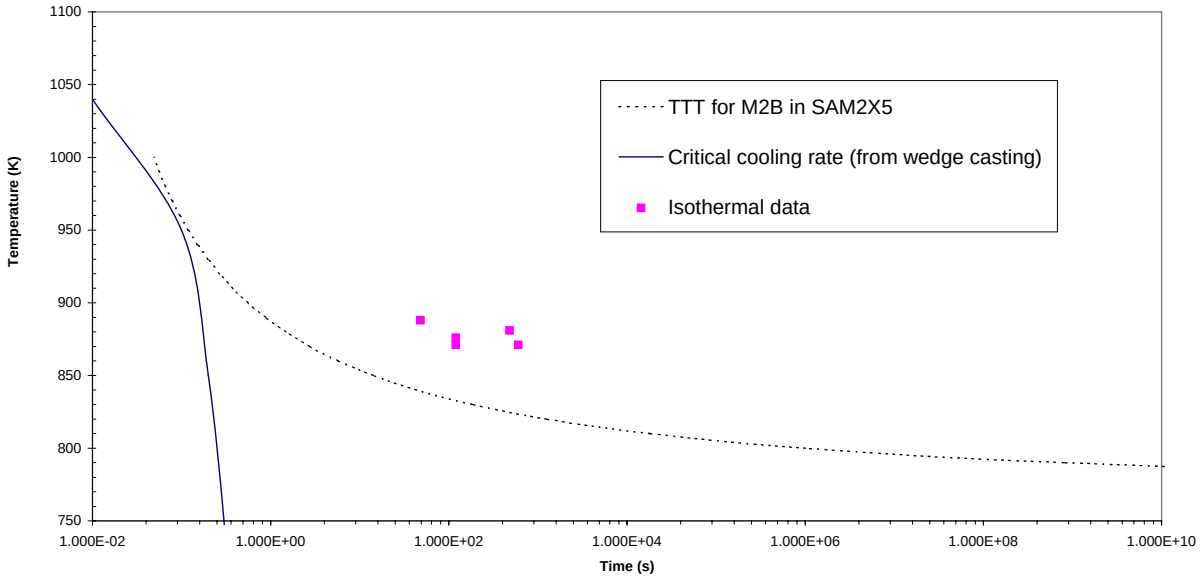

Figure 64. [Figure 26, Perepezko] Preliminary kinetics transformation curve for SAM2X5. The isothermal data were not utilized in the calculation as significant growth preceded the nucleation onset. Instead, data from annealing as-spun ribbons of SAM40X3 (a similar composition) and the corresponding kinetics parameters were used along with the critical cooling rate measured from wedge casting of SAM2X5 to assess a preliminary TTT-curve.

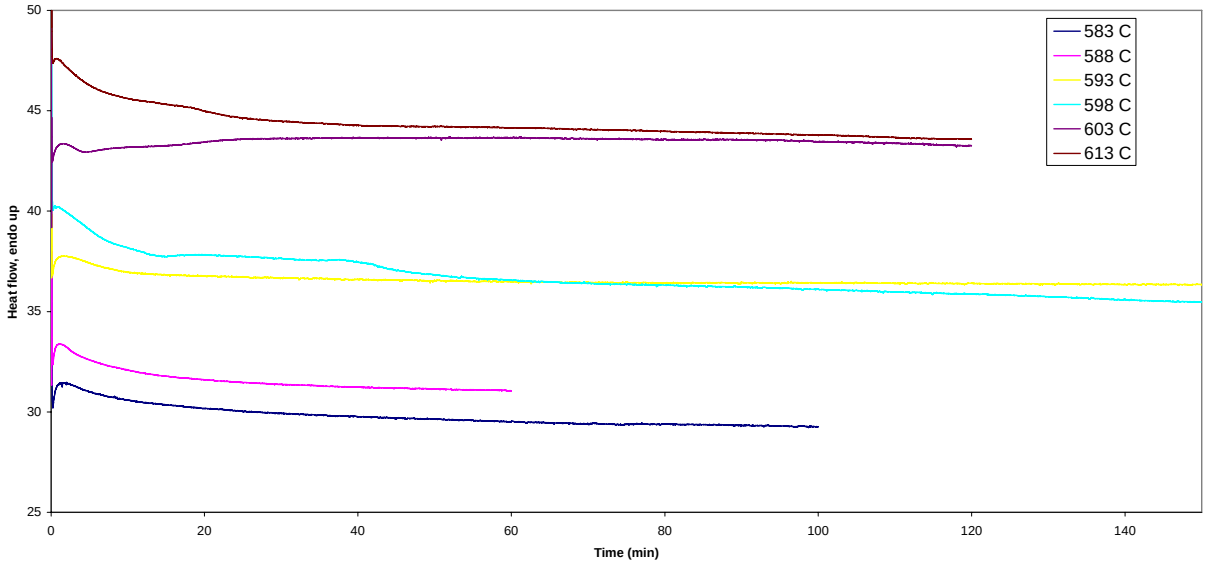

Figure 65. [Figure 27, Perepezko] Isothermal annealing of as-spun SAM2X5 ribbons. No observable peaks for T=583,588 and 593 C, only a decreasing heat flow signal typical for growth processes. For T=598, 603 and 613 some onsets are seen but they are always preceded by a growth-type signal.

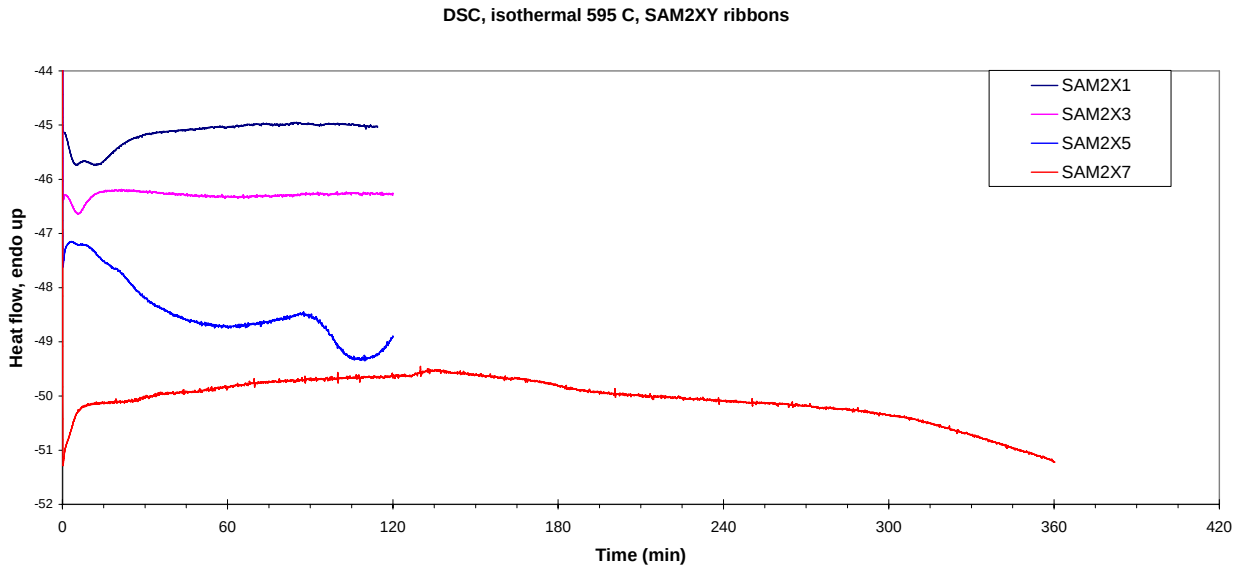

Figure 66. (Figure 28) DSC isothermal annealing data for SAM2XY ribbons. The curves are not normalized with respect to sample mass, but the effect of additional Mo seems to delay the crystallization process, particularly the onset second peak (~10 minutes for SAM2X1).

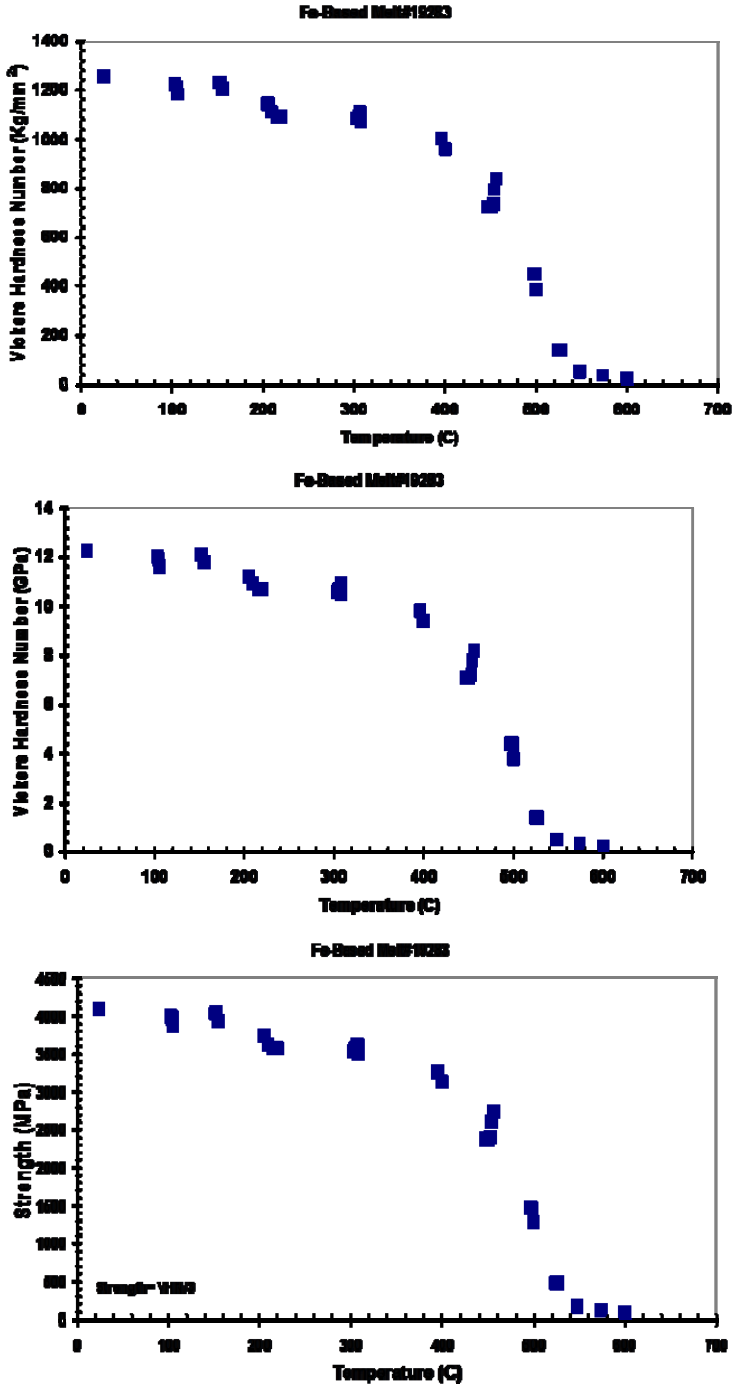

Figure 67. [Figure 1, Lewandowski] (a) Microhardness in kg/mm^2 of SAM1651 at different temperatures; (b) microhardness in GPa of SAM1651 at different temperatures; and (c) estimated compressive strength, which is VHN/3, of SAM1651 at different temperatures.

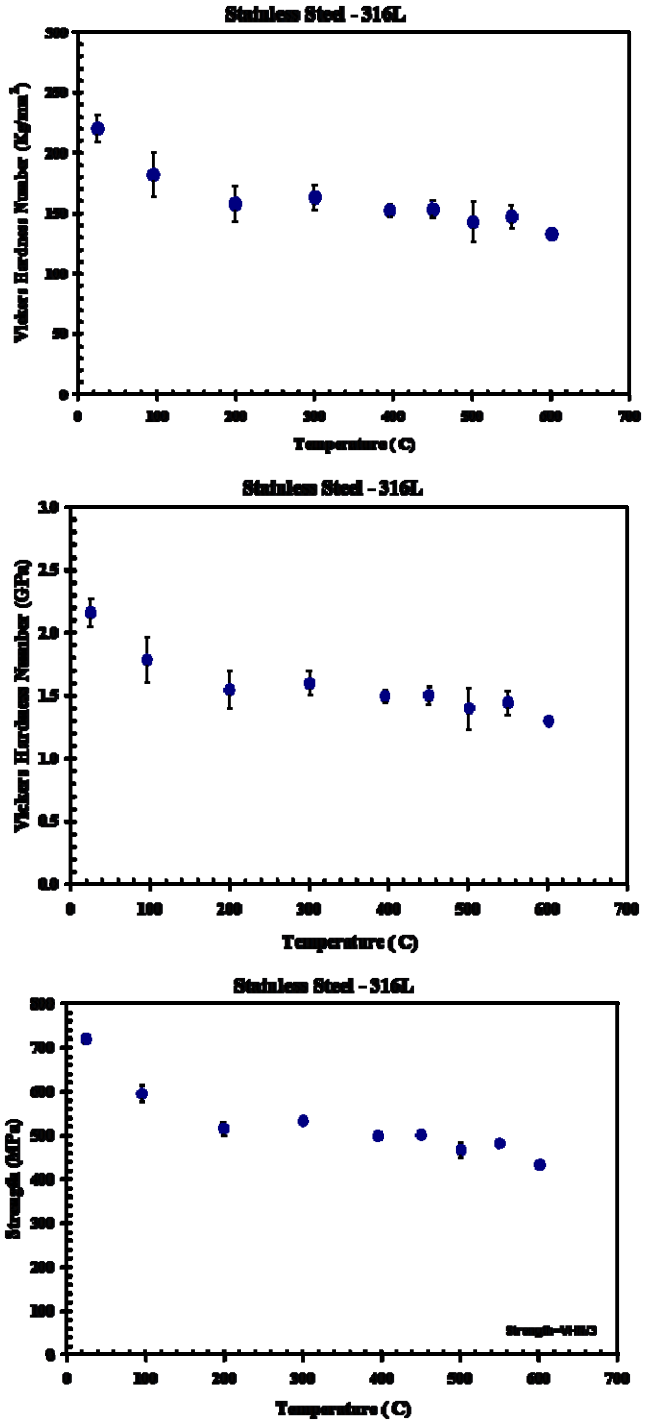

Figure 68. [Figure 2, Lewandowki] (a) Microhardness in kg/mm^2 of 316L at different temperatures; (b) microhardness in GPa of 316L at different temperatures; and (c) estimated compressive strength, which is VHN/3, of 316L at different temperatures.

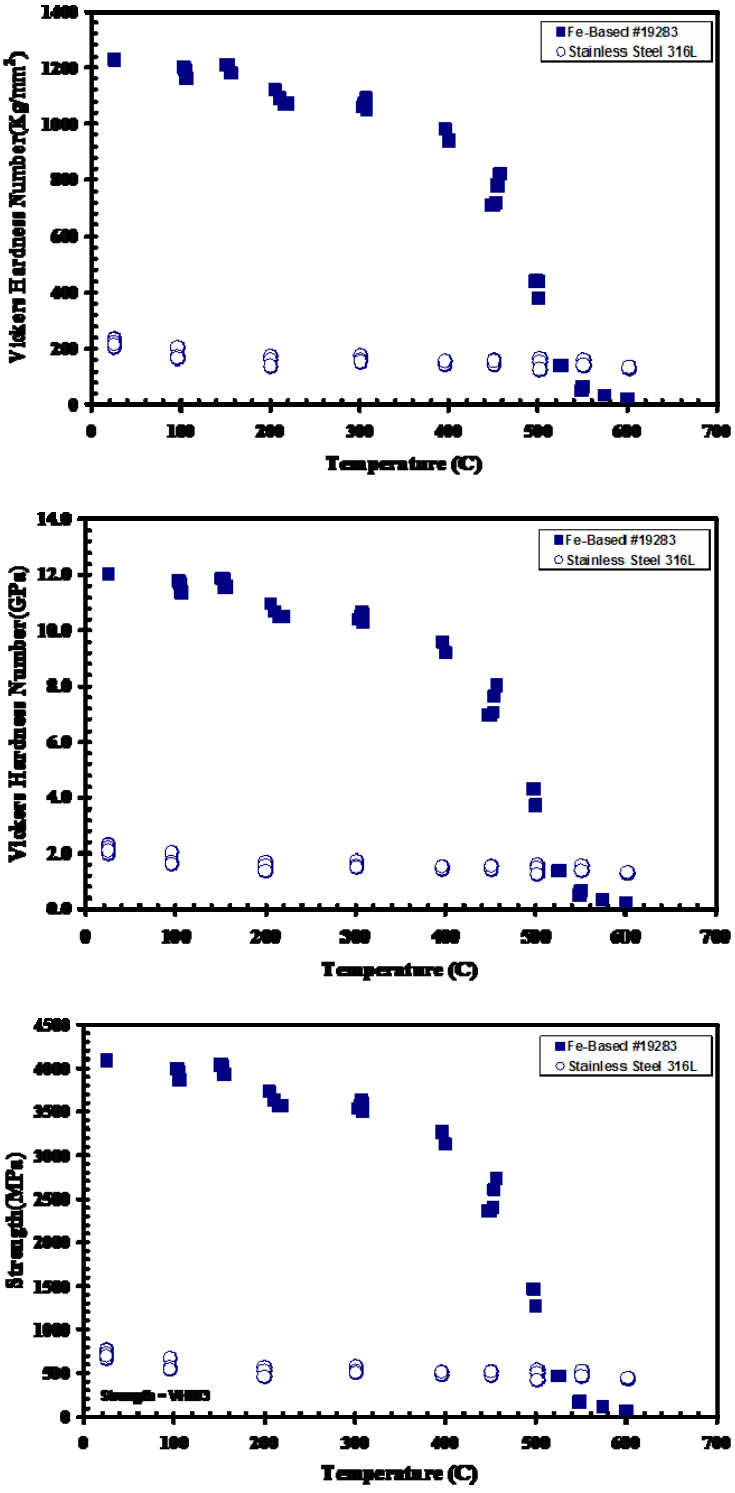

Figure 69. [Figure 3, Lewandowski] (a) Comparison of microhardness in kg/mm^2 of 316L and SAM1651 at different temperatures; (b) comparison of microhardness in GPa of 316L and SAM1651 at different temperatures; and (c) estimated compressive strength, which is VHN/3, of 316L and SAM1651 at different temperatures.

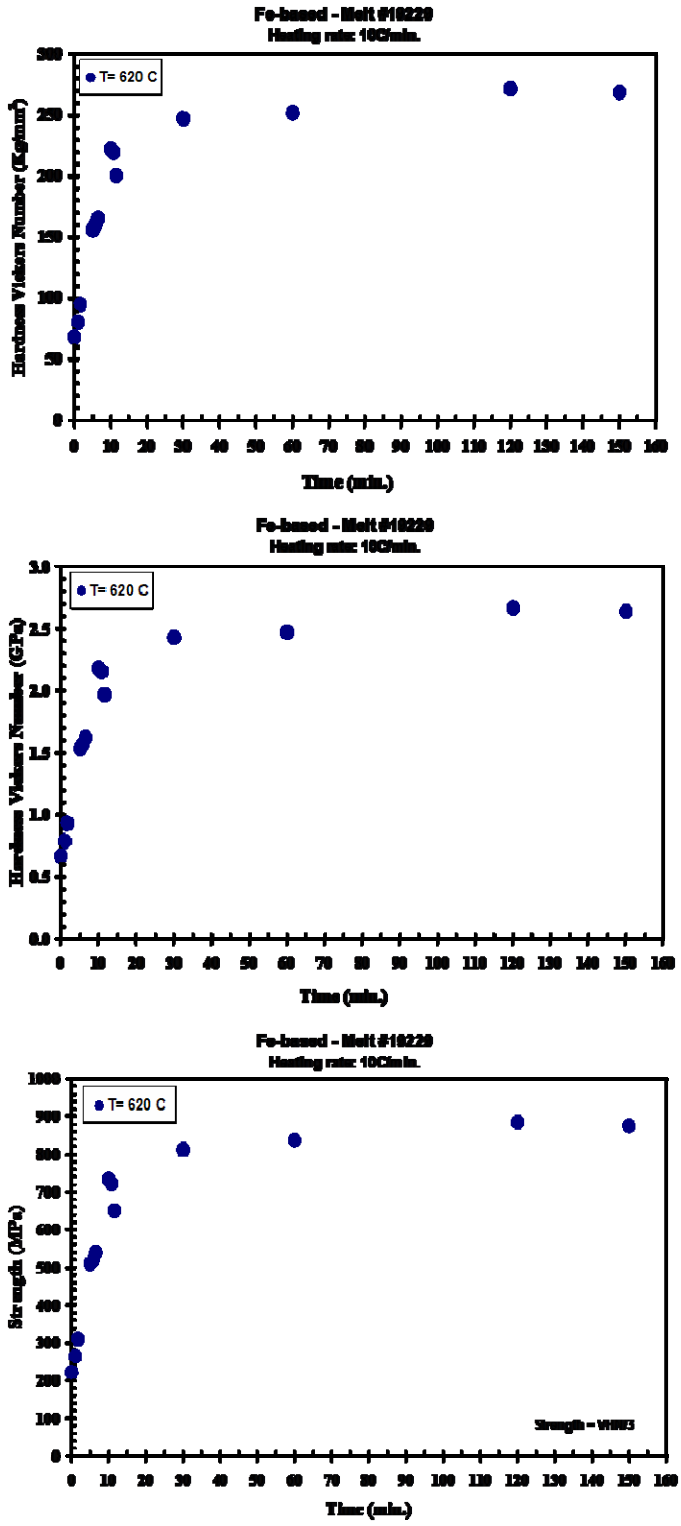

Figure 70. [Figure 4, Lewandowski] (a) Effects of exposure time at 620ºC on microhardness in kg/mm^2 of SAM1651; (b) effects of exposure time at 620ºC on microhardness in GPa of SAM1651; and (c) estimated compressive strength, which is VHN/3, for various exposure times at 620ºC for SAM1651.

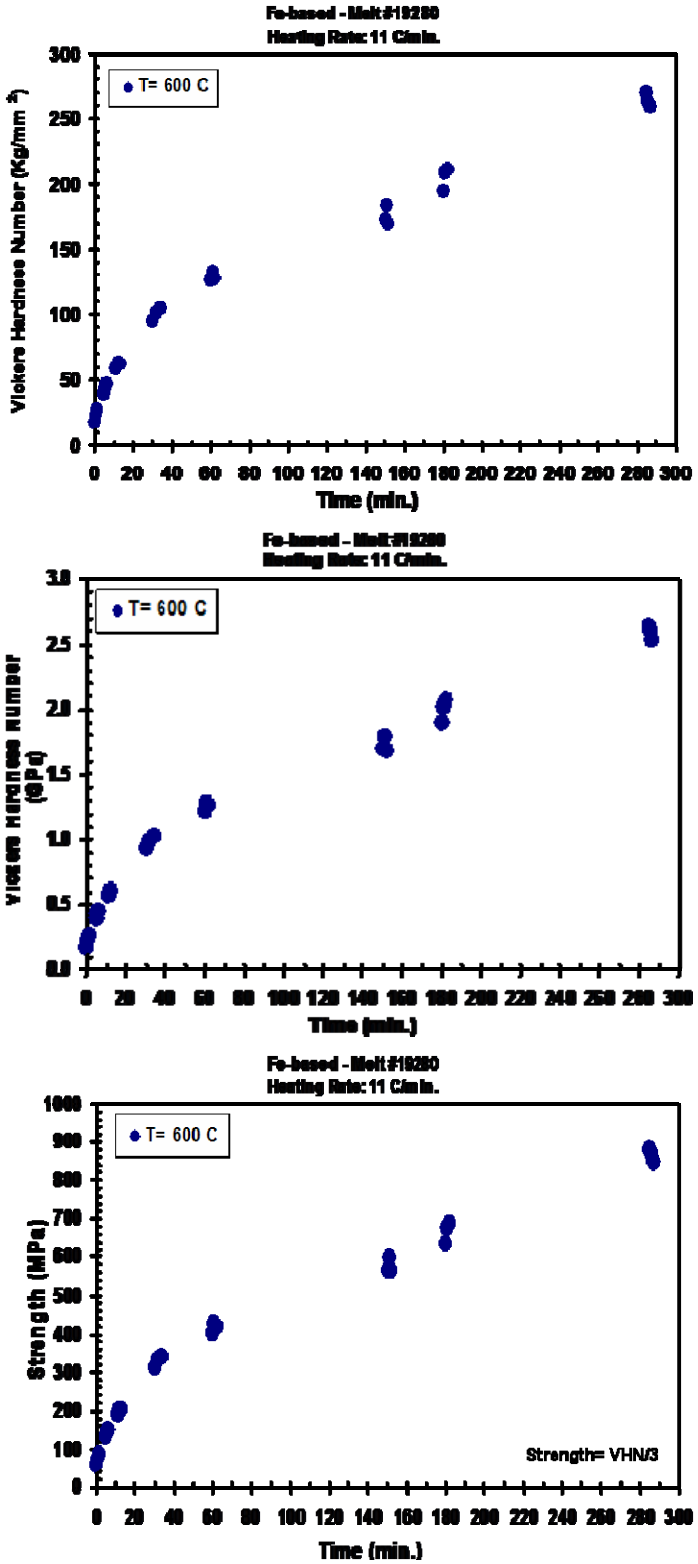

Figure 71. [Figure 5, Lewandowski] (a) Effects of exposure time at 600ºC on microhardness in kg/mm^2 of SAM1651; (b) effects of exposure time at 600ºC on microhardness in GPa of SAM1651; and (c) estimated compressive strength, which is VHN/3, for various exposure times at 600ºC for SAM1651.

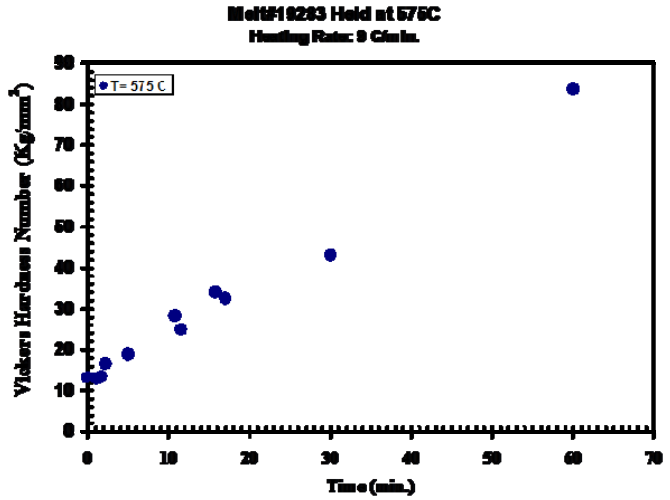

(a)

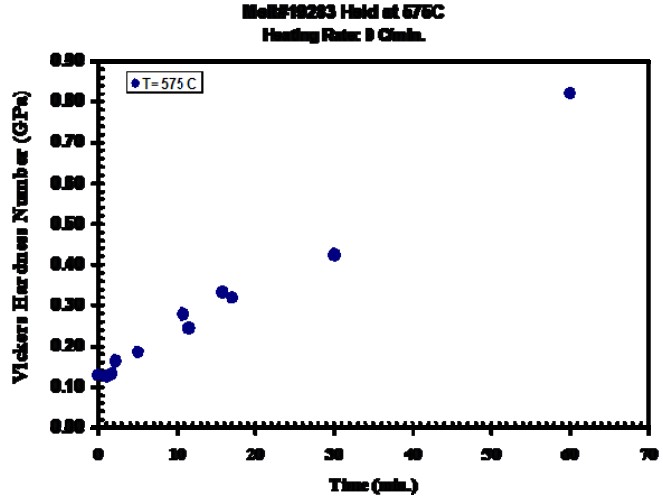

(b)

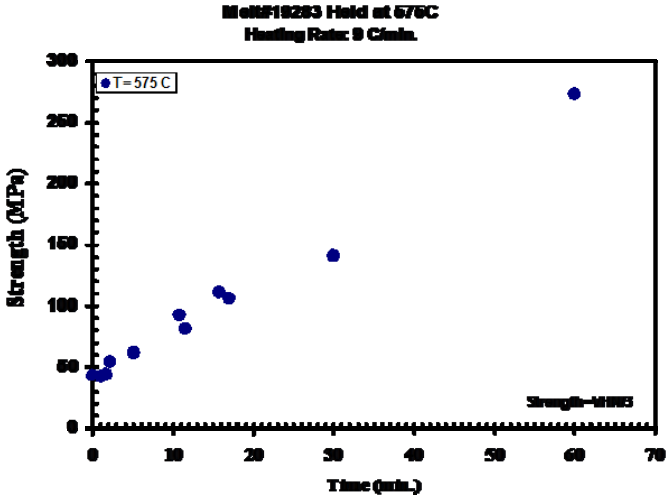

(c)

Figure 72. [Figure 6, Lewandowski] (a) Effects of exposure time at 575ºC on microhardness in kg/mm^2 of SAM1651; (b) effects of exposure time at 575ºC on microhardness in GPa of SAM1651; and (c) estimated compressive strength, which is VHN/3, for various exposure times at 575ºC for SAM1651.

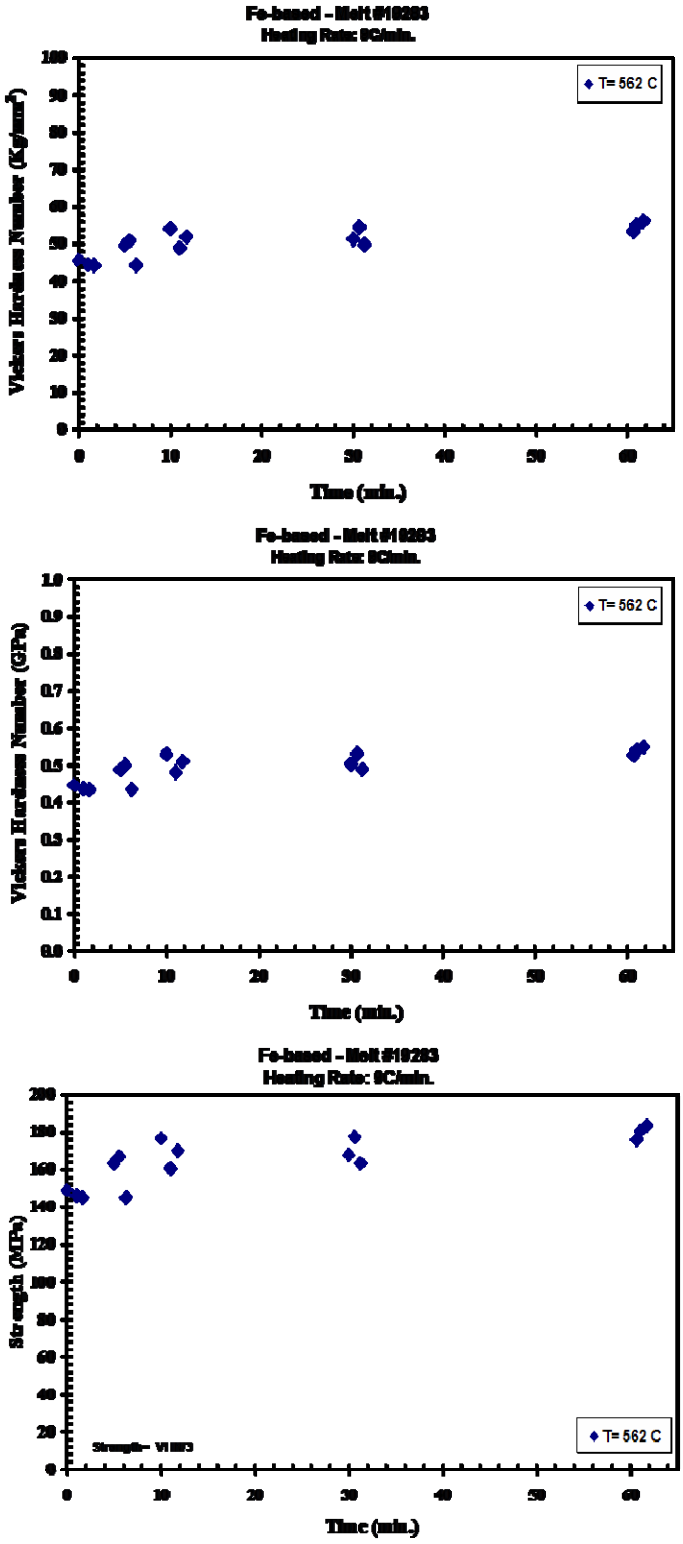

(a)

(b)

(c)

Figure 73. [Figure 7, Lewandowski] (a) Effects of exposure time at 562ºC on microhardness in kg/mm^2 of SAM1651; (b) effects of exposure time at 562ºC on microhardness in GPa of SAM1651; and (c) estimated compressive strength, which is VHN/3, for various exposure times at 562ºC for SAM1651.

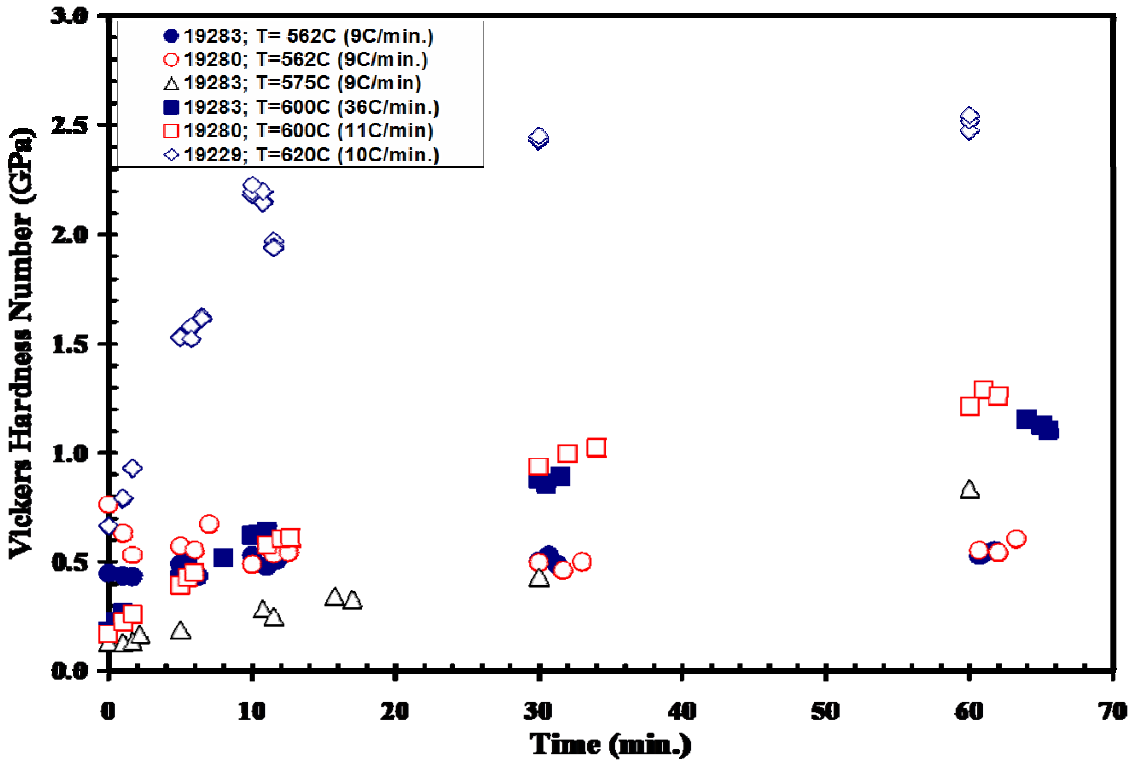

Figure 74. [Figure 8, Lewandowski] Summary showing effects of exposure time at test temperatures of 562ºC, 575ºC, 600ºC, and 620ºC on microhardness in GPa.

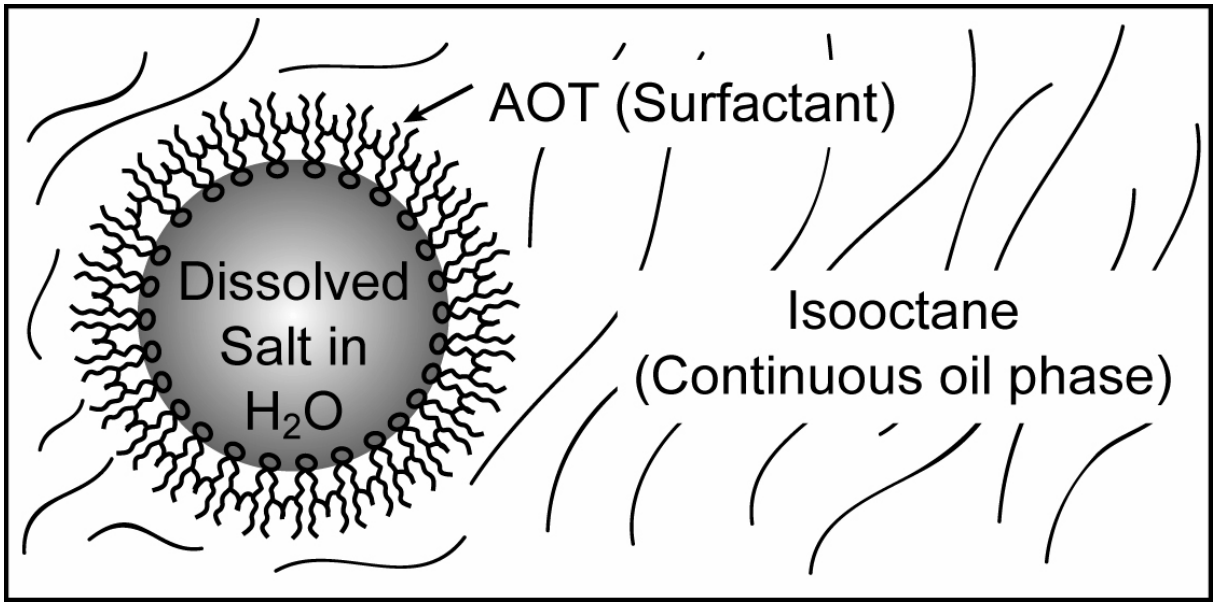

Figure 75. [Figure 1, Graeve] Schematic of a reverse micelle.

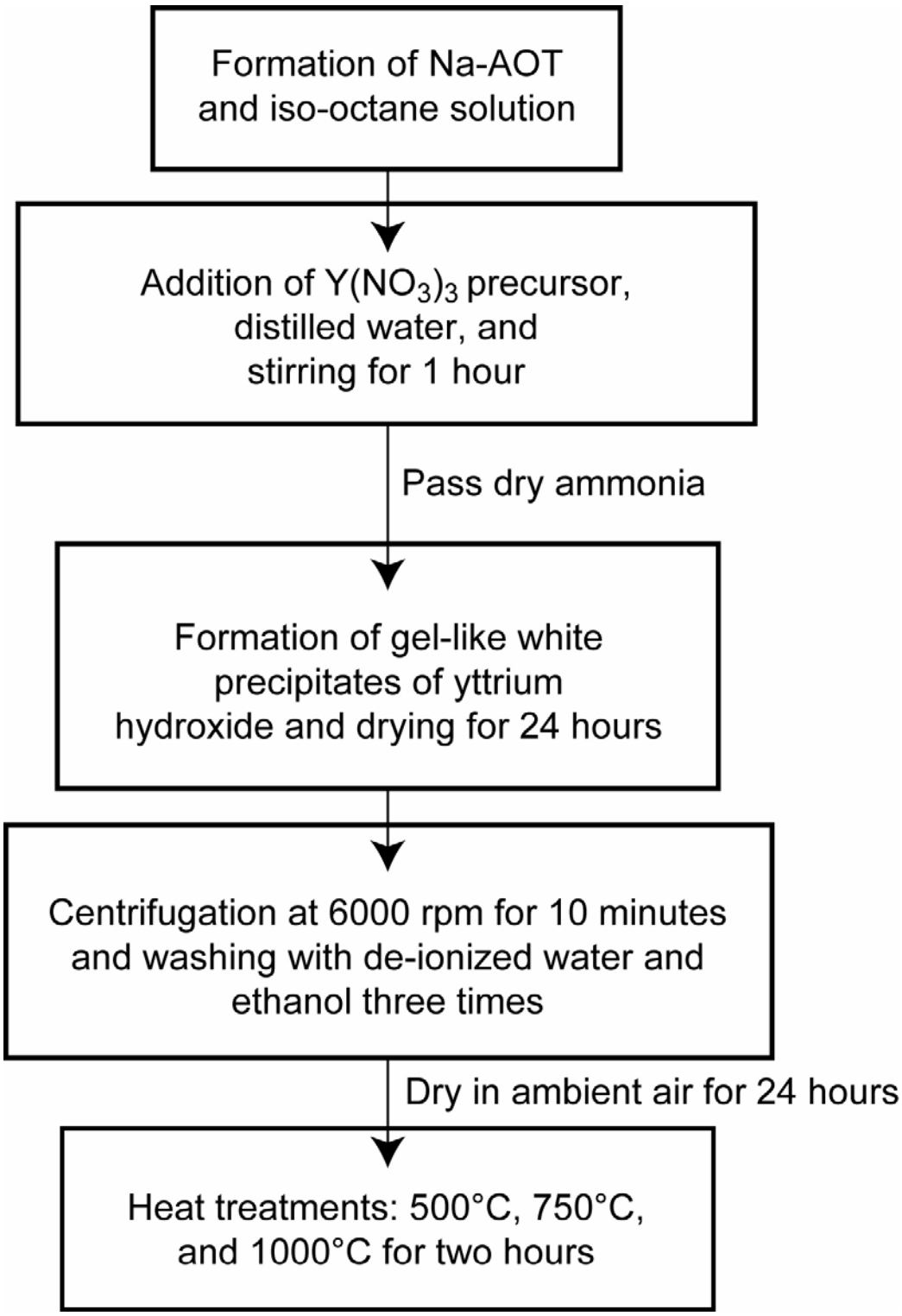

Figure 76. [Figure 2, Graeve] Process flow chart for the formation of Y_2O_3 nanopowders via the reverse micelle synthesis technique.

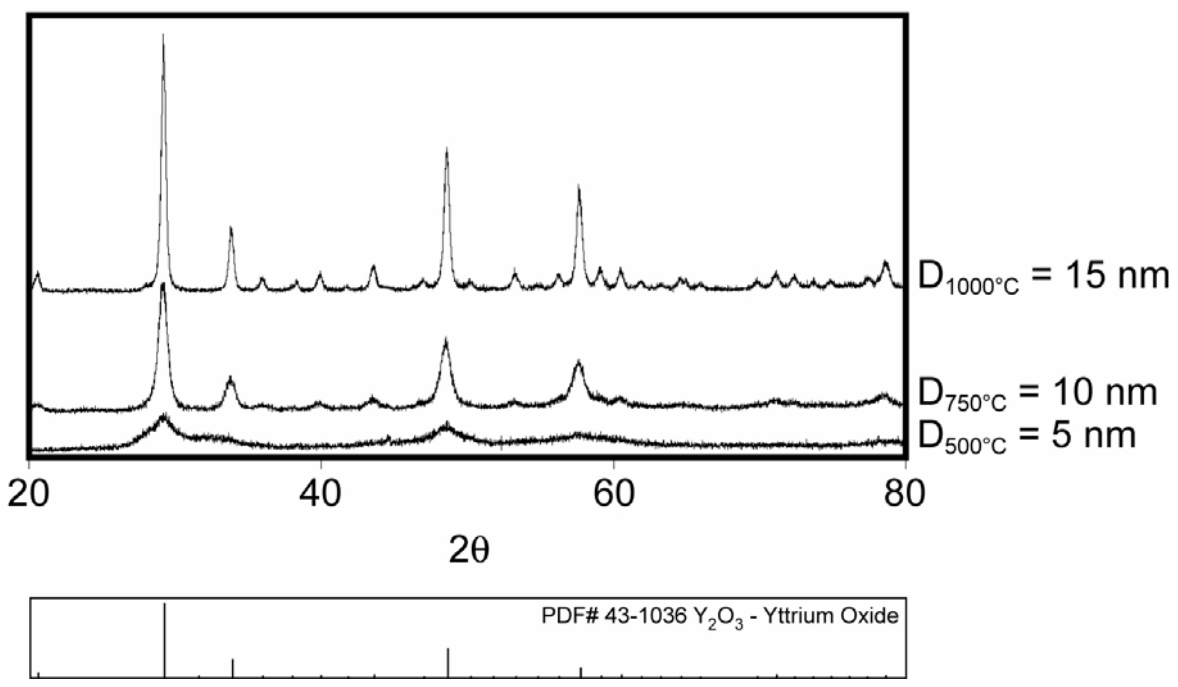

Figure 77. [Figure 4, Graeve] X-ray diffraction patterns for Y_2O_3 treated at 500°C, 750°C, and 1000°C.

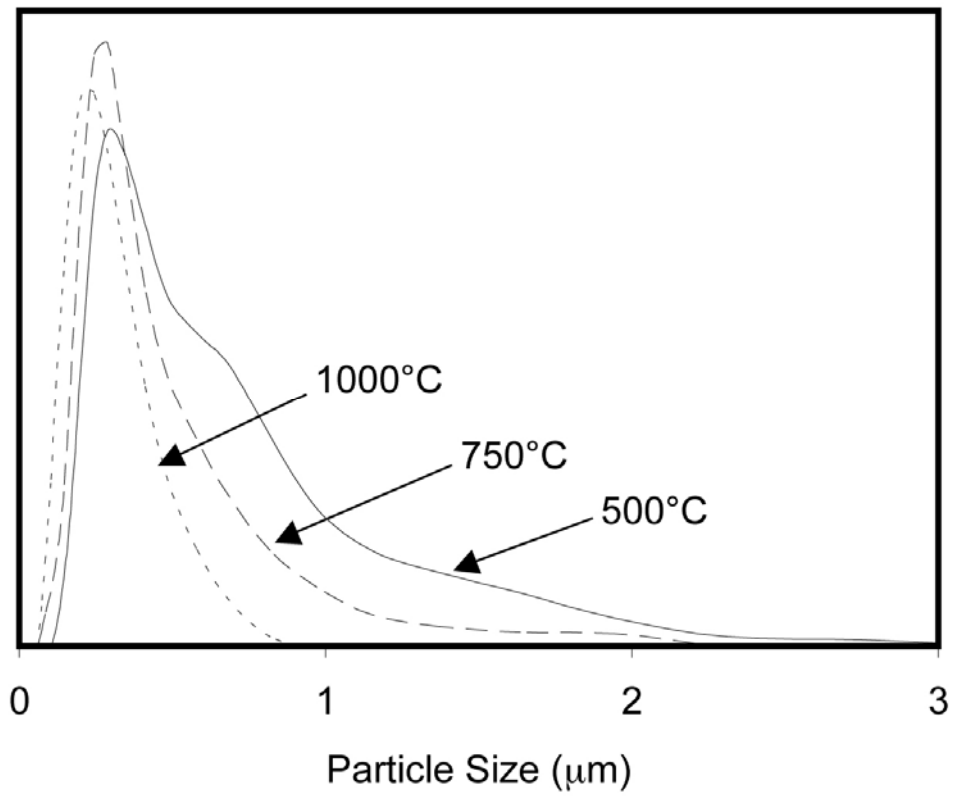

Figure 78. [Figure 5, Graeve] Particle size distribution of Y_2O_3 nanopowders.

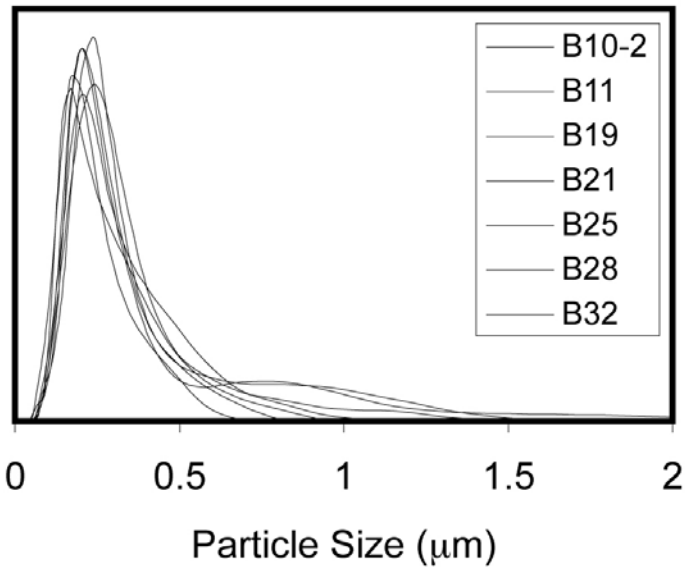

Figure 79. [Figure 6, Graeve] Particle size distribution of Y_2O_3 nanopowders treated at 1000°C for two hours.

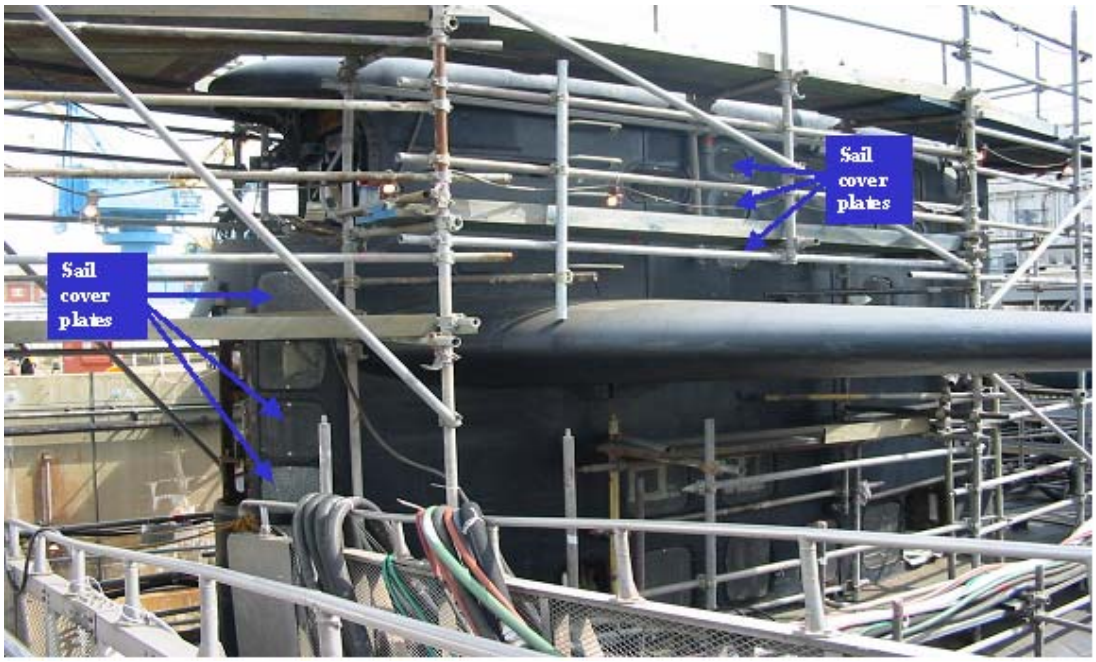

Figure 80. [Figure 1, Brown] Ex-Portsmouth 688 Class submarine sail with black epoxy coating on exterior.

Figure 81. [Figure 2, Brown] Extensive corrosion of the internal forward sail on the Ex-Portsmouth 688 Class submarine is shown.

Figure 82. (left) [Figure 3, Brown] Extensive corrosion on the internal aft sail of the Ex-Portsmouth 688 Class submarine; (right) [Figure 4, Brown] exterior forward sail of the Ex-Portsmouth 688 Class submarine with cover plates removed.

Figure 83. [Figure 5, Brown] Sail Cover Plates from 688 Class Submarine Ready for Coating at Caterpillar

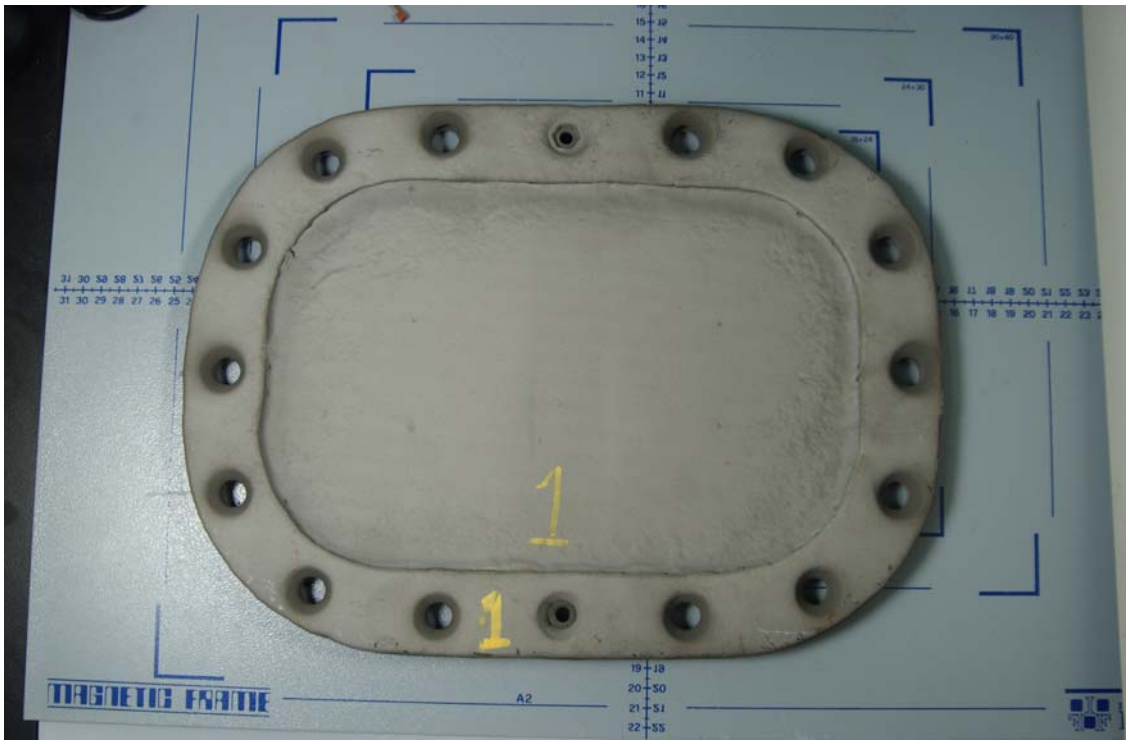

Figure 84. [Figure 6, Brown] Sail cover plate after application of thermal spray coating of SAM2X5. This plate and others like it are being tested in seawater at NRL Key West, with alternating immersion.

Figure 85. [Figure 7, Brown] Close up of sail cover plate edge, showing coating of only the front surface with the initial demonstration. More recently, articulation of the HVOF gun has enabled much better coating of the edges of these plates.

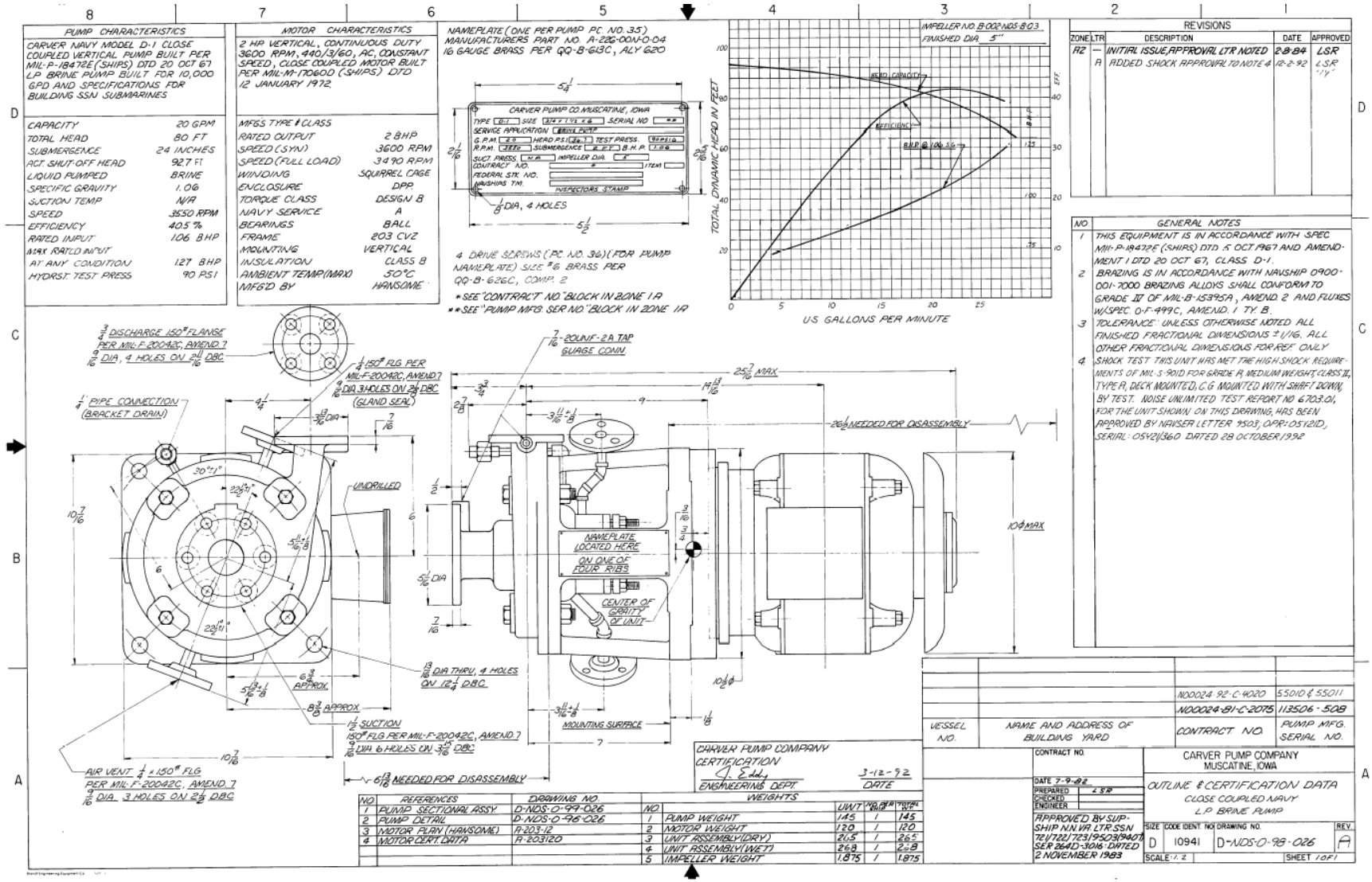

Figure 86. [Figure 8, Brown] Drawing of submaring brine pump.

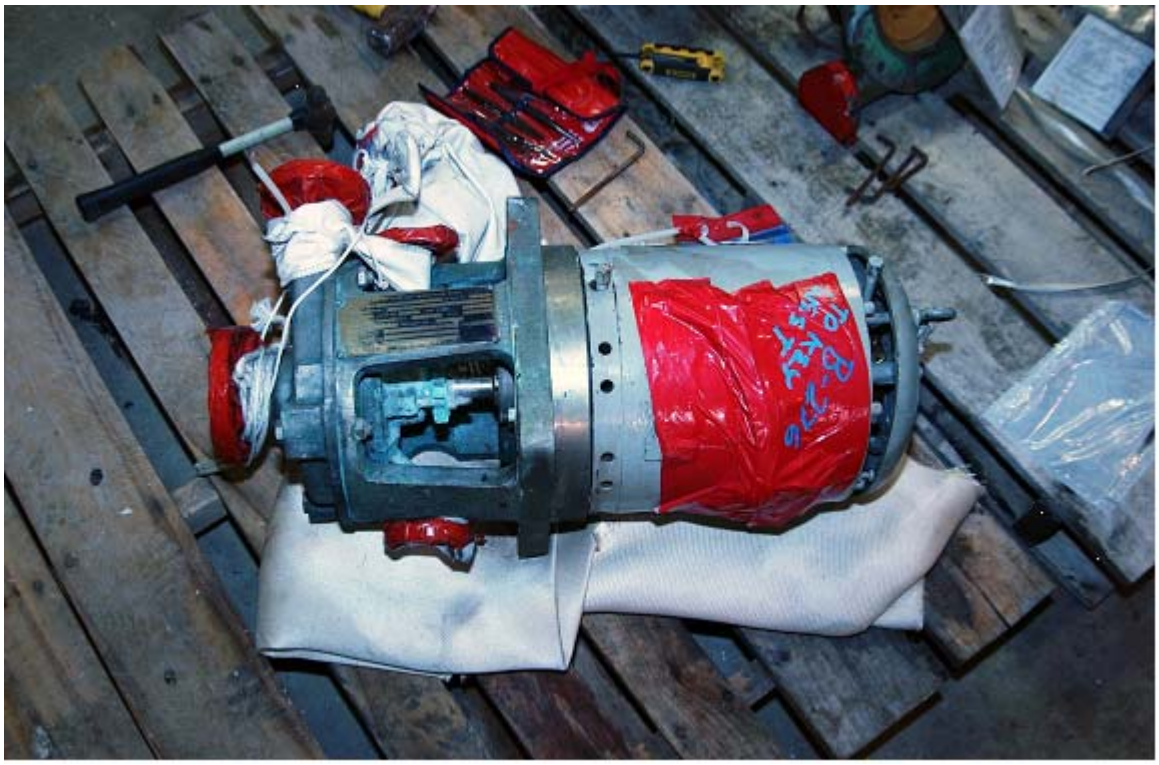

Figure 87. [Figure 9, Brown] Brine pump after removal from submarine.

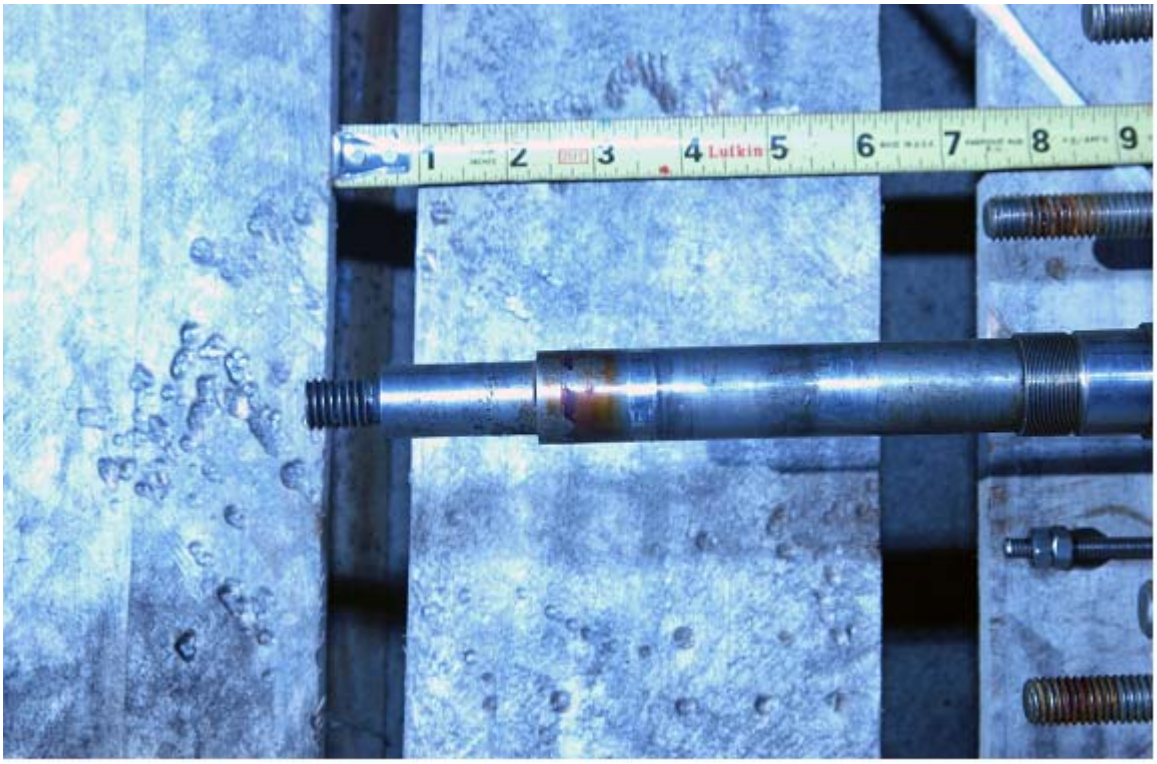

Figure 88. [Figure 10, Brown] Brine pump shaft after removal from pump housing, in preparation for thermal spray coating.

Figure 89. [Figure 1, Bayles] The amphibious naval ship USS PONCE.

Figure 90. [Figure 2, Bayles] Air intake plenum insert coated with SAM2X5.

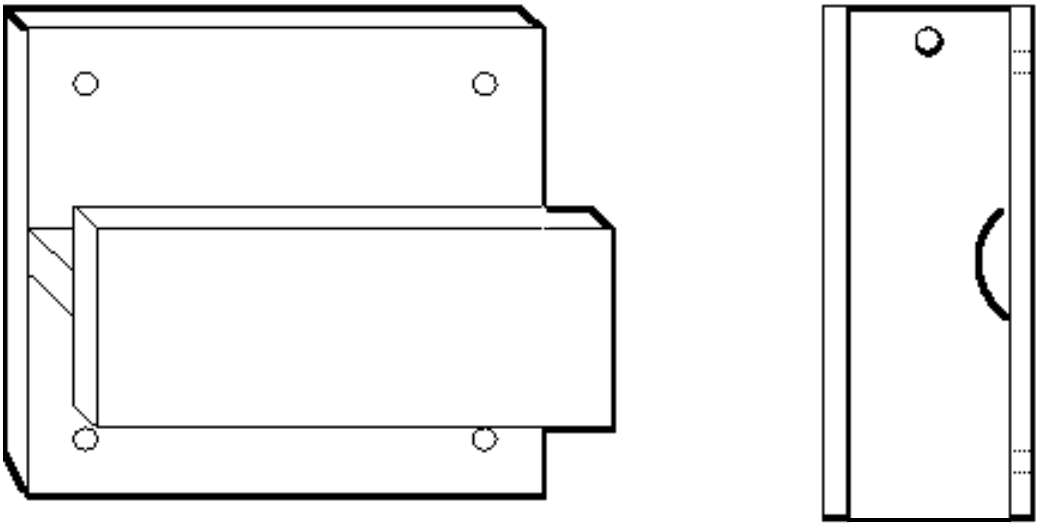

Figure 91. [Figure 3, Bayles] Schematic representation of air intake plenum insert coated with SAM2X5.

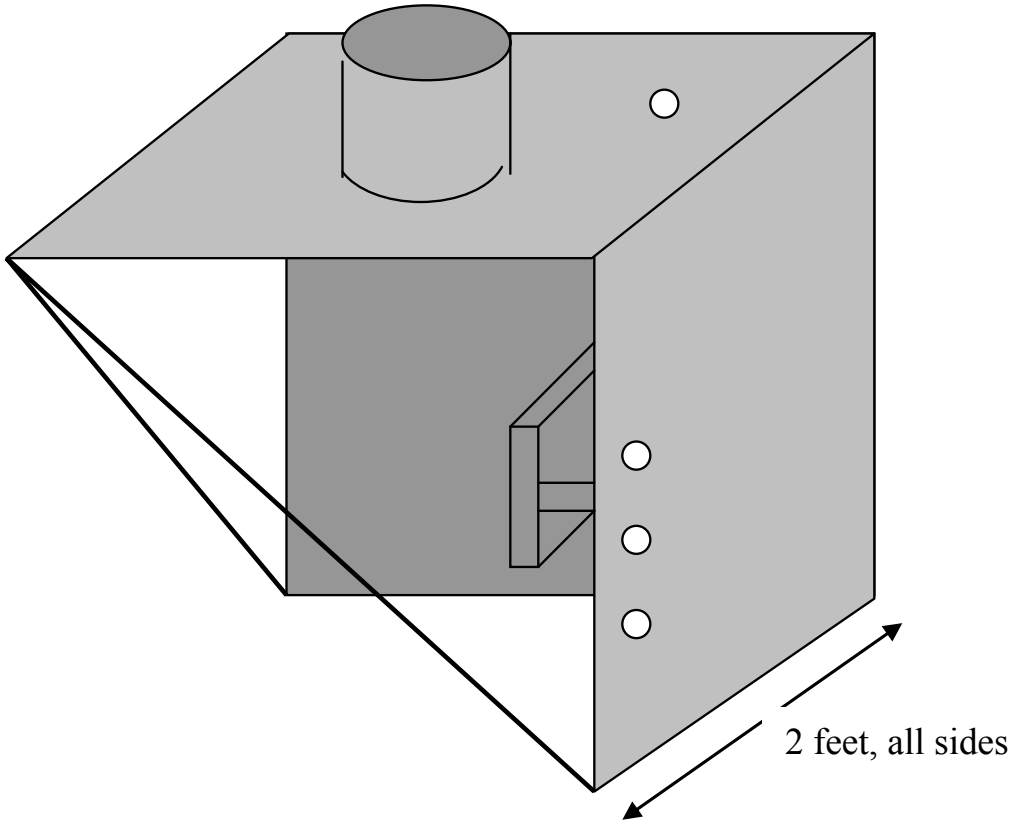

Figure 92. [Figure 4, Bayles] Simulated air intake plenum.

Figure 93. [Figure 5, Bayles] Well deck tank hatch covers.

Figure 94. [Figure 6, Bayles] Howitzer spades.

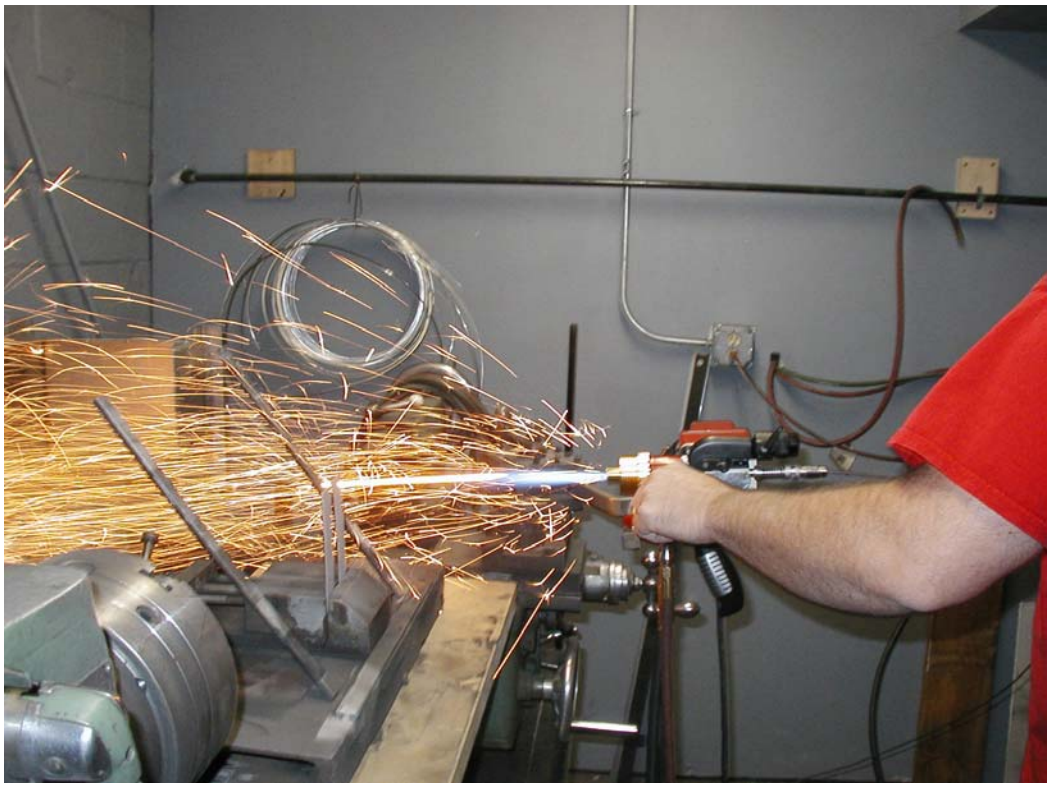

Figure 95. [Figure 7, Bayles] Wire HVOF process for dock-side coating.

Criticality Safety Analysis Results

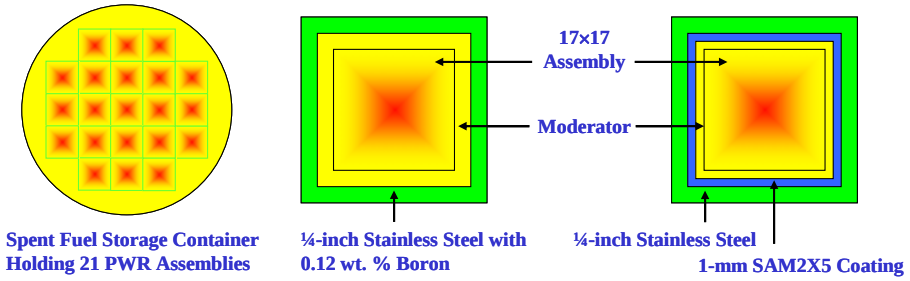

	¼-inch (6.4 mm) Stainless Steel Basket								
	No Boron	0.12 wt. % Boron	1 wt. % Boron	2 wt. % Boron	No Boron 1-mm SAM2X5	0.12 wt. % Boron 1-mm SAM2X5	No Boron 1-mm SAM1651	0.12 wt. % Boron 1-mm SAM1651	¼-inch Ni-Gd Basket Material
k_{eff}	0.96	0.91	0.85	0.83	0.87	0.86	0.90	0.88	0.86
Δk_{eff}	0.0	0.05	0.11	0.13	0.09	0.10	0.06	0.08	0.10

Figure 96. A formal criticality analysis of a 21-PWR container, with an amorphous metal coated basket, shows enhanced criticality safety. The benefits of using such materials on the basket material are evident.